High Relaxivity Contrast Agents for Magnetic Resonance Imaging (MRI)

Thesis Submitted for the Degree of
Doctor of Philosophy
at the University of Leicester

by

Marco Giardiello MChem (Leicester)
Department of Chemistry
University of Leicester

July 2007

Abstract

The development of Gd(III)-based contrast agents for MRI applications has intensified in recent years due to the paramagnetic ion's long electron spin relaxation time and large effective magnetic moment, μ_{eff}. Secondly, the exploitation of the long lived luminescent properties of the Ln(III) ions has lead to the development of luminescent lanthanide probes for sensing, time resolved immunoassay and imaging applications. Herein a series of novel Ln-DO3A based complexes are reported. Modulation of relaxivity, r_1, (Gd) and emission intensity (Eu, Tb, Sm and Dy) has been achieved in three ways:

Firstly, mono- and bis-methyl Ln-dpp-DO3A based complexes have been prepared, where dpp is a pendant diphenylphosphinamide moiety. These show pH responsive relaxivity (Gd) and luminescence (Eu) with calculated pK_a values of 8.65 (± 0.09) and 8.59 (± 0.14). Sensitised emission of Eu(III), Tb(III), Dy(III) and Sm(III) has been observed following excitation of the dpp antenna at λ_{ex} ~ 270 nm. Relaxivities have been measured as r_1 = 7.9 $mM^{-1}s^{-1}$ and r_1 = 8.2 $mM^{-1}s^{-1}$ in acidic media, q = 2 and r_1 = 5.4 $mM^{-1}s^{-1}$ and r_1 = 4.4 $mM^{-1}s^{-1}$ in basic media, q = 1 for the mono- and bis-methyl Gd-dpp-DO3A complexes respectively. The pH responsive behaviour has been attributed to the reversible ligation of the dpp moiety.

Secondly, non-covalent attachment of the mono- and bis-methyl Gd-dpp-DO3A-based complexes to Human Serum Albumin (HSA) at pH 7.4 resulted in a 64% (r_1 = 11.7 $mM^{-1}s^{-1}$) and a 146% (r_1 = 16.0 $mM^{-1}s^{-1}$) enhancement in relaxivity, with binding affinities, K, determined from luminescence studies as K = 22,268 ± 12% M^{-1} and K = 20,059 ± 14% M^{-1} for the mono- and bis-methyl dpp Eu-dpp-DO3A complexes respectively. The negatively charged $[Gd\text{-}dpp\text{-}aDO3A]^{3-}$ complex was developed in order to improve the observed relaxivity of the HSA bound species: r_1 = 16.0 $mM^{-1}s^{-1}$, K = 17,915 (± 14%) M^{-1}. Competitive binding studies with the fluorescent probes dansylsarcosine and warfarin showed each of the dpp complex analogues to bind preferentially to HSA site II, only the S-enantiomer of the mono-methyl Gd-dpp-DO3A showed an affinity for site I.

Finally, an accumulation and activation strategy following enzyme activity has been demonstrated. Neutral q = 2 Gd(III) ethyl and acetoxymethyl ester Ln-DO3MA based complexes have shown decreased relaxivity in the presence of carbonate due to the inner sphere water molecule displacement by bidentate anion binding. The binding is suppressed by the introduction of negative charge to the complex following enzymatic hydrolysis of the ester groups, resulting in ~ 84% relaxivity enhancement (Gd) as well as Eu luminescence quenching. The high observed relaxivity of the ethyl ester model: r_1 = 10.2 $mM^{-1}s^{-1}$ is attributed to the extremely short observed water exchange lifetime, τ_m = 7.9 ns.

Acknowledgements

Firstly, I would like to say thanks to my supervisor Dr Mark Lowe, for all his support during my PhD, as well as the rest of our group: Dr Jackie Hamblin, Rowena Griffin, Katie Proctor, Chris Wynn, Sheila Msami and James M^{c}Gregor. A big thank you to all the other members of the lab group, as well as Dr Gerry Griffith for the NMR analysis, Dr Graham Eaton for the mass spectrometry and Dr Chris Harrington for the ICP-MS measurements.

Secondly, I'd like to acknowledge Prof. Mauro Botta and Prof. Silvio Aime at the Università degli Studi di Torino, Italy and the rest of his research group: Elisa Elemento, Stefano Avedano and Dr Eliana Gianolio for hosting me in Turin and allowing me to run and collect all the relaxation measurements and data.

Also, thanks to my Mum, Dad and my brothers Dino and Danny for their support throughout my PhD, as well as all my friends.

Finally, I'd like to thank the EPSRC and The University of Leicester for funding.

Abbreviations

Å	Angstroms
acac	Acetylacetonato
aDO3A	1,4,7-tris[(4'-(carboxyl)-1'-carboxybutyl]-1,4,7,10-tetraazacyclododecane
a.u.	Arbitrary Units
BOC	tert-butoxycarbonyl
B.M.	Bohr Magnetons
Bp	Boiling Point
BPCA	Blood Pool Contrast Agent
Calcd	Calculated
CEST	Chemical Exchange Saturation Transfer
c.f.	confer (compare)
cm^{-1}	Per centimetre
C.N.	Coordination Number
^{o}C	Degrees Centigrade
δ	Delta (NMR Chemical Shift)
δ	Delta (Chelate Ring Helicity) Right Hand
Δ	Delta (Change in) or Configurational Chirality, Right Hand
Da	Dalton
DAB	Diaminobutane
ΔG	Gibbs Free Energy Change
ΔH	Enthalpy Change
ΔS	Entropy Change
DCM	Dichloromethane
DELFIA®	Dissociation Enhanced Lanthanide Fluoroimmunoassay
DIPEA	N,N-Diisopropylethylamine
DMF	Dimethylformamide
DPE/PA	Phosphatidyl Ethanolamine/Palmatic acid
DO3A	1,4,7-tris(carboxymethyl)-1,4,7,10-tetraazacyclododecane
DO3AMPh	1,4,7,10-tetraazacyclododecane-1,4,7-tris(*N*-(1-phenylethyl)acetamide)
DO3MA	1,4,7-tris(1'-carboxyethyl)-1,4,7,10-tetraazacyclododecane
DOTA	1,4,7,10-tetra(carboxymethyl)-1,4,7,10-tetraazacyclododecane
DOTAM	1,4,7,10-tetraazacyclododecane-1,4,7,10-tetraacetamide
DOTMA	1,4,7,10-tetra(1'-carboxyethyl)-1,4,7,10-tetraazacyclododecane

dpp	diphenylphosphinamide
DTPA	Diethylenetriamine Pentacetate
DTTA	Diethylene Triamine Tetraacetic Acid
ED	Electric Dipole
EDTA	Ethylenediaminetetraacetato
e.g.	exempli gratia (for example)
ENDOR	Electron-nuclear double-resonance
EOB	Ethoxybenzyl
EPTA	Ethylenepropylenetriaminepentaacetic Acid
ESMS	Electrospray Mass Spectrometry
EtOH	Ethanol
eV	Electronvolts
Exp	Experimental
FAB	Fast Atom Bombardment
FID	Free Induced Decay
GDCEP	Gadolinium Cysteine Diethyl ester Copolymer
G	Grams
GDCP	Gadolinium Cysteine Copolymers
gDO3A	1,4,7-tris[(3'-(carboxyl)-1'-carboxypropyl]-1,4,7,10-tetraazacyclododecane
gDOTA	1,4,7,10-tetra-azacyclododecane-1,4,7,10-tetraglutamic acid
HOPO	Hydroxypyridonato
HPLC	High-performance liquid chromatography
HSA	Human Serum Albumin
Hz	Hertz
ICP-MS	Inductively Coupled Plasma Mass Spectrometry
i.e.	id est (that is)
in vitro	In an artificial environment outside a living organism
in vivo	Within a living organism
IR	Infrared
ISC	Intersystem Crossing
K	Kelvin
KJ mol^{-1}	Kilojoules Per Mole
λ	Lambda (Chelate Ring Helicity) Left Hand
Λ	Lambda Configurational Chirality, Left Hand

λ_{ex}	Wavelength of Excitation
λ_{em}	Wavelength of Emission
λ_{max}	Wavelength of Maximum Emission/Absorption
LIS	Lanthanide Induced Shift
LMCT	Ligand to Metal Charge Transfer
M	Molar
M^{-1}	Per Molar
μg	Microgram
μl	Microlitre
μM	Micromolar
μmol	Micromole
mg	Milligram
ml	Millilitre
mM	Millimolar
$mM^{-1}s^{-1}$	Per Millimolar Per Second
mmol	Millimole
ms	Millisecond
ms^{-1}	Per Millisecond
MALDI	Matrix Assisted Laser Desorption Ionisation
MD	Magnetic Dipole
MeOH	Methanol
MeCN	Acetonitrile
MHz	Megahertz
MR	Magnetic Resonance
MRA	Magnetic Resonance Angiography
MRI	Magnetic Resonance Imaging
NBA	Nitrobenzyl Alcohol
NMR	Nuclear Magnetic Resonance
NMRD	Nuclear Magnetic Resonance Dispersion
ns	Nanosecond
PAMAM	Polyamidoamide
PARACEST	Paramagnetic Chemical Exchange Saturation Transfer
PBS	Phosphate Buffered Saline
Per Se	Itself
PEG	Polyethylene Glycol

PGA	Poly(L-glutamic Acid)
ppm	Parts Per Million
ps	Picosecond
rad s^{-1}	Radians Per Second
RIME	Receptor induced Magnetisation Enhancement
RF	Radio Frequency
SAP	Square Antiprismatic
T	Tesla
TAFI	Thrombin-Activatable Fibrinolysis Inhibitor
TFA	Triflouroacetic acid
THF	Tetrahydrofuran
TMS	Tetramethylsilane
TSAP	Twisted Square Antiprismatic
UV	Ultraviolet
via	By means of
ν_{max}	Maximum Vibrational Frequency
vs.	Versus
VT	Variable Temperature
wt	Weight
ZFS	Zero Field Splitting

Contents

Equations

Figures

Schemes

Tables

Chapter 1

Introduction

1.1 Metals in Medicine

Biomedical inorganic chemistry offers great potential to pharmaceutical industries for the design of novel diagnostic and therapeutic agents, which have traditionally been dominated by organic chemistry. Metal ions play an important role in biological processes e.g. the iron containing oxygen carriers haemoglobin and myoglobin; the zinc and copper containing superoxide dismutase for elimination of the extremely reactive superoxide radical, $O_2^{\bullet -}$.

Medicinal inorganic chemistry has been greatly enhanced by the success of the anticancer agent cisplatin.[1, 2] The vast range of research into metal-containing drugs includes:

- enzyme inhibitors (e.g. Au (glutathione peroxidase), Zn (HIV-1 integrase))
- radiopharmaceuticals, both diagnostic (e.g. γ-emitting ^{99m}Tc for Single Photon Emission Computated Tomography (SPECT) and β^+-emitting ^{68}Ga for Positron Emission Tomography (PET)) and therapeutic (e.g. ^{186}Re, ^{153}Sm; both γ and β^- emitters)
- essential elements mineral supplements (e.g. Fe (haemoglobin), Cu (cytochrome c oxidase), Zn (superoxide dismutase; Cu and Zn), purple acid phosphatase; (Fe and Zn), Se (co-factor for thyroid hormone deiodinase)
- therapeutic agents (e.g. Pt (cancer), Au (arthritis), V (insulin mimic))
- diagnostic contrast agents; Magnetic Resonance Imaging (e.g. Gd(III) and Mn(II); both paramagnetic)

1.1.1 Metal Containing Drug Design

When designing metal-containing drugs it is important to take into account several factors, such as:

- toxicity
- stability
- biodistribution

To avoid toxicity metal ions are not usually administered as salts, the antidepressant lithium carbonate being one of the few exceptions. An excess of metal ions in the body can be extremely harmful, for example, mercury ions attack the central nervous system leading to neuropsychiatric problems when in excess.[3] The treatment for excess metal ions is the administration a chelating agent, which forms a stable complex with the ion and is then excreted by the patient.

If metal ions are to be used in drugs they must therefore be administered as stable complexes. The chelate effect is the increased stability of chelated complexes compared with their monodentate analogues. The addition of a chelating agent results in an increase in the number of independent molecules in solution and, therefore, a more positive entropy, ΔS, contribution to the Gibbs free energy, ΔG, of the complex formation. This leads to a more favourable negative ΔG value (Equation 1).[4]

$$\Delta G = \Delta H - T\Delta S \qquad (1)$$

The hard/soft nature of the metal ion will determine the choice of chelating ligand used i.e. hard metals, such as Al(III), will favour hard donors, such as the oxygen and nitrogen in 1,2-dimethyl-3hydroxypyrid-4-one, **L1**[5, 6]; soft metals, such as Hg(II), will favour soft donors, such as the thiols in 2,3-dimercapatopropanol, **L2**.[7]

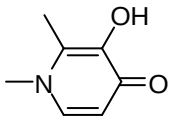

L1

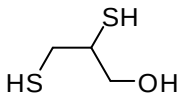

L2

To ensure metal ions will not leach from the complex once administered, the chelating ligands chosen must ensure complex stability. Biological systems operate at 37^{o}C and at thermodynamic equilibrium, maintained by enzymes, whole cells and proteins such as albumin. Local pH of the stomach, however, is low while local concentrations of endogenous metal ions may be high. Kinetic stability of the complex is essential to ensure acid or cationic catalysed demetallation does not occur. If the timescale of the demetallation process is longer than the duration of the complex *in vivo*, the thermodynamic stability may not be an issue. To increase kinetic stability coordination numbers of the complex must be high, oxidation states must be stable and charge must be positive or neutral to avoid protonation or cationic interactions.[8]

Biodistribution of metal complexes by perfusion (blood flow) is determined by shape, charge, redox properties and lipophilicity. Localisation of metal complexes is also achieved by coordinating the complex to a targeting vector such as a small peptide or an antibody fragment.

Low molecular weight, charge neutral complexes are desired for e.g. cell permeation and passage through the blood brain barrier. The γ-emitting technetium-based charge neutral imaging agent, **Tc.L3**, is used in single photon emission computed tomography (SPECT). The agent undergoes enantiospecific enzyme activation, where upon penetration of the blood brain barrier the SS enantiomer transforms to a more hydrophilic negatively charged species following esterase hydrolysis. The RR enantiomer is not a substrate for esterase in the brain and, therefore, the complex is not hydrolysed and readily diffuses back out.[9]

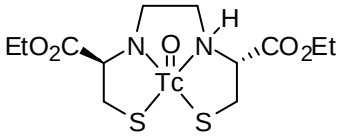

Tc.L3

The overall complex charge influences the biodistribution and accumulation by perfusion and complex clearance. Neutral, hydrophobic compounds tend to accumulate in fatty tissue and clear through the hepatobiliary system (liver), while charged complexes tend to clear *via* the renal system (kidney). Small lipophilic positively charged species often accumulate in the heart while negatively charged compound accumulate in the kidneys. **Tc.L4** and **Tc.L5** are technetium-based imaging agents which accumulate in the heart and are cleared *via* the blood, lungs and liver.[10, 11]

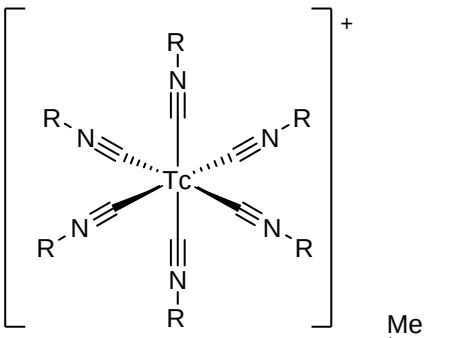

Tc.L4

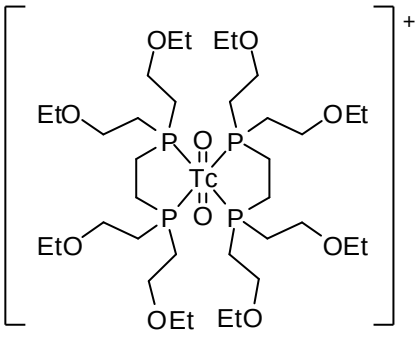

Tc.L5

1.2 Magnetic Resonance Imaging (MRI)

The concept of magnetic resonance imaging was developed in 1972 by Paul Lauterbur, a chemist at the University of Illinois, U.S.A., and Sir Peter Mansfield, a physicist at the University of Nottingham, U.K., who jointly won the Nobel Prize in 2003 for

Physiology or Medicine.[12, 13] MRI is essentially a proton NMR experiment carried out on the human body, visualising water protons due to the high abundance of water molecules in biological systems. Application of varying pulse sequences and magnetic field gradients allows for highly detailed, non-invasive three-dimensional images of the body to be obtained.

1.2.1 Principles of NMR

An important factor in understanding NMR is the concept of angular momentum. Angular momentum refers to an object moving on a circular path around a reference point. This is related to nuclei as spin angular momentum, the magnitude of which, $|I|$, is defined as

$$|I| = \hbar\sqrt{I(I+1)},\ \hbar = \frac{h}{2\pi} \tag{2}$$

where h is Planck's constant and I is the spin quantum number.

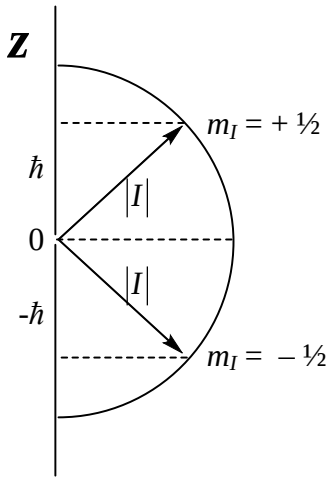

Figure 1. Orientation of m_I around the z-axis for an I = ½ nucleus. There are two possible orientations for an I = ½ nucleus; +½ and –½.

The most commonly observed nuclide by NMR is the spin ½ ^{1}H. The angular momentum is arbitrarily quantisised along the z-axis of an orthogonal coordination system. Figure 1 shows the possible orientations of the spin angular momentum around the z-axis for a spin ½ nuclei, where m_I, the magnetic quantum number, is equal to $-I$, $-I+1$,…, I totalling $2I+1$; the total number of orientations.

Nuclear spin is the fundamental term which will determine if nuclei are observable by NMR spectroscopy. The spin quantum number, I, is composed of the sum of the individual contributions of each of the unpaired protons and neutrons present, each possessing spin of ±½. In order to be observable by NMR the nuclei must posses a non zero value of I. The properties of nuclei commonly observed in NMR experiments are show in Table 1.[14]

Nuclide	Spin	Magnetic Moment	Gyromagnetic Ratio
	I	μ / μ_N	γ (10^7 $T^{-1}s^{-1}$)
^{1}H	½	2.79285	26.752
^{2}H	1	0.85745	4.1067
^{13}C	½	0.7023	6.7272
^{14}N	1	0.40356	1.9328
^{31}P	½	1.1317	10.840

Table 1. Magnetic properties of nuclei commonly observed by NMR spectroscopy (where μ_N is the nuclear magneton, 5.05079×10^{-27} J T^{-1})

The spin of any nuclide is proportional to its magnetic moment, μ

$$\mu = \gamma I \tag{3}$$

where γ is the gyromagnetic ratio. Each value of m_I corresponds to a different orientation of nuclear spin and, therefore, nuclear magnetic moment. When placed in a magnetic field, nuclei with spin angular momentum will behave as bar magnets and will align themselves along the external magnetic field, B_o, which by convention is oriented along the *z*-axis. The *z*-components of the magnetic moment will align either parallel or antiparallel with the magnetic field (Figure 2). The magnitude of the magnetic moment in the *z*-direction, μ_z, is

$$\mu_z = \gamma I_z = m_I \gamma \hbar \tag{4}$$

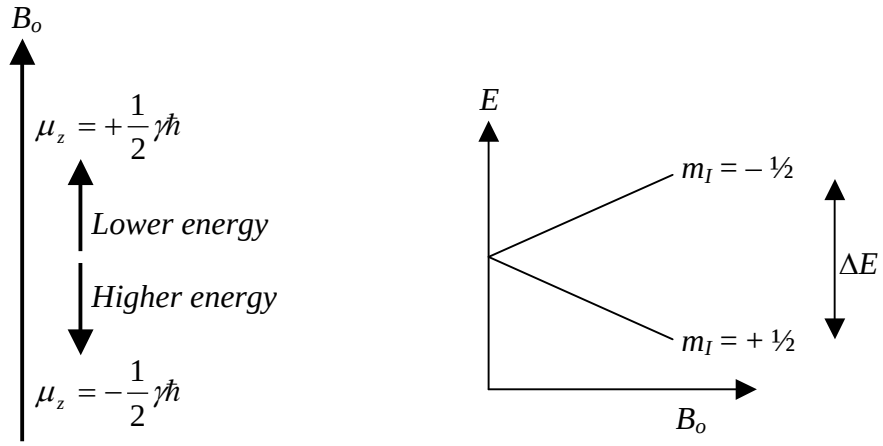

Figure 2. Alignment of magnetic moments, μ_z, in a magnetic field, B_o.

The magnetic energy of a nucleus placed in a magnetic field is

$$E = -\mu_z B_o = -m_I \hbar \gamma B_o \tag{5}$$

The selection rule for an NMR transition between the m_I-states is

$$\Delta m_I = \pm 1 \tag{6}$$

The energy difference between two m_I-states is

$$\Delta E = \gamma \hbar B_o \tag{7}$$

and is therefore proportional to the magnetic field strength. The nucleus must be supplied with the required energy, ΔE, in the form of electromagnetic radiation in order for a transition into a higher energy state to occur. Likewise, if a transition is to a lower energy state electromagnetic radiation equal to the energy difference, ΔE, is emitted.

The angular frequency for the electromagnetic radiation of an m_I-state transition is

$$\omega_o = \gamma B_o \tag{8}$$

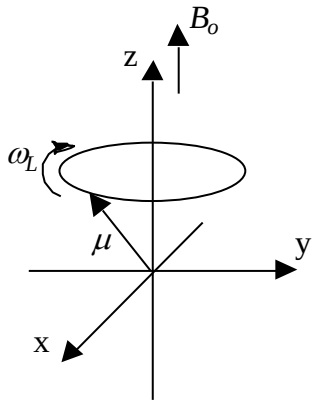

Figure 3. Angular velocity of nuclei.

In a magnetic field, μ revolves around B_o with angular velocity, ω_L (Figure 3).

$$\omega_L = -\gamma B_o \tag{9}$$

The angular velocity, ω_L, is known as the Larmor frequency, and is identical to the angular frequency, ω_o, required for an energy transition to take place. For this reason, angular frequency is also known as Larmor frequency.[15]

1.2.2 NMR Signal

An NMR signal arises from the difference in energy absorbed or emitted during transitions between two m_I-states. Boltzman distribution is employed in order to calculate the relative populations of the lower energy, N^+, and higher energy, N^-, m_I-states (Equation 10)

$$\frac{N^+}{N^-} = e^{\frac{-\Delta E}{kT}} \tag{10}$$

where ΔE is the energy difference between the m_I-states, k is the Boltzman constant (1.3805×10^{-23} J K^{-1}) and T is the temperature in Kelvin. According to the Boltzman distribution the lower energy, N^+ m_I-state is most populated in the absence of a magnetic field. The individual spins rotate at random phases around the *x*,*y*-plane when placed in a magnetic field. Application of a 90° radio frequency (RF) pulse, B_1, equivalent to the Larmor frequency along the *x*,*y*-plane will cause bunching of the individual spins, known as coherence. If the RF field is applied for a long enough time the net magnetisation, *M*, will flip onto the *x*,*y*-plane. All the spins are now in the same phase and precess around B_o at the Larmor frequency (Figure 4). Application of a 90° RF pulse causes the m_I-states to be equally populated as longitudinal magnetisation has been converted to transverse magnetisation. After a 180° RF pulse has been applied the Boltzman distribution is inverted. The spins will continue to precess around B_o until the RF field is removed, at which point spin relaxation processes will cause loss of coherence as magnetisation returns to its equilibrium position. The individual spins begin to precess about the *x*,*y*-plane at different resonant frequencies, inducing a radiofrequency in the NMR spectrometer detector coils, which detects only transverse magnetisation. As equilibrium is re-established the coils detect a loss in radiofrequency known as free induced decay (FID), which is transformed into an NMR spectrum by the mathematical technique Fourier Transformation.

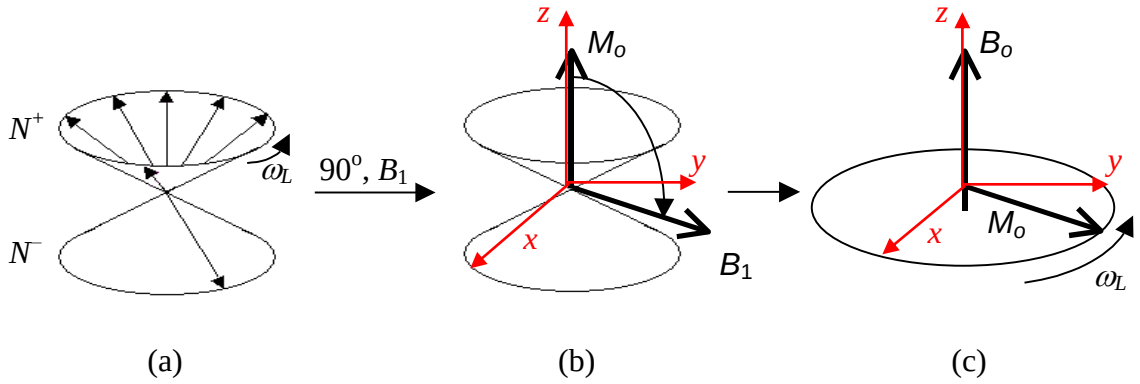

(a) (b) (c)

Figure 4. Coherence of individual spins following a 90° RF pulse. (a) the equilibrium Boltzman distribution of spins when nuclei are placed in a magnetic field. (b) the net magnetisation, M, flips 90° onto the x,y, plane. (c) the m_I-states are now all in the same phase and precess around the magnetic field, B_o, at Larmor frequency, ω_L.

1.2.3 Longitudinal (Spin-Lattice) Relaxation Time, T_1

Figure 4 shows that at equilibrium the net magnetisation, M_o, is in line with the applied magnetic field, B_o, and, therefore, the z-component of magnetisation, M_z, is equal to M_o, and is referred to as the longitudinal magnetization. Following a 90° RF pulse, the longitudinal magnetisation is converted to transverse as the spins revolve about the x,y-plane and thus $M_z = 0$. The time taken for M_z to return to its equilibrium value is known as the longitudinal relaxation time, T_1. The motions of molecules in the surroundings (the lattice) cause fluctuations in the local magnetic field, re-establishing Boltzman distribution of the m_I-states. The equation for the return to equilibrium following this process is

$$M_z = M_o\left(1-e^{-\tau/T_1}\right) \tag{11}$$

where τ is the delay time following the 90° RF pulse.

If a 180° RF pulse is applied, the net magnetisation will be inverted along the z-axis. M_z will then return back to its equilibrium position along the z-axis at a rate governed by T_1. The equation for the return to equilibrium following this process is

$$M_z = M_o\left(1-2e^{-\tau/T_1}\right) \tag{12}$$

where τ is the delay time following the 180° RF pulse.

1.2.4 *Measurement of T_1: The Inversion Recovery Experiment*

T_1 can be accurately measured by a pulsed NMR technique known as inversion recovery. Nuclei are subjected to a 180° RF pulse and are allowed to relax back towards equilibrium for a delay time, τ, after which a 90° RF pulse is employed and a FID is detected and the intensity of the signal is determined (Figure 5). The sequence is repeated for a series of τ. Equation 11 shows that by plotting $\ln[I(\infty)-I(\tau)]$ *vs.* τ, T_1 can be determined (where $\ln I(\infty)$ is the intensity of the fully relaxed sample).

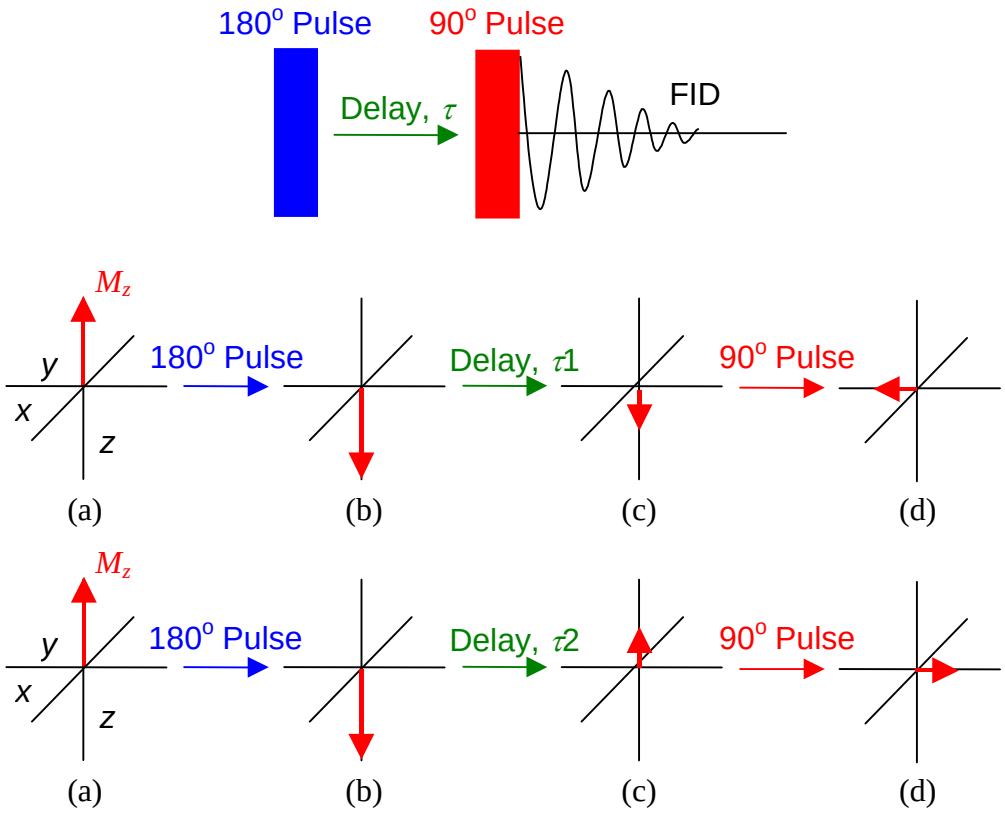

Figure 5. The inversion recovery experiment. (a) the M_z component of the net magnetisation is in line with the magnetic field, B_o, and, thus $M_o = M_z$. (b) M_z flipped across the z-axis following a 180° RF pulse. (c) the M_z returning to equilibrium following a delay time, τ, where above shorter delay is employed, $\tau 1$, compared to the longer $\tau 2$ below. (d) M_z to be flipped onto the x,y-plane following a 90° RF pulse, from where a FID is detected and the signal intensity is recorded.

1.2.5 *Transverse (Spin-Spin) Relaxation Time, T_2*

Following a 90° RF pulse, the spins precess coherently around the x,y-plane. Coherence is lost as each of the individual spins return to equilibrium and "fan out" around the x,y-plane, re-establishing transverse magnetisation, M_{xy} (Figure 6).

The process for M_{xy} to return to its equilibrium value is known as transverse relaxation time, T_2. Transverse relaxation occurs at the same time as longitudinal relaxation, however T_2 is always shorter than or equal to T_1.

$$M_{xy} = M_{xyo} e^{-\tau/T_2} \tag{13}$$

Determination of T_2 can be carried out by measurement of spectral line width at half height. The length of transverse relaxation time has an effect on the line broadening of NMR spectra. The line width at half height is governed by

$$\Delta\nu_{1/2} = \frac{1}{\pi T_2} \tag{14}$$

where $\Delta\nu_{1/2}$ is the frequency, in hertz, at half height. Therefore, as T_2 increases, line widths become narrower in NMR spectra.

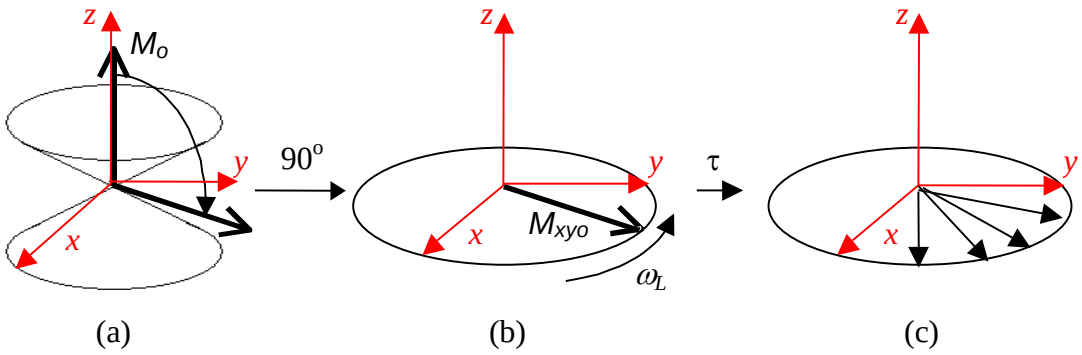

Figure 6. Transverse relaxation, T_2. (a) the spins are flipped onto the *x*,*y*-plane following a 90° RF pulse. (b) the net magnetisation processes around the *x*,*y*-plane at Larmor frequency. (c) the spins start to return to equilibrium, restoring transverse magnetization M_{xy}, as they "fan out" around the *x*,*y*-plane.

So far it has been assumed that the varying frequencies of the spins away from Larmor frequencies arise solely due to interactions within the sample. It is important, however, to bear in mind the bulk inhomogenity of the magnet, ΔB_o, i.e. the field varies at different locations of the sample, and contributes to the observed transverse relaxation time in an NMR signal, T_2^*.

$$\frac{1}{T_2^*} = \frac{1}{T_2} + \gamma\Delta B_o \tag{15}$$

1.2.6 Measurement of T_2: The Hahn Spin Echo Experiment

Measurement of spectral line width may not necessarily be a very accurate way to measure T_2 as magnet inhomogenity and T_1 each have an effect. T_2 can be accurately determined *via* the pulsed NMR technique known as the Hahn Spin Echo experiment.

Following a 90° RF pulse there is loss of phase coherence around the *x*,*y*-plane. The spins precess at differing frequencies due to both the inhomogenity effects and the true T_2 effect. A 90° pulse is applied followed by a delay time, τ, and the spins begin to fan out. Application of a 180° RF pulse, along the *x*,*y*-plane, followed by a delay time, τ, will re-focus the spins such than they are all in phase. The true T_2 process, however, will cause a reduction in the transverse magnetisation that cannot be re-focussed following a 180° RF pulse. A FID is measured and the experiment is repeated for several values of τ (Figure 7).

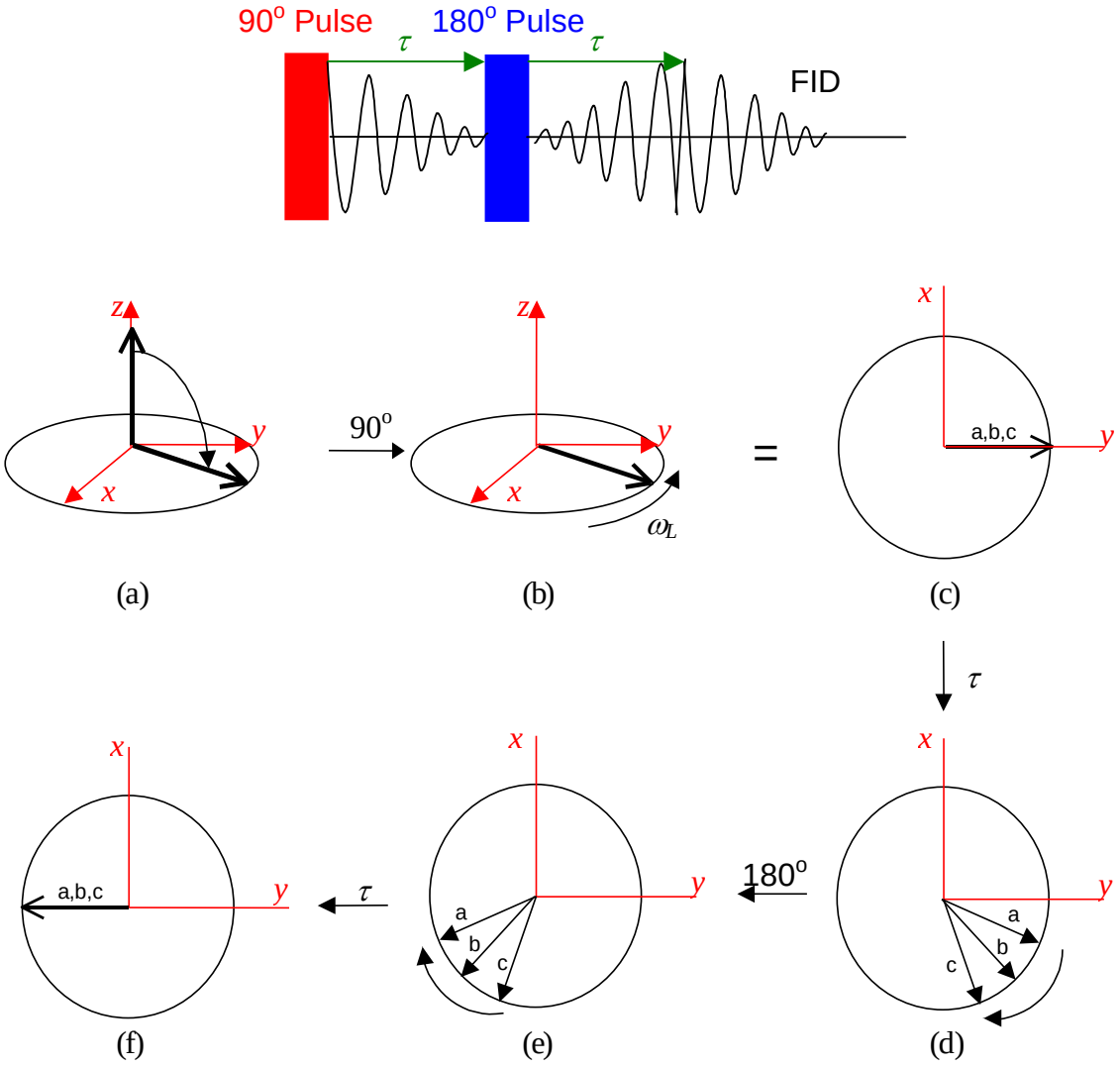

Figure 7. The Hahn Spin Echo Experiment. (a) the spins are inverted onto the *x*,*y*-plane and (b) and (c) they precess at Larmor frequency. (d) shows that after delay time, τ, the spins precess at differing frequencies where a is the slowest and c is the fastest. The spins are inverted along the *x*,*y*-plane following a 180° pulse, (e), and phase coherence is re-established after delay time, τ,(f).

The relaxation occurs over time 2τ and, therefore, using Equation 13 the NMR signal intensity is defined as

$$I_{2\tau} = I_o e^{-2\tau/T_2} \qquad (16)$$

and, therefore, a plot of $\ln I_{2\tau}$ *vs.* τ will give T_2.

1.2.7 Magnetic Field Gradients

In order to produce three-dimensional images of the body MRI scanners employ a series of magnetic field gradients in order to spacially encode observed nuclear spin densities. Consider the two solid blocks in Figure 8. Projection of the proton spin density onto the *x*-axis alone would give the same readout for each sample and therefore the same image.

In order to determine the proton spin density dispersion three-dimensionally measurements must be made along the *x*, *y* and *z*-axis together. Gradient field detection along each axis is, therefore, carried out and the results combined to produce a three-dimensional image.

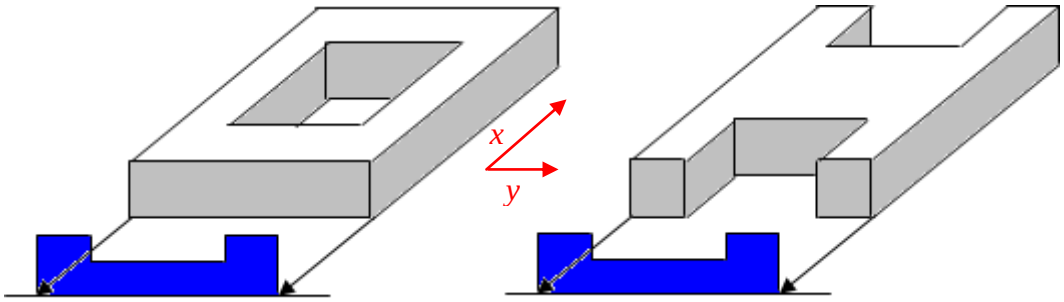

Figure 8. Proton spin density. The spin density readout (blue) along the *x*-axis only shows both three-dimensional objects (a) and (b) to appear identical.

1.2.8 Image Contrast

Different tissue types contain varied concentrations of water molecules, which in turn provide a varied amount of water proton spin density at differing regions of the body. However, variation between tissue types is not as simple as mere variations in concentration in providing high proton signal intensities. It was seen in Sections 1.2.3 and 1.2.5 that the signal intensities are affected by both T_1 and T_2; tissue where water protons are quite immobile (e.g. bone) will have very long longitudinal relaxation times and very short transverse relaxation times, which will result in low intensity, broad spectral signals. Therefore, imaging based on longitudinal and transverse relaxation times provides high contrast between tissue types.

1.2.9 Inversion Recovery Imaging

The mechanisms of the inversion recovery experiment have been previously discussed (Section 1.2.4). Application of this technique can provide highly detailed images based on longitudinal relaxation times. Following a 180^o pulse, in tissue types where water proton T_1 is short, M_z will be re-established quickly after the delay time, τ, and therefore more bulk

magnetisation will be flipped onto the *x*,*y* plane following the 90^{o} pulse. This leads to a higher intensity transverse magnetisation signal being detected. Therefore, tissue types with shorter water proton longitudinal relaxation times will provide higher signal intensities and, thus, appear brighter in MR images. An advantage of short T_1 is that the delay time can be quite short and, therefore, many more scans can be accumulated within a short time, allowing for a higher signal to noise ratio and clearer images.

1.2.10 Spin Echo Imaging

Although T_1 varies from tissue to tissue, the degree of variation may not be large enough in some cases to provide clear contrast between tissue types, i.e. if T_1 is very fast in two tissues. As T_2 is always shorter or equal to T_1, imaging based on transverse relaxation times, T_2, can be employed in order to show contrast between the fast T_1 tissues.

The spin echo experiment has been previously discussed (Section 1.2.6). As T_2 results in a loss of coherence about the *x*,*y*-plane, transverse magnetisation is therefore lost. Thus, the faster the transverse relaxation the lower signal intensities are detected resulting in darker MR images.

Contrast between tissue types is, therefore, determined by the longitudinal and transverse relaxation times of the water protons present. Enhancement of image contrast results from enhancement of the water proton relaxation processes. This is achieved by administering agents to the patient, which have an effect on the water proton relaxation times.

1.3 MRI Contrast Agents

Contrast agents are the MRI equivalent of a dye, increasing proton relaxation rates of water molecules within their vicinity. It is not the contrast agent *per se* which is seen in the image; rather its effect on the longitudinal relaxation (T_1) and transverse relaxation (T_2) of surrounding water proton nuclei.[16] Relaxation rate enhancement is achieved by the introduction of chelates containing paramagnetic ions, such as manganese (II)[17] and iron (III).[18, 19]

However, with seven unpaired *f*-electrons the highly paramagnetic gadolinium (III) is the most used and studied metal ion in contrast agent development with its long electron spin relaxation time coupled with its large effective magnetic moment, μ_{eff} = 7.94 B.M.[20] Since the Lauffer review in 1987, Gd(III) based contrast agent development has soared.[21] Today there are several clinically approved contrast agents used worldwide, with approximately 30% of all MRI scans incorporating some kind of non-specific Gd(III)-based contrast agent.[22] Other metal contrast agents used are superparamagnetic iron oxide nanoparticles known as

ferumoxides[23] and the liver specific manganese based mangafodipir trisodium,[24] known as Teslascan®.

T_1 is much longer than T_2 for most tissues and, therefore, the relative effect of the contrast agent on T_1 is much greater.[15] Although contrast agents will have an effect on both T_1 and T_2, they can still be categorised into two classes depending on the process they affect the most. A T_1 agent will have a greater effect in reducing the longitudinal relaxation time of surrounding water protons. Such contrast agents are known as positive agents as the increase in longitudinal relaxation rate will lead to greater MR image intensity. A T_2, agent on the other hand, has a greater effect the transverse relaxation time. An increase in transverse relaxation rate leads to a decrease in MR image intensity, and such T_2 contrast agents are referred to as negative agents.

1.3.1 Gd(III)-based Contrast Agents

The first concern when preparing Gd(III)-based contrast agents is to ensure metal ion complex stability. Gd(III) is of a similar ionic radius to calcium(II) (1.05 Å and 1.12 Å for Gd(III) and Ca(II) respectively, C.N. = 8).[25, 26] Due to the higher charge density of Gd(III) there is a greater affinity for Ca^{2+} sites on biological molecules. This can lead to inhibition of calcium transfer processes in biological systems, e.g. bone-deposition and the blocking of the Na^+/Ca^{2+} synaptic plasma membrane exchange resulting in inhibition of skeletal, smooth and cardiac muscle contraction.[27]

The majority of research into Gd(III)-based contrast agent development involves complexation of the metal ion with derivatives of either diethylenetriamine pentaacetate (DTPA)[28, 29] or 1,4,7,10-tetra-azacyclododecane-1,4,7,10-tetraacetic acid (DOTA).[30] The commercially available Gd(III)-based contrast agents are the anionic complexes $[Gd\text{-}DTPA]^{2-}$ (Magnevist®, Scherring, A.G., Germany, 1988), $[Gd\text{-}DOTA]^{-}$ (Dotarem®, Guerbert S.A., France, 1989) and $[Gd\text{-}DO3A\text{-}butrol]^{2-}$ (Gadovist®, Scherring A.G., Germany, 1999), the neutral complexes Gd-HP-DO3A (ProHance®, Bracco Diagnostics, Italy, 1992), Gd-DTPA-BMA (Omniscan®, Winthrop University Laboratories, U.S.A., 1993) and Gd-DTPA-BMEA (OptiMARK®, Mallinckrodt, U.S.A., 1998), and the blood-pool contrast agent MS-325 (Vasovist®, Scherring A.G., Germany, 2005). Each of the complexes shows high *in vivo* kinetic stability and, importantly for MRI contrast agent design, one free coordination site for exchanging water molecules. (This is discussed in more detail in Section 1.3.2).[31] Each of the ligands form highly stable, octadentate complexes with the Gd(III) ion. Table 2 shows the association constants, log K_{ML} and the acid dissociation rate constant, k_{obs} for each of the commercially available contrast agents.

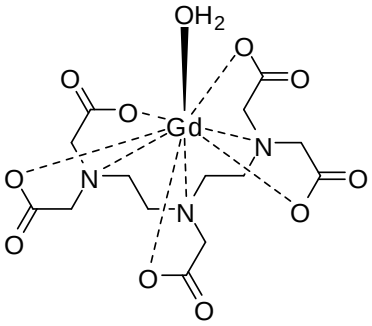

[Gd-DTPA]$^{2-}$
Magnevist

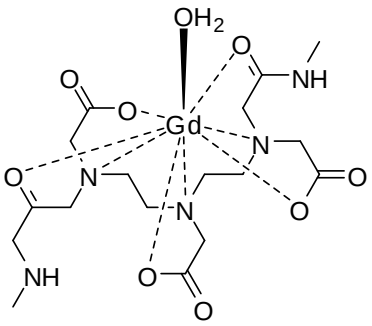

Gd-DTPA-BMA
Omniscan

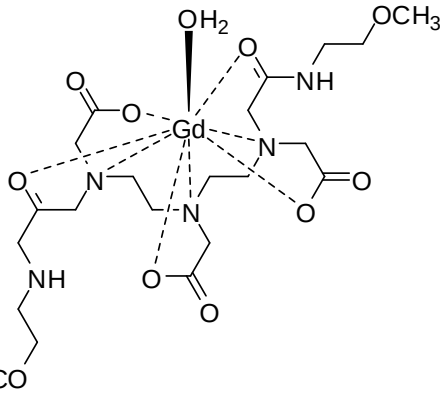

Gd-DTPA-BMEA
OptiMARK

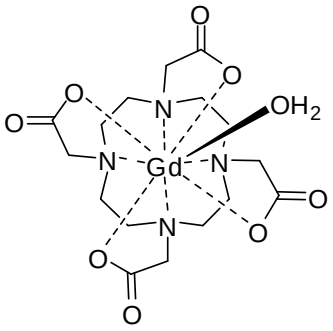

[Gd-DOTA]$^{-}$
Dotarem

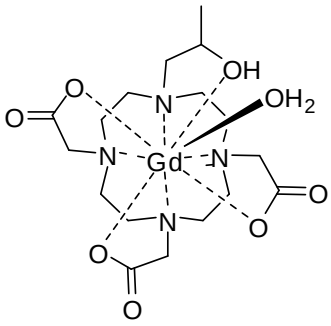

Gd-HP-DO3A
ProHance

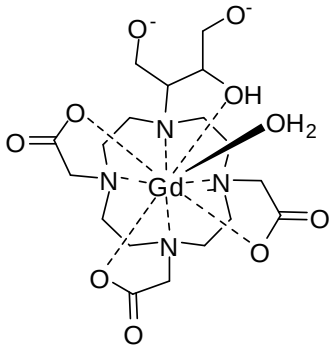

[Gd-DO3A-butrol]$^{2-}$
Gadovist

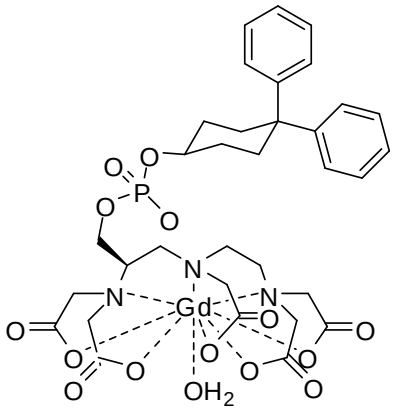

[MS-325]$^{3-}$
Vasovist

Contrast Agent	Chemical Name	log K_{ML} [32-37]	k_{obs} ($10^3 s^{-1}$) [38]
Magnevist®	$[Gd\text{-}DTPA]^{2-}$	22.46	1.2
Omniscan®	Gd-DTPA-BMA	16.85	> 20
OptiMARK®	Gd-DTPA-BMEA	16.84	-
Dotarem®	$[Gd\text{-}DOTA]^{-}$	25.30	0.021
ProHance®	Gd-HP-DO3A	23.80	0.064
Gadovist®	$[Gd\text{-}DO3A\text{-}butrol]^{2-}$	21.80	-

Table 2. Association constants, log K_{ML}, and acid dissociation rate constants, k_{obs}, for the commercially available Gd(III) contrast agents.

The association (equilibrium) constant, K_{ML}, is defined as

$$K_{ML} = \frac{[\mathrm{ML}]}{[\mathrm{M}][\mathrm{L}]} \tag{17}$$

The large K_{ML} values observed in Table 2 show equilibrium to shift to the side of the metal-ligand complex, hence very little free metal ion in solution.

The kinetic inertness of the ligands is demonstrated by the low acid disassociation rate constants, k_{obs}. Unsurprisingly, DOTA exhibits more kinetic stability that DTPA, which can be attributed to the macrocyclic effect of addition of a cyclic chelating ligand such as DOTA as opposed to the linear DTPA.

Transmetallation studies have also been carried out to assess the preferential binding selectivity for Gd(III), K_{sel}, over other physiologically present metal ions;[37-42] Cu(II), Ca(II) and Zn(II), as well as H^+. Table 3 shows the calculated high K_{sel} values for each complex and, therefore, high preferential selectivity for Gd(III).

$$K_{sel} = K_{ML}\left(\frac{K_{H^+L}}{[\mathrm{H}^+]} + \frac{K_{CaL}}{[\mathrm{Ca}^{2+}]} + \frac{K_{CuL}}{[\mathrm{Cu}^{2+}]} + \frac{K_{ZnL}}{[\mathrm{Zn}^{2+}]}\right) \tag{18}$$

Contrast Agent	Ligand	K_{sel}	K_{CaL}	K_{CuL}	K_{ZnL}
Magnevist®	DTPA	7.04	10.75	21.38	18.29
Omniscan®	DTPA-BMA	9.04	7.17	13.03	12.04
OptiMARK®	DTPA-BMEA	-	-	-	-
Dotarem®	DOTA	8.30	17.23	22.63	21.05
ProHance®	Gd-HP-DO3A	6.95	14.83	22.84	19.37
Gadovist®	Gd-DO3A-butrol	4.13	11.74	22.87	19.26

Table 3. Association constants for the commercially available contrast agent ligands with selected metal ions.

1.3.2 Water Proton Relaxivity, r_1

The longitudinal paramagnetic relaxation rate enhancement of free water protons, R_{1p}, is made up of contributions from both the inner sphere (i.e. water molecules coordinated directly to the metal centre) relaxation mechanism, R_{1p}^{IS}, and the outer sphere (i.e. closely diffusing water molecules in the bulk) relaxation mechanism, R_{1p}^{OS}.[43]

$$R_{1p} = R_{1p}^{IS} + R_{1p}^{OS} \tag{19}$$

The efficiency of a contrast agent is defined by its relaxivity, r_1; the total paramagnetic relaxation rate enhancement of the water protons per unit concentration of the contrast agent ($mM^{-1}s^{-1}$).[43]

$$r_1 = R_{1p}/[\mathrm{Gd}] \tag{20}$$

The design of contrast agent ligands is such that one or two coordination sites of the usually nine coordinate Gd(III) ion are left to allow waters to bind and exchange with the bulk waters. Therefore, the most significant relaxation contribution with regards contrast agent design is the inner sphere. The longitudinal inner sphere relaxation rate is expressed by Equation 21[44]

$$R_{1p}^{IS} = \frac{Cq}{55.6}\frac{1}{T_{1M} + \tau_m} \tag{21}$$

where C is the concentration of paramagnetic ion, q is the number of coordinated water molecules, T_{1M} is the longitudinal relaxation time of the inner sphere waters and τ_m is the water exchange lifetime. It is clear from Equation 21 that increasing the hydration state, q, of the complex will increase the overall relaxivity. Likewise, an increase in the water exchange rate, k_{ex} ($1/\tau_m$), will allow more water molecules from the bulk to feel the increased paramagnetic effects as they come into contact with the Gd(III) ion.

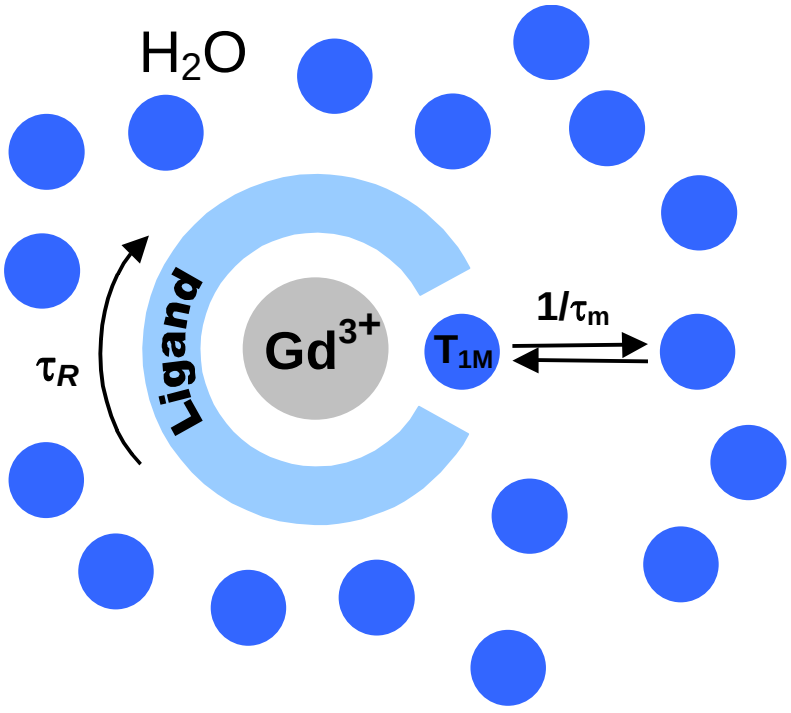

Figure 9. Schematic representation of a contrast agent.

Figure 9 shows a schematic representation of the inner sphere and outer sphere contributions influencing the relaxivity of a contrast agent. A further contribution to water proton relaxation rate enhancement is the rotational correlation time, τ_R. Clinical MRI scanners operate at around 1.5 T (64 MHz) and at these field strengths T_{1M} is dominated by τ_R, such that by slowing down the rotational motion of the contrast agent, water proton relaxivity enhancement is achieved. (This is discussed in more detail later in this Chapter, Section 1.3.7).

1.3.3 Hydration State, q

The variation of hydration state, *q*, has been the focus of much contrast agent development since the production of the first generation contrast agents.[45] Increasing hydration state does, however, come at the expense of the complex stability as ligands with lower coordination numbers are employed.

The Raymond group has worked extensively in the production of hydroxypyridonato (HOPO), **L6**, ligands to produce Gd(III) complexes with higher hydration states.[46-48] Comparison of the relaxivity values for the q = 2, **Gd.L6** complex with those of the commercially available MRI contrast agents (all q = 1) show that doubling the number of coordinated water molecules increases relaxivity by more than 100% (Table 4). The overall stability of **Gd.L6**, however, is generally lower than most of the commercially available agents as the coordination number of the chelating ligand decreases to seven. Nevertheless, the stability is comparable to those in clinical use and hydroxypyranodate ligand development in order to increase stability is ongoing.[50]

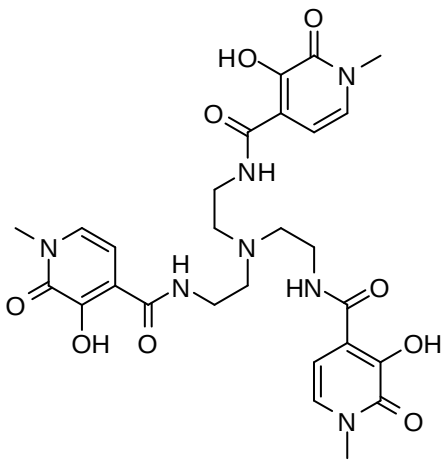

L6

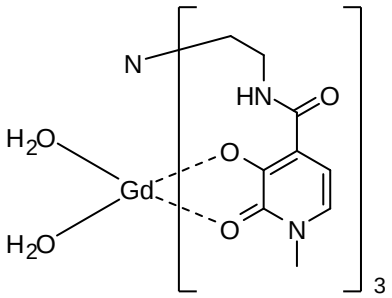

Contrast Agent	Chemical Name	q	log K_{ML}	r_1 ($mM^{-1}s^{-1}$)[47, 49]
Magnevist®	$[Gd\text{-}DTPA]^{2-}$	1	22.46	4.30[a]
Omniscan®	Gd-DTPA-BMA	1	16.85	4.39[a]
OtiMARK®	Gd-DTPA-BMEA	1	16.84	4.70[b]
Dotarem®	$[Gd\text{-}DOTA]^-$	1	25.30	4.20[a]
ProHance®	Gd-HP-DO3A	1	23.80	3.70[c]
Gadovist®	[Gd-DO3A-butrol]	1	21.80	3.60[c]
Gd.L6		2	18.25*	10.50[c]

Table 4. Hydration state values, q, stability constants, log K_{ML} (* determined from the pM value of 19.2 (-log[free Gd(III)] at pH 7.4 where [Gd(III)] = $1x10^{-6}$ M, and [L] = $1x10^{-5}$ M)[48]), and relaxivity values, r_1 (20 MHz at 25°C[a], 40°C[b] or 37°C[c]), for each of the commercially available MRI contrast agents and of **Gd.L6**.

$[Gd\text{-}DOTA]^-$ has also been modified in order to increase q values by removal of one of the acetate groups creating the seven coordinate chelating ligand, DO3A.

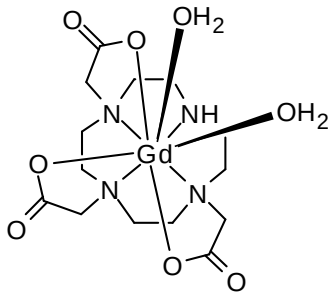

Gd-DO3A

The measured relaxivity of Gd-DO3A is r_1 = 4.8 $mM^{-1}s^{-1}$ (20 MHz, 40°C). Under the same conditions, Gd-DOTA has a relaxivity of r_1 = 3.5 $mM^{-1}s^{-1}$. The considerable difference being attributed to the difference in hydration states.[51] Relaxivity has also been recorded at 25°C as r_1 = 5.7 $mM^{-1}s^{-1}$ (20 MHz), the higher value being attributed to the slower motional tumbling and longer rotational correlation time, τ_R, of the complex at lower temperature (τ_R is discussed in more detail in Section 1.3.7). The stability constant, log K_{ML}, for Gd-DO3A has been measured as 21.00[33, 38] which is much lower than the value for Gd-DOTA (log K_{ML} = 25.30), once again showing considerable loss of thermodynamic stability upon removal of a coordination site (although, the stability still remains comparable to the rest of the commercially available contrast agents, Gd-DO3A is not kinetically stable enough to use *in vivo* as Gd(III) loss is too great).

1.3.4 Inner Sphere Water Proton Relaxation

Equation 21 shows that inner sphere water proton relaxation rate, R_{1p}^{IS}, is controlled by a number of factors, most noticeably the longitudinal relaxation time, T_{1M} and the water exchange lifetime, τ_m, of bound water molecules.

For the first generation contrast agents, T_{1M} is much greater that τ_m and, therefore, is the limiting factor in contrast agent development.[45]

$$\frac{1}{T_{1M}} = \frac{2}{15}\frac{\gamma_H^2 g_e^2 \mu_B^2 S(S+1)}{r_{GdH}^6}\left[\frac{7\tau_{c2}}{1+\omega_S^2\tau_{c2}^2} + \frac{3\tau_{c1}}{1+\omega_H^2\tau_{c1}^2}\right] \tag{22}$$

Equation 22, where γ_H is the proton gyromagnetic ratio, g_e is the electron *g*-factor, μ_B is the Bohr magneton and *S* is the spin quantum number (7/2 for Gd(III)), shows T_{1M} to be dependant on several factors; Gd-H distance, $r_{GdH,}$ the proton Larmor frequency, $\omega_{H,}$ the electron Larmor frequency, ω_S and the correlation times τ_{c1} and τ_{c2}, which themselves are comprised of the water exchange lifetime, τ_m, the rotational correlation time, τ_R, and the electronic relaxation time of the metal Gd(III) ion, T_{1e},[44] shown in Equation 23.

$$\frac{1}{\tau_{ci}} = \frac{1}{\tau_m} + \frac{1}{\tau_R} + \frac{1}{T_{1e}};\ i = 1, 2 \tag{23}$$

Optimisation of contrast agent relaxivity can therefore be achieved by decreasing the Gd-H distance, increasing the water exchange rate, slowing down the rotational motion of the complex and increasing the electronic relaxation rate.

1.3.5 Gd(III)-Water Distance, r_{GdH}

The variation of the Gd(III)-water distance could lead to large enhancement of relaxivity as T_{1M} dependence is proportional to $1/r^6$. Gd-H is generally reported within the range 2.5 Å to 3.3 Å, which have been determined by x-ray diffraction or calculated indirectly by relaxivity studies. More recently, however, the Gd-H distance has been determined as 3.1 ± 0.1 Å for several DTPA and DOTA derivatives by pulsed ENDOR spectroscopy.[52, 53]

1.3.6 Electronic Relaxation Time, T_{1e}

The relaxation rate is affected by the imposed magnetic field strength. For Gd(III) complexes, T_{1e} is related to modulation of the zero field splitting (ZFS) of the electronic spin

states, which arise from dynamic distortions of the ligand field interaction.[51] Bloembergen-Morgan theory[54] show the magnetic field dependence to be expressed by

$$\frac{1}{T_{1e}} = \frac{1}{25}\Delta^2\tau_v\left[4S(S+1)-3\right]\times\left(\frac{1}{1+\omega_s^2\tau_v^2}+\frac{4}{1+4\omega_s^2\tau_v^2}\right) \quad (24)$$

$$\frac{1}{T_{2e}} = \frac{1}{50}\Delta^2\tau_v\left[4S(S+1)-3\right]\times\left(3+\frac{5}{1+\omega_s^2\tau_v^2}+\frac{2}{1+4\omega_s^2\tau_v^2}\right) \quad (25)$$

where Δ^2 is the mean square zero field splitting energy and τ_v is the correlation time for its modulation.[44]

As the magnetic field frequency increases both the electron and proton Larmor frequencies are increased as well. The electron Larmor frequency, ω_S, is 658 times greater than the proton Larmor frequency, ω_H, which therefore means that the first term in square brackets of Equation 22 disperses at much lower fields than the second term.[45] There is complete dispersion at higher frequencies as the proton Larmor contribution becomes negligible.

Although the Gd(III)-water distance, r_{GdH}, and the electronic relaxation time, T_{ie}, are important factors in the enhancement of contrast agent efficiency, the most important factor effecting relaxivity at clinical MRI field strengths is the rotational correlation time, τ_R.

1.3.7 Rotational Correlation Time, τ_R

Clinical MRI scanners operate at around 1.5 T (64 MHz) frequency where the electronic contribution has almost fully dispersed. The correlation time, τ_c, is therefore dependant solely on the water exchange lifetime, τ_m, and the rotational correlation time, τ_R. The magnitude of τ_c will be dictated by the smaller of the remaining two contributers.[38] For Gd(III) based complexes with the molecular weight and size of DOTA, τ_m is of the order of nanoseconds, where as τ_R is much shorter and of the order of picoseconds.[55]

At clinical MRI scanner field frequencies, relaxivity is therefore dominated by contrast agent rotational correlation time. Slowing down molecular tumbling will cause an increase in the rotational correlation time, which in turn will increase τ_c and enhance relaxivity.[56] The NMRD profiles in Figure 10 show a dramatic increase in relaxivity at the field frequency range 0.5-1.5 T (20-60 MHz) upon increase of the molecules rotational correlation time.

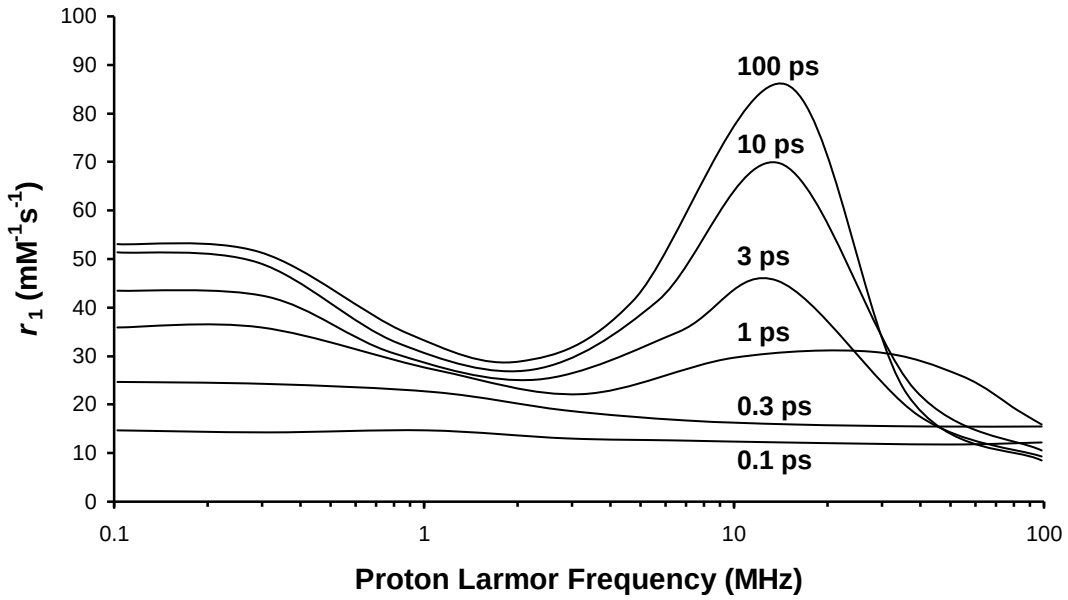

Figure 10. NMRD profiles of hypothetical complexes with varying τ_R of 0.1 to 100 ps.

It is possible to use data calculated from an NMRD profile to determine the rotational correlation time by fitting the parameters from Equation 22 as well as those obtained from the closely diffusing outer sphere contribution, discussed in the following section.

1.3.8 Outer Sphere Water Proton Relaxation

The outer sphere contribution accounts for around 40% of the overall relaxivity of monoaqua Gd(III) complexes at imaging fields.[57] It arises from the diffusion of bulk water molecules nearby the paramagnetic complex, and is expressed by Equation 26.

$$R_{1p}^{OS} = C^{OS}\left(\frac{1}{aD}\right)\left[7J(\omega_s)+3J(\omega_H)\right] \tag{26}$$

$$J(\omega) = R_e\left[\frac{1+1/4\left(i\omega\tau_d+\frac{\tau_d}{\tau_{si}}\right)^{1/2}}{I+\left(i\omega\tau_d+\frac{\tau_d}{\tau_{sj}}\right)^{1/2}+4/9\left(i\omega\tau_d+\frac{\tau_d}{\tau_{sj}}\right)+1/9\left(i\omega\tau_d+\frac{\tau_d}{\tau_{sj}}\right)^{3/2}}\right] \tag{27}$$

$$j = 1, 2;\ \ \tau_d \frac{a^2}{D}$$

where C^{OS} is a constant (5.8×10^{-13} $s^{-2}M^{-1}$), $J(\omega)$ is the non-Lorenzian spectral density, which is dependant on τ_s, the electronic correlation time, a is the shortest distance of approach (i.e. the radius of the outer sphere) and D is the diffusion coefficient of the solvent.[58]

1.3.9 Water Exchange Lifetime, τ_m

Fast water exchange is essential so as to allow more water molecules from the bulk to coordinate to the paramagnetic metal centre enhancing the overall water proton relaxation rates. The water exchange lifetime cannot be too short, however, as Equation 23 shows. τ_m contributes to τ_c, a decrease of which would result in a reduction of relaxation rates.

Measurement of τ_m is carried out by variable temperature ^{17}O NMR, in which the temperature dependence of the paramagnetic contribution, R_{2p}^O, to the observed transverse relaxation rate, R_{2obs}^O, of water ^{17}O nuclei is observed

$$R_{2p}^O = R_{2obs}^O - R_{2d}^O \tag{28}$$

where the paramagnetic term R_{2d}^O is determined from a solution containing a diamagnetic analogue of the chelate being studied.[59]

R_{2p}^O is related to τ_m^O, *via* the ^{17}O chemical shift difference between coordinated and bulk water molecules, $\Delta\omega_m^O$, and the transverse relaxation rate of the coordinated water ^{17}O, R_{2m}^O, following the Swift and Connick theory,[60] and is expressed by

$$R_{2p}^O = \frac{qC}{55.6}\tau_m^{O-1}\frac{R_{2m}^{O2} + \tau_m^{O-1}R_{2m}^O + \Delta\omega_m^{O2}}{\left(R_{2m}^O + \tau_m^{O-1}\right)^2 + \Delta\omega_m^{O2}} \tag{29}$$

where R_{2m}^O is determined as[61]

$$R_{2m}^O = \frac{1}{3}\left(\frac{A}{\hbar}\right)^2 S(S+1)\left(\tau_{e1} + \frac{\tau_{e2}}{1+\omega_s^2\tau_{e2}^2}\right) \tag{30}$$

$$\frac{1}{\tau_{ei}} = \frac{1}{\tau_m^O} + \frac{1}{T_{1e}}$$

where S is the electronic spin quantum number (7/2 for Gd(III), ($A/\hbar$) is the Gd-O scalar coupling constant (approx -3.8×10^6 rad s^{-1}),[51] τ_{ei} (i = 1, 2) is the correlation times of modulating the scalar interaction and T_{1e} is the electronic relaxation time.

The temperature dependence of $\Delta\omega_m^O$ is expressed by

$$\Delta\omega_m^O = \frac{g_e \mu_B S(S+1) B_o}{3k_B T} \frac{A}{\hbar} \tag{31}$$

where B_o is the magnetic field strength and k_B is the Boltzman constant.[61]

The temperature dependence of R_{2p}^O is expressed in terms of the ^{17}O water exchange lifetime, τ_m^O, and to τ_v (the correlation time for modulation of the ZFS) by the Eyring equation, (Equation 32)

$$\frac{1}{\tau_j} = \frac{k_B T}{h} \exp\left(\frac{\Delta S_j^{\neq}}{R} - \frac{\Delta H_j^{\neq}}{RT} \right) = \frac{\left(\tau_i^{-1}\right)^{298.15} T}{298.15} \exp\left(\frac{\Delta H_j^{\neq}}{R} \left(\frac{1}{298.15} - \frac{1}{T} \right) \right) \tag{32}$$

where the suffix j refers to the different correlation times (m, v), $\Delta S^{\neq}$ and $\Delta H^{\neq}$ are the entropy and enthalpy of activation for the corresponding dynamic process respectively and $\left(\tau_j^{-1}\right)^{298.15}$ is the rate at 298.15 K.[62] Water exchange rate, k_{ex}, can be expressed in terms of the inverse of the water exchange lifetime, τ_m^O.

The paramagnetic contribution to the ^{17}O transverse relaxation rate, R_{2p}^O, increases with temperature in the slow kinetic region (i.e. when temperatures are low) and is directly determined by k_{ex} ($1/\tau_m^O$). In the fast exchange region (i.e. when temperatures are high) the water exchange lifetime, τ_m^O, becomes short enough with respect to the relaxation rate of the coordinated water ^{17}O, R_{2m}^O, resulting in a decrease in R_{2p}^O.[63]

The plot maximum shows the change over from the slow to fast regions, which shifts to lower temperatures with increasing water exchange rates. The plot maxima of the bell-shaped curves move to lower temperatures as the water exchange rate of the complex increases, as shown in Figure 11. Variable temperature ^{17}O NMR profiles can be fitted by utilising Equations 29-32 to yield the water exchange lifetime, τ_m, as well as τ_v and the activation entropy and enthalpy, $\Delta S^{\neq}$ and $\Delta H^{\neq}$ respectively.

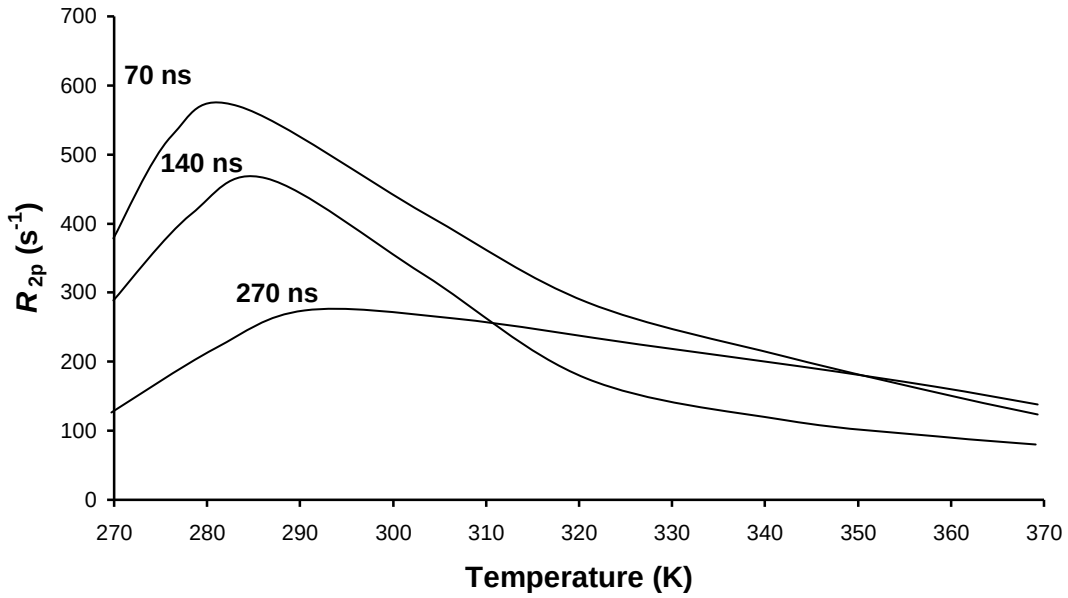

Figure 11. Variable temperature ^{17}O NMR profile of a hypothetical [Gd-DOTA]$^{-}$ complex with τ_m ranging from 70-270 ns.

1.4 Contrast Agent Enhancement

The focus of contrast agent research in recent years has centred on the exploitation of the water exchange lifetime and rotational correlation time contributions to overall relaxivity. Table 5 shows the τ_m and τ_R values for [Gd-DTPA]$^{2-}$, [Gd-DOTA]$^{-}$ and Gd-DO3A.[51, 64]

Contrast Agent	Chemical Name	τ_m (ns)	τ_R (ps)
Magnevist®	[Gd-DTPA]$^{2-}$	303[a]	58[a]
Dotarem®	[Gd-DOTA]$^{-}$	244[a]	77[a]
	Gd-DO3A	160[b]	66[b]

Table 5. Water exchange lifetime, τ_m, and rotational correlation time, τ_R, for [Gd-DTPA]$^{2-}$, [Gd-DOTA]$^{-}$ and Gd-DO3A. a = 25°C, 9.4 T (^{17}O)[64], b = 25°C, 2.1 T (^{17}O)[51].

1.4.1 Shortening of the Water Exchange Lifetime, τ_m

Manipulation of the water exchange dynamics of Gd(III) chelates has been achieved by either the modification of pendant groups to the chelate or by manipulation of the steric compression surrounding the Gd(III) centre.

The latter was achieved by Merbach and co-workers who increased the steric crowding of monoaqua [Gd-DTPA]$^{2-}$ and [Gd-DOTA]$^{-}$ chelates by replacing the one or two of the ethylene bridges of the chelates with propylene bridges.[65, 66] Despite the slight loss in stability of the chelates, the induced steric compression around the Gd(III) centre facilitated the leaving of the Gd(III) bound water. Water exchange rates were increased from ~ 30-50 fold for the [Gd-DOTA]$^{-}$ analogues and ~ 45-100 fold for the [Gd-DTPA]$^{2-}$ analogues.

It is well known that [Ln-DOTA]$^{-}$ exists in solution as four interchangeable stereoisomeric complexes, related as two enantiomeric pairs: the mono-capped square antiprismatic geometry (SAP) and the mono-capped twisted square antiprismatic geometry (TSAP) (Figure 12).[67] Each possesses a C_4-rotation axis perpendicular to the plane through the four nitrogens of the cyclen ring, capped by the water oxygen atom.[68]

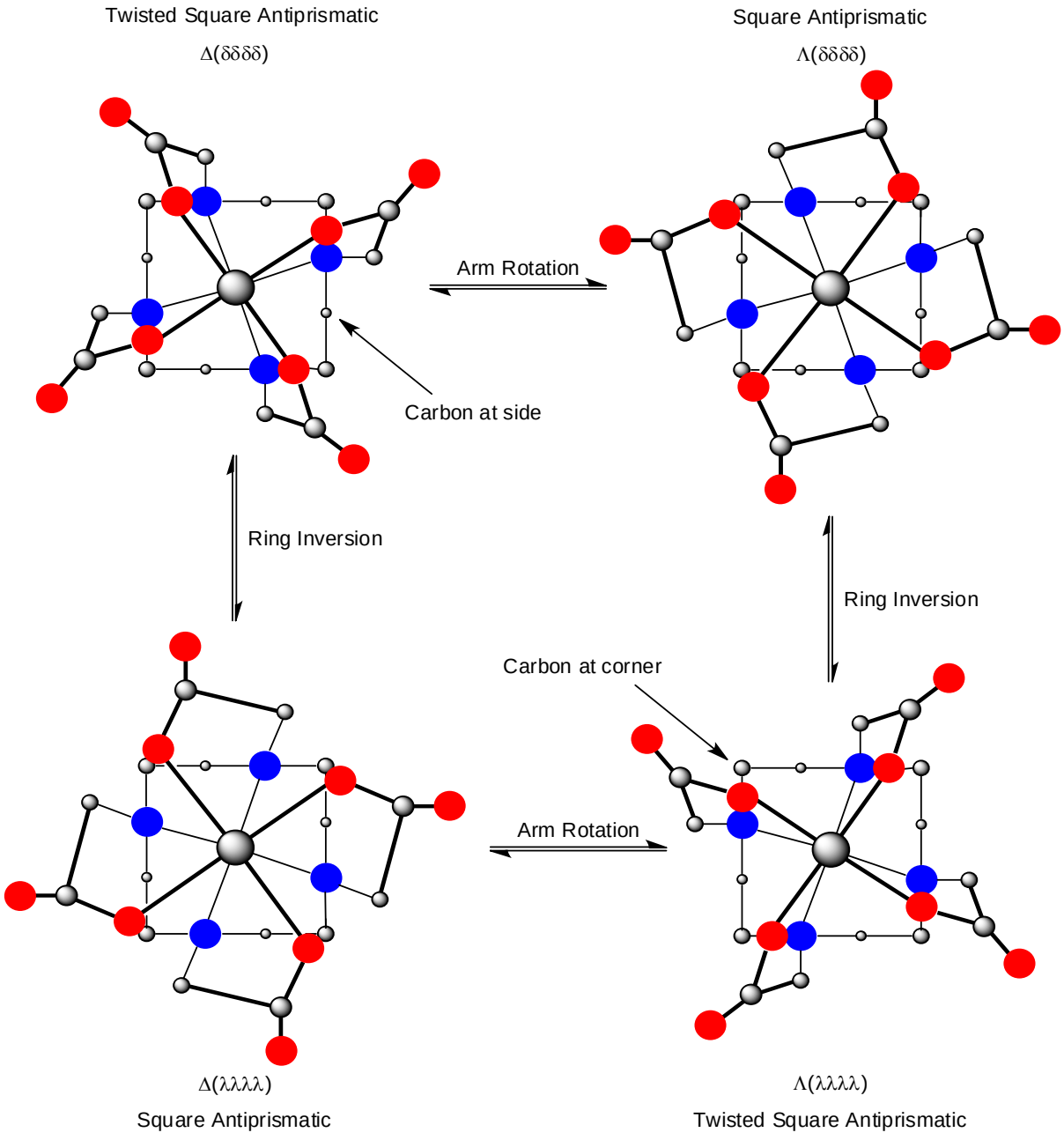

Figure 12. [Ln-DOTA]$^{-}$ stereoisomeric structures present in solution.[67]

Figure 12 shows that the inversion between the two isomers, SAP and TSAP, occurs either by cooperative ring inversion (λ to δ) or by concerted arm rotation (Δ to Λ).[69] The activation energy for the inversion of SAP to TSAP is greater, at $\Delta G^{\neq}$ = 65.6 kJ mol^{-1} compared to the reverse inversion, $\Delta G^{\neq}$= 61.4 kJ mol^{-1}, causing the SAP geometry to be the major isomer in solution for Eu(III) complexes.[70, 71] The minor TSAP isomer posses greater

steric crowding about the Eu(III) centre, which is the cause of its less abundant presence in solution. The increased steric crowding, however, facilitates the release of the Ln(III) bound waters, lowering the water exchange lifetime from τ_m = 1.88 x 10^{-5} s (SAP) to τ_m = 4.16 x 10^{-3} s (TSAP) ([Eu-DOTA]$^-$, 400 MHz ^{1}H NMR spectrometry, CD_3CN, 298 K).[72, 73] The faster observed water exchange has lead to the production of DOTA chelates incorporating pendant side chains designed to lock the species in the minor TSAP form in solution.

^{1}H NMR spectroscopy is an extremely useful tool in determining the abundance of each isomer in solution as the inversion process is slowed at lower NMR operating temperatures. It is worth noting at this point that the above water exchange rate was measured using the ^{1}H NMR spectrum of the [Eu-DOTA]$^-$ analogue, where the observed Eu(III) bound water resonances vary upon increasing temperature, allowing for exchange rate determination. Comparison between the isomeric water molecules was made easier by the large chemical shift difference between the Eu(III) bound water proton resonance of the SAP isomer at $\delta \sim$ 82 ppm compared to $\delta \sim$ 9 ppm for the TSAP isomer.[72] The same trend is observed when comparing the axial proton shifts of the cyclododecane ring of the DOTA chelate. When coordinated to the Eu(III) ion the orientation of four of the axial protons are in close proximity with the highly paramagnetic metal ion, inducing the large chemical shift in the ^{1}H NMR spectrum. The chemical shifts of the axial protons of the ring carbon atoms at the side and not the corner of the macrocycle are observed as isomers invert from the SAP to TSAP isomer, causing a reorientation of the associated axial protons with respect to the Eu(III) centre.[67]

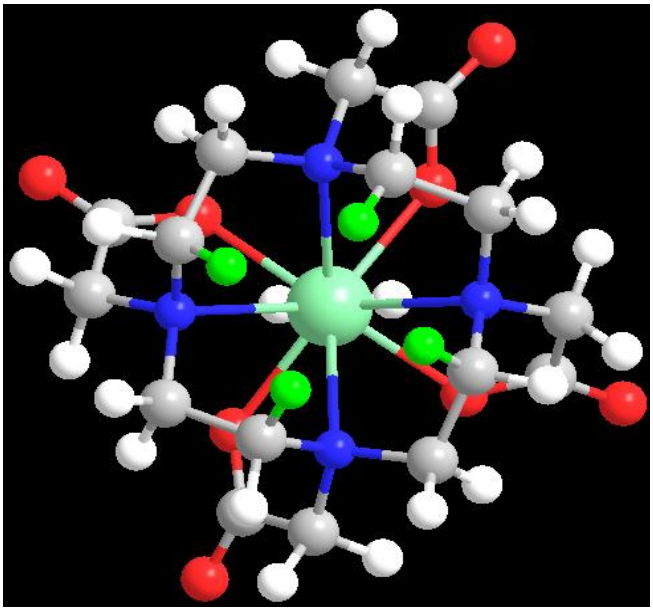

Figure 13. Three-dimensional view of [Gd-DOTA]$^-$ in the SAP isomeric form showing the axial protons (green) oriented towards the Eu(III) centre.

Figure 13 shows the axial protons in green, which are oriented towards the Eu(III) centre of the [Eu-DOTA]$^-$ complex. Axial proton resonances are observed at ~ 30-50 ppm for the SAP isomer, while the same axial protons appear at ~ 20-30 ppm for TSAP, allowing for clear distinction between the two isomeric forms.[69]

The introduction of substituents in the α-carbon positions, such as the addition of glutamic acid groups as in Ln-gDOTA, brings about increased rigidity, particularly inhibiting arm rotation and sterically locking the complex.[74] The addition of such substituents results in the formation of two diastereoisomeric pairs, rather than enantiomeric pairs,[75] and gives rise to six possible stereoisomeric configurations in solution with respect to the aliphatic substituents; *RRRR*, *SSSS*, *RSSS*, *SRRR*, *RSRS*, *RRSS*, defined by the absolute configuration at the α-carbon.[74]

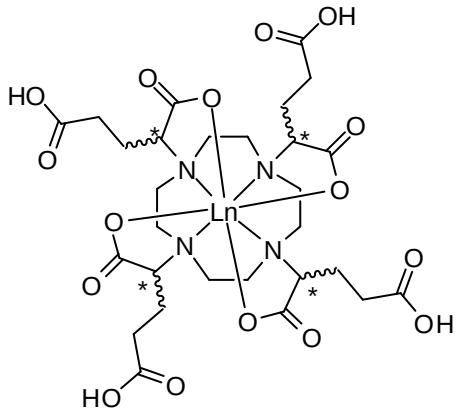

Ln-gDOTA

Sherry and co-workers developed a ligand incorporating a nitrobenzyl pendant group into a DOTMA chelate, **L7**, in which methyl groups are present in the α-carbon positions.[76]

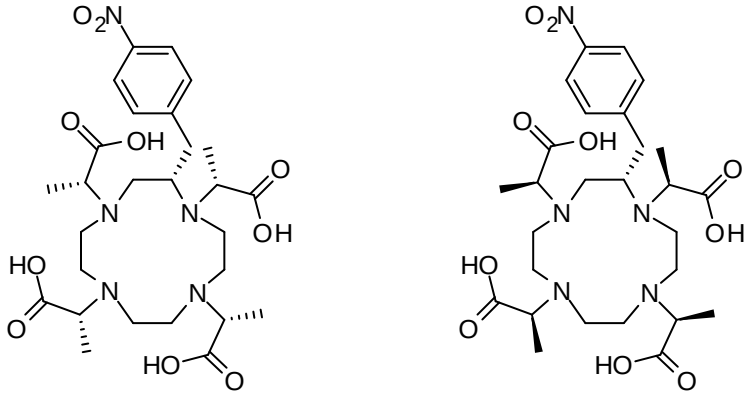

L7

S-RRR **(Δ(λλλ)** ***S-SSS*** **(Λ(δδδ)**

The presence of the *p*-nitrobenzyl moiety sterically locks the complexes in their respective configurations and using the Eu(III) analogues the isomers were characterised *via* ^{1}H NMR spectrometry. A clear distinction between the two isomeric structures is the presence

of the axial ring proton chemical shifts at either δ ~ 35-45 ppm, corresponding to the SAP isomer or δ ~ 5-22 ppm, corresponding to the TSAP isomer. Relaxometric studies of the Gd(III) analogues measured τ_m = 120 ns and τ_m = 15 ns (67.8 MHz) for the monoaqua SAP and TSAP isomers respectively showing a large difference between the two as expected. The corresponding relaxivities were measured as r_1 = 4.96 $mM^{-1}s^{-1}$ and r_1 = 5.20 $mM^{-1}s^{-1}$ (25°C, 20 MHz) for SAP and TSAP, which is not as high as might be expected. Nevertheless, it has been demonstrated that the coordination geometry of DOTA based complexes can be controlled, which has lead to further synthetic studies in optimisation of enantiomeric purity.[67]

Pendant group modification is also used as a strategy to enhance water exchange rate. The variation of charge and structure of such moieties leads to organisation of the solvent spheres, providing lower energy routes to more efficient water exchange. The incorporation of negative charge by the substitution of the α-carbon methyl groups of DO3MA with adipic acid gave rise to a five-fold reduction in the water exchange lifetime and ~ 100% increase in relaxivity from the resulting ligand aDO3A; τ_m = 160 ns and τ_m = 30 ns (0.5 T); r_1 = 6.0 $mM^{-1}s^{-1}$ and r_{1p} = 12.3 $mM^{-1}s^{-1}$ for [Gd-DO3MA] and $[Gd\text{-}aDO3A]^{3-}$ respectively (25°C, 20 MHz).[77] The presence of the negative charge increases the degree of organisation of the second sphere water molecules, facilitating the water exchange process.

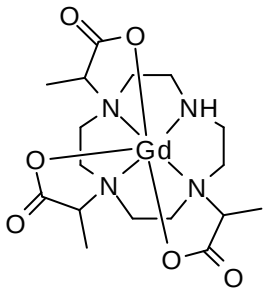

Gd-DO3MA

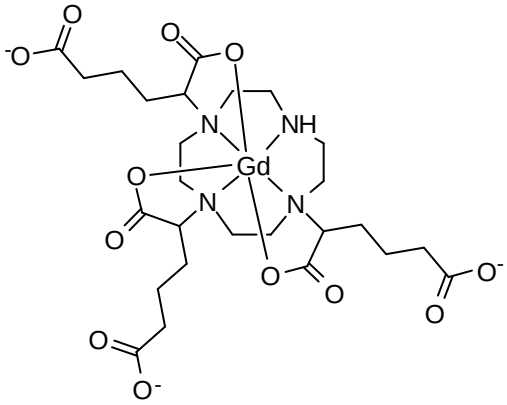

$[Gd\text{-}aDO3A]^{3-}$

Variations in the structure and chain lengths of neutral pendant groups can also have an effect on both the steric hindrance and the hydrophobicity of the complex shell. Muller and co-workers devised a series of neutral Gd-DTPA bis-amide derivatives with varied amide substituents to asses the degree in which they effected the water exchange lifetime.[78] It was determined that the nature of the side chains could have an effect on the hydrophobic repulsion between the complex and the bulk, which in turn would disrupt the hydration shell and modify the hydrogen bonds between the exchanging water molecules with those of the bulk, enhancing the water exchange rate. A 30% increase in the water exchange lifetime was

observed upon the addition of a hydroxyl group to the propyl side chains of DTPA-BnPA, **L8**, to produce DTPA-(R/S)BHPA, **L9**; τ_m = 1,128 ± 95 ns and 845 ± 35 ns respectively (40.65 MHz). The increase in hydrophobicity in this case, therefore, has a positive effect in the enhancement of water exchange rate, k_{ex} (1/ τ_m).

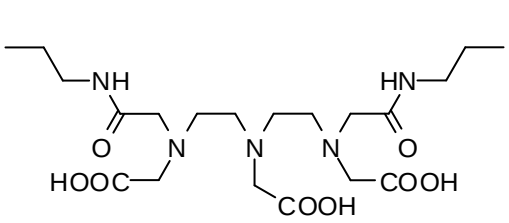

L8

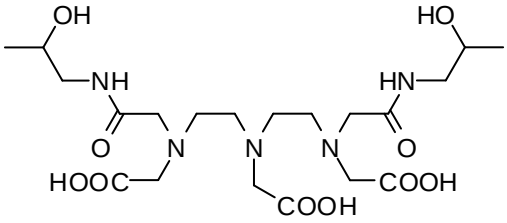

L9

Wong and co-workers have recently prepared a Gd-DO3A ligand bearing an aza-15-crown-5 crown ether, **Gd.L10**, which demonstrated a near 5 fold reduction in τ_m in comparison to its parent Gd-DO3A analogue; τ_m = 32 ns and τ_m = 160 ns respectively.[79]

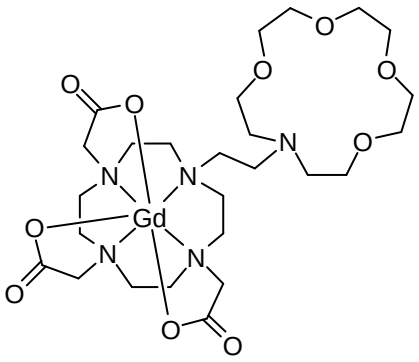

Gd.L10

The fast water exchange is attributed to both the increased steric compression around the Gd(III) centre as well as the increased negative charge density owed to the addition of the pendant crown ether. The measured relaxivity of the q = 2 species is 9.5 $mM^{-1}s^{-1}$ around a 65% increase to that observed for Gd-DO3A; r_1 = 5.7 $mM^{-1}s^{-1}$ (20 MHz, 25^oC). The complexes were used to image rats in order to determine *in vivo* stability and toxicity. An injection of 0.04 mM kg^{-1} of the crown ether-bearing complex was administered to the anaesthetised rats. MR signals were most apparent in the kidney, liver, adrenal gland and abdominal aorta, with increased retention time particularly in the abdominal aorta as significant enhancement was still observed at around 100 minutes post injection. Non-covalent binding to the plasma protein human serum albumin, HSA, was attributed to be the reason for the prolonged excretion time. A non-specific affinity constant, K_a, for protein binding was measured as 3,009 M^{-1} following titrations at fixed complex concentration with increasing [HSA]. The binding to HSA compartmentalises the contrast agent within the

vasculature, leading to slower excretion times and, therefore, allowing for smaller doses to be administered. Significant contrast enhancement was observed at doses as low as 0.02 mM Kg^{-1}, one fifth of the clinical contrast agent's administered dosages.

1.4.2 Lengthening the Rotational Correlation Time, τ_R

As discussed in Section 1.3.7, at clinical MRI frequencies T_{1m} is dominated by the rotational correlation time, τ_R; the lengthening of which resulting in an increase in relaxivity and enhancement of image intensity. The rotational correlation time of contrast agents has been lengthened by the preparation of slowly tumbling Gd(III) macromolecules, with the incorporation of several pendant groups, such as cyclams[80] and tris(hydroxymethyl)aminomethanes.[81] The increase of the molecular weight reduces the motional tumbling of the Gd(III) complex, increasing τ_R.

The preparation of high molecular weight dendrimeric macromolecules has been of considerable interest in the production of MRI contrast agents.[82, 83] The incorporation of several Gd(III) chelates into large molecular weight spherical macromolecules bearing polymeric cores has lead to the production of contrast agents which display high MR image contrast with a much lower dosage administered to the patient. Two such polymer core based dendrimers are the commercially available diaminobutane (DAB) and polyamidoamide (PAMAM)[84], each highly water-soluble spherical molecules bearing primary amino acid groups exposed on their surface, capable of Gd(III) chelation. The incorporation of lanthanide based chelates into PAMAM dendrimers has been extensively researched in recent years.[85, 86]

Hermann and co-workers recently developed a series of G2-, G3- and G4-PAMAM dendrimers incorporating monophosphinated Gd-DOTA based chelates, **Gd.L11**.[87, 88] The dendrimers are denoted G2- G3- and G4-, which refers to the number of exposed primary amino groups on the surface the macrocycle (8 amino groups for G1-, 16 for G2-, 32 for G3- and 64 for G4-) surrounding the PAMAM backbone. This allows for the production of increasing molecular weight macromolecules containing increasing numbers of Gd(III) chelates. The measured relaxivities for each of the generated dendrimeric species increased with increasing size; r_1 = 10.1$mM^{-1}s^{-1}$, r_1 = 14.1 $mM^{-1}s^{-1}$ and r_1 = 18.1 $mM^{-1}s^{-1}$ (37°C, pH 7.5, 20 MHz), attributed to the increasing global rotational correlation time of the dendrimers; τ_{Rg} = 1,560 ± 280 ps, 2,690 ± 270 ps and 3,140 ± 210 ps (25°C, pH 7.5) for G1-8 Gd(III), G2-16 Gd(III) and G4-59 Gd(III) respectively. The relaxivity enhancement was not as great as was hoped due to the low rigidity factor, S^2 ~ 0.26, causing fluctuations within the molecule and lowering the effective rotational correlation time; τ_R = 115 ± 4 ps 100 ± 3 ps and 133 ± 4 ps (25°C, pH 7.5) for G1-8 Gd(III), G2-16 Gd(III) and G4-59Gd(III) respectively.

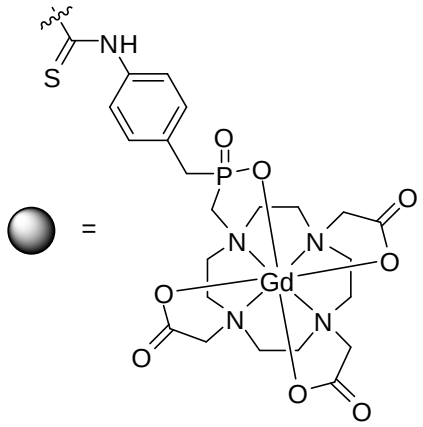

Gd.L11

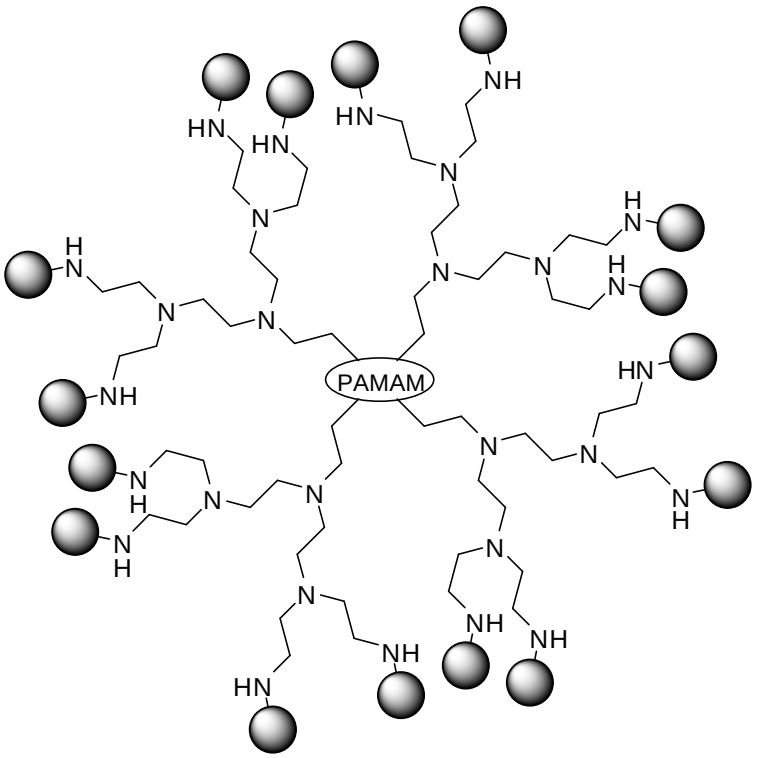

G2-16 Gd(III) PAMAM

In order to reduce the effects of independent rotation Parker and co-workers recently developed as series of increasing molecular weight conjugates incorporating either glucose or galactose groups, **L12**.[89] The incorporation of sugar groups into the ligand framework served to both increase the solubility of the dendrimeric Gd(III) chelate as well as to place the Gd(III) ion at the barycentre of the spherical molecular complex, which improves the effective motional coupling of the Gd(III) ion by reducing the degree of its independent rotation.[90] The macromolecule bearing twelve glucose groups linked *via* four amido bridges to the monohydrated **Gd.L12** chelate yields the highest relaxivity of the macrocycles produced; r_1 = 23.5 $mM^{-1}s^{-1}$ (25°C, pH 7.0, 20 MHz). This high relaxivity is owed to the reduction of the rotational correlation time of the 3,220 Da molecular weight species with τ_R measured as τ_R = 390 ns, which is considerably longer than the $[Gd\text{-}DOTA]^-$ parent molecule at 77 ps. The organisation of the second sphere water molecules between the glucose groups and the Gd(III) centre further enhanced τ_R by forming a more compact solution structure as well as serving to enhance the water exchange rate; τ_m = 198 ns. Interestingly, the measured relaxivity and rotational correlation time obtained for the larger molecular weight species bearing four longer bis-amide linkers (3,448 Da) were less enhanced; r_1 = 19.6 $mM^{-1}s^{-1}$ and τ_R = 318 ns (25°C, pH 7.0). The lower efficiency was attributed to the increased fluctuations of the less rigid macromolecular species, decreasing the effective motional coupling of the Gd(III) ion centre allowing for its greater independent rotation.

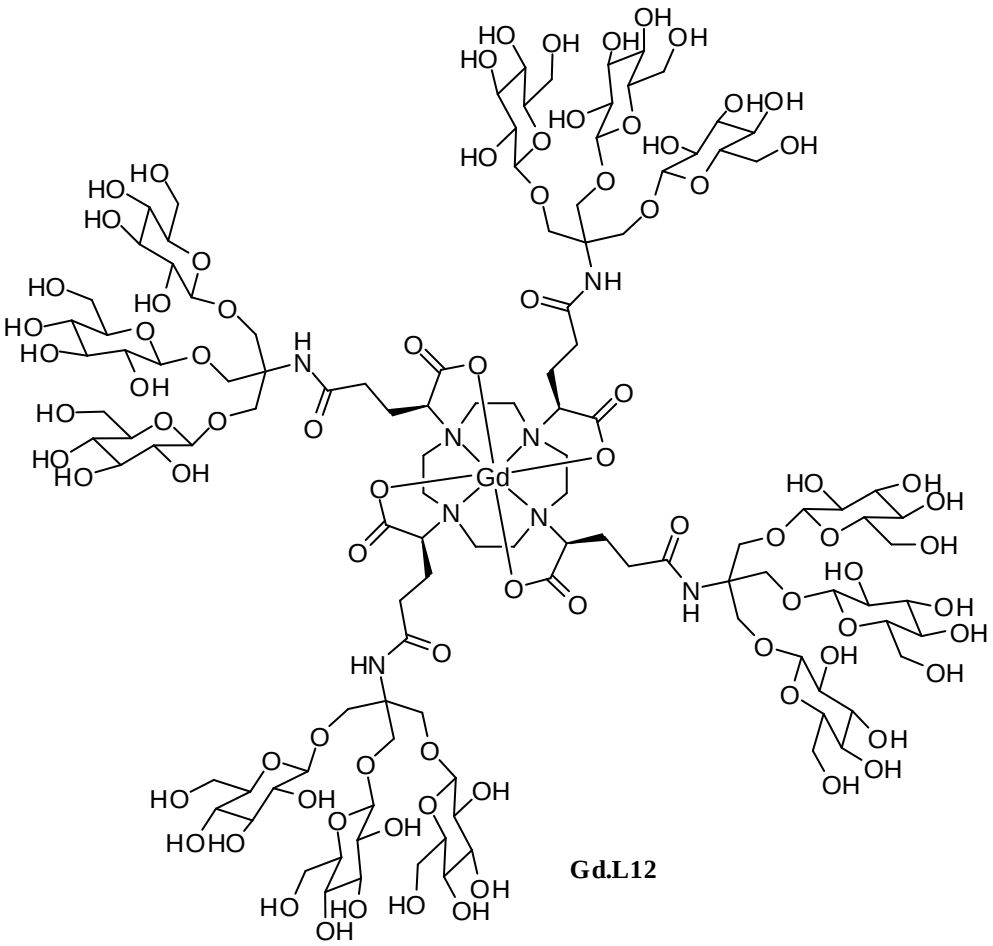

Gd.L12

The lengthening of the rotational correlation time, τ_R, has also been achieved by the receptor induced magnetisation enhancement (RIME) strategy in which pendant groups are attached to the Gd(III) chelate enabling binding to slowly tumbling molecules, such as serum proteins.[91] The attachment of hydrophobic moieties has lead, for example, to the development of contrast agents which bind non-covalently to the plasma protein human serum albumin (HSA), which is discussed in more detail in Chapter 3. A second strategy is the incorporation of amphiphilic, hydrophobic side chains allowing for the incorporation of several Gd(III) chelates into slowly tumbling liposomes either within the liposome vesicle or immobilized in the membrane.[92]

Tóth and co-workers recently developed a system in which the attachment of a pendant C_{16} lipophilic chain to the hydroxymethyl group on the ethylendiamine bridge of the Gd(III) chelating group EPTA, **L13**, through ester bond formation yielded an amphiphilic conjugate, which *via* self assembly, forms micelles in aqueous solution.[93] Upon micellar aggregation of the Gd(III) chelates the measured relaxivity rose from r_1 = 9.11 $mM^{-1}s^{-1}$ for the monomeric species to r_1 = 22.59 $mM^{-1}s^{-1}$ (25°C, 20 MHz), owed to the reduced global motion of the generated micelle; τ_{Rg} = 2,100 ps (25°C). The relaxivity enhancement was lower

than expected, once again due to the internal flexibility of the micelle reducing the effective rotational correlation time of each of the Gd(III) components; τ_R = 330 ps (25°C).

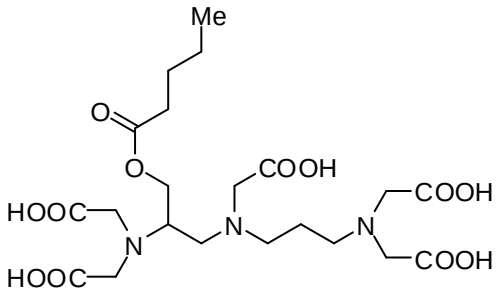

L13

1.4.3 Second Generation Contrast Agents

Current MRI contrast agent design has focused on the development of Gd(III) chelates whose relaxivities are modulated by physiological conditions or activity.[94] The incorporation of functionalised moieties into Gd(III) chelates which respond to biological events, such as variation in pH or enzyme activity, has been of great interest and are discussed in more detail in the following chapters.

The development of targeted contrast agents for cellular and molecular imaging is also of great interest in current contrast agent design.[95-97] MRI offers extremely high spacial resolution allowing for highly detailed whole body images to be achieved. The inherent insensitivity, however, makes it impossible for use in detecting the low concentrations of cell or disease sites. Clinically available contrast agents are administered in dosages at around 0.1 mmol Kg^{-1} to the patient to overcome the inherent insensitivity of the MRI scanner. The observed background signal due to the administration of such high concentration of contrast agents drowns out the cellular and molecular signals in the MR image. This has been overcome, however, by the incorporation of targeting vectors into contrast agents, which allow for the localisation and accumulation of contrast agents in specific sites through, for example, peptide binding[98, 99] or carbohydrate recognition.[100] The exploitation of the high affinity of avidin for biotin, $K_d \sim 10^{-15}$ M, has been used in a multistep approach for specific disease site imaging (Figure 14).[101]

A biotin labelled antibody is administered to the patient, which accumulates specifically at its preferred disease site. Once molecular targeting has been achieved an avidin labelled contrast agent is introduced to the patient which localises and binds with great affinity to the biotin allowing for accumulation of the contrast agent at the desired disease site, enhancing MR image intensity on a molecular level. Dendrimeric contrast agents or

multi Gd(III) bearing liposomes can be administered in this way to maximise the local relaxivity enhancement.

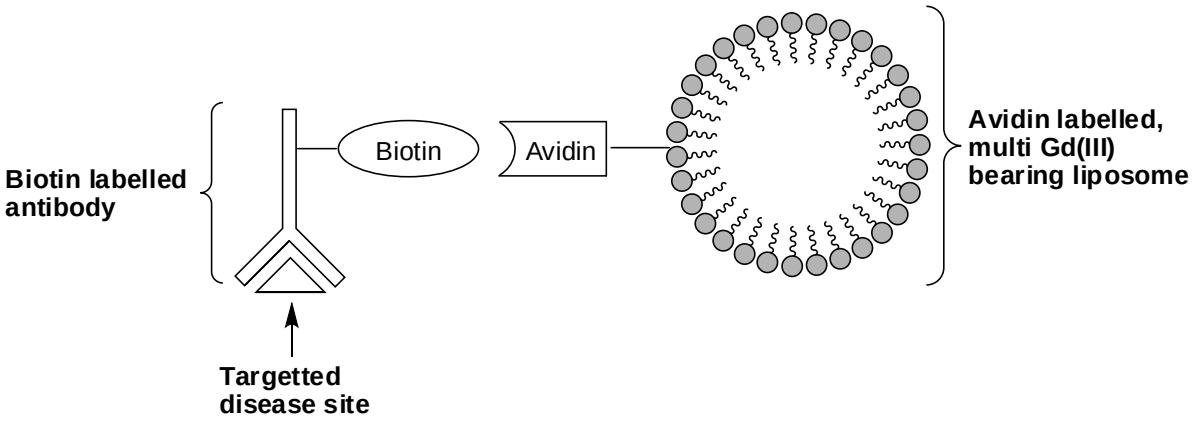

Figure 14. Specific disease site targeting of multi-Gd(III)-containing liposome *via* avidin-biotin recognition.

A new type of MRI contrast method has recently been reported where the bulk water signal intensity is varied *via* chemical exchange saturation transfer (CEST). The incorporation of paramagnetic ions into chelates incorporating interchangeable protons has lead to the development of so called PARACEST agents.[102, 103] Aime and co-workers developed a pH responsive PARACEST agent, in which the DOTAM-Gly, **L14**, ligand chelate incorporates amide protons which are interchangeable with those of the bulk water.[104] An RF pulse is applied at the resonance frequency of the interchangeable amide protons, which results in a reduction of the bulk water proton signal as the saturation effect is transferred through the chemical exchange process. Similar to T_2 contrast agents, PARACEST agents serve to lower MR image intensity.

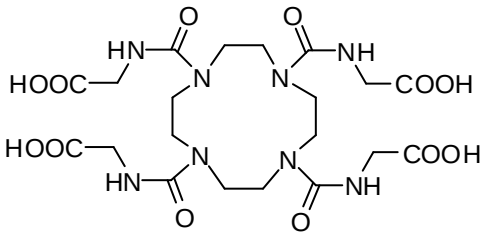

L14

Several paramagnetic lanthanides were incorporated into **L14** (Eu(III), Dy(III), Ho(III), Er(III), Tm(III) and Yb(III)), which each provided varying chemical shift differences between the amide and bulk water proton resonances, which allows for dual contrast agent administration for concentration independent determination of pH. The interchangeable proton exchange process is base-catalysed and, therefore, the rate of proton exchange, k_{ex}, showed pH dependence leading to varying degrees of saturation to be observed within the pH range 5.5-8.1.

1.5 The Lanthanides

1.5.1 Properties of the Lanthanides

The lanthanides are the series of highly electropositive period 6 metals, which intervene between the *s* and *d*-blocks of the periodic table. The series comprises the elements from lanthanum (atomic number 57) to lutetium (71) with electronic configurations consisting of a xenon core with periodical filling of the seven 4*f* orbitals, from f^o to f^{14}. The lanthanides are often referred to as the rare earth elements, which is rather misleading as over 100 minerals are known to contain the metals, such as monoazite; a phosphate mineral of mixed lanthanides and thorium, $(Ln,Th(PO)_4)$ and bastnaesite; a lanthanide fluorocarbonate. The most abundant lanthanide is cerium (Ce), the first member of the series to be discovered in 1803, which is present at ~ 66 ppm in the earth's crust; the 26th most abundant element on earth. Even the least common naturally occurring lanthanide, thulium (Tm, discovered in 1879) is more abundant than iodine. The final member of the series to be discovered was the radioactive element promethium (Pm) in 1947.[105]

Unlike the *d*-block elements, the chemical properties along as the lanthanide series is traversed are extremely uniform. The common oxidation state in aqueous solution is +3, however Eu(II) can be prepared by reduction with zinc but is easily oxidised. Likewise, Yb(II) and Sm(II) can also be prepared but are also rapidly oxidised. Reduction potentials, E^o, for the Ln^{3+}/Ln^{2+} process are E^o = –0.35 V, –1.05 V and –1.55 V for Eu(II), Yb(II) and Sm(II) respectively. Cerium is the only lanthanide of interest which can exist in the +4 oxidation state, with the Ce^{4+}/Ce^{3+} reduction potential of E^o = +1.72 V, and can remain present in solution for several weeks.[106] The common trivalent state results sequential loss of the $4f^16s^2$ electrons from the $[Xe]6s^24f^n$ core (for Gd and Ce loss of the $5d^16s^2$ electrons from the $[Xe]5d^16s^24f^n$ core occurs). The uniformity of the +3 oxidation state is highlighted by the similar observed Ln^{3+}/Ln^o reduction potential across the series measured at around E^o = –2.30 V in acidic media and E^o = –2.80 V in basic media for each of the metals in the series, with europium the only exception at E^o = –1.99 V (acidic) and E^o = –2.51 V (basic).[105]

The ionic radii decrease along the lanthanide series, however the extent of the observed decrease is greater than expected, with the ionic radii measured as 1.16 Å (La(III)) and 0.97 Å (Lu(III) (C.N. = 8).[25, 26] The phenomenon is known as lanthanide contraction and is the result of the poor shielding properties of the 4*f* orbitals. The increasing effective nuclear charge, Z_{eff}, along the series is therefore not compensated by the addition of the electrons to the 4*f* shell, resulting in the large contraction of the ionic radii.[4]

1.5.2 Lanthanide Coordination Chemistry

The lanthanide ions are hard Lewis acids, preferentially binding hard bases, such as nitrogen and oxygen.[107] The 4*f* orbitals are buried within the Ln(III) ions, shielded by the 5*s* and 5*p* orbitals. As a consequence, the 4*f* orbitals are not available for covalent interactions with coordinating ligands. The shielding results in large similarities in the chemical behaviour of each of the Ln(III) ions. Ln(III)-ligand interactions are largely electrostatic, with the coordination geometry of complexes formed being affected by steric factors due to lanthanide contraction.[106]

In aqueous solution the Ln(III) aquo ion is formed, with C.N. 9 for the larger ions (La(III)-Nd(III)) and 8 for the smaller (Dy(III)-Lu(III)). The Ln(III) ions undergo hydrolysis at pH > 6 resulting in precipitation of $Ln(OH)_3$. pH control is, therefore, particularly important during the preparation of lanthanide complexes in aqueous solution.[106]

The large size of the lanthanide ions results in complex formation with coordination numbers of 8 or 9 very common. The arrangement of the ligands around the Ln(III) ion, minimizing repulsion, is effected by the varying sizes of the lanthanide ions, leading to irregular complex geometries across the series. One example is shown by the contrasting geometries of the acac ($CH_3COCHCOCH_3$) complexes formed with Yb(III) and La(III). The $[Yb(acac)_3H_2O]$ complex forms a capped trigonal prismatic structure. The monohydrated species is seven coordinate as a result of the small ionic radius of the metal ion centre. La(III) is larger and the eight coordinate $[La(acac)_3(H_2O)_2]$ complex formed adopts a square antiprismatic geometry as a result.[4]

As mentioned above, the strong hard Lewis acid behaviour of the Ln(III) ions causes a preference for ligation with hard Lewis bases such as nitrogen and oxygen, with the 4*f* orbitals unaffected by the largely electrostatic interactions. With the exception of La(III) and Lu(III), each of the Ln(III) ions contain 1-7 unpaired 4*f* electrons and they are therefore paramagnetic. This has lead to the use of lanthanide complexes as shift reagents in NMR spectrometry. The NMR active nuclei of a Lewis base coordinated to the Ln(III) ion will feel the effect of the unpaired electrons leading to its paramagnetic relaxation, spectral line broadening and shift of resonances in of the NMR spectra. Lanthanide induced shift (LIS) methods have been applied to the structural determination of several biological macromolecules, such as proteins and nucleic acids.[108, 109]

1.5.3 Lanthanide Luminescence

The photophysical properties of the lanthanide ions have been of intense research in recent years leading to the development of many devices, such as optical fibres, luminescent

lamps, television and computer displays and lasers, as well as luminescent sensors in diagnostic medicine. Lanthanide luminescence arises from three types of electronic transition. The first is *via* promotion of a 4*f* electron into the 5*d* subshell and the second is *via* both ligand-to-metal and metal-to-ligand charge transfer. Such transitions are allowed but due to their high energies very few are commonly observed. The most important source of lanthanide luminescence arises from the Laporte forbidden *f-f* transitions. The 4*f* orbitals are buried within the lanthanide ion, shielded by the $5s^2 5p^6$ orbitals, and as such are not affected by ligand field effects. With the exception of La(III) and Lu(III) ($4f^0$ and $4f^{14}$ respectively) each of the trivalent lanthanide ions are luminescent, with emission occurring in the visible and near IR regions of the electromagnetic spectrum; Gd(III) being the only exception requiring high excitation energies and emitting in the UV region.[110]

Interelectronic repulsions split the 4*f* orbitals into $^{(2S+1)}\Gamma$ terms (*S* = spin), which are separated by around 10^4 cm^{-1}, where Γ = S, P, D and F representing the quantum numbers *L* = 0, 1, 2, and 3 respectively. Spin-orbit coupling further splits these terms into *J* states (*J*=*L*+*S* → *L*–*S*), which are separated by around 10^3 cm^{-1}.[111] The ease of excitation is governed by the energy gap, Δ*E*, between the ground and excited states of the Ln(III) ion.

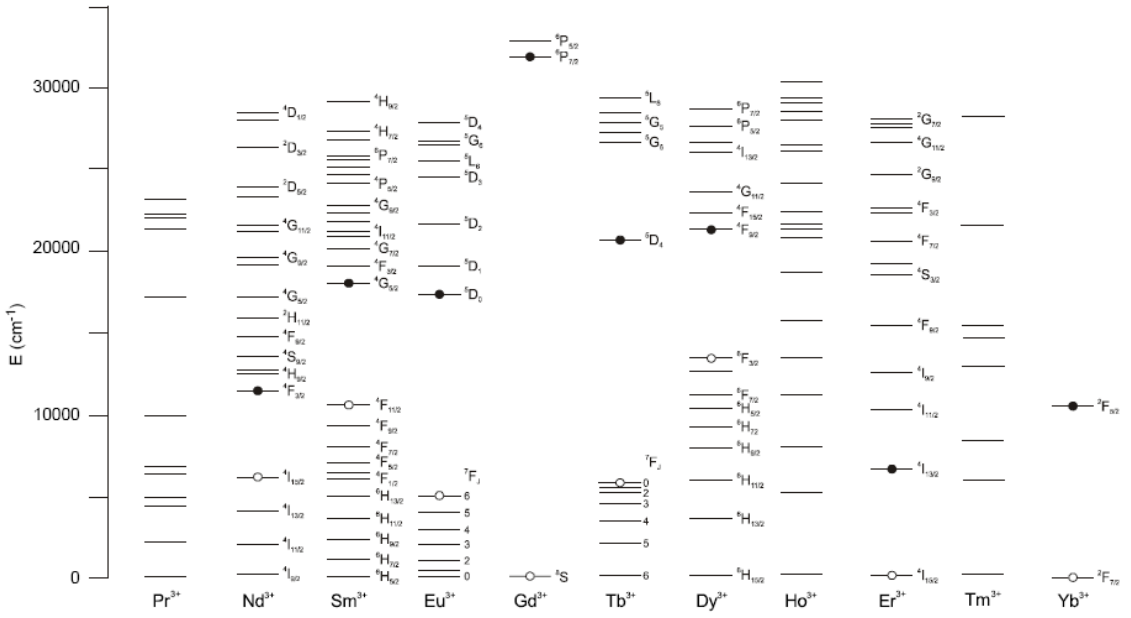

Figure 15. Energy diagram showing the electronic energy levels of several lanthanide ions. Filled circles represent the lowest energy excited state, while the open circle represents the highest energy ground state. Δ*E* values are measured between these two states.

Figure 15 shows the 4*f* energy level diagram for each of lanthanide ions. Significantly, Δ*E* for the Gd(III) ion is large at around 32,000 cm^{-1} ($^8S_{7/2}$ to $^6P_{7/2}$) which would require significant energy input to achieve excitation. Furthermore, as a result of the high energy of the excited state, the maximum emission wavelength, λ_{max}, occurs in the UV region of the

electromagnetic spectrum, which would overlap with the emission of organic chromophores that may be present in solution.[112] For the purposes of Gd(III) contrast agent development, luminescence studies with the Eu(III) and Tb(III) analogues are carried out. Observation of the two ions, which sit either side of gadolinium in the periodic table, are extremely useful due to the similar chemical properties of each ion in the lanthanide series, therefore conclusions drawn from luminescent studies with Eu(III) and Tb(III) complexes can be attributed to the Gd(III) analogue with considerable confidence.

Transitions between the energy levels occur *via* two operators; the electric dipole operator (ED) and the magnetic dipole operator (MD). ED transitions are forbidden by the Laporte rule, which states that the only allowed transitions are transitions that are accompanied by a change of parity.[14] If there is symmetry within the complex with respect to the inversion centre (*g*-symmetry) parity must be inverted, i.e. *g-u* are allowed while *g-g* transitions are forbidden (where *u*-symmetry denotes a complex where there is no symmetry with respect to the inversion centre). Therefore *d-p* or *p-f* transitions are allowed, where as *p-p* or *f-f* are forbidden. This can be overcome, however, if the centre of symmetry is eliminated by asymmetric vibrations, induced by both the ligand field and surrounding solvent oscillations, interconverting electronic states with different *J* values, but the same *S* and *L*, known as *J* mixing.[113] MD transitions are not forbidden by the parity rule, however their oscillator strength is extremely low, within the range 10^{-9} to 10^{-7}. The selection rules are $\Delta S = 0$, $\Delta L = 0$ and $\Delta J = 0 \pm 1$ allowed while $\Delta J = 0$ to 0 is forbidden.[113]

Ln(III)	Ground State	Excited State	Excited State Energy (cm^{-1})	ΔE (cm^{-1})	τ (ms)	λ_{max} (nm)	Emission Colour
Sm(III)	^6H_J	$^4G_{5/2}$	17,900	7,400	6.26	590	Orange
Eu(III)	^7F_J	$^5D_0$	17,277	12,300	9.67	620	Red
Tb(III)	^7F_J	$^5G_4$	20,500	14,800	9.02	550	Green
Dy(III)	^6H_J	$^4F_{9/2}$	21,100	7,850	1.85	570	Yellow

Table 6. Luminescent properties of selected aquo Ln(III) ions (Sm(III) and Eu(III) C.N. = 9 H_2O, Tb(III) and Dy(III) C.N. = 8 H_2O).

The Laporte forbidden electronic transitions between the 4*f* energy states result in long-lived radiative emission. Extinction coefficients, ε, are small at < 10 $M^{-1}cm^{-1}$ and the resulting narrow emission bands at specific wavelengths for each lanthanide, making them very recognisable as luminescent probes. Competition for radiationless energy transfer processes occurs through coupling of the emissive states with the vibration energies of nearby oscillators, such as O-H and N-H, resulting in the quenching of the observed luminensence.[114]

The larger the energy gap, ΔE, between ground and excited state energy levels, the more difficult it is for vibrational quenching to occur (Table 6).[112]

1.5.4 Luminescent Lifetime Studies: Determination of Hydration State, q

The hydration state, *q*, is of considerable importance in the development of Gd(III) based MRI contrast agents. The radiationless energy transfer processes that occur between the vibrational energy levels of H_2O and the excited states of Eu(III) and Tb(III) can be exploited in order to determine *q*.

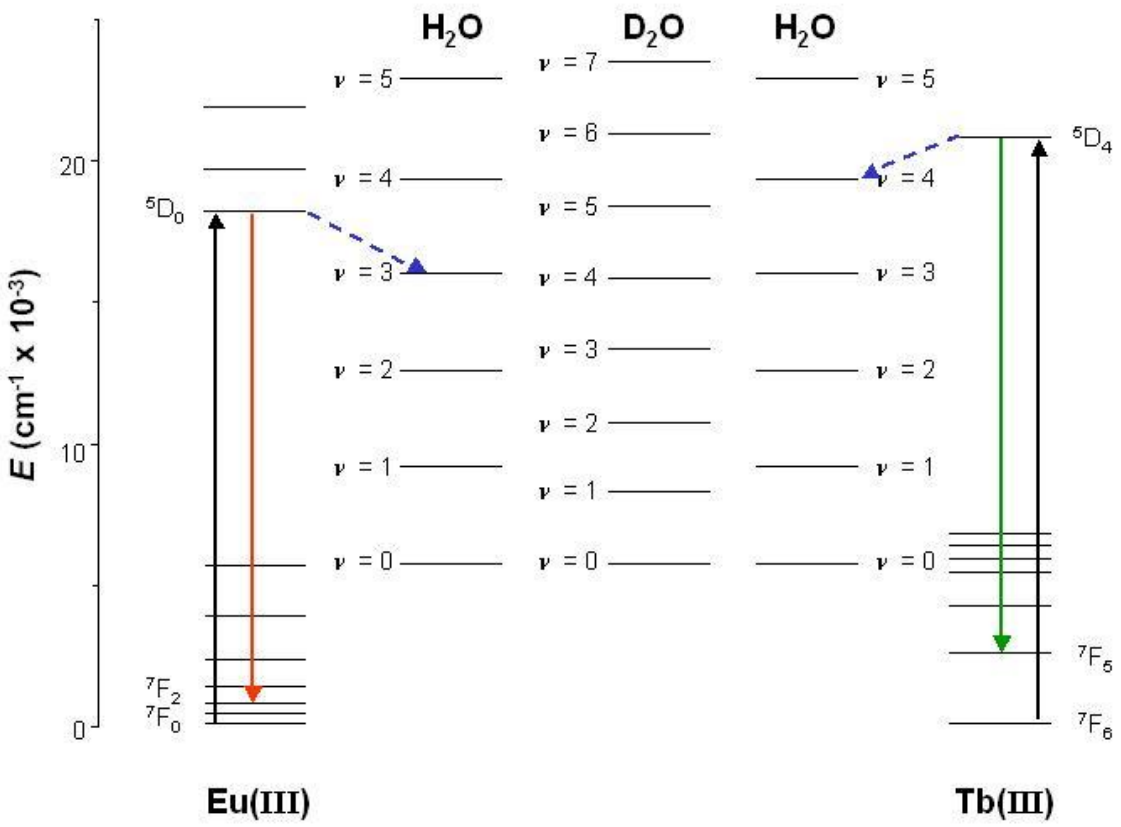

Figure 16. Vibrational quenching of Eu(III) and Tb(III) excited states. Excitation (black arrow) occurs from the ground to excited state ($^7F_0$ to $^5D_0$ for Eu(III) and $^7F_6$ to $^5D_4$ for Tb(III)) followed by emission, showing the $\Delta J = 2$ transition for Eu(III) (red arrow, $^5D_0$ to $^7F_2$ ~ 615 nm) and $\Delta J = 1$ for Tb(III) (green arrow, $^5D_4$ to $^7F_5$ ~ 545 nm). There is greater overlap of the $\nu = 3$ vibrational level of H_2O with the $^5D_0$ excited state of Eu(III) than with the $^5D_4$ excited state of Tb(III) resulting in greater quenching and shorter lifetime of Eu(III) emission *via* radiationless energy transfer (blue dashed arrow). Overlap of the less populated $\nu = 4$ and $\nu = 5$ vibrational level of D_2O with the excited states of Eu(III) and Tb(III) respectively results in reduced quenching and longer emission lifetimes in this media.

Figure 16 shows the overlap between the excited energy states of Eu(III) and Tb(III) with the vibrational energy levels of H_2O and D_2O. $\Delta\nu_{OH}$ and $\Delta\nu_{OD}$ are 3,405 cm^{-1} and 2,520 cm^{-1} respectively with no anharmonicity assumed in the vibrational ladder.[111] Radiationless energy transfer between the $^5D_0$ excited state of Eu(III) with the $\nu = 3$ vibrational level of H_2O occurs due to the efficient overlap of the two energy states. In

accordance with the Frank-Condon principle, the vibrational state populations decrease dramatically with increasing energy. Therefore energy transfer efficiency is much reduced for Tb(III) in aqueous media as the $^5D_4$ excited state overlaps with the less populated $\nu = 4$ vibrational level of H_2O, resulting in longer emission lifetimes in comparison to Eu(III). Similarly, vibrational quenching in the presence of D_2O is lower with respect to H_2O due to the overlap of the ^5D_o to $\nu = 4$ and the $^5D_4$ to $\nu = 5$ energy levels of Eu(III) and Tb(III) respectively. Consequentially, the rate of decay of the emission of both Eu(III) and Tb(III) is approximately 200 times slower in D_2O than in H_2O due to the lower vibrational frequency of the O–D oscillations.[111] Measurement of emission intensity *vs.* time in both H_2O and D_2O enables measurement of the first order decay constants, k_{H_2O} and k_{D_2O}, which are applied to Equations 33 and 34 in order to calculate the hydration state value, q.[115, 116]

$$q_{Eu} = 1.2[(k_{H_2O} - k_{D_2O}) - 0.25] \quad (33)$$

$$q_{Tb} = 5[(k_{H_2O} - k_{D_2O}) - 0.06] \quad (34)$$

1.5.5 Sensitised Emission

The intrinsic low extinction coefficients of the lanthanide ions (ε = < 10 $M^{-1}cm^{-1}$) lead to the direct excitation of the Laporte forbidden *f-f* transitions to be very difficult. The use of laser light, such as tunable dye lasers and argon lasers, has been implemented to overcome the required high energy. However, the most efficient form of lanthanide excitation arises from the incorporation of an organic chromophore into the Ln(III) ligand, energy transfer from which results in the indirect excitation of the Ln(III) ion.[117]

Organic chromophores (often referred to as antennas) with high extinction coefficients, ε, are attached to the Ln(III) ligand. These absorb light efficiently in the UV region resulting in population of their singlet excited state. The heavy-atom effect, arising from the presence of the large (Ln(III) ion) strengthens the spin-orbit coupling of the organic chromophore, inducing the increased rate of intersystem crossing (ISC) from the singlet to the triplet excited state.[118] Provided the triplet excited state energy of the chromophore is higher than the Ln(III) excited state, energy transfer can occur to the lanthanide, enhancing the emission intensity of the Ln(III) ion and increasing the effective extinction coefficient of the complex, represented by the Jabloński diagram in Figure 17.[119]

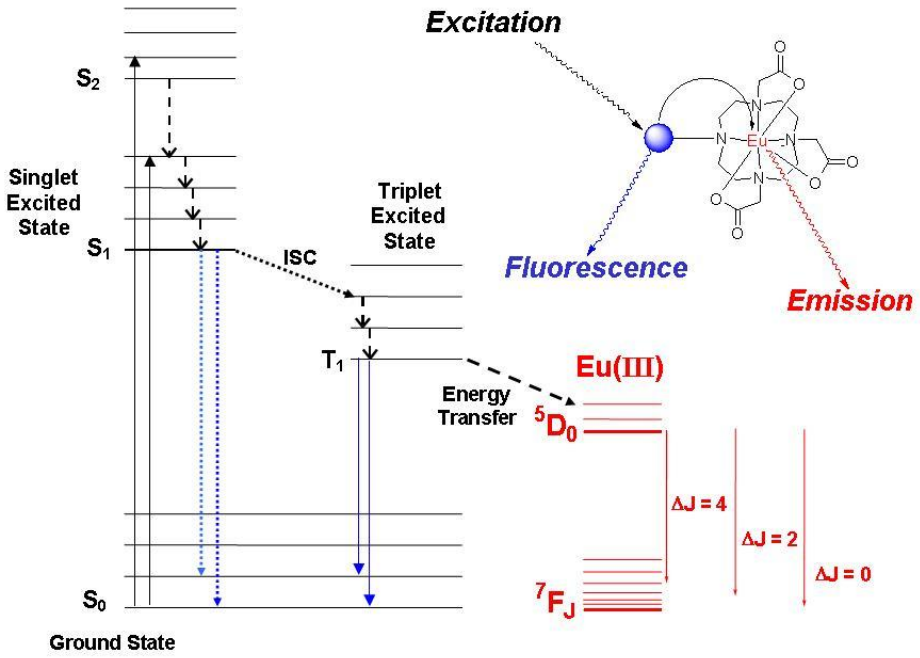

Figure 17. Jabloński diagram demonstrating Eu(III) sensitised emission. The excitation (black, solid arrows) of an organic chromophore to its singlet excited states (S_1 and S_2) is followed by its short-lived fluorescence (blue dotted arrows). ISC to the chromophore triplet excited state, T_1, occurs due the heavy-atom effect, caused by the presence of the Ln(III) ion (black dotted arrow), followed by its associated phosphorescence (blue solid arrows). Energy transfer from T_1 to the ^5D_o excited state of Eu(III) occurs as T_1 is higher in energy (black, dashed arrow), resulting in enhanced Eu(III) emission (red, solid arrows). Inset; schematic representation of an organic antenna bearing Eu-DO3A species. Note: if the ISC and energy transfer processes are efficient no organic fluorescence or phosphorescence is observed.

The efficiency of sensitised emission is indicated by the overall quantum yield, $\Phi_{overall}$, which is governed by three factors. Firstly, the quantum yield of formation of the chromophore triplet excited state, Φ_A, which is dependant on the efficiency of the ISC process. Secondly, the rate of energy transfer to the Ln(III) excited state, η_{ET}, which is enhanced by reduction of the Ln(III)-antenna distance which in turn reduces the degree of back energy transfer. Finally, the emissive quantum yield of the Ln(III) ion, Φ_{em}, which comprises the reduced emissive lifetime, τ, caused by vibrational energy transfer to nearby O-H and N-H oscillators, and the natural radiative rate constant, k_o (i.e. the rate of decay of Ln(III) emission in the absence of the induced decay processes, Equations 35-37).[120]

$$\Phi_{overall} = \Phi_A \eta_{ET} \Phi_{em} \tag{35}$$

$$\Phi_{em} = k_o \tau \tag{36}$$

$$\Phi_{overall} = \Phi_A \eta_{ET} k_o \tau \quad (37)$$

Greater efficiency is therefore achieved by the incorporation of organic chromophores within the Ln(III) chelate, minimising the Ln(III)-distance and reducing the degree of interaction with solvent oscillations. The rate of energy transfer is $1/r^6$ distance dependent, where r is the distance between the metal and chromophore centre.[120] Quenching of the singlet excited state must also be reduced in order to enhance the efficiency of the ISC process. Quenching may occur by either intermolecular electron transfer, i.e. through anionic species present in solution, such as halides, or intermolecular electron transfer, i.e. through the central Ln(III) ion (typically Eu(III) and Sm(III), each known to exist in the +2 oxidation state). Equation 38 shows the free energy of the excited state electron transfer process, ΔG_{ET}, in which E_{ox} is the oxidation potential of the donor, E_{red} is the reduction potential of the acceptor, E_s is the singlet excited state energy, n is the number of moles, F is the Faraday constant (9.64853 x 10^4 C mol^{-1}) and $e^2/\varepsilon r$ is related to the formation of a radical ion pair (usually less than 0.2 eV).[120]

$$\Delta G_{ET} = nF\left([E_{ox} - E_{red}] - E_s - e^2/\varepsilon r\right) \quad (38)$$

The quenching effects are reduced by modulation of the redox potentials of the chromophores. For example, the addition of electron withdrawing groups to aromatic ring chromophores increases its oxidation potential, resulting in the reduction of electron transfer to Eu(III).[121]

Finally, the energy of the triplet excited state chromophore must be higher than the Ln(III) excited state, with efficient overlap. Several heteroaromatic compounds have been used to achieve this, the parameters of which are shown in Table 7.[120]

Chromophore	E_s (eV)	E_t (cm^{-1})	E_{ox} (V)	E_{red} (V)
Phenanthrene	3.57	21,500	+1.50	-2.44
Triphenylene	3.65	23,400	+1.55	-2.46
1-O-Me-naphthalene	3.88	20,900	+1.38	-2.65
O-Me-benzene	4.46	28,200	+1.76	> -2.70

Table 7. Parameters of several heteroaromatic chromophores.[120] E_s and E_t represent the singlet and triplets energies respectively. Redox potentials were measured in DMF and MeCN.

Not only does the incorporation of organic chromophores enhance the effective extinction coefficient of the Ln(III) complex, it does so with almost no background fluorescence. Organic chromophores absorb light and fluoresce in the UV region of the electromagnetic spectrum, with λ_{ex} ~ 270-300 nm for aromatic compounds and λ_{em} ~ 350-400 nm. Lanthanide emission is within the visible light region, λ_{em} ~ 570-720 nm for Eu(III) complexes, resulting in a large Stokes' shift observed in the emission spectra.[122] Figure 18 show the typical excitation and emission spectra for an Eu(III) complexes bearing an organic chromophore, demonstrating the large observed Stokes' shift between the organic absorption and the Eu(III) emission.

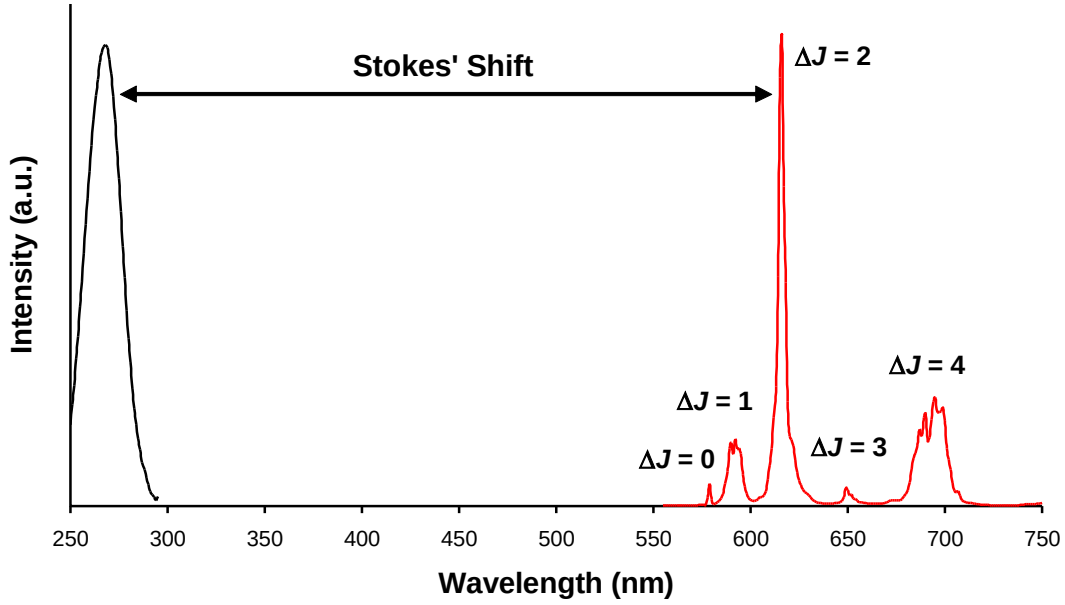

Figure 18. Typical Eu(III) emission spectrum (red) of an organic antenna bearing Eu-DO3A species. Excitation (black) of the organic chromophore occurs at much shorter wavelengths in the UV region, resulting in a large Stokes' shift from the Eu(III) emission in the visible light region.

Figure 18 shows a typical Eu(III) emission spectrum, in which the narrow bands correspond to the varying J values between the $^5D_0$ to ^7F_J transitions, i.e. $\Delta J = 0$ corresponds to the $^5D_0$-$^7F_0$ transition, $\Delta J = 1$ corresponds to the $^5D_0$-$^7F_1$ transition etc. The inherent low extinction coefficient of the Eu(III) ion arising from the transitions between the deeply buried 4*f* orbitals, which are not involved in bonding and therefore not affected by ligand field effects result in the appearance of the narrow bands in the emission spectrum with little variation in the emission wavelength. The bands, however, vary in intensity and spectral form depending on the Eu(III) coordination environment, which is summed up in Table 8.[111, 113]

ΔJ	λ_{em} range (nm)	Intensity	Comments
0	577 - 581	Very weak	ED Forbidden transition, gains intensity through *J*-mixing
1	585 - 600	Strong	MD allowed, intensity independent from environment. Three transitions observed for low symmetry, with two for C_3 and C_4
2	610 – 625	Strong to very strong	ED hypersensitive, increases intensity as symmetry is lost and donor atom type is changed
3	640 - 655	Very weak	ED forbidden always weak
4	680 – 710	Medium to strong	ED, sensitive to Eu(III) coordination environment
5	740 - 770	Very weak	Forbidden, rarely observed
6	810 - 840	Very weak	Rarely observed

Table 8. Factors effecting Eu(III) ΔJ transitions.[111, 113]

1.5.6 Time Resolved Immunoassay

A further advantage of sensitised emission is the lifetime of the Ln(III) emission with respect to that of the chromophore. Ln(III) emission lifetimes are on the millisecond timescale, much longer lived than the organic fluorescence, with lifetimes on the nanosecond timescale. The incorporation of a delay time, around 200 ms, following initial excitation allows for the organic fluorescence to be gated-out completely, leaving only the Ln(III) emission to be observed.[123] The principle has lead to the development of time resolved immunoassay probes, such as the widely used DELFIA® (dissociation enhanced lanthanide fluoroimmunoassay) method developed by PerkinElmer.

A receptor targeted lanthanide bearing luminescent probe is administered to a urine or blood sample from the patient *in vitro*. Following excitation by a flash lamp, a delay time is applied during which the background fluorescence of the biological surroundings disappears, leaving the longer Ln(III) emission alone, which is measured during the counting time. The scan is over in a matter of milliseconds, which allows for many scans to be carried out within a short period, maximising the signal to noise ratio. Figure 19 illustrates the principles behind time resolved fluorometry, while below are the structures of SCN-Ph-EDTA, **L15**, and SCN-Ph-DTTA, **L16**, which are employed in the DELFIA® system, which incorporate an isothocyanatophenyl chromophore, which is replaced by a targeting vector such as an antibody, into the non-fluorescent Ln-EDTA and Ln-DTTA complexes.[122]

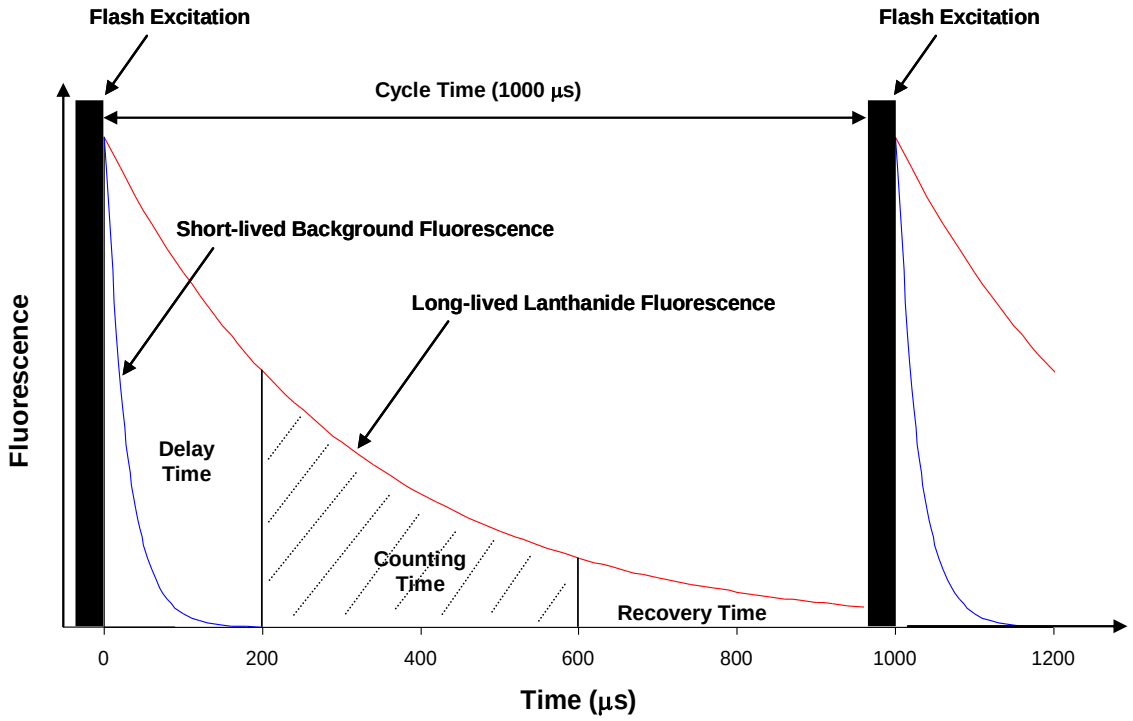

Figure 19. Illustration of the principles of time-resolved fluorometry. A delay time of 200 µs is applied to the sample following flash lamp excitation. The organic background fluorescence (blue) has expired leaving only lanthanide fluorescence (red) to be measured during the 400 µs counting time. Further excitation occurs after 1000 µs and the experiment is repeated.

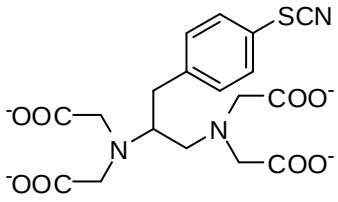

L15

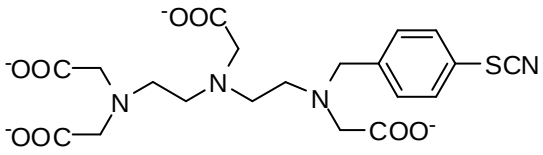

L16

1.5.7 Luminescent Lanthanide Probes

The preparation and incorporation organic chromophores into ligands for efficient Ln(III) sensitised emission has been of considerable interest in recent years in the development of luminescent probes for diagnostic imaging applications.[112, 117, 124] Faulkner and co-workers recently developed a Ln-DO3A complex incorporating a triazolophthalazine moiety, **L17**, which displayed sensitisation of a series of lanthanide ions; Eu(III), Yb(III), Nd(III) and Er(III).[125]

The triplet energy state of the chromophore was estimated at E = 23,600 cm^{-1} *via* measurement of the phosphorescent emission of the free ligand in an optical glass at 77 K. This overlapped well with the excited state of Eu(III) (E = 17,277 cm^{-1}) but was significantly higher than the other lanthanides, each with excited state energies of E ~ 10,000 cm^{-1} emitting in the near-IR region of the electromagnetic spectrum. The result is slower energy transfer and

reduced sensitised emission compared to the Eu(III) complex. Calculation of the hydration state, *q*, proved the ligand to bind in an octadentate manner to the Ln(III) centre, assumed to be *via* the pendant nitrogen resulting in the formation of a five-membered chelate. Vibrational quenching was more pronounced for the Nd(III) and Er(III) complexes, which posses several intermediate energy states resulting in more efficient quenching by O-H and N-H oscillators. Table 9 shows the luminescent observations for each of the Ln(III) analogues.

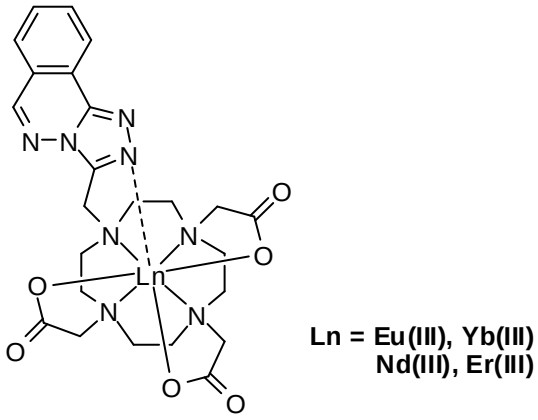

Ln.L17

Ln(III)	λ_{ex} (nm)	λ_{em}(nm)	τ_{H_2O} (ms)	τ_{D_2O} (ms)	*q*
Eu(III)	304	617	620	1670	0.9
Yb(III)	337	980	1.87	7.88	0.3
Nd(III)	337	1055	0.09	0.33	-
Er(III)	337	1540	< 0.02 (weak)	1.3	-

Table 9. Luminescent observations for **Ln.L17**. Note, *q* values for Nd(III) and Er(III) unable to be measured due to rapid quenching from O-H oscillators.

Pikramenou and co-workers developed a dinuclear lanthanide complex in which three bis(*β*-diketone) ligands bearing a 1,3-phenylene spacer, **L18**, bind bidentate to the Ln(III) ion.[126, 127]

The ligand phosphorescence was studied using the Gd(III) analogue, which displayed an emission band with λ_{max} = 490 nm corresponding to the $^3\pi\pi^*$ triplet energy state. The measured energy from the phosphorescence studies was 20,408 cm^{-1} (DMF, 77 K, λ_{ex} = 368 nm), which is sufficiently high for energy transfer to occur to Eu(III), Sm(III) and Nd(III) but to low for both Tb(III) and Dy(III). Each of the Ln(III) ligand complexes showed similar emission and excitation spectra, with λ_{ex} = 360 nm and λ_{ex} = 357 for the R = H and R = OCH_2CH_3 ligands respectively, with ε = 13 x 10^4 $M^{-1}cm^{-1}$. Lifetime measurements of the Eu(III) analogue confirmed the presence of three bidentate ligands as *q* values were measured as *q* = 3.4 and *q* = 2.6 (room temperature and 77 K respectively) as three of the nine

coordination sites were free for water to bind. The overall emission quantum yields, $\Phi_{overall}$, were measured as 5% and 0.6% for Eu(III) and Sm(III) respectively and estimated to be 0.6% for Nd(III).

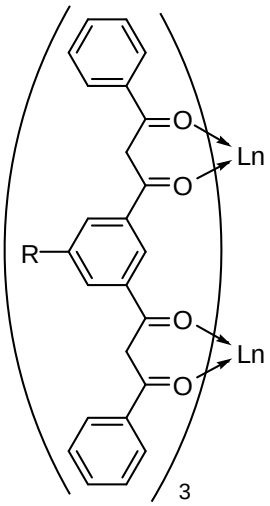

Ln = Eu(III), Sm(III)
Nd(III), Gd(III)
R = H, OCH_2CH_3

L18

As the excited states of Eu(III) and the ligand were are 3,000 cm^{-1} apart the poor efficiency for Eu(III) sensitisation was not attributed to back energy transfer processes but instead to potential LMCT processes thermally quenching the ^5D_o level of Eu(III). The lifetime measurements were 220 μs, 13 μs and 1.5 μs for Eu(III), Sm(III) and Nd(III) respectively. The short lifetimes observed are attributed to vibrational energy transfer due to the presence of three coordinated water molecules.

Parker and co-workers have worked extensively in the development of responsive luminescence sensors for the detection of varying serum anion concentrations.[128, 129] Recently, a cationic Eu(III) complex bearing a pyridothioanthone antenna, **[Eu.L19]$^{3+}$**, was developed as a pH insensitive, ratiometric chemosensor for citrate anions.[130]

The triply charged Eu(III) complex possesses two free coordination sites, permitting bidentate anionic binding. Phosphorescence studies of the free ligand measured the triplet excited state energy as E = 23,700 cm^{-1}, with ε = 6,670 M^{-1} cm^{-1} (λ_{ex} = 370 nm, λ_{em} = 424 nm, 4:1 EtOH:MeOH, 77 K), which is sufficiently high in energy to sensitize both Eu(III) and Tb(III). Upon sensitised excitation of the Eu(III) complex at λ_{ex} = 384 nm the overall quantum yield, $\Phi_{overall}$, was measured as 8.8% in water (18% D_2O), with the lifetimes of the ^5D_o excited state measured at 0.30 ms (H_2O) and 0.47 ms (D_2O), which in turn lead to the determination of the hydration state to be q = 1.15 ± 20%. The titration of sodium citrate with 5 mM of the Eu(III) complex resulting in variations in the luminescence spectral form, with the ΔJ = 2 band (616 nm) increasing in intensity with the ΔJ = 0 band (579 nm) decreasing as

a result of both the displacement of water molecules and conformational changes of the Eu(III) geometry. The maximum hydration state value was q = 0.7 ± 2% in the presence of citrate. The affinity constant, K, was determined as 3.3 ± 0.6 x 10^6 M^{-1} from the titration curve. Similar titrations with other serum anions demonstrated bidentate binding occurs, but did not result in significant changes in the ratio of intensities of the ΔJ = 2 / ΔJ = 0 bands. Furthermore, variation of pH titrations showed the ΔJ = 2 / ΔJ = 0 ratio of intensities to remain constant between the physiological pH values of 6.8 and 8.2. This allows for the use of this complex as a ratiometric sensor for variations of citrate concentrations, which is independent of the presence of other serum anions and variations of pH. A further citrate titration was carried out in the presence of a simulated ionic background (0.9 mM Na_2HPO_4, 2.3 mM sodium lactate, 0.1 M NaCl, 20 mM $KHCO_3$), from which the binding affinity of citrate was determined as 3.7 ± 0.4 x 10^3 M^{-1}, which is somewhat lower than that measured for the complex in the presence of citrate alone due to the binding competition from the other anions present in solution.

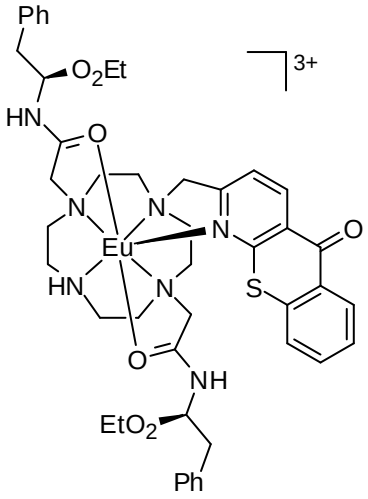

[Eu.L19]$^{3+}$

1.5.8 Thesis Outline

The factors affecting the efficiency of MRI Gd(III) contrast agents, such as the hydration state, q, and the rotational correlation time, τ_R, have been manipulated in order to enhance relaxivity and MR image intensity. Furthermore, the luminescent properties of the chemically similar lanthanide ions has been explored, which has lead to the development of responsive luminescent probes.

In Chapter 2, modulation of the hydration state, q, was achieved following the incorporation of diphenylphosphinamide (dpp) moieties into Gd-DO3A chelates. Reversible, pH responsive intramolecular anion binding was observed. The relaxivity of the Gd(III) analogues increased in acidic media as the dpp moiety moved away from the metal centre.

The opposite trend was observed following luminescent investigations of the Eu(III) analogues. Sensitized Eu(III) emission was observed following excitation of the dpp antenna. The energy transfer to the Eu(III) was more efficient in basic media as the dpp moiety was bound the metal centre. In acidic media Eu(III) emission was decreased as energy transfer was reduced and quenching water molecules became coordinated.

The affinity of the hydrophobic dpp moieties for the serum protein HSA was explored in Chapter 3. Non-covalent attachment of a contrast agent to a slowly tumbling protein increases the rotatational correlation, τ_R, of the Gd(III) complex and, therefore, increase relaxivity (Section 1.4.2). The dpp complexes showed a high affinity and site specific binding to the protein, which was investigated by both relaxometric (Gd) and luminescent (Eu) methods.

The intermolecular binding affinity of serum anions, such as carbonate, to neutral Gd(III)-based $q = 2$ contrast agents was exploited in Chapter 4 in order to develop an enzyme responsive contrast agent. An activation and accumulation strategy was employed in which a neutral contrast agent, incorporating acetoxymethyl ester groups, would pass into cells. Low relaxivity would be expected as carbonate anions bind to the Gd(III) centre displacing exchanging water molecules. Intracellular esterases would enzymatically hydrolyse the pendant acetoxymethyl ester groups unmasking a negatively charged complex, which would both repel the bound carbonate anions allowing waters to exchange with the metal centre, enhancing relaxivity while reducing the outflow from the cell. The contrast agent would effectively be "switched on" and accumulated inside the cell following enzymatic activation. Investigations were carried out by both relaxometric (Gd), luminescent (Eu) and ^{1}H NMR spectroscopy (Y) methods following the preparation of model ethyl ester and free acid complexes as well as the acetoxymethyl ester complex.

Chapter 2

pH Responsive Contrast Agents and Luminescent Sensors

2.1 Introduction

Since the production of the first generation contrast agents there has been intense research into the design of imaging agents that are tailored to respond to changes in their biological environment. The production of contrast agents and luminescent sensors which respond to local changes in pH is born out of the knowledge that tumour tissue is more acidic (around pH 6.8-6.9) than normal, healthy tissue (pH 7.4).[43, 131] pH dependant variations of the rotational correlation time, τ_R, and water exchange lifetime, τ_m, as well as variations of the hydration state, *q*, within the narrow physiological pH range provide great scope for pH responsive Gd(III) contrast agent design. Likewise, variations in hydration state, *q*, and ligand based sensitisation of luminescent lanthanide complexes (e.g. Eu(III) and Tb(III)) provide routes to pH responsive lanthanide-based luminescent sensors.

2.2 pH Responsive Contrast Agents

2.2.1 Reversible Anion Binding

Water proton relaxivity, r_1, is enhanced by the presence of exchanging water molecules at the Gd(III) centre. In more basic media (pH > 10) exchanging water molecules are deprotonated resulting in the binding of hydroxide anions to the metal centre, which in turn decreases the *q* value and lowers relaxivity.[132]

The modulation of hydration state as a result of pH-dependant anionic binding has been studied further with the aim of narrowing the pH range to suit physiological conditions. Parker and co-workers investigated this area in two ways: the first involved the reversible intermolecular binding of endogenous anions to seven co-ordinate cyclen-based Gd(III) complexes bearing pendant alanine groups, **Gd.L20**.[133] In a simulated extracellular anionic background (30 mM $NaHCO_3$, 0.1 M NaCl, 0.9 mM Na_2HPO_4, 2.3 mM sodium lactate, 0.13 mM sodium citrate) displacement of the exchanging inner sphere waters, particularly by the more abundant carbonate anion, was observed, resulting in a decrease in water proton relaxivity as the $q = 2$ species changed to $q = 0$ (Scheme 1).

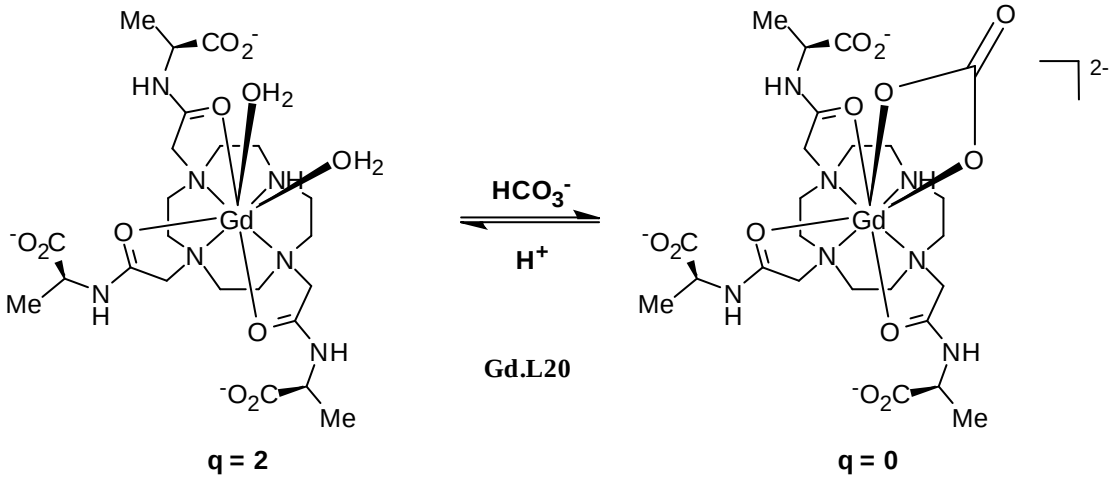

Scheme 1

The measured relaxivity in the pH range 8-12 was r_1 = 1.90 $mM^{-1}s^{-1}$ (20 MHz, 25°C) corresponding to the outer sphere water molecule contribution of the q = 0 species. Between pH 8-6, where competitive binding of carbonate anions was gradually reduced, the relaxivity rose dramatically to r_1 ~ 7.2 $mM^{-1}s^{-1}$ at pH 6 (20 MHz, 25°C) as the affinity for carbonate diminished and the q = 2 species was restored.

The second strategy adopted, involved the intramolecular reversible ligation of a pendant arylsulfonamide moiety, **[Gd.L21]$^{3-}$**. The base-promoted deprotonation of the pendant group varied the hydration state of the Gd(III) centre and consequently provided pH dependent relaxivity within a narrow pH range (Scheme 2).[134]

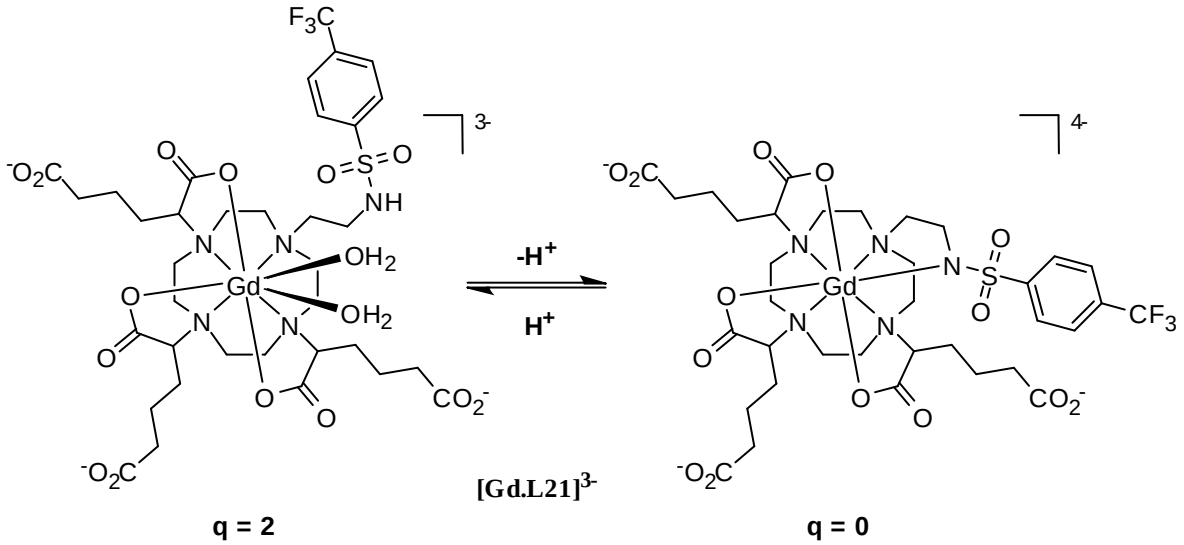

Scheme 2

Deprotonation of the sulfonamide at pH > 8 allowed the pendant moiety to bind to the metal centre, displacing coordinated water molecules and creating a q = 0 species with a measured relaxivity of r_1 = 2.5 $mM^{-1}s^{-1}$ (65 MHz, 25°C). This rose to r_1 = 8.7 $mM^{-1}s^{-1}$ at pH 5 in a simulated biological anionic background (Figure 20). The repulsion of such endogenous

anions was enhanced by the presence of the negatively charged carboxylate side chains on the complex, i.e. intermolecular anion binding is suppressed. The large increase in relaxivity over the relatively small physiological pH range allowed for preliminary pH mapping of murine tumours, shown in Figure 20.[135]

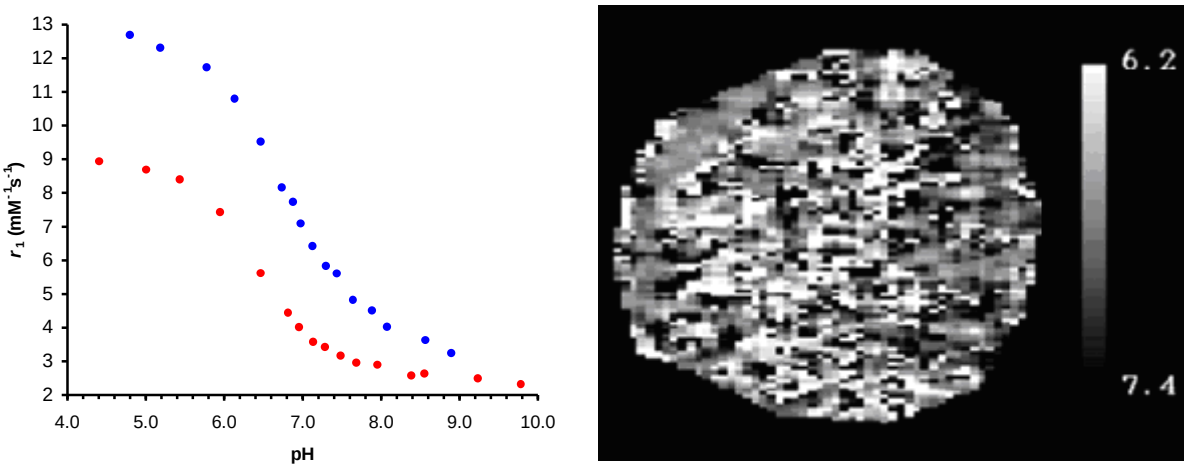

Figure 20. Left; the variation of relaxivity of **[Gd.L21]**$^{3-}$ (65.3 MHz, 298 K) with pH in a simulated extra cellular anion background (red dots, 0.5 mM complex) and in the presence of human serum solution,[134] diluted by a half (blue dots, 0.7 mM complex). Right; preliminary pH map of murine tumour.[135]

Complexes bearing a pendant moiety, which reversibly binds as a function of pH is of keen interest in contrast agent design, allowing for the variation of such groups in order to alter the pH range of the contrast agent.[136]

2.2.2 Modulation of the Rotational Correlation Time, τ_R, with pH

Increasing the relaxivity of a contrast agent can be achieved by slowing down its molecular tumbling (discussed in Chapter 1, Section 1.4.2). This was achieved by Aime and co-workers who prepared macromolecular systems containing thirty Gd(III) chelates bound to poly amino-acid chains containing an average of 114 ornithine residues, **Gd.L22**.[137] In acidic conditions the measured relaxivity was r_1 ~ 23 mM^{-1}s^{-1} (pH 4, 20 MHz, 25^{o}C), which is rather high and is accounted for by the large size of the molecule. At this pH the amino groups are protonated and highly hydrated and tend to remain far apart from each other, allowing greater mobility of the Gd(III) chelates so that the overall slow mobility of the molecule is 'felt less'. As pH moves to more basic conditions the NH_3^+ groups become deprotonated causing intermolecular hydrogen bonds to form between adjacent peptide chains, rigidifying the molecule, increasing τ_R, and increasing relaxivity to r_1 ~ 32 mM^{-1}s^{-1} (pH 8, 20 MHz, 25^{o}C).

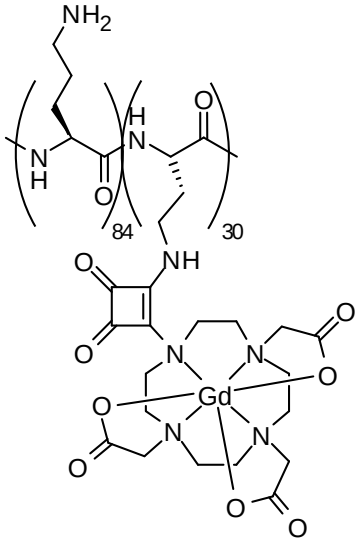

Gd.L22

Recently, a similar macromolecule has been used for concentration independent, R_2/R_1 ratiometric pH response.[138] The longitudinal water proton relaxation rate, R_{1p}, was seen to be responsive to pH, as described above. However, at higher magnetic fields its pH dependence is lost. The transverse water proton relaxation rate, R_{2p}, is field independent; therefore, its pH response is maintained even at higher field strengths. Ratiometric R_2/R_1 analysis at high field strengths (600 MHz) allows for pH determination, which is independent of the concentration of contrast agent used; a common problem in pH responsive contrast agent design.

Enhanced complex rigidity with decreasing pH was achieved by Merbach and co-workers who devised a series of PAMAM macromolecules incorporating the Gd-EPTPA chelate, **L23**. Three dendrimeric structures were prepared; G5-(Gd-**L23**)$_{111}$, G7-(Gd-**L23**)$_{253}$ and G9-(Gd-**L23**)$_{1157}$ with measured relaxivities of r_1 = 20.5 $mM^{-1}s^{-1}$, r_1 = 28.3 $mM^{-1}s^{-1}$ and r_1 = 27.9 $mM^{-1}s^{-1}$ respectively (pH 7.4, 37^{o}C, 30 MHz).[139]

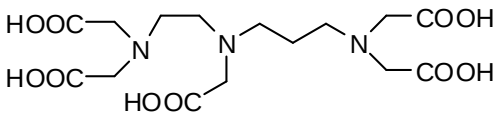

L23

Protonation of the tertiary amine groups in the PAMAM skeleton in acidic media causes an expansion of the dendrimeric structure. The increased rigidity with decreasing pH increases the rotational correlation time and enhances water proton relaxivity. The reversible pH response leads to decreasing relaxivity values as pH moved from 6 to 11; r_1 ~ 20 $mM^{-1}s^{-1}$ to r_1 ~ 13 $mM^{-1}s^{-1}$ (G5-(Gd-**L23**)$_{111}$), r_1 ~ 29 $mM^{-1}s^{-1}$ to r_1 ~ 16 $mM^{-1}s^{-1}$ (G7-(Gd-**L23**)$_{253}$) and r_1 ~ 27 $mM^{-1}s^{-1}$ to r_1 ~ 12 $mM^{-1}s^{-1}$ (G9-(Gd-**L23**)$_{157}$).

Tóth and co-workers also studied the reversible pH dependence of water-soluble endohedral gadofullerenes as potential pH responsive contrast agents.[140] Gd@60(OH)$_x$ (x = ~ 27) and Gd@60[C(COOH)$_2$]$_{10}$ were prepared, each showing high water exchange rates and consequentially maximum relaxivity values were measured as r_1 = 38.5 mM^{-1}s^{-1} and r_1 = 10.4 mM^{-1}s^{-1} respectively (measured from NMRD 30-60 MHz, 26^{o}C, pH ~ 9.5). A dramatic increase in relaxivity was observed in more acidic conditions as the aggregation of the cluster formation or aggregation of the gadofullerene complexes occurred,[141] increasing the rotational correlation time and enhancing relaxivity to r_1 ~ 22 mM^{-1}s^{-1} and r_1 ~ 78 mM^{-1}s^{-1} for each complex respectively.

pH dependent molecular aggregation has also been employed by Hovland and co-workers who derived a series of phospholipid mimicking Gd-DO3A derivatives possessing tertiary amino containing side chains, **Gd.L24**.[142] Relaxivity of **Gd.L24** was enhanced from r_1 = 7.9 mM^{-1}s^{-1} (pH range 3-6, 10 MHz, 25^{o}C) to r_1 = 19.1 mM^{-1}s^{-1} (pH range 8-10, 10 MHz, 25^{o}C). The 142% increase in relaxivity within the ideal physiological pH range arises from formation of colloidal aggregates as a result of deprotonation of the tertiary amine groups, leading to higher lipophilicity of the generated neutral, deprotonated species (Scheme 3).

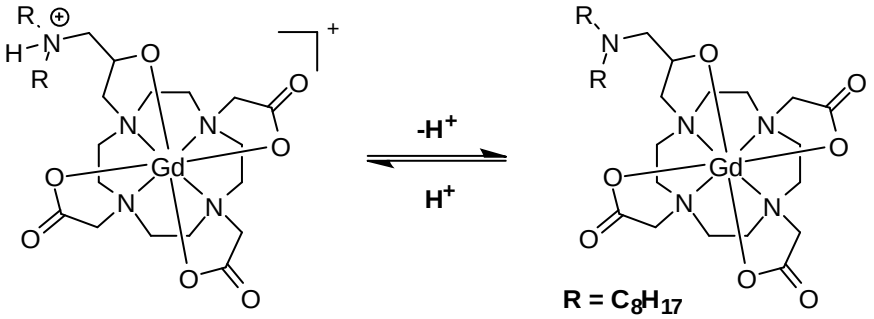

Gd.L24

Scheme 3

2.2.3 Modulation of the Water Exchange Lifetime, τ_m, with pH

In order to modulate water exchange rates as a function of pH, Sherry and co-workers have developed the phosphonate bearing Gd-DOTA based complex, **[Gd.L25]$^{5-}$**.[143] Measured relaxivities within the physiological pH range ~ 6-8 decrease from r_1 = 9.8 mM^{-1}s^{-1} to r_1 = 3.8 mM^{-1}s^{-1} (20 MHz, 25^{o}C). The increase in relaxivity in more acidic conditions is attributed to an increase in water exchange rates due to the formation of hydrogen bonded networks as a result of the progressive protonation of the pendant phosphonates. This provides a catalytic pathway for exchange of the Gd(III) bound water molecules with those of the bulk solvents. The contrast agent has been used *in vivo* in mice.[144] A dual contrast agent strategy was employed using the pH insensitive **[Gd.L26]$^{5-}$**. Comparison between the *in vivo*

and *in vitro* relaxivity measurement between the two contrast agents was used to calculate and map pH of the kidneys in mice.

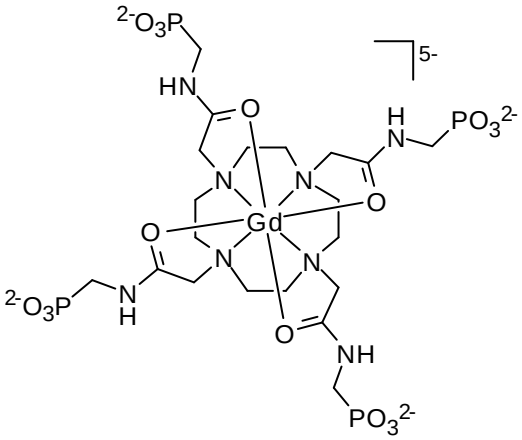

[Gd.L25]$^{5-}$

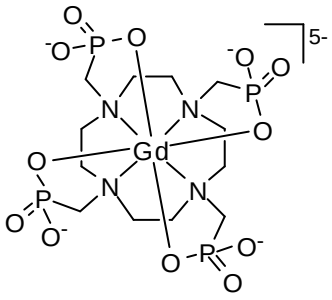

[Gd.L26]$^{5-}$

Further work by the same group has lead to the development of a series of tetra-amide DOTA complexes, **Gd.L27**.[145] In the physiological pH range ~ 6-9, there is an 84% enhancement in relaxivity (r_1 ~ 3.0 $mM^{-1}s^{-1}$ to r_1 ~ 5.5 $mM^{-1}s^{-1}$ (20 MHz, 25^{o}C) for the hydroxypyridyl bearing complex. Deprotonation of the amides in basic media results in the formation of highly organized second sphere waters as a result of intramolecular acid-base pair interactions with the phenolic protons, which in turn enhances water exchange rates.

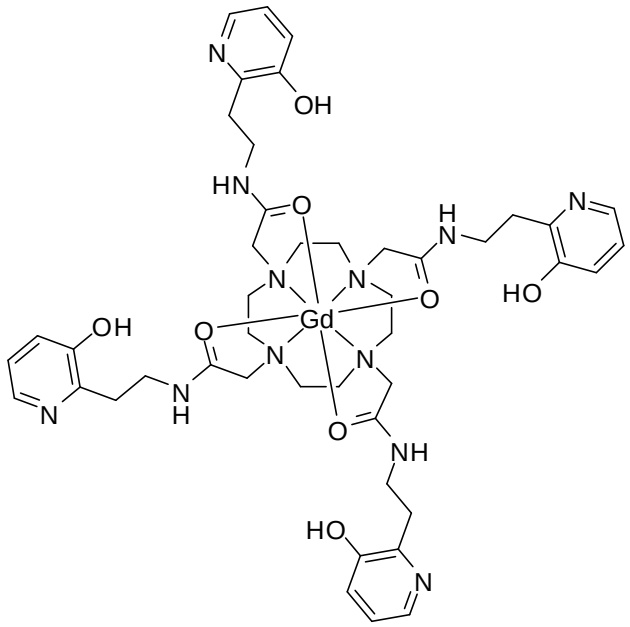

Gd.L27

A different approach to increasing water exchange was investigated by the incorporation of low molecular weight Gd(III) chelates within pH-sensitive liposomes by Lokling and co-workers.[146] Commercially available Gd-DTPA-BMA was encapsulated within saturated phosphatidyl ethanolamine/palmatic acid (DPE/PA) liposomes. The observed

relaxivity in simulated anionic background of the non-liposomal Gd-DTPA-BMA chelate was unaffected by change in pH with a mean value of r_1 = 4.6 $mM^{-1}s^{-1}$ (10 MHz, 25°C). However, the liposomal Gd-DTPA-BMA showed much lower relaxivity values of r_1 ~ 0.6 $mM^{-1}s^{-1}$ at pH > 7.3. Relaxivity rose to r_1 ~ 3.9 $mM^{-1}s^{-1}$ as pH was lowered from 7 to 6. The membrane composition of the liposome is destabilised in more acidic conditions allowing leakage of the liposomal Gd(III) chelate and therefore, increasing relaxivity as the contrast agent moves from a low to a high water exchange rate environment. More recent *in vivo* studies have shown increased liposomal aggregation and membrane destabilisation at physiological pH, 7.4. After only a few minutes large amounts of Gd(III) chelate leakage was observed, attributed to the presence of large quantities of serum cations, particularly Ca^{2+} and Mg^{2+}, as well as human serum albumin, HSA.[147] Prolonged blood circulation time was achieved by addition of polyethylene glycol (PEG) to the liposomal systems, however a reduction of pH sensitivity was also observed. A compromise between liposomal stability and loss a pH sensitivity was overcome by the incorporation of low molecular weight Gd(III) chelates with a high affinity for HSA. Upon leakage, binding to HSA would occur within the tumour leading to higher relaxivities due to the increased rotational correlation times as the Gd(III) chelate binds to the slowly tumbling protein.[148, 149]

2.3 pH Responsive Luminescent Sensors

2.3.1 Displacement of Water Molecules as a Function of pH

Luminescent lanthanides complexes, such as Eu(III) and Tb(III), are used in biological systems as optical probes. Their long-lived emissive properties in the visible light region, at wavelengths far away from shorter-lived organic fluorescence makes them ideal for use in imaging applications such as time resolved immunoassays, discussed in Chapter 1. An increase in the hydration state, *q*, of emissive Ln(III) complexes will cause a decrease in the emission intensity and the lifetime, due to the Ln(III) excited state being quenched by the increase in vibrational energy transfer processes from the bound H_2O molecules.[111]

Modulation of the hydration state is achieved by inter- and intramolecular anion binding. The Eu(III) analogue of the previously mentioned carbonate binding **Eu.L20** complex was studied for its pH responsive luminescent properties.[133] The observed trend was similar, yet opposite to the corresponding relaxivity data of the Gd(III) analogue in the presence of a full, extracellular anionic background (Section 2.2.1). Over the physiological pH range (6-8) a sharp nine-fold increase in the intensity of the ΔJ = 2 (618 nm) band was observed as quenching water molecules were displaced by the binding carbonate anion.

Faulkner and co-workers adopted a pH responsive self-assembly approach toward water displacement of Eu-DO3A derivatives bearing a benzoic acid pendant group, **Eu.L28**.[150] In basic conditions the carboxylate group is deprotonated and acts as a ligand, displacing waters from another Eu(III) complex and forming the less hydrated and more emissive dimetallic complex (Scheme 4).

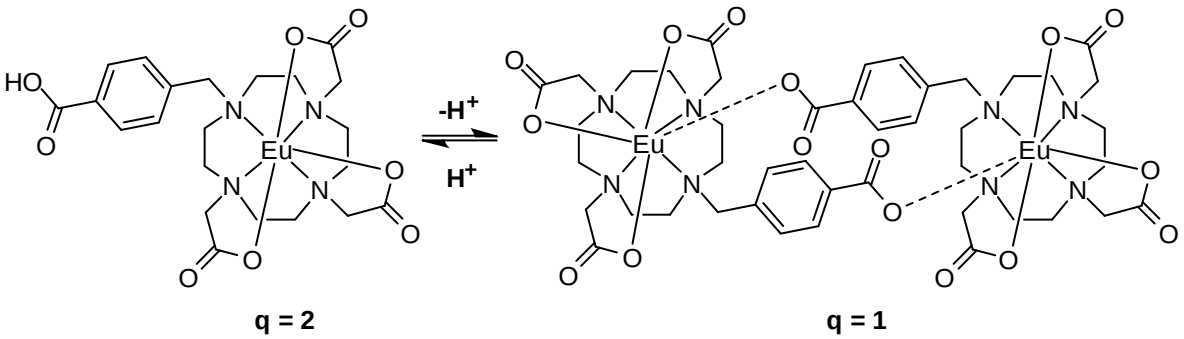

Eu.L28

Scheme 4

The emission intensities of the $\Delta J = 1$ band (595 nm) increased dramatically with pH corresponding to the change in the Eu(III) coordination environment, while the $\Delta J = 2$ band remained the same throughout, leading to the potential for the development of ratiometric probes used for concentration independent determination of pH.

2.3.2 Variation in Sensitisation as a Function of pH

Direct excitation of lanthanides is difficult to achieve due to their low extinction coefficients. For this reason, organic chromophores are often incorporated into Ln(III) complexes. Provided the excited state energy of the chromophore 'antenna' is above that of the lanthanide ion, energy transfer can occur from the chromophore to the luminescent lanthanide ion, enhancing its emission (Chapter 1, Section 1.5.5). The variation of the efficiency of energy transfer as a function of pH has been the focus of much development.

Parker and co-workers developed the *p*-CH_3, *p*-OCH_3 and *p*-OCF_3 derivatives of the Eu(III) and Tb(III) charge-neutral complexes bearing an arylsulfonamide moiety, **Ln.L29**, in order to asses their pH responsive luminescent behaviour.[151] Sensitised emission of the lanthanide ions was achieved upon excitation of the sulfonamide chromophore at λ_{ex} = 270 nm. Intensity of the $\Delta J = 2$, (612 nm) band and the $\Delta J = 1$ (541 nm) band of the Eu(III) and Tb(III) emission spectra respectively were enhanced in basic media as the sulfonamide nitrogen was deprotonated and binding to the metal centre occurred. Ligation of the sulfonamide moiety to the lanthanide ion not only displaced the two quenching waters but also enhanced the efficiency of transfer energy transfer process as the antenna was brought

closer to the Ln(III) centre (Scheme 5). This was further proved by quantum yield measurements; 0.39% (pH 10) and 0.11% (pH 4) for the Eu(III) *p*-CF_3 analogue and 3.5% (pH 10) and 0.17% (pH 4) for Tb(III) *p*-OCH_3. The measured pK_as of each of the Ln(III) *p*-OMe derivatives lie within the physiological pH range at pK_a = 6.7 for both the Eu(III) and Tb(III) analogues.

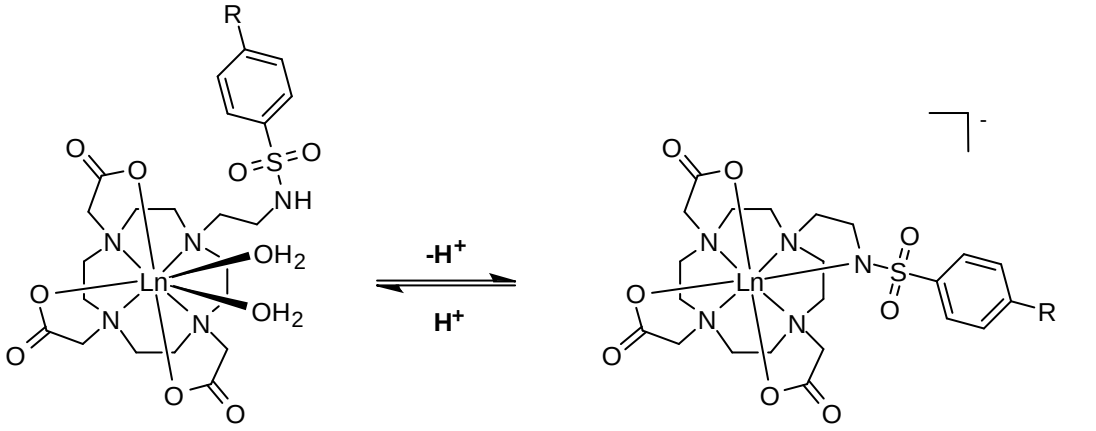

Scheme 5

Further research into the luminescent behaviour of similar Ln-DO3A derivatives has lead to the development of the Eu(III), Tb(III) and Y(III) analogues of the dansyl-bearing complex, **[Ln.L30]$^{3-}$**.[152] Sensitised emission of the Eu(III) and Tb(III) analogues was not observed until acidic pHs were reached as the protonation of the dimethylamino group on the naphthalene occurred.

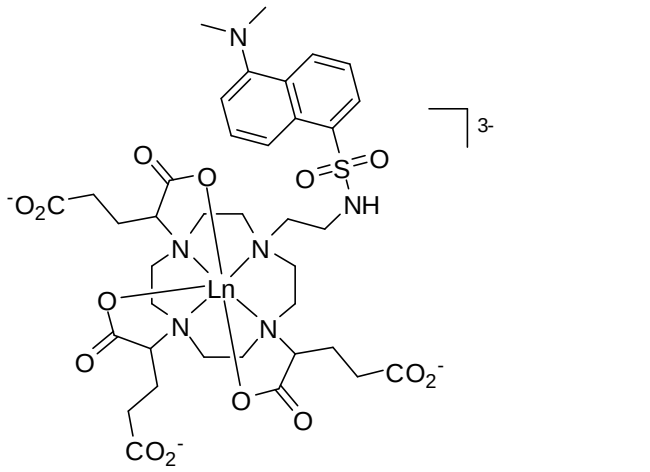

[Ln.30]$^{3-}$

The lack of population of the triplet state of the deprotonated chromophore accounts for the lack of sensitisation. Even in basic media, despite the ligation of the now deprotonated sulfonamide nitrogen no sensitisation is observed. Large shifts in absorbance wavelengths of

the free ligand chromophore were observed upon protonation of the dimethylamino group (λ_{max} = 288 nm, ε = 5,840 $M^{-1}s^{-1}$) and deprotonation of the sulfonamide nitrogen (λ_{max} = 318 nm, ε = 4,010 $M^{-1}s^{-1}$). Excitation of the Eu(III) complex at λ_{ex} = 290 nm, followed by a delay showed the increase in emission intensity in acidic media as a result of the variation in absorption of the chromophore and the hydration state of the complex as a function of pH. Such complexes and derivatives have been immobilized onto thin-film sol gel matrixes for use as pH sensors in biological systems. The sensors formed appeared to be quite robust and the observed pH response well defined.[153]

The effect of variation of the Eu(III) coordination environment was demonstrated by the preparation of the Eu(III) analogue of the *tetra*-amide DOTA complex **Eu.L31** by Sherry and co-workers.[154] An increase in emission intensity of the ΔJ = 2 band (613 nm) was observed in basic media, while the ΔJ = 1 (593 nm) band remained relatively the same throughout following sensitised excitation *via* the aryl chromophores (λ_{ex} = 363 nm). The ratio of intensities of the ΔJ = 2 / ΔJ = 1 bands therefore allow for concentration independent determination of pH to be achieved. The increase in emission intensity is ascribed to the change in coordination environment around the Eu(III) centre upon deprotonation of the amide NH protons increasing the electron donation to the metal centre. However, the hydroxypyridine species showed low emission intensity throughout, limiting its potential use as a pH probe, while removal of the hydroxyl group yields higher emission intensities.

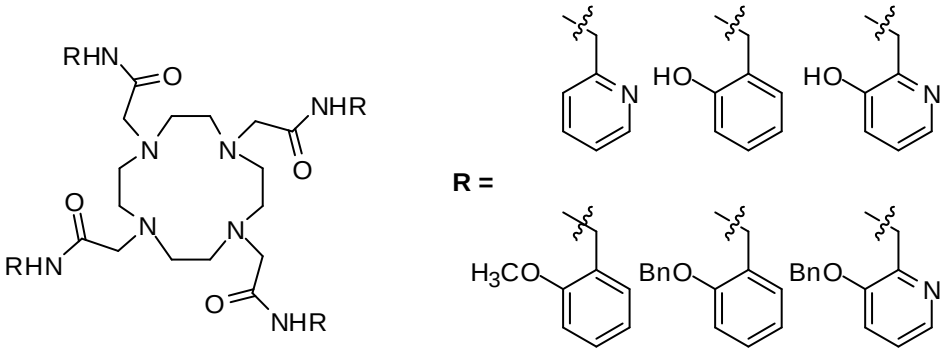

L31

An "off-on-off" luminescent sensor was developed by Gunnlaugsson and co-workers in which the Eu(III) emission of the phenanthroline bearing complex **Eu.L32** is highly emissive at between pH 8.5 and pH 5.5, but decreases in both the acidic and basic direction.[155] The hydration state of the complex remained q = 1 throughout the titration, therefore proving the variation in emission intensity to due to modulation of the sensitisation of the antenna. A decrease in emission intensity in basic media is attributed to the deprotonation of the aryl amide proton which decreases the reduction potential of the antenna, while in acidic media the protonation one of the *phen* nitrogen moieties results in an increase in its oxidation potential.

Each process has an adverse effect on the ability to populate the Eu(III) excited state, and therefore causes a decrease in emission intensity resulting in the bell-shaped pH dependence.

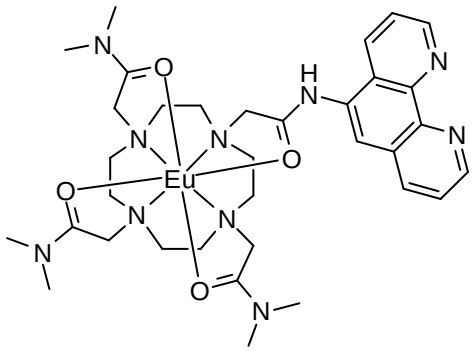

Eu.L32

2.4 Diphenylphosphinamide (dpp) Complexes

Diphenylphosphinamides have been used as amino protecting groups in peptide synthesis.[156] In this work amino functionality has been incorporated into cyclen based lanthanide complexes by means of aziridine ring opening reactions. The original aim was to prepare dpp DO3A chelates. Removal of the dpp moiety with TFA would then reveal a primary amine functionality (or secondary if derivatised further at the phosphinamide nitrogen with a second DO3A-based moiety). This was to be used to develop multi-Gd(III) containing contrast agents (Scheme 6). The incorporation of several Gd(III) ions, as well as the increased molecular mass would be expected to greatly increase the observed relaxivity by increasing the number of paramagnetic ions as well as reducing the overall rotational correlation time, τ_R, of the macromolecule in a similar manner to the examples discussed in Chapter 1, Section 1.4.2. Mono- and bis-methyl dpp groups were to be incorporated to explore the effect of rigidifying the dpp-ethyl linker in reducing the independent rotations of each individual Gd(III) ion.

Dpp protecting groups were to be removed by addition of TFA as shown in Scheme 7. Prior to this, it was hypothesised, however, that the pendant dpp moieties may show pH responsive character similar to the sulphonamide-bearing Ln(III) complexes developed by Parker and co-workers, (Sections 2.2 and 2.3) where the pendant group reversibly binds to the Ln(III) centre as a function of pH *via* the nitrogen atom generating a stable five membered chelate. Here it was proposed that reversible binding through the dpp nitrogen or oxygen may occur to form a five or seven membered chelate, displacing coordinated water molecules and varying the hydration number, *q*, as a function of pH. The development of mono- and bis-methyl Ln-dpp-DO3A complexes (**Ln.4a** and **Ln.4b)** was therefore achieved by base hydrolysis of the methyl ester groups of the dpp bearing DO3A compound followed by the

addition of $Ln(III)Cl_3$. The pH responsive nature of the resulting complexes has been investigated and is reported herein.

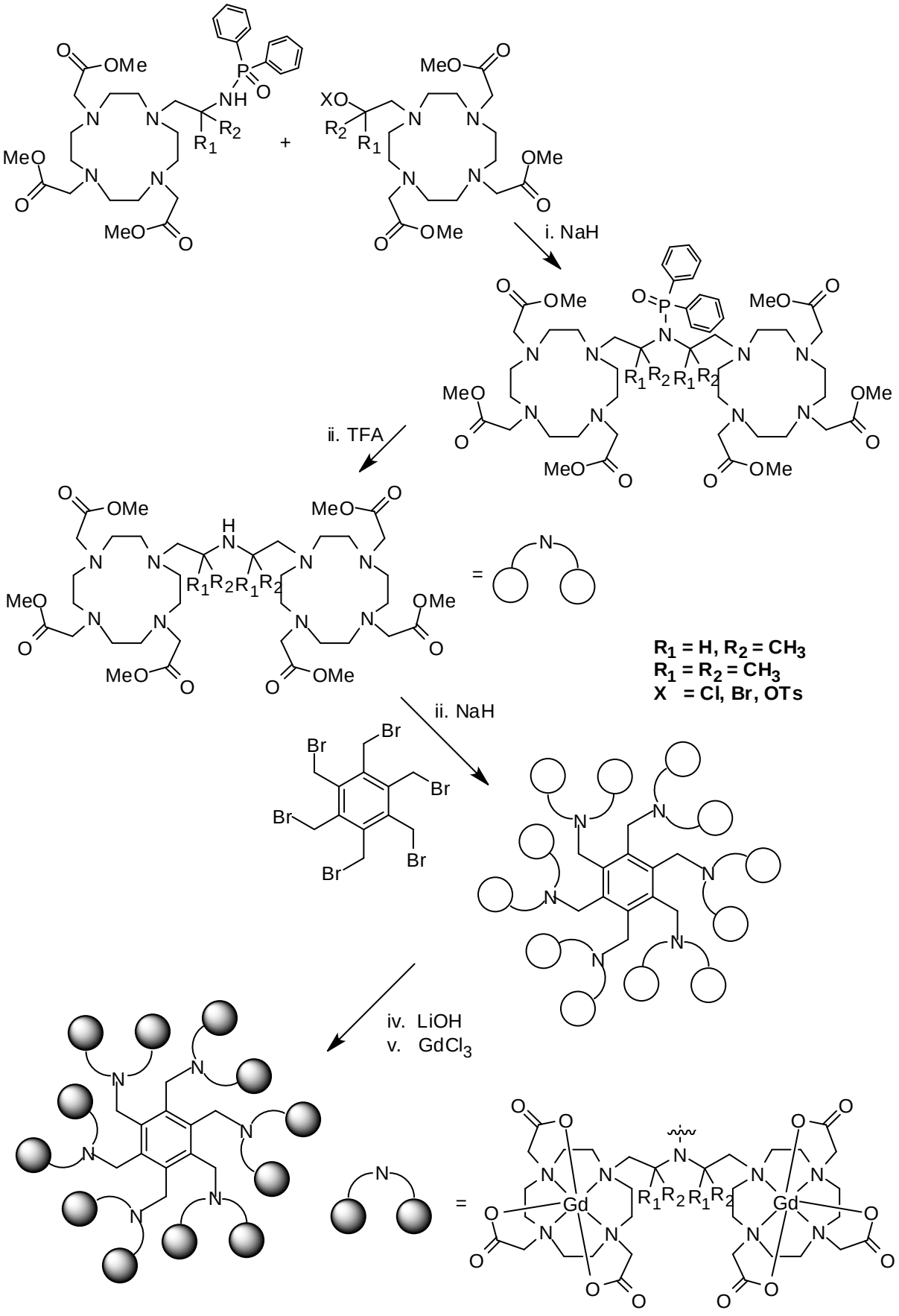

Scheme 6

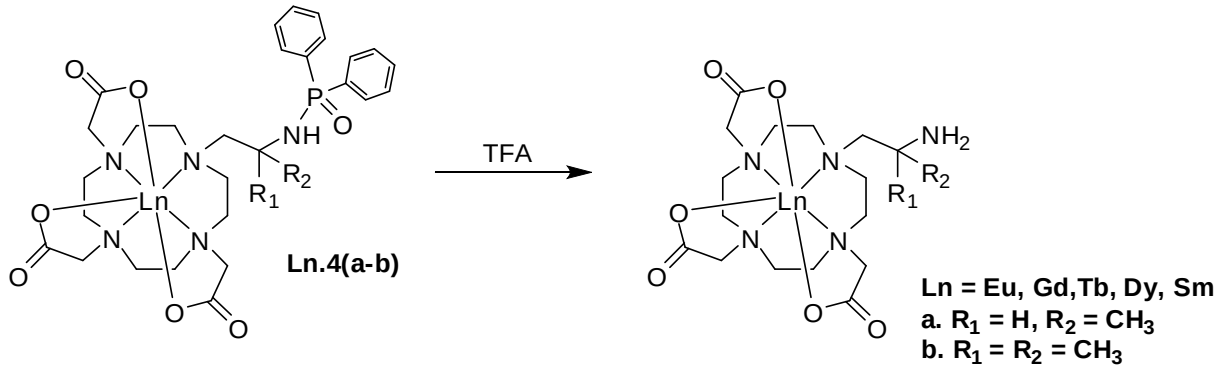

Scheme 7

2.4.1 Aziridine Synthesis

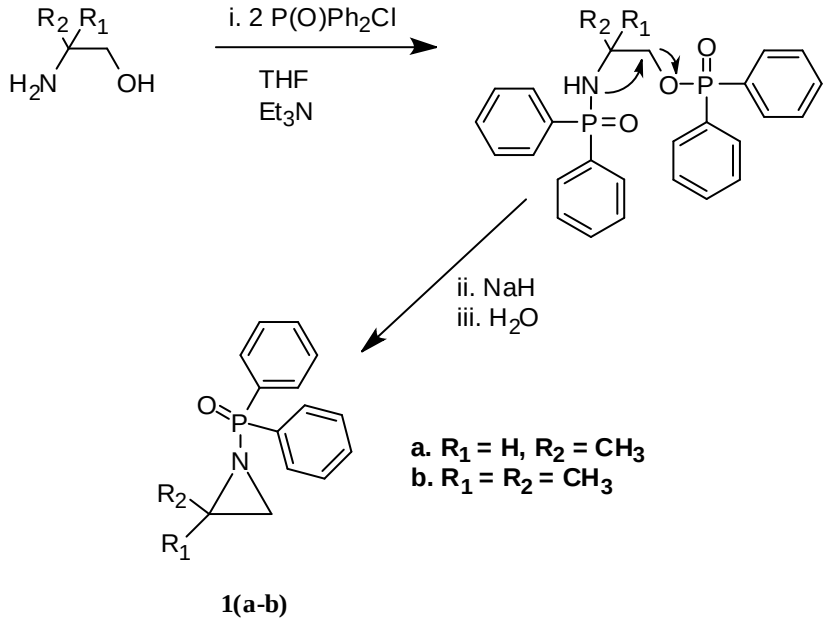

Scheme 8

Racemic 1-(diphenyl-phosphinoyl)-2-methyl-aziridine, **1a**, and 1-(diphenyl-phosphinoyl)-2-2-dimethyl-aziridine, **1b**, were prepared in good yields following literature methods following the addition of two equivalents of diphenylphosphinyl chloride and three equivalents of triethylamine were added to the appropriate amino alcohol in dry THF (Scheme 8).[157, 158] The yield of **1a** (87%) was considerably higher than that of **1b** (21%) as the addition of a second group increases the steric hindrance about the aziridine ring causing ring closure to be much more difficult.

Attempts were also made to produce 1-(diphenylphosphinoyl)aziridine, **1c**, following the same method as above. However, due to the insolubility of the intermediates the reaction did not go to completion following the addition of sodium hydride. A further reaction was carried out isolating the intermediate **1d** as an extremely hygroscopic white powder. **1d** was isolated in a 25% yield and was used in further reactions, explained in Section 2.4.2.

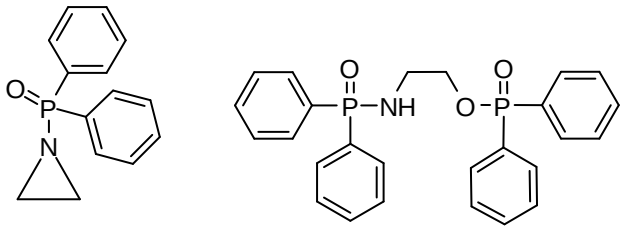

1c **1d**

2.4.2 Dpp Complex Preparation

Aziridines **1a** and **1b** were ring-opened with the macrocycle 1,4,7-tris(methoxycarbonylmethyl)-1,4,7,10-tetraazacyclododecane, **2**, which was prepared by addition of methyl 2-bromoacetate to cyclen in the presence of K_2CO_3 in chloroform[159] (Scheme 9).

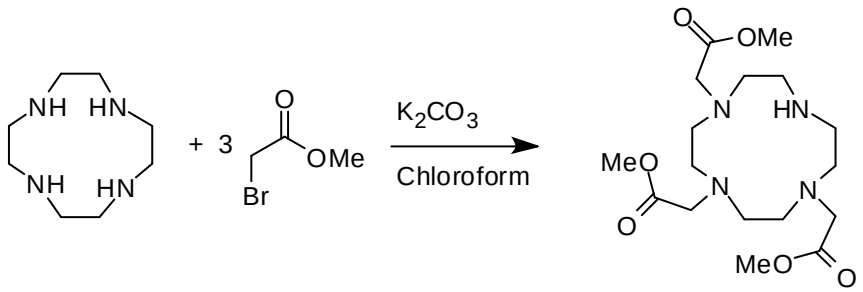

2

Scheme 9

The ring opening reaction of the mono-methyl substituted aziridine **1a** was carried out at 60°C in acetonitrile. The reaction of the bis-methyl substituted aziridine **1b** proved to be much more difficult due to the increased steric hindrance of the added methyl group. Reaction would only take place when carried out in DMF at 130°C (Scheme 10). Products **3a** and **3b** were both purified by silica column chromatography using graduated elution with MeOH/DCM solutions. An attempt to react **2** with **1d** was carried out with no success as the aziridine ring opening reaction is aided by the ring strain present in the aziridine ring. The secondary amine group on the macrocycle did not prove to be sufficiently nucleophilic to react with the non-ring closed intermediate **1d**.

The methyl esters were hydrolysed using 1M LiOH and subsequent addition of the lanthanide chloride was carried out in water at pH 6 according to literature preparations.[134] Care had to be taken when adjusting the reaction mixture to pH 6, as the pendant dpp groups were readily removed at pH < 4. In order to avoid this, separate solutions of $LnCl_3.6H_2O$ and pro-ligands were adjusted to pH 7 independently and added to each other. As the solutions were added together the pH drops to around 6 as protons on the macrocyclic ring would exchange with the Ln(III) causing a higher H^+ concentration in solution. Complex formation

was verified by both ESMS and ^{1}H NMR spectroscopy of the Eu(III) analogues. Axial ring nitrogen resonances observed at δ = 25.7 ppm, 33.0 ppm, 34.7 ppm and 34.9 ppm (**Eu.4a**) and δ = 24.8 ppm 26.2 ppm, 33.6 ppm and 35.6 ppm (**Eu.4b**) (400 MHz; D_2O, pD 10, 4^{o}C), are typical of the square antiprismatic geometry (SAP) about the Eu(III) centre.[69]

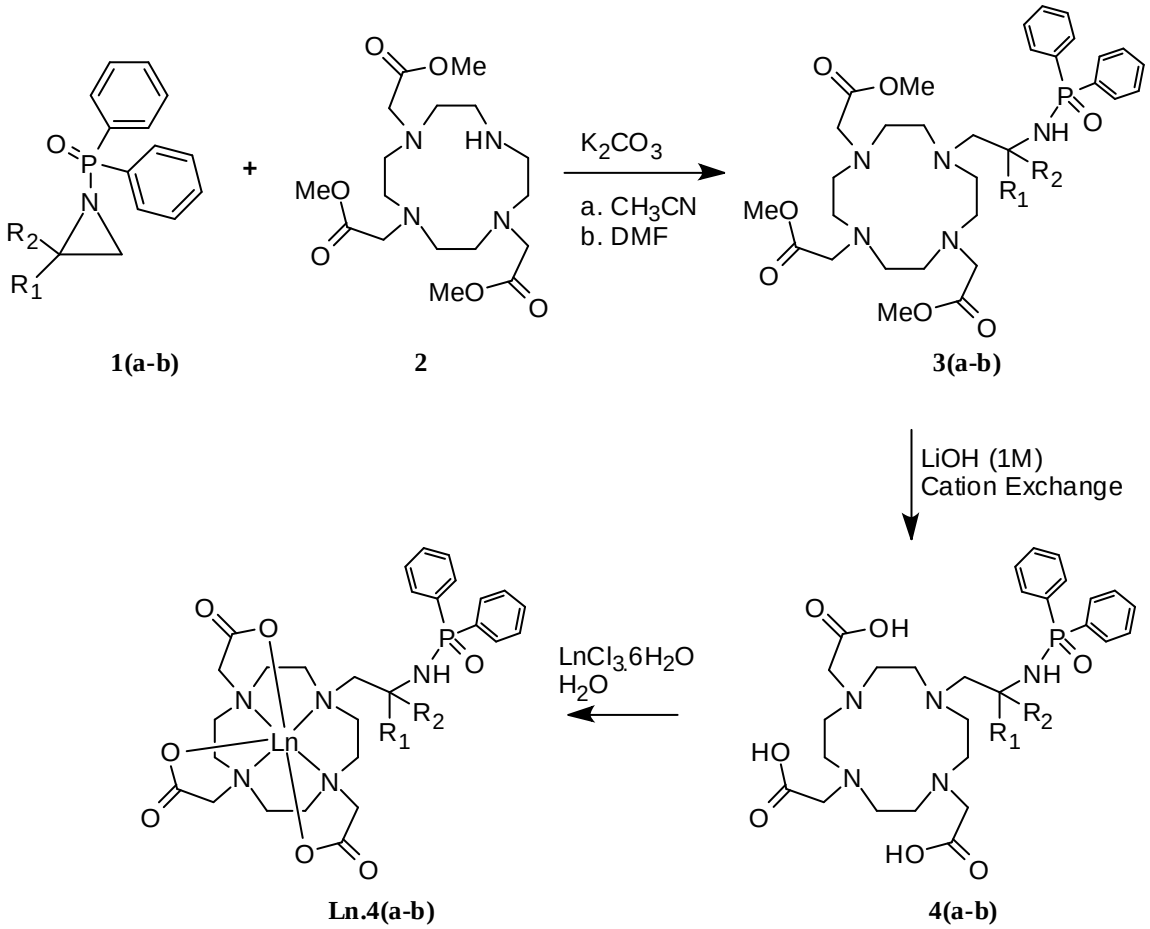

Scheme 10

Any unreacted lanthanide salts were removed by raising the pH of the aqueous complex solutions to 10 to produce insoluble $Ln(OH)_3$ which was filtered through a celite plug. The solutions were then tested for the presence of uncomplexed lanthanide ions using urotropine buffered solutions of xylenol orange at pH 5. If the solutions remained orange no free lanthanide ions were left in the solution.[160] In order to determine the concentration of free lanthanide ions in solution xylenol orange calibrations were carried out (Chapter 6, Section 6.1.14). Attempts to purify the complexes further using DOWEX MAC-3® weak acid cation exchange resin did not work. As the protons on the resin exchanged with the unreacted lanthanide ions in solution the solution pH dropped to pH ~ 3, which proved to be too acidic for the pendant dpp group which were easily lost during the process. Repeated filtration of

solutions through celite were carried out until unreacted Ln(III) ions were not observed following addition to solutions of xylenol orange.

2.5 Luminescent Investigation of the Eu(III) Dpp Complexes

2.5.1 Sensitised Eu(III) Emission via Excitation of the Dpp Chromophore

The Eu(III) analogues of the racemic mono-methyl **Ln.4a** and bis-methyl **Ln.4b** were prepared and their luminescent properties were investigated**.** The Eu(III) energy of the ^5D_o excited state is E = 17,277 cm^{-1}.[111] Provided the triplet state energy of the dpp moiety is greater than that of the Eu(III), energy transfer can occur, which should increase the intensity of the Eu(III) emission (Chapter 1, Section 1.5.5). The triplet excited states of phenyl groups usually lie between E ~ 20,000-30,000 cm^{-1} and therefore it was hypothesised that sensitised emission would occur.[161] An increase in emission intensity was indeed observed as the complexes were excited *via* the chromophore at λ_{ex} ~ 270 nm compared with direct excitation of Eu(III) at λ_{ex} ~ 395 nm; a wavelength at which the dpp moiety does not absorb (Figure 21).

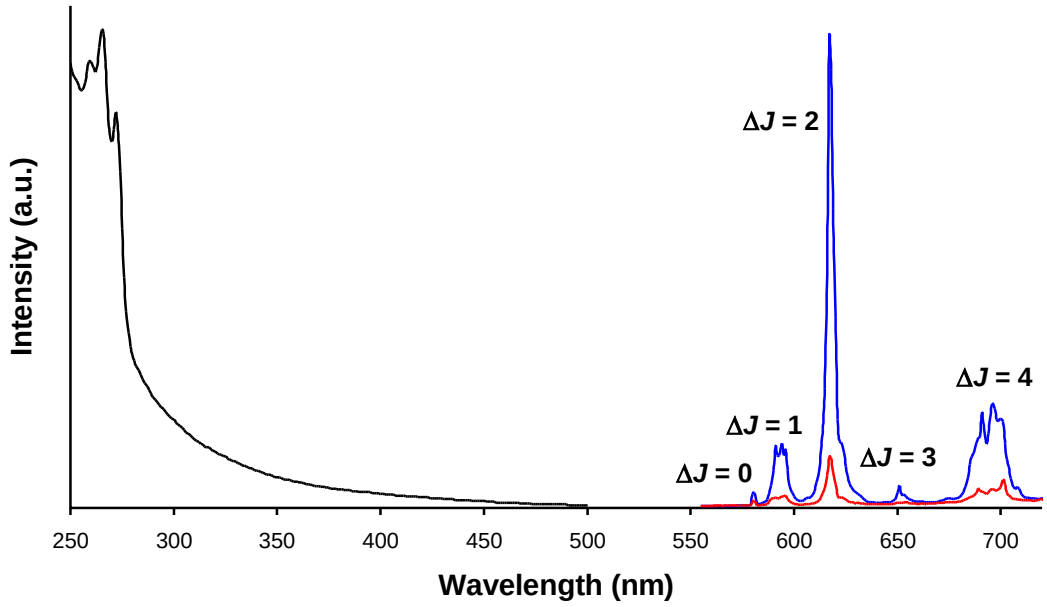

Figure 21. Eu(III) emission spectra for **Eu.4a** following direct excitation (red, λ_{ex} = 395 nm) and sensitised excitation (blue, λ_{ex} = 271 nm). 1.0 mM **Eu.4a**, 0.1 M NaCl, pH 10.34, 25°C. The dpp absorbsion spectrum (black) shows no absorbance at 395 nm.

*2.5.2 Eu(III) Emission Intensity vs. pH for **Eu.4(a-b)***

Eu(III) emission was more intense with increasing pH. This could arise from the deprotonation of coordinated water molecules in more basic media, resulting in the ligation of a single hydroxide ion to the Eu(III) centre, which would increase the electron density of the metal centre and therefore disfavour binding of a second water molecule (Scheme 11A). This is unlikely, however, as at pH 10 only a slight increase in Eu(III) emission intensity compared

to pH 5 was observed for the none pH responsive, q = 2 dpp bearing complex **[Eu.9]**$^{3-}$, which was attributed to the presence of exchanging hydroxide ions (discussed in greater detail in Chapter 3, Section 3.4.7, Figure 50).

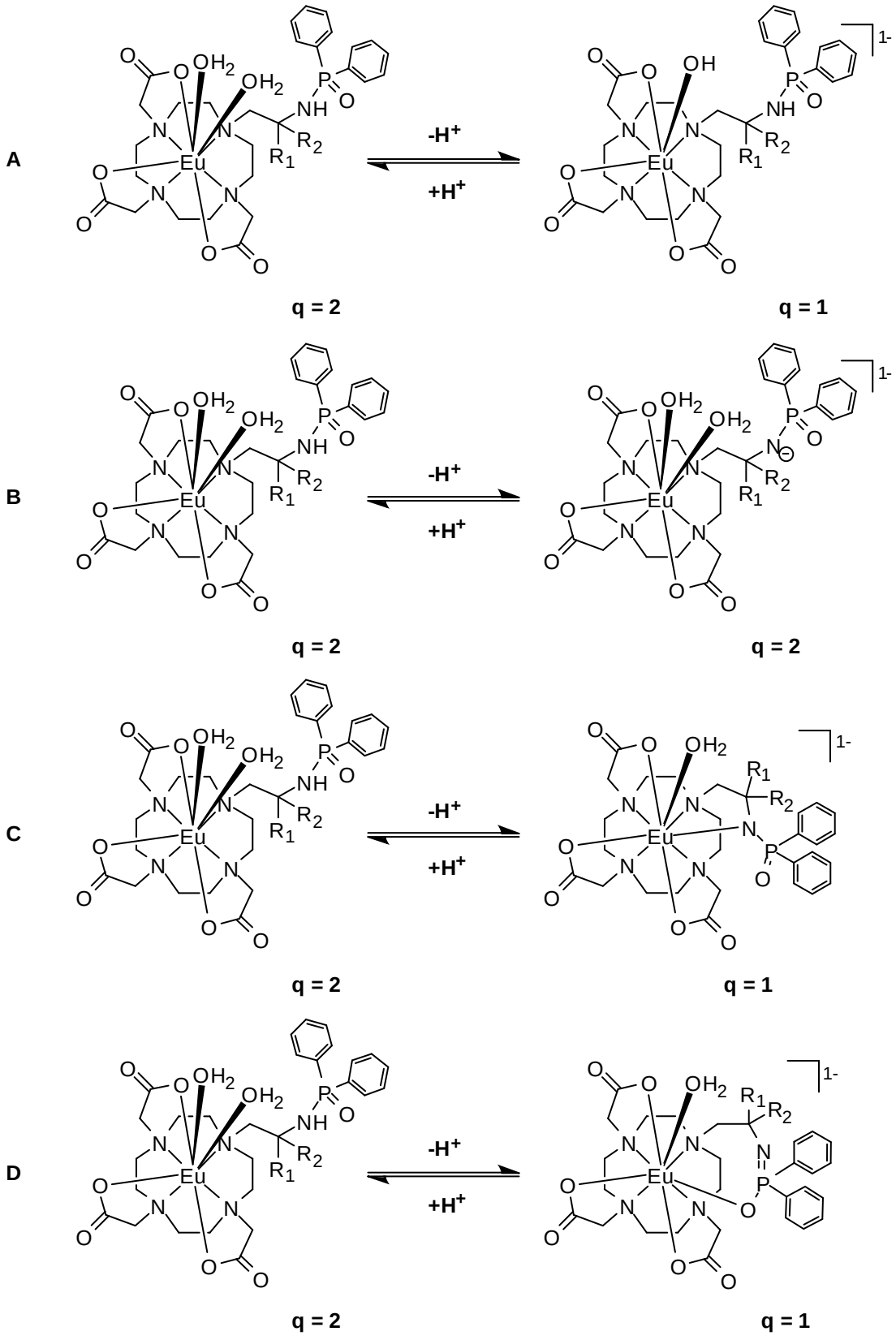

Scheme 11

Secondly, the pH response may arise from the deprotonation of the dpp moiety causing a variation in the singlet and triplet excited state energies, effecting the energy transfer to the Eu(III) (Scheme 11B). Once again, this was seen to be unlikely as the measured hydration states of the dpp complexes in basic media showed a reduction the observed hydration state from q = 2 (pH 5) to q = 1 (pH 10) suggesting displacement of one of the inner sphere water molecules (discussed in Section 2.5.3). Furthermore, following direct excitation of Eu(III) at λ = 395 nm the same pH responsive behaviour is observed, i.e. independent of energy transfer from the dpp chromophore (Chapter 3, Section 3.4.7, Figure 50). Finally, the pH response could be due to the deprotonation of the pendant dpp group causing ligation to the Eu(III) centre, most likely *via* the dpp oxygen, however possibly through the dpp nitrogen (Scheme 11C-D). This results in both an increase in the efficiency of energy transfer to the Eu(III) centre as the dpp group moves closer, and, due to a decrease in the hydration number q, a reduction in the number of vibrational quenching O–H oscillators. This is the most likely explanation for the observed pH response, not only because of the reasons given above but also due to the ^{1}H NMR data, which was recorded at pD 10. In such basic conditions the dpp complexes were in the more rigid dpp coordinated form, which slows the fluxional processes, e.g. arm rotation, thus the ^{1}H NMR spectra show well resolved resonances for the cyclen ring hydrogens. The equivalent ^{1}H NMR spectra recorded at pD 5 were broad and featureless, typical of less rigid q = 2 Eu(III) complexes (seven coordinate with respect to ligand).

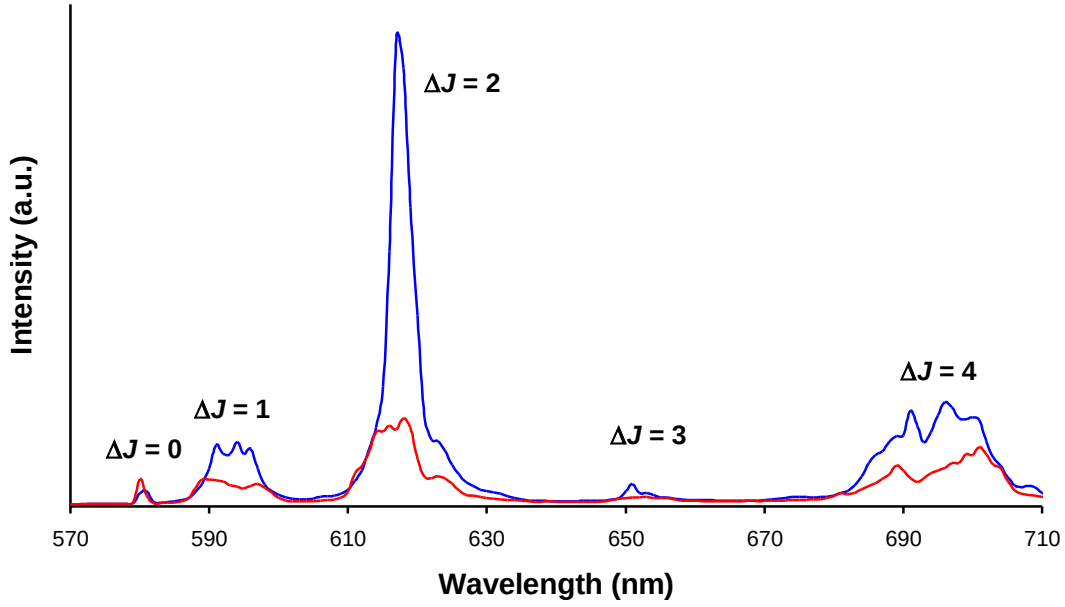

Figure 22. Eu(III) emission spectra for **Eu.4a** at pH 10.34 (blue) and pH 5.08 (red). 1.0 mM **Eu.4a**, 0.1 M NaCl, λ_{ex} = 271 nm, 25°C.

Figure 22 shows the emission spectra for **Eu.4a** in both acidic and basic media. (**Eu.4b** showed similar behaviour). The excitation spectra were also recorded, which are plots

of the intensity of the $\Delta J = 2$ emission band as the excitation wavelength is varied. They are similar to UV- absorption spectra (Figure 23) in that they show the wavelength of light that is absorbed by the chromophore. The excitation maxima show the wavelength at which optimum energy transfer, i.e. sensitisation occurs. The decrease in sensitisation in acidic media is a result of the dpp pendant group becoming protonated and no longer binding to the Eu(III). Energy transfer has a $1/r^6$ distance dependence and therefore a decrease in the efficiency of energy transfer to the Eu(III) centre occurs as the dpp moiety moves further from the Eu(III).[120]

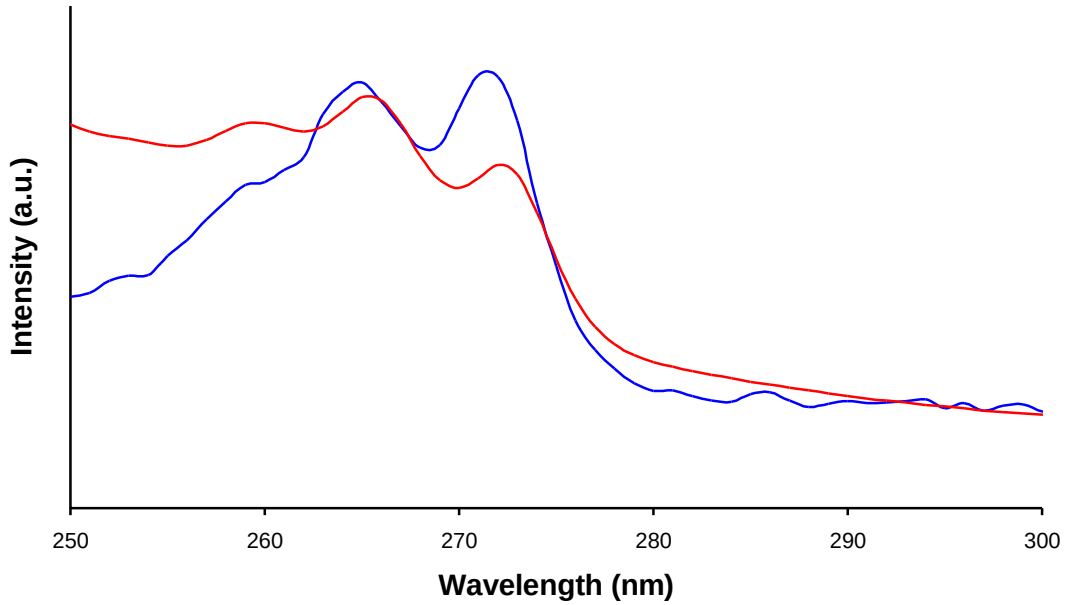

Figure 23. **Eu.4a** excitation spectrum (blue) and UV absorption spectrum (red). 1.0 mM **Eu.4a**, 0.1 M NaCl, pH 10.34, 25°C.

The increase in Eu(III) emission intensity can be clearly seen in Figures 24 and 25. Although there is an overall increase in the intensity of the spectra as the pH moves towards more basic media, the most interesting change is the increase of the hypersensitive $\Delta J = 2$ band at around 617 nm, which is greatly affected by coordination geometry about the Eu(III) centre. By plotting the relative change of intensity of the $\Delta J = 2$ band (I/I_o) a clear sigmoidal change in emission intensity is observed, typical of a deprotonation trace, from which pK_a can be determined. The apparent pK_as for each complex were calculated as 8.65 (± 0.09) and 8.59 (± 0.14) for **Eu.4a** and **Eu.4b** respectively using the $\Delta J = 2$ I/I_o plots (Figures 24 and 25). A more interesting observation, however, is the plot showing variation of ratio of intensities of the $\Delta J = 2$ and $\Delta J = 1$ bands (Figure 26). The $\Delta J = 1$ band is not effected as much by the binding of dpp, therefore, ratiometric comparisons between the $\Delta J = 2$ and $\Delta J = 1$ bands allow for concentration independent determination of pH within the range ~ 7-9, with pK_as determined as 8.15 (± 0.19) and 8.36 (± 0.17) for **Eu.4a** and **Eu.4b** respectively (Figure 26).

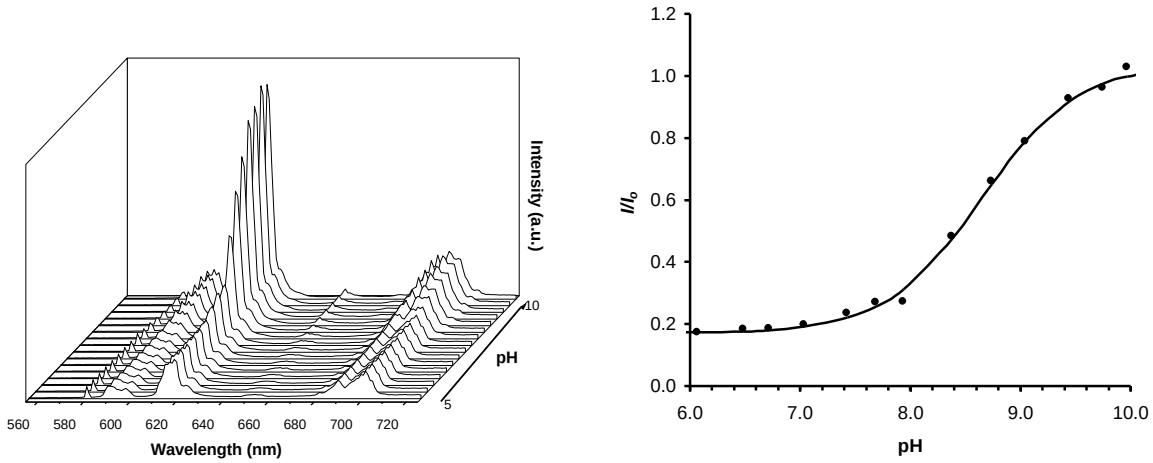

Figure 24. Left; Eu(III) emission spectra *vs*. pH for **Eu.4a**. Right; Eu(III) emission intensity I/I_o ($\Delta J = 2$) *vs*. pH for **Eu.4a** showing the experimental data (dots) and the calculated data (line). 0.1 mM **Eu.4a**, 0.1 M NaCl, λ_{ex} = 269 nm, 25^{o}C.

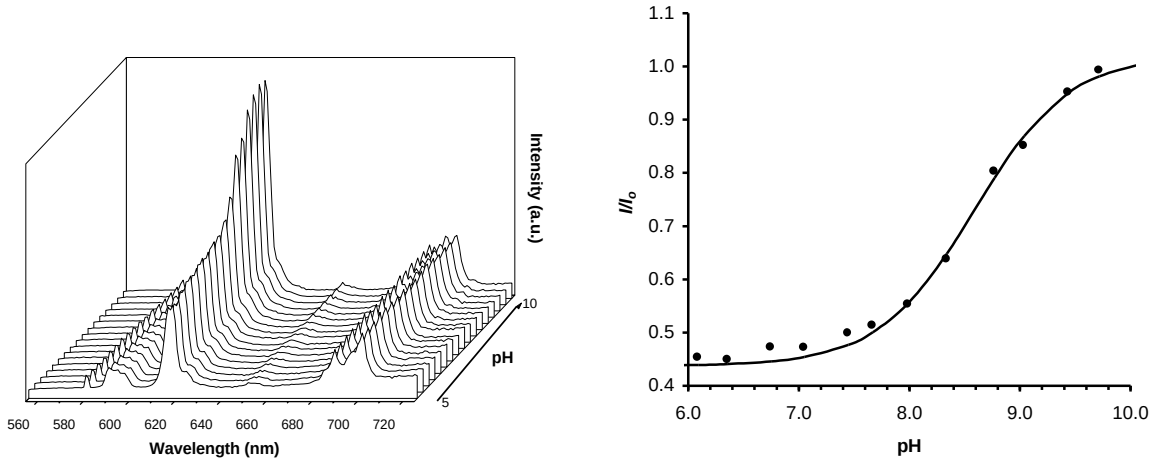

Figure 25. Left; Eu(III) emission spectra *vs*. pH for **Eu.4b**. Right; Eu(III) emission intensity I/I_o ($\Delta J = 2$) *vs*. pH for **Eu.4b** showing the experimental data (dots) and the calculated data (line). 0.1 mM **Eu.4b**, 0.1 M NaCl, λ_{ex} = 269 nm, 25^{o}C.

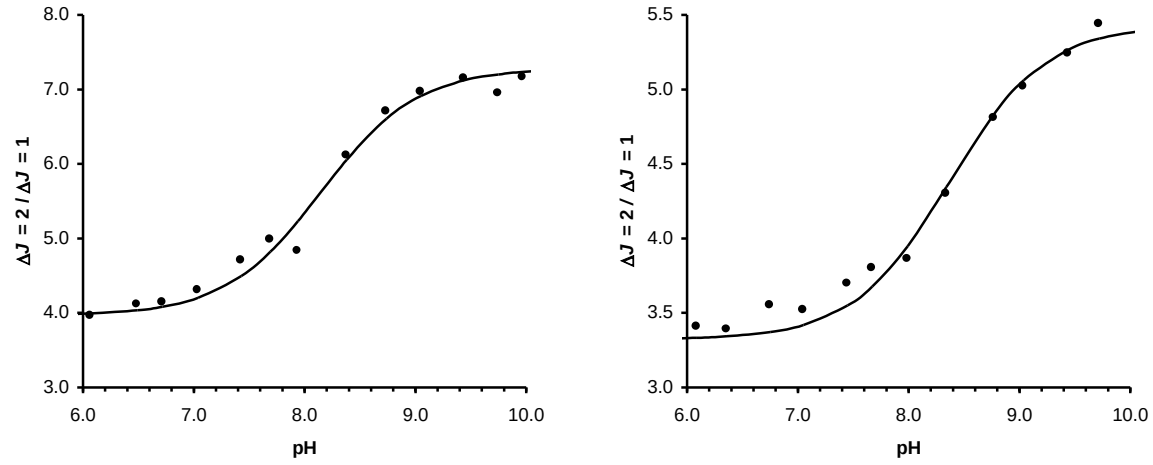

Figure 26. Eu(III) emission intensity $\Delta J = 2/\Delta J = 1$ *vs*. pH for **Eu.4a** (left) and **Eu.4b** (right) showing the experimental data (dots) and the calculated data (line). 0.1 mM **Eu.4(a-b)**, 0.1 M NaCl, λ_{ex} ~ 270 nm, 25^{o}C.

*2.5.3 Determination of Hydration State, q, for **Eu.4(a-b)***

As mentioned in Chapter 1, Eu(III) emission intensity is decreased by both the loss of sensitisation and by an increase in hydration number *q*. Water molecules quench the ^5D_o excited state and lower the emission intensity. In order to determine the hydration state of the Eu(III) complex, luminescent lifetime measurements were carried out. First order rates of decay for the Eu(III) excited state can be calculated by monitoring the emission intensity *vs.* time in both H_2O and D_2O. The experimentally determined rate constants, *k*, in both H_2O and D_2O are applied to Equation 33 (Chapter 1) to calculate the hydration state, *q*.[115, 116] The calculated rate constants and hydration state values for both **Eu.4a** and **Eu.4b** are shown in Table 10.

	$k_{(H_2O)}$ (ms^{-1})	$\tau_{(H_2O)}$ (ms)	$k_{(D_2O)}$ (ms^{-1})	$\tau_{(D_2O)}$ (ms)	*q*
Eu.4a pH 5.45	2.34	0.43	0.65	1.53	1.7
Eu.4a pH 10.45	1.46	0.67	0.65	1.53	0.7
Eu.4b pH 5.45	2.84	0.35	1.19	0.84	1.7
Eu.4b pH 10.45	1.56	0.64	0.82	1.21	0.6

Table 10. First order rate constants, *k*, Eu(III) excited state lifetime, τ, and measured hydration state values, *q*, for **Eu.4a** and **Eu.4b**. For full data analysis see Appendix **A1** and **A2**.

The calculated *q* values in acidic media are *q* = 1.7 for both **Eu.4a** and **Eu.4b**. The value is typical of a complex containing two inner-sphere waters, i.e. they are essentially *q* = 2. Water molecules are in constant exchange with the Eu(III) centre leading to a "long water" effect (Figure 27).

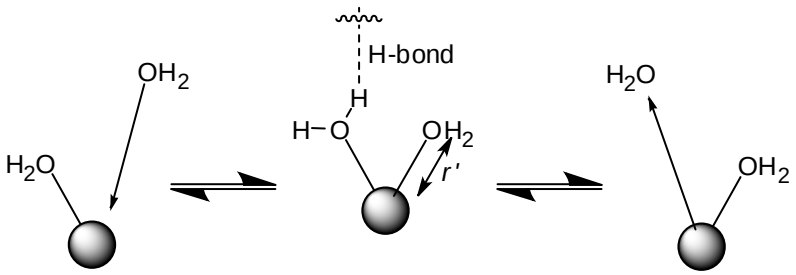

Figure 27. Water exchange dynamics about the Eu(III) centre demonstrating the long water effect. Hindrance between exchanging waters and H-bond interactions with the dpp moiety may cause measured hydration state values, *q*, to appear lower than expected.

The apparent value of *q* is a function of the Ln(III)-OH_2 distance, *r'*, an increase in which results in the reduction of the measured hydration state. Lengthening of *r'* is caused by both steric hindrance between exchanging water molecules, and by possible H-bond interactions between ligated and bulk water molecules caused by the pendant dpp moiety. An increase in *r'* of just 0.2 Å can result in *q* values measured at *q* ~ 0.3 lower than expected.[162]

In basic media the *q* values are *q* = 0.7 and *q* = 0.6 for **Eu.4a** and **Eu.4b** respectively. At higher pH values bound waters are likely to deprotonated, i.e. at pH 10 it is likely that OH^- rather than H_2O is bound. As there are fewer O–H oscillators coordinated to the Eu(III) centre, decreased quenching of the Eu(III) excited states occurs as OH^- coordinates, lowering the calculated *q* value. The complexes, therefore, can be said to be *q* = 1 in basic media.

2.6 Reversible Binding Nature of Dpp

As both nitrogen and oxygen are good donors for the hard Lewis acid lanthanide ions, binding could conceivably occur *via* the dpp nitrogen or oxygen.[107]

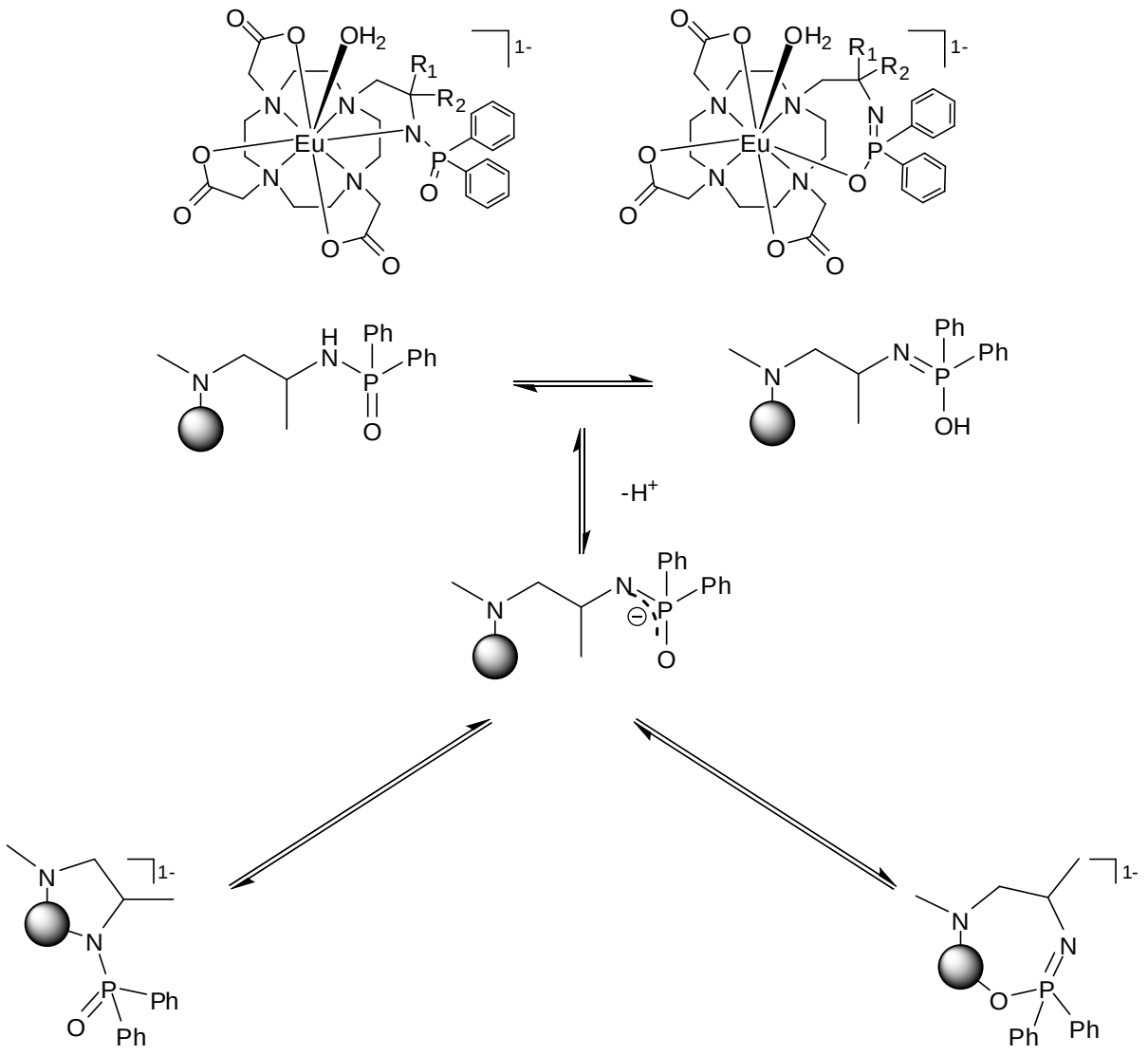

Figure 28. Dpp to Eu(III) ligation *via* either the nitrogen or oxygen upon deprotonation in basic media.

Binding *via* the nitrogen would result in the formation of a more stable five membered chelate ring. However, due to the oxyphilic properties of lanthanide ions the formation of the 7 membered chelate *via* oxygen binding was considered to be equally likely. Attempts to grow crystals for x-ray diffraction studies proved to be unsuccessful, possibly due to the inherent chirality of the complexes (Figure 28).

2.6.1 IR Studies

IR studies were carried out in order to determine if there was a change in stretching frequency of the phosphorus to oxygen bond. Deprotonation could result in either direct ligation to the lanthanide ion from the nitrogen itself or formation of a phosphorus to nitrogen double bond where binding to the lanthanide centre would occur *via* the oxygen

Infrared spectra were recorded at pH 5 and pH 10 for both **Eu.4a** and **Eu.4b**. Ligation *via* the nitrogen would result in the presence of a P=O absorption at around $\nu_{P=O}$ ~ 1200 cm^{-1}; however, if binding occurs *via* the oxygen, the characteristic P–O stretching vibration would be expected at lower frequencies, i.e. at ν_{P-O} ~ 1100 cm^{-1}. The spectral form is the same for each Eu(III) complex in both acidic and basic media. IR bands were observed with stretching frequencies 1,083 cm^{-1} (pH 5) and 1,083 cm^{-1} (pH 10) for **Eu.4a** and 1,085 cm^{-1} (pH 5) and 1,085 cm^{-1} (pH 10) for **Eu.4b**, characteristic of a P–O stretching vibration.[163, 164] The spectra suggest ligation *via* the dpp oxygen occurs. Little change is seen in P–O stretching frequencies between acidic and basic media which suggests the dpp moiety exists in the form P–OH, as ν_{P-OH} would be expected to be similar to ν_{P-OEu}.

Ligation *via* the oxygen can also be hypothesised from the calculated q = 1 hydration state of the dpp complexes in basic media. Ligation from the oxygen results in the formation of a seven-membered chelate ring. Less steric crowding of the Eu(III) centre would arise compared to the five membered chelate ring, which would be formed following ligation *via* the nitrogen atom, this allows for one water molecule to exchange with the Eu(III) centre. The reversible binding of the sulphonamide groups of **Eu.L29** (Section 2.3.1), developed by Parker and co-workers, occurred *via* the sulfonamide nitrogen, resulting in the formation of a five-membered chelate ring.[151] The hydration state of the resulting complex in acidic media was calculated as q = 0 due to the increased steric crowding about the Eu(III) centre. The reversible binding nature may therefore arise from the formation of the less stable seven-membered ring with respect to the five membered chelate ring allowing for greater ease of reversible ligation.

2.7 Relaxometric Investigation of the Gd(III) Dpp Complexes

As hydration states vary with pH both **Gd.4a** and **Gd.4b** were prepared and studied for their relaxivity properties. Relaxivity is greatly affected by hydration states (Equation 21, Chapter 1) and, therefore, similar pH responsive behaviour was expected.

*2.7.1 Relaxivity vs. pH for **Gd.4(a-b)***

The pH response of the relaxivity of the Gd(III) analogues is opposite to that observed for the luminescent intensities of the (Eu(III)) compounds (Figures 29 and 30). This is as expected as relaxivity is enhanced upon an increase in hydration state (Equation 21, Chapter 1) whereas Eu(III) excited states are quenched by the inner-sphere water molecules causing a decrease in emission intensities. For this reason the pH responses for both the Eu(III) and Gd(III) analogues mirror each other (Figure 29).

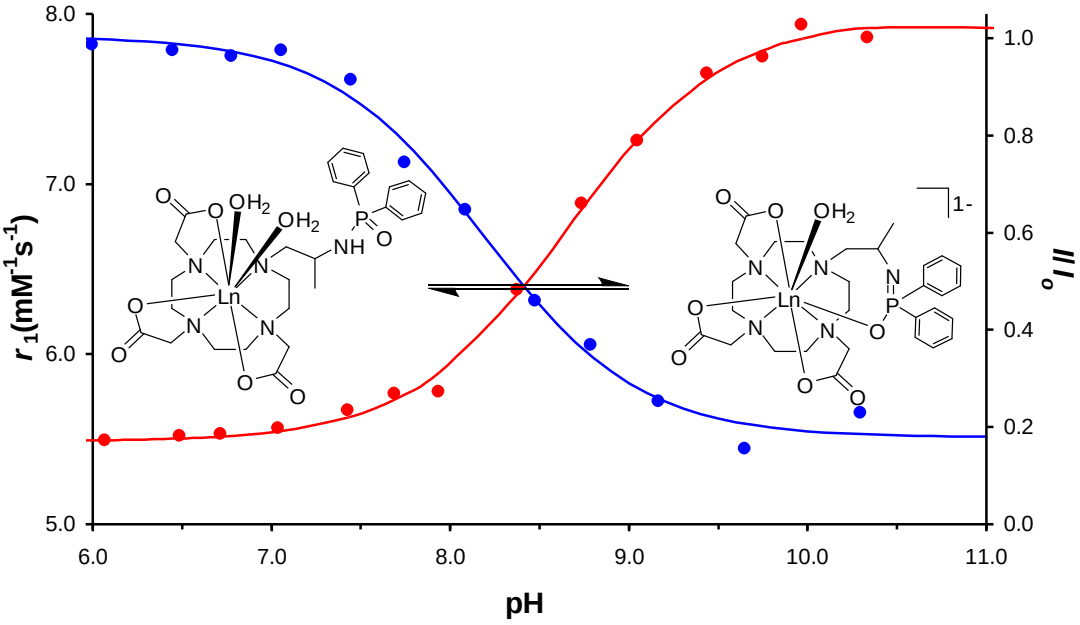

Figure 29. Eu(III) emission intensity *vs.* pH (blue) and Gd(III) relaxivity (r_1) *vs.* pH (red) for **Ln.4a**.

pK_a values were calculated from the data series in Figure 30 as 8.12 (± 0.12) and 7.84 (± 0.08), for **Gd.4a** and **Gd.4b** respectively (Table 11).

	pK_a	r_1 pH 5.0 ($mM^{-1}s^{-1}$)	r_1 pH 7.4 ($mM^{-1}s^{-1}$)	r_1 pH 10.0 ($mM^{-1}s^{-1}$)
Gd.4a	8.12 (± 0.12)	7.9	7.6	5.4
Gd.4b	7.84 (± 0.08)	8.2	7.3	4.4

Table 11. Measured pK_a values for **Gd.4a** and **Gd.4b** as well as relaxivity values, r_1, at pHs 5.0, 7.4 and 10.0.

The pK_a values are slightly different to those calculated for the Eu(III)) complexes *via* luminescence intensity. This is due to two factors: firstly, there is a slight change in ionic

radius on moving from Eu(III) (1.07 Å) to Gd(III) (1.05 Å), which may affect the dpp ligation and secondly, the pK_a measured *via* luminescence corresponds to an excited state pK_a.

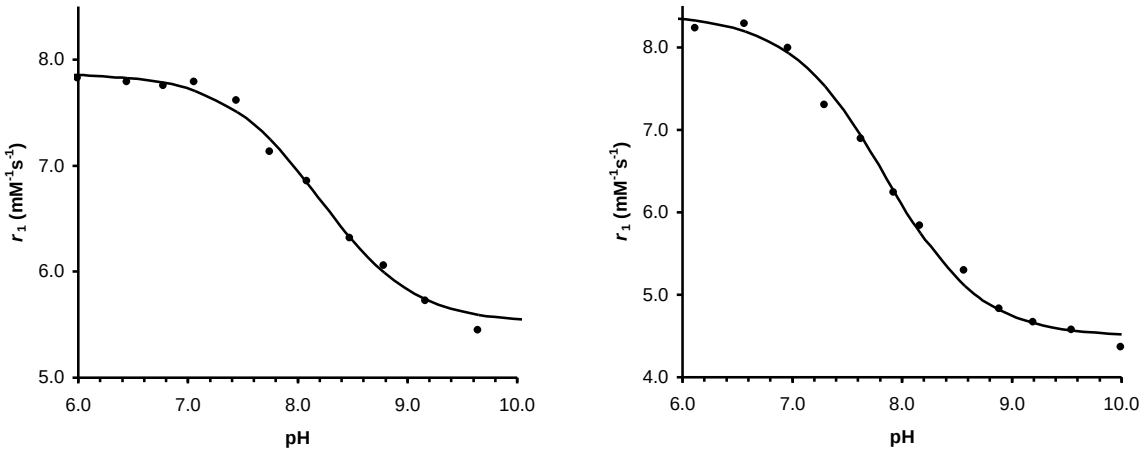

Figure 30. Relaxivity (r_1) *vs*. pH for **Gd.4a** (left) and **Gd.4b** (right) showing the experimental data (dots) and the calculated data (line). 1.0 mM **Gd.4(a-b)**, 0.1 NaCl, 20 MHz, 25^{o}C.

The measured relaxivities, r_1, clearly show a variation as the complex moves from a q = 2 to a q = 1 species, further confirming the reversible binding nature of the dpp moiety and not the coordination of a single hydroxide ion at pH 10 (suggested in Section 2.5.2, Scheme 11A). Previous relaxivity *vs*. pH experiments of Gd-DO3A have shown little difference at pH 10 compared to pH 5 due to hydroxide binding, which has a more significant effect in lowering relaxivity at pH's > 10.5. Furthermore, the observed relaxivity values are more typical of a q = 1 complex. The coordination of a single, non-exchanging hydroxide molecule would result in the observed relaxivity based entirely on outer sphere water contributions, which would be expected to be at around $r_1 \sim 2$ mM^{-1}s^{-1}.[51] The r_1 values, shown in Table 11, are somewhat higher than the measured relaxivities of the q = 1 commercially available contrast agents e.g. [Gd-DOTA]$^-$ r_1 = 4.2 mM^{-1}s^{-1} (20 MHz at 25^{o}C)[49] while the q = 2 compound Gd-DO3A r_1 = 5.7 mM^{-1}s^{-1} (20 MHz, 25^{o}C).[51] Further relaxivity studies were carried out in order to explore this increase in relaxivity.

*2.7.2 NMRD: Rotational Correlation Time, τ_R, for **Gd.4(a-b)***

Nuclear magnetic resonance dispersion (NMRD) profiles are measured in order to calculate the rotational correlation time (τ_R) of a Gd(III) complex. These values are extremely important in determining the relaxivity of a contrast agent; the slower a complex tumbles, the higher the relaxivity at clinical MRI magnetic field frequencies (Chapter 1, Section 1.3.7).

NMRD profiles of both **Gd.4a** and **Gd.4b** were measured and shown in Figures 31 and 32. The data is fit to Equations 22, 26 and 27 (Chapter 1) using Microcal Origin with the fitting parameters shown in Table 12.

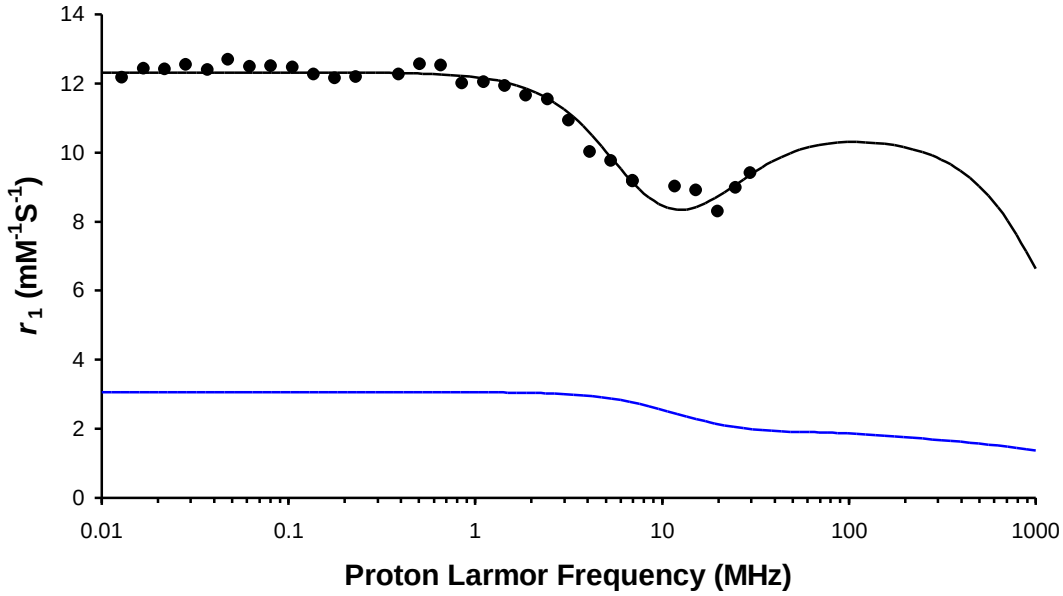

Figure 31. NMRD profile of **Gd.4a** showing the experimental data (black dots) and the calculated data (black line). The outer sphere contribution is shown as a blue line. 1.0 mM **Gd.4a** 0.1 M NaCl, pH 5.5, 25°C.

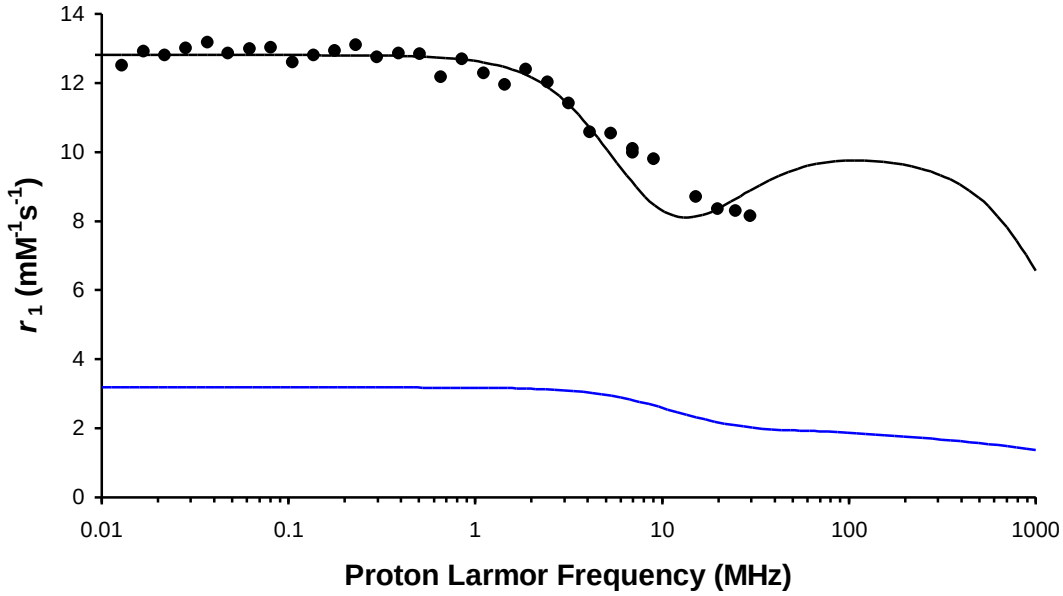

Figure 32. NMRD profile of **Gd.4b** showing the experimental data (black dots) and the calculated data (black line). The outer sphere contribution is shown as a blue line. 1.0 mM **Gd.4b** 0.1 M NaCl, pH 5.5, 25°C.

	τ_R (ps)	τ_v(ps)	τ_m (ns)	q	Δ^2 (s^{-2} x 10^{19})	r (Å)	a (Å)	D (cm^2 sec^{-1} x 10^{-5})
Gd.4a	127.6	15.5	35.8	2	9.0	3.05	4.0	2.24
Gd.4b	119.2	14.1	14.0*	2	9.0	3.05	4.0	2.24

Table 12. Fitting parameters for NMRD profiles of **Gd.4a and Gd.4b** where τ_m is the water exchange lifetime (*estimated), Δ^2 is the mean square zero field splitting energy and τ_v is the correlation time for its modulation, r is the Gd-H water distance, a is the shortest distance of approach and D is the diffusion coefficient. Data was collected using 1.0 mM complex, 0.1 M NaCl, pH 5.5 at 25°C.

The similar size and shape of **Gd.4a** and **Gd.4b** accounts for the similarity of the calculated rotational correlation times. The calculated τ_R for each complex is longer than that of the analogous q = 2 compound Gd-DO3A (τ_R = 66 ps).[51] This is not surprising, however, as the molecular weights for both **Gd.4a** and **Gd.4b** (756 Da and 773 Da respectively) are considerably larger than Gd-DO3A (501 Da), resulting in slower tumbling in solution.

*2.7.3 Variable Temperature ^{17}O NMR: Water Exchange Lifetime, τ_m, for **Gd.4a***

Variable temperature ^{17}O NMR studies are carried out in order to determine the water exchange lifetime (τ_m) as discussed in Chapter 1, Section 1.3.9. The variable temperature ^{17}O NMR profile for **Gd.4a**, Figure 33, was recorded at pH 5.5 and applied to Equations 29-32 (Chapter 1) using Microcal Origin with the fitting parameters shown in Table 13. As **Gd.4a** is similar in size, shape and charge to **Gd.4b** the same values were approximated for each complex.

	Gd.4a
τ_m (ns)	35.8
τ_v(ps)	15.5
ΔH_m (kJ mol^{-1})	47.0
ΔH_v (kJ mol^{-1})	6.9
$A/\hbar$ (x10^6 rad s^{-1})	-3.8
Δ^2 (s^{-2} x 10^{19})	9.0

Table 13. **Gd.4a** fitting parameters for variable temperature ^{17}O NMR where Δ^2 is the mean square zero field splitting energy and τ_v is the correlation time for its modulation, ΔH_m is activation enthalpy of water exchange, ΔH_v is the activation enthalpy for the modulation of the zero field splitting (ZFS) and $A/\hbar$ is the Gd-O scalar coupling constant. 10.2 mM **Gd.4a**, pH 5.5, 2.1 T.

A fast water exchange was observed and is shown by the non bell-shaped curve in Figure 33, which demonstrates a short, slow exchange period. The exchange is faster than the analogous Gd-DO3A complex (τ_m = 160 ns), providing an explanation for the large observed relaxivity with respect to Gd-DO3A; r_1 = 5.7 mM^{-1}s^{-1} (20 MHz, 25^{o}C).[51] The two factors that influence the short τ_m are the presence of the hydrophobic dpp moiety and the coordination geometry about the Gd(III) ion. ^1H NMR spectroscopy studies of the Eu(III) analogues showed resonances at δ = 25.7, 33.0, 34.7 and 34.9 ppm (**Eu.4a**) and δ = 24.8, 26.2, 33.6 and 35.6 ppm (**Eu.4b**) (400 MHz, D_2O, pD 10, 4^{o}C), which is typical of the square antiprismatic geometry (SAP) about the Eu(III) centre.[69] As mentioned in Chapter 1, Section 1.4.1, the twisted square antiprismatic (TSAP) geometry has increased steric crowding about the metal centre and facilitates the release of the coordinated water molecules, enhancing the exchange

rate in comparison to the SAP isomer.[72, 73] Therefore, the fast observed water exchange cannot be attributed to the coordination geometry about the Eu(III) centre. The addition of the hydrophobic dpp amide group to the Gd-DO3A hub provides a faster route for water exchange *via* the dpp induced organisation of the second sphere waters that may occur, which affects the H-bond formation between the bulk and ligated water molecules enhancing the exchange rate.[78] The hypothesis is further confirmed by reference to the calculated hydration state values of q = 1.7 for both **Eu.4a** and **Eu.4b**, which are lower than the expected value of q = 2 due to the lengthening of the Ln(III)-OH_2 distance, *r'*, as a result of the H-bond formation.

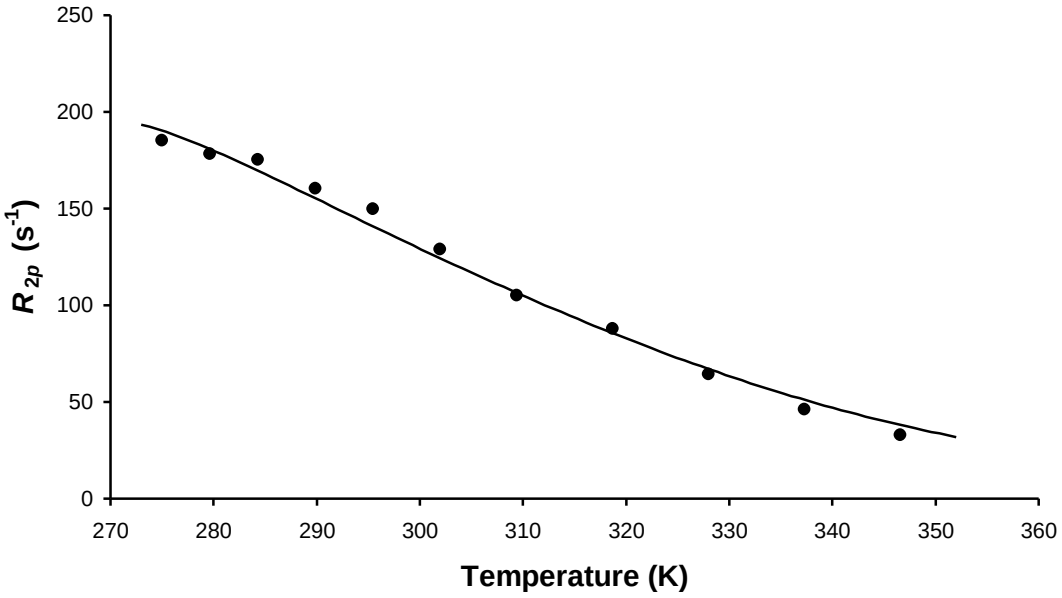

Figure 33. Variation of ^{17}O transverse relaxation rate, R_{2p}, with temperature for **Gd.4a** showing the experimental data (dots) and the calculated data (line). 2.1 T, 10.2 mM **Gd.4a**, pH 5.5.

2.8 Luminescent Investigation of the Tb(III), Dy(III) and Sm(III) Dpp Complexes

*2.8.1 Tb(III) Emission Intensity vs. pH for **Tb.4a***

The terbium analogue **Tb.4a** was prepared. The $^5D_4$ excited state of Tb(III) is much higher in energy than the ^5D_o excited state of Eu(III) (E = 20,500 cm^{-1} for Tb(III) in comparison to E = 17,277 cm^{-1} for Eu(III)).[111] In order for energy transfer to occur the chromophore must be higher in energy than the excited state of the lanthanide ion. Terbium lies to the right of gadolinium in the lanthanide series and is, therefore, smaller in size. This may affect the binding of the dpp moiety. Luminescence studies were carried out to see if sensitisation occurred. Likewise, pH titrations were carried out to see if the same reversible pH response occurred as for the Eu(III) and Gd(III) analogues (Figure 34).

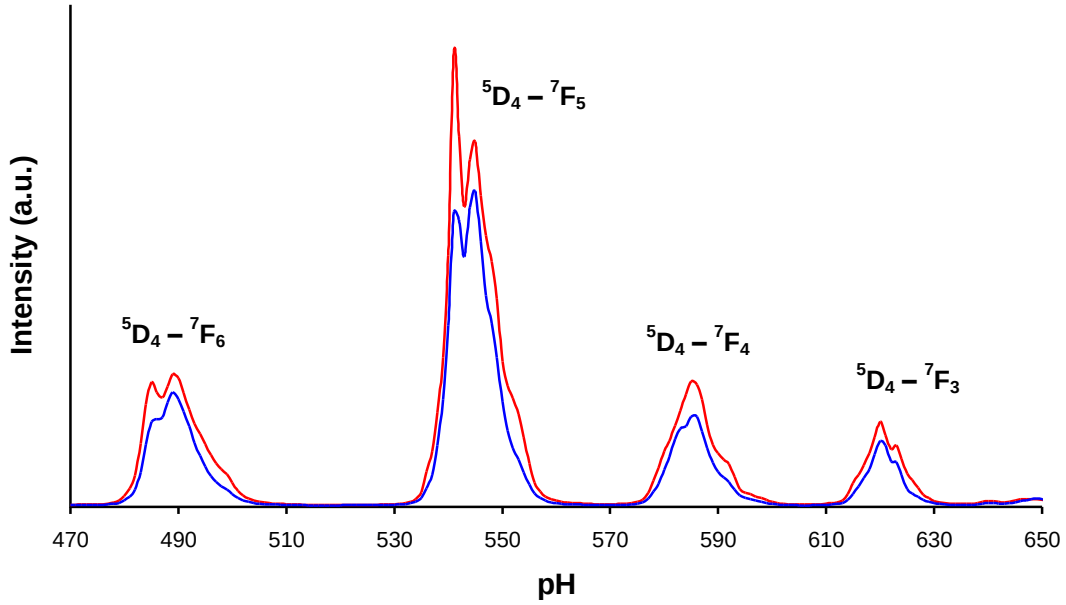

Figure 34. Tb(III) emission spectra for **Tb.4a** at pH 9.40 (blue) and pH 5.20 (red). 1.0 mM **Tb.4b**, 0.1 M NaCl, λ_{ex} = 265 nm, 25°C.

The emission spectra in Figure 34 was recorded following excitation of the dpp chromophore at λ_{ex} = 265 nm, which demonstrates that energy transfer and sensitization from the dpp chromophore to the Tb(III) excited state does occur. There is not, however, much difference in the emission intensity as pH varies. This, therefore, means that the dpp moiety remains either bound to or free of the Tb(III) throughout the pH titration. Luminescent lifetime studies were carried out with **Tb.4a** in both acid and basic media. The results are, however, not as accurate as for Eu(III) due to the less efficient quenching by water molecules as overlap occurs *via* the less populated $v = 5$ vibrational levels of water with the $^5D_4$ excited state energy level of Tb(III). First order rate constants were measured and q values were calculated as q = 0.2 (pH 5) and q = 0.3 (pH 10) (Equation 34, Chapter 1).[111] For full data see Appendix **A3**).

As the hydration state values, q, are close to 0 and vary very slightly between acid and basic media is suggests that the dpp moiety remains bound to the Tb(III) centre throughout the pH titration. Whilst surprising, this is not entirely unlikely as the ionic radius of Tb(III) is smaller than both Gd(III) and Eu(III) (Table 14); therefore, would have a greater charge density which may cause the dpp moiety to bind more strongly, i.e. the metal effectively competes with protons for the dpp group.

	Sm(III)	Eu(III)	Gd(III)	Tb(III)	Dy(III)	Ho(III)	Y(III)
Ionic Radii (Å)	1.08	1.07	1.05	1.04	1.03	1.02	1.02

Table 14. Ionic radii of lanthanide ions (and Y(III)) in their eight coordinate geometry.[25, 26]

The smaller size and increased charge density of the Tb(III) ion would also explain why the complex hydration state is closer to 0 and not 1 as for the Eu(III) analogue due to the increased steric crowding about the metal centre.

*2.8.2 Dy(III) and Sm(III) Emission Intensity vs. pH for **Dy.4a** and **Sm.4a***

The varied emission wavelengths and excited state lifetimes of the lanthanides make for interesting studies when designing probes for applications such as immunoassay (discussed in Chapter 1, Section 1.5.6). With this in mind, the dysprosium and samarium analogues **Dy.4a** and **Sm.4a** were prepared and their luminescent properties were compared with **Eu.4a** and **Tb.4a**. As for **Eu.4a** and **Tb.4a** the compounds both showed sensitisation from the dpp chromophore when excited at λ_{ex} = 270 nm. Sensitisation *via* excitation of the dpp antenna was expected, as the excited state energies of Dy(III) and Sm(III) are E = 21,100 cm^{-1} and E = 17,900 cm^{-1} respectively.[111] Neither compound, however, showed pH response. The ionic radius of Dy(III) is smaller that of Tb(III) and, therefore, similar conclusions can be drawn as to why no reversible binding is observed (Figure 35). Samarium lies to the left of europium in the periodic table and therefore the Sm(III) ionic radius is larger (Table 14). The increase in torsional strain around the Sm(III) may, therefore, disfavour binding of the dpp moiety (Figure 36). The resulting emission spectra recorded for **Sm.4a** are relatively poor in comparison to the **Dy.4a** and **Tb.4a** spectra, which is attributed to the decreased sensitization which occurs as the dpp moiety remains free from the Sm(III) centre.

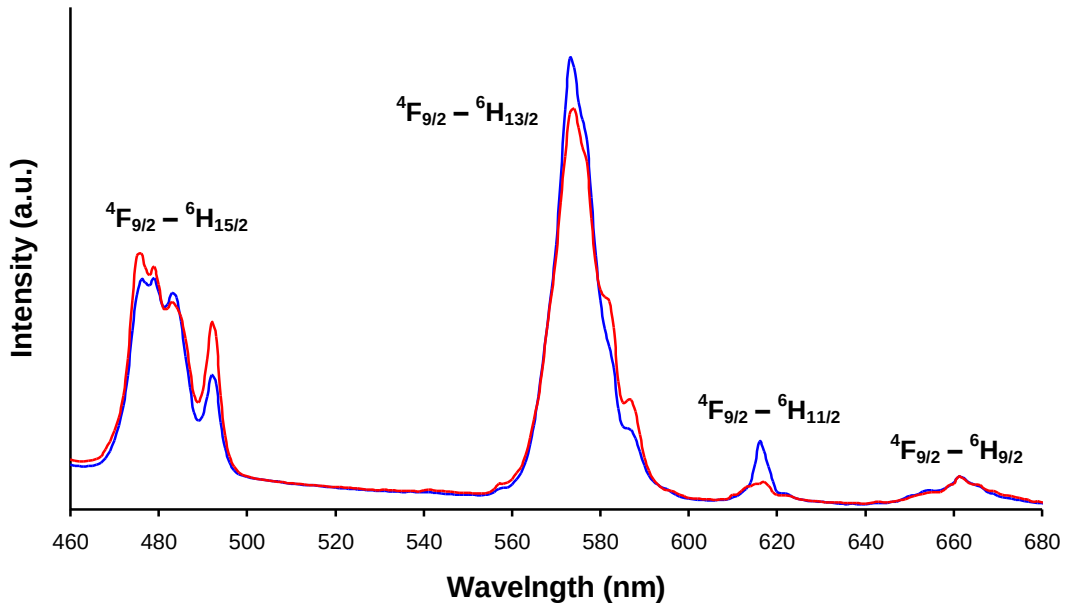

Figure 35. Dy(III) emission spectra for **Dy.4a** at pH 10.18 (blue) and pH 5.97 (red). 1.0 mM **Dy.4b**, 0.1 M NaCl, λ_{ex} = 265 nm, 25°C.

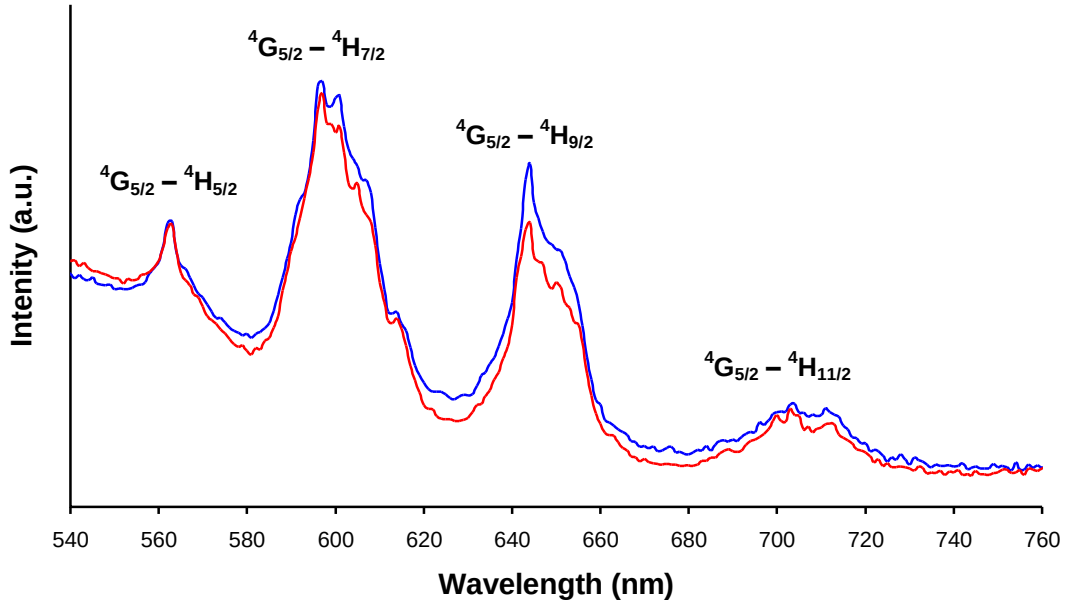

Figure 36. Sm(III) emission spectra for **Sm.4a** at pH 10.65 (blue) and pH 6.54 (red). 1.0 mM **Sm.4b**, 0.1 M NaCl, λ_{ex} = 265 nm, 25°C.

2.8.3 Luminescent Lanthanide Dpp Complexes as Time Resolved Immunoassay Probes

The four lanthanide complexes **Ln.4a** all emit at different spectral wavelengths as shown in Figure 37. This could be exploited in time resolved immunoassay as potentially four target vectors could each be labelled with a different lanthanide containing probe. This would allow for detection of multiple analytes in immunoassay.

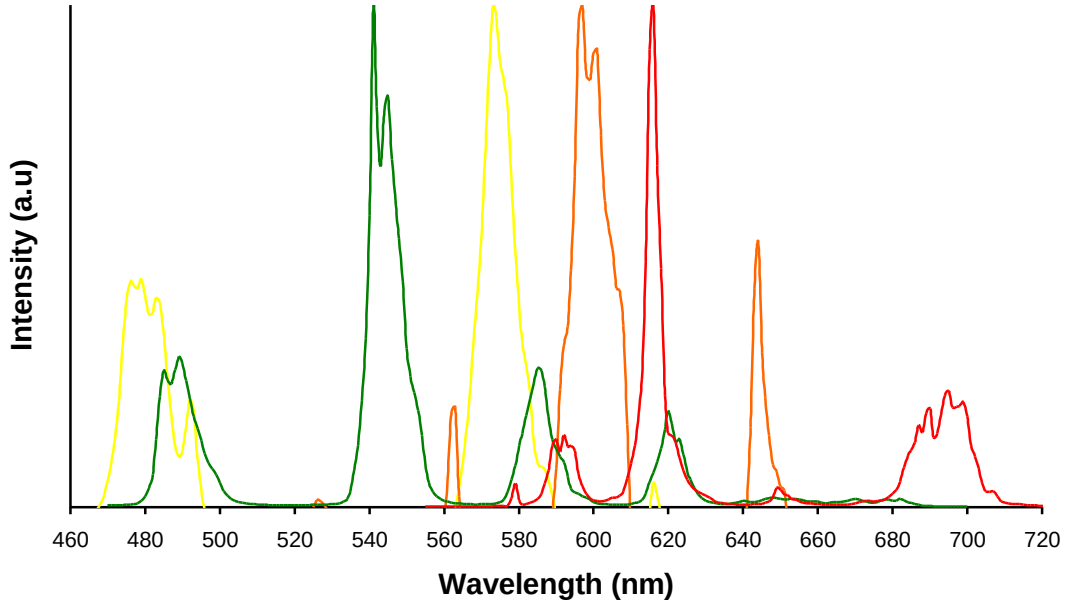

Figure 37. **Ln.4a** emission spectra, shown in their respective lanthanide emission colour; Tb(III) (green), Dy(III) (yellow), Sm(III) (orange) and Eu(III) (red).[112]

Furthermore, the excited state lifetimes also vary dramatically for each lanthanide. This, again, could be exploited as increasing delay times could be employed during the immunoassay allowing for the initial detection of the shorter lived Sm(III) probe, followed by Dy(III), Eu(III) and finally Tb(III). Figure 38 shows in graphical form the difference between the excited state lifetimes of each of the **Ln.4a** complexes. The calculated rate constants for decay are shown in Table 15 for varying acidic and basic media in water, as well as the excited state lifetime, τ, ($1/k$).

	$k_{(H_2O)}$ pH 5 , ms^{-1}	$\tau_{(H_2O)}$ pH 5, μs	$k_{(H_2O)}$ pH 10, ms^{-1}	$\tau_{(H_2O)}$ pH 10, μs
Eu.4a	2.34	430	1.46	670
Tb.4a	0.474	2110	0.411	2433
Dy.4a	66.90	14.94	64.00	15.63
Sm.4a	87.06	11.49	77.04	12.98

Table 15. First order rate constants, k, and excited state lifetime, τ, for each of the lanthanide analogues, **Ln.4a**, in H_2O. For full data analysis see Appendix **A1**, **A3** and **A4**.

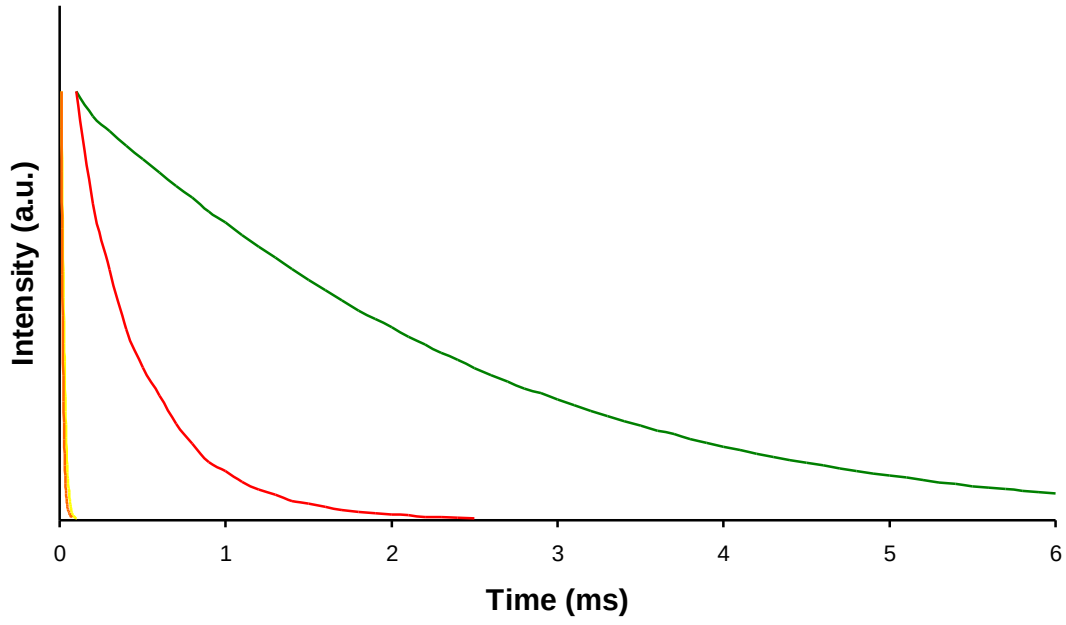

Figure 38. **Ln.4a** excited state lifetime determination in H_2O shown in their respective lanthanide emission colours; Tb(III) (green), Dy(III) (yellow), Sm(III) (orange) and Eu(III) (red). 1.0 mM **Ln.4a**, 0.1 M NaCl, λ_{ex} = 270 nm, λ_{em} = 541nm (**Tb.4a**), 573 nm (**Dy.4a**) 597nm (**Sm.4a**) and 617nm (**Eu.4a**), excitation : emission slits 5:5 nm, sample window 0.1 s (0.05 s **Dy.4a**), initial delay 0.1 s (**Eu.4a** and **Tb.4a**) and 0.01 ms (**Dy.4a** and **Sm.4a**), number flashes 500, flash time 40 ms 25°C, pH 5.0.

The shorter observed emission lifetimes for **Dy.4a** and **Sm.4a** shown in Table 15 arise from the smaller ΔE values between the ground and excited states (ΔE = 7,400 cm^{-1} (Sm(III)) and 7,850 cm^{-1} (Dy(III)) compared to those of Eu(III) (ΔE = 12,300 cm^{-1}) and Tb(III)

(ΔE = 14,800 cm^{-1}) (Table 6, Chapter 1), which provides greater ease for vibrational energy transfer from O–H oscillators. The Eu(III) excited state lifetime of **Eu.4a** shows a large difference in acidic and basic media as the dpp groups binds at pH 10 and the complex exists in the longer lived, q = 1 form. Little difference is observed for **Tb.4a** and **Dy.4a** as the dpp groups remains bound at both pH 5 and pH 10 with the hydration state q = 0. The **Sm.4a** excited state lifetime is slightly longer at pH 10 compared to that observed at pH 5. The dpp group remains free from the Sm(III) centre with the hydration state q = 2 throughout. The slight increase in the excited state lifetime at pH 10 may arise from the deprotonation of coordinated water molecules, which would reduce the number of O–H oscillators present and therefore increase the observed excited state lifetime. The Sm(III) excited state lifetime values are nevertheless quite similar, which suggests the hydration state remains q = 2 in both acidic and basic media.

2.9 Summary and Conclusions

Mono- and bis-methyl analogues of dpp-DO3A based Ln(III) complexes have been prepared. Upon excitation of the dpp antenna at λ_{ex} ~ 270 nm, sensitised emission of Eu(III), Tb(III), Dy(III) and Sm(III) has been observed. pH responsive reversible ligation of the dpp pendant moiety has been observed for both the Gd(III) and Eu(III) analogues, which is not the case for the other lanthanide analogues. This is thought to be due to the variation in ionic radii across the lanthanide series. pH responsive behaviour has been studied by Eu(III) luminescence, from which hydration state values have been measured at q = 1 and q = 2 in basic and acidic media respectively. Furthermore, the variation in emission intensities between the ΔJ = 1 and ΔJ = 2 bands demonstrate the potential application of such compounds a ratiometric probes for concentration determination of pH. Relaxometric studies have also demonstrated the reversible binding nature of the pendant dpp moiety with the Gd(III) analogue. Relaxivities have been measured as r_1 = 7.9 $mM^{-1}s^{-1}$ (mono-methyl, **Gd.4a**) and r_1 = 8.2 $mM^{-1}s^{-1}$ (bis-methyl, **Gd.4b**) in acidic media with the complex in its q = 2 form. As deprotonation and ligation of the dpp oxygen occurs in basic media and the complex hydration state is q = 1, the measured relaxivity values are r_1 = 5.4 $mM^{-1}s^{-1}$ (**Gd.4a**) and r_1 = 4.4 $mM^{-1}s^{-1}$ (**Gd.4b**).

The precise binding nature of the dpp moiety is still not fully understood. Attempts were made to grow crystals for x-ray diffraction studies, which were unfortunately unsuccessful. IR studies of the complexes showed little variation in the P–O stretching frequencies in both acidic and basic media of the Eu(III) dpp analogues, showing that $\nu_{P–O}$

remains similar throughout the titration. The IR studies suggest that ligation occurs *via* the dpp oxygen ahead of the nitrogen to form a seven membered chelate.

The pK_a values are 8.65 (± 0.09) and 8.59 (± 0.14) for the **Eu.4a** and **Eu.4b** respectively, calculated from luminescent studies, which fall somewhat higher than physiological pH conditions (pH 7.4). Substitution of the dpp methyl's with more electron withdrawing groups, such as CF_3's etc., may lower the pK_as to more suitable values for use of such compounds as biological pH probes. As they are, however, in the mostly non-ligated form at pH 7.4, studies into the non-covalent attachment of the dpp complexes to human serum albumin (HSA) were carried out and are discussed in detail in the following chapter.

Chapter 3

Contrast Agents with a High Affinity for Human Serum Albumin, HSA

3.1 Introduction

In recent years there has been a vast amount of research into contrast agent development towards the imaging of blood vessels and the circulatory system.[165, 166] The utilisation of MRI for this purpose is known as Magnetic Resonance Angiography (MRA).[167] The compartmentalisation of blood pool contrast agents (BPCAs) within the vasculature leads to high-resolution images with a low signal to noise ratio from non contrast agent enhanced extravascular tissue.[168] There are several advantages to blood pool contrast agents with a large cardiovascular retention time, such as: high dose efficiency leading to reduced contrast agent concentrations, longer time window for acquisition, the ability to measure tissue blood volume and perfusion, and the ability to visualise changes in capillary membrane integrity.[165] Such advantages from increased agent compartmentalisation within the time frame of an MRA scan allows for disease detection such as arterial disease, strokes and heart disease.[169]

Compartmentalisation of BPCAs has been achieved by the generation of large polymeric or dendrimeric Gd(III) chelates, increasing the vasculature retention time.[166] Macromolecular contrast agents with a diameter of around 7-12 nm have been shown to be retained in circulation due to slower diffusion through capillaries.[170] Lu and co-workers developed a biodegradable macromolecular polysulfide Gd(III)-DTPA based complex.[171] Endogenous thiols, such as cysteine and glutathione, readily break down disulfide bonds of the polymer backbone of the complex, resulting in degradation of the macromolecular agent into smaller, extractable chelates *via* the disulfide-thiol exchange reaction. These chelates can be cleared *via* the renal system. The disulfide-thiol exchange reaction occurs in many biological systems at a slow enough rate to allow for vasculature compartmentalisation during the MRI time window. The co-polymers prepared ranged from molecular weights of 15,000 Da to 35,000 Da, with relaxivities measured at r_1 = 4.42 $mM^{-1}s^{-1}$ and r_1 = 6.28 $mM^{-1}s^{-1}$ (64 MHz, 25^{o}C) respectively, the increase in r_1 being due to the increased rotational correlation times of the larger macromolecules. *In vitro* studies demonstrated that the complexes completely degraded over a period of about six hours in the presence of endogenous concentrations of *L*-cysteine (15 μM, pH 7.4, 37^{o}C). *In vivo* imaging of rat hearts

and aortas showed initial high contrast enhancement, which gradually decreased over a period of 27 minutes. Degradation products were identified using mass spectrometry of the urine samples, demonstrating clearance *via* the renal system.

The same group more recently have used the concept to develop a biodegradable poly(*L*-glutamic acid) (PGA) spacer into the paramagnetic conjugate, PGA-cystamine (Gd-DO3A), **Gd.L33a**.[172] *In vitro* relaxivity was measured as r_1 = 7.86 $mM^{-1}s^{-1}$ (128 MHz, 25°C) for the larger molecular weight macromolecule (118,000 Da). *In vivo* studies were carried out using mice bearing MDA-MB-231 human breast cancer carcinoma xenografts. Significant contrast enhancement of the blood pool was observed for up to four hours post injection allowing for enhanced tumour imaging. Results were compared to the non biodegradable PGA-1,6-hexadiamine-(Gd-DO3A), **Gd.L33b**, which showed contrast enhancement for up to seven hours post injection and was found present in tissue ten days later.

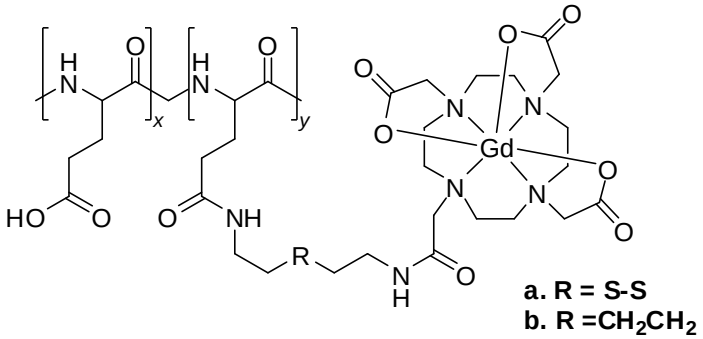

Gd.L33

Effects of complex charge on the macromolecular degradation *via* the disulfide-thiol exchange reaction have also been investigated.[173, 174] The negatively charged polydisulfide complex, (Gd-DTPA)-cysteine copolymers (GDCP) were compared with the neutral (Gd-DTPA)-cysteine diethyl ester copolymers (GDCEP). The neutral complexes showed much more rapid degradation in blood plasma and therefore demonstrated that the negatively charged species showed more prolonged contrast enhancement in the blood pool. An increase in the molecular weight of GDCP further prolonged the retention time within the vasculature.

3.2 Complexes with an Affinity for Human Serum Albumin, (HSA)

3.2.1 Human Serum Albumin

HSA is the most abundant protein in the circulatory system.[175] The protein is made up of 585 amino acids, has a total molecular weight of 66,400 Da and is present in human serum at a concentration of ca 0.67 mM.[176] The protein is comprised of three homologous domains (*I – III*), which are sub-divided into two domains A and B (Figure 39). Comprising of six hydrophobic binding sites, the primary function of the protein is the transportation of fatty acids, however the protein has a large affinity for several drugs as well. Sudlow and co-

workers identified two primary binding sites denoted site I (subdomain *IIA*) and site II (subdomain *IIIA*) which are capable of binding a variety of small molecules.[177, 178]

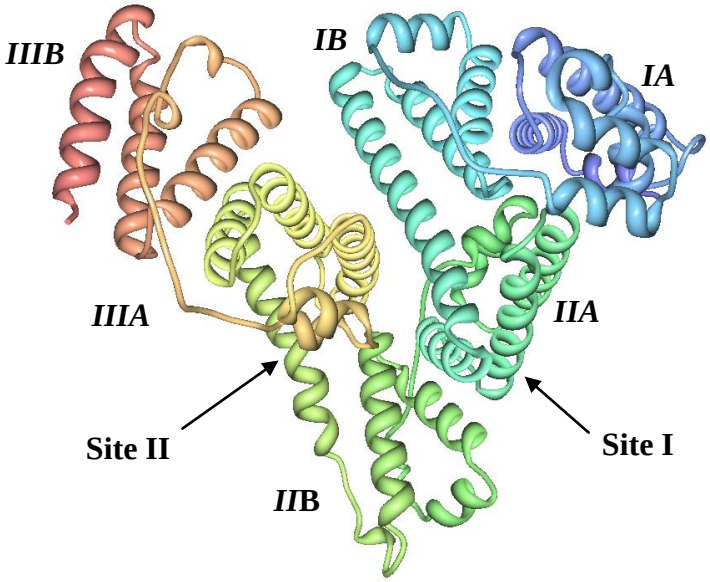

Figure 39. Structure of HSA showing all six sub-domains and the two primary binding sites I and II.

The depth of site I is ill-defined. Ligands tend to be large heterocyclic anions with a centrally located charge, such as warfarin, bonding mainly through hydrophobic interactions. Site II has a depth of around 16-25 Å and ligands are typically aromatic and either charge neutral or with a peripherally located anionic charge, such as dansylsarcosine, with bonding through a combination of hydrophobic, hydrogen bonding and electrostatic interactions. [179, 180]

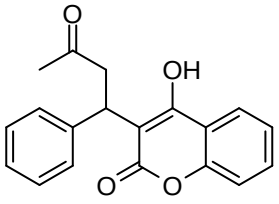

Warfarin

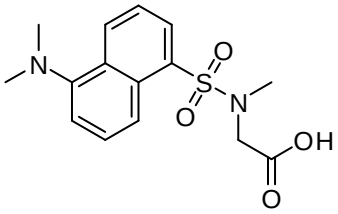

Dansylsarcosine

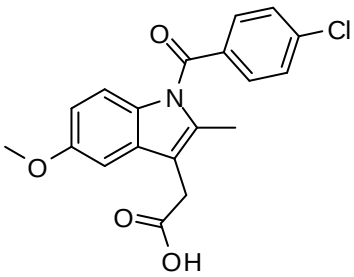

Indomethacin

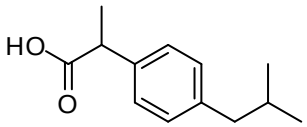

Ibuprofen

The affinity constant for both warfarin and dansylsarcosine are K = ~ 2 x 10^5 M^{-1}; both are frequently used as fluorescent probes in order to determine the site specificity of HSA

binding agents (discussed in more detail in Section 3.6.2).[177, 178] Several drugs have been found to locate at sites I and II, such as the anti-inflammatory drugs indomethacin and ibuprofen, which bind at sites I and II respectively with affinity constants of $K = 1.4 \times 10^6$ M^{-1} and $K = 2.7 \times 10^6$ M^{-1}.[181, 182]

3.2.2 Reversible, Non-Covalent Binding to HSA

Increased cardiovascular retention has also been achieved by the conjugation of low molecular weight Gd(III) chelates to serum proteins such as HSA. The strategy is known as receptor induced magnetisation enhancement (RIME) and is achieved by the incorporation of a hydrophobic moiety into the contrast agent. This enables reversible, non-covalent binding of the Gd(III) chelate to the protein.[91] The HSA-Gd(III) chelate interaction is established *in vivo*, with the HSA bound agent in equilibrium with non-bound agent, which is excreted over time. Therefore, long intravascular retention is achieved while prolonged excretion problems are avoided. Furthermore, the rotational motion of the low molecular weight Gd(III) chelate is slowed down by attachment to the slowly tumbling protein. Therefore, the rotational correlation time, τ_R, is increased and, the observed relaxivity and cardiovascular image intensity is enhanced (discussed in Chapter 1, Section 1.4.2).

3.2.3 HSA Binding Contrast Agents

Lauffer and co-workers at Epix Medical Inc. developed a HSA binding BPCA which relies on the incorporation of a lipophilic diphenylcyclohexyl moiety into a Gd-DTPA chelate, known as MS-325 (Figure 40). [183, 184] The contrast agent has recently been approved for European clinical use under the trade name Vasovist® (Scherring A.G., Germany, 2005).

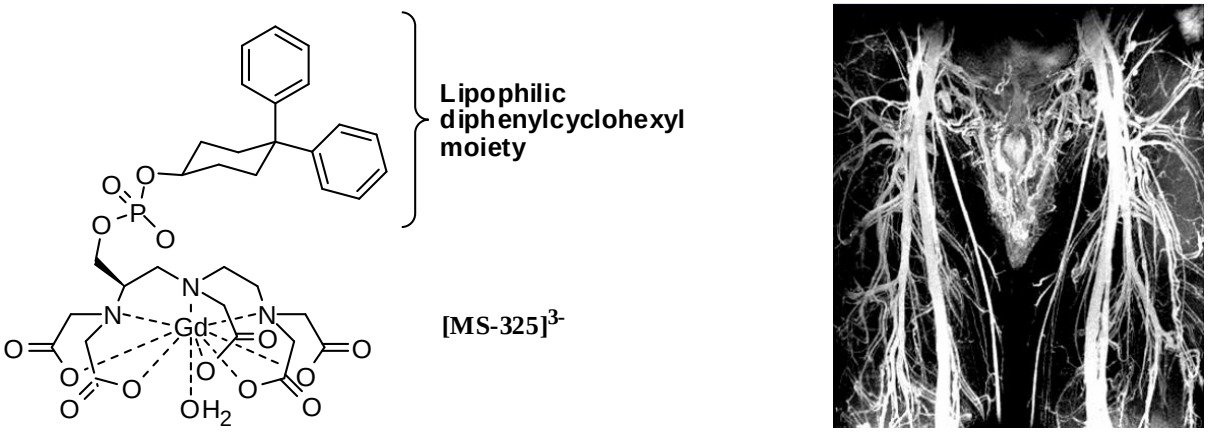

Figure 40. Left; structure of MS-325. Right; MS-325 enhanced MRA image of the groin and upper thighs (image from Epix Medical Inc.).

Initial pre-clinical trial studies showed MS-325 to be 80% (1.0 mM) to 96% (0.1 mM) bound to HSA in human blood plasma, with corresponding relaxivities of $r_1 \sim 30$ $mM^{-1}s^{-1}$ to $r_1 \sim 45$ $mM^{-1}s^{-1}$ (20 MHz, 37°C); around an eight fold increase when compared to free

MS-325 at r_1 = 6.6 $mM^{-1}s^{-1}$ (20 MHz, pH 7.4 (PBS) 37^oC).[185] MS-325 binds to multiple sites of the protein and the decrease in relaxivity upon increase in MS-325 concentration is attributed to the secondary protein binding sites having a lower affinity for MS-325 than the primary binding sites. The high level of protein binding decreases the volume of distribution, V_d, and increases the elimination half-life, T_e, of MS-325. Monkeys (3.0 – 5.6 kg) were injected with 0.025 and 0.10 mM kg^{-1} of MS-325;[186] the level of protein binding was observed at 80% to 85%, determined by ultrafiltration of the blood plasma. Elimination occurred *via* the renal system as enhanced kidney and bladder activity was observed five minutes post injection. After 72 hours almost complete clearance was observed, which was backed by analysis showing 92% of the administered MS-325 to be present in urine samples 72 hours post injection.

Caravan and co-workers carried out a more complete *in vitro* analysis in determining the non-covalent HSA binding affinity, K, and relaxometric properties of HSA coupled MS-325.[187] Following a classical stochiometric model of the equilibria, four stepwise binding constants were determined *via* ultrafiltration experiments as K_1 = 11.0 ± 2.7 mM^{-1}, K_2 = 0.84 ± 0.16 mM^{-1}, K_3 = 0.26 ± 0.14 mM^{-1} and K_4 = 0.43 ± 0.24 mM^{-1}. Under physiological conditions and imaging concentrations (0.1 mM MS-325, pH 7.4, 37^oC) such binding affinities equate to 88 ± 2% of MS-325 bound to HSA. Displacement of the site II binding fluorescent probe dansylsarcosine was observed, with a measured inhibition constant of K_i = 85 ±3 μM. Displacement of the site I specific dansyl-L-asparagine was also observed, albeit to a much lower degree with K_i = 1,500 ± 850 μM. No such displacement of the site I specific fluorescent probe warfarin occurs. This demonstrates that MS-325 binds primarily to site II of the protein. Luminescent lifetime studies of the Eu(III) analogue measured the hydration state of the complex to be consistently q = 1 both bound to, and free from the protein. Variable temperature ^{17}O NMR studies measured the water exchange lifetime, τ_m, of the unbound species to be τ_m = 69 ± 20 ns (10 mM MS-325, pH 7.4 PBS, 40.6 MHz). NMRD studies determined that the increase in relaxivity observed is due to a 60-100 fold increase in the rotational correlation time, τ_R, upon binding to the protein, with an estimated increase in the water exchange lifetime, measured at τ_m = 170 ± 40 ns. The rotational correlation times were measured as τ_R = 115 ps for the free species compared to τ_R = 10.1 ± 2.6 ns when bound to HSA. (0.1 mM MS-325, pH 7.4 PBS, 22.5% (w/v) HSA, 37^oC). The thermodynamic and kinetic stability studies have shown that MS-325 is more inert to metal ion substitution than the commercially available $[Gd\text{-}DTPA]^{2-}$ (Magnevist®)[188] and during clinical trials was found to be safe and effective at imaging vascular diseases[189, 190] as well as organ function and blood flow.[191] More recently it has been shown that MS-325 exhibits species dependant

enhancement of relaxivity in a variety of animal blood plasma. Human showed the highest relaxivity, followed by pig, rabbit, dog, rat and mouse with 91% to 64% decrease in relaxivity observed.[192]

The RIME strategy has been followed in developments of many other HSA binding contrast agents. Binnemans and co-workers have prepared an amphiphilic ligand, in which two $[Gd\text{-}DTPA]^{2-}$ chelates are bridged by a 2,3-disubstituted bisindole derivative bearing three methoxy groups, **L34**.[193]

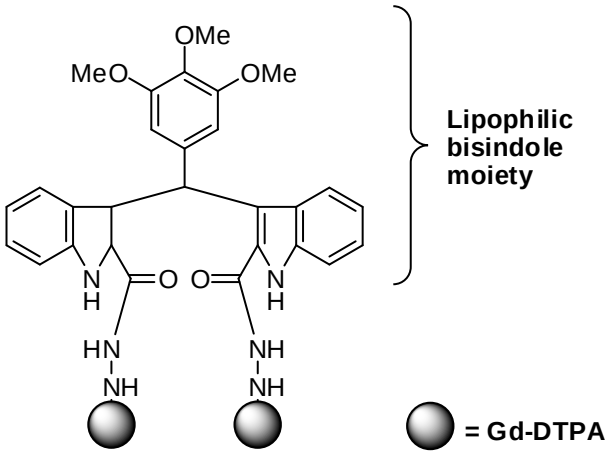

L34

The measured relaxivity of the unbound species was r_1 = 6.8 $mM^{-1}s^{-1}$ (i.e. per Gd(III) ion), which is higher than that observed for $[Gd\text{-}DTPA]^{2-}$ (20 MHz, 37°C) due to the increased rotational correlation time of the larger species. Relaxivity is increased to r_1 = 15.2 $mM^{-1}s^{-1}$ when fully bound to HSA. Such an increase would require a lower administered dose of the contrast agent. The HSA binding affinity, *K*, was as 10,100 M^{-1}. Despite the enhancement in relaxivity upon addition of HSA, the observed values are not as high as those recorded for HSA bound MS-325 ($r_1 \sim$ 45 $mM^{-1}s^{-1}$). The lower relaxivity values are thought to be due to the orientation of the bound species and protein interaction hindering water Gd(III) water exchange, as well as potential independent rotations of the protein bound Gd(III) chelates.

Observed relaxation rates for HSA bound Gd(III) chelates are generally much lower than theoretical values where r_1 > 100 $mM^{-1}s^{-1}$ is expected for q = 1 complexes with a rotational correlation time of τ_R = 10-30 ns.[63] The reason for lower observed relaxivity values is frequently attributed to independent rotation of the HSA conjugated complex, as well as decreased water exchange rates due to protein interactions.[194]

Lowe and co-workers designed a ligand incorporating a rigid, chiral 3,5-dihydro-4H-dinaphth[2,1-c:1’2’-e]azepine moiety onto a DOTA chelate, **L35**. The hydrophobic binaphthyl group, coupled with an amide linker was designed to bind to HSA with reduced

independent rotation.[195] The Eu(III) analogue was prepared and interactions with HSA were studied *via* luminescence spectroscopy. Following excitation of the binaphthyl group (λ_{ex} = 303 nm) Eu(III) emission was observed following sensitisation *via* energy transfer from the chromophore to the excited state of Eu(III) (Chapter 1, Section 1.5.5). Upon addition of HSA the excitation maxima shifted to lower energy, longer wavelengths at λ_{ex} = 320 nm while the intensity of the binaphthyl fluorescence decreased and the HSA tryptophan emission increased (0.1 mM complex, 4.5% HSA, pH 7.4 (PBS), 25°C).

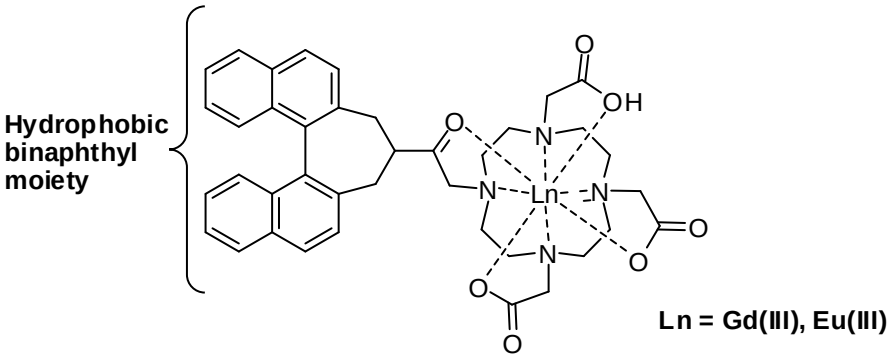

Ln.L35

A 6.5-fold increase in Eu(III) emission intensity was observed, which is attributed to better overlap of the now lower energy chromophore triplet excited state with the ^5D_o excited state of Eu(III). The Eu(III) enhancement was monitored at fixed concentrations of both the R and S-enantiomers of the binaphthyl group with increasing concentrations of HSA to determine binding affinities, *K*, (0.01 mM. **Eu.L35**, pH 7.4 PBS). No chiral discrimination was observed with *K* values measured at 8,200 ± 810 M^{-1} and 7,710 ± 460 M^{-1} for the R and S-enantiomers respectively, corresponding to around 83% protein bound complexes at imaging concentrations and physiological conditions (0.1 mM **Eu.L35**, 0.67 mM HSA, pH 7.4). Further luminescent lifetime measurements measured hydration state values as q = 1 when both bound and free from the protein. Relaxometric studies measured the relaxivity of the HSA bound complex at r_1 ~ 20 $mM^{-1}s^{-1}$ (20 MHz, 25°C), which is limited by the long water exchange lifetime, $\tau_{m,}$ inherent with amide conjugated Gd(III) complexes. Work is continuing with the Gd(III) analogues with modifications to the ligand structure being carried out in order to increase water exchange rates and relaxivity.

Aime and co-workers have followed a similar strategy in preparing two Gd-DOTMA based complexes incorporating a rigid 4-methoxy biphenyl, **[Gd.L36]**$^-$, or triphenyl, **[Gd.L37]**$^-$, moiety.[196] The measured relaxivities of the complexes were r_1 = 6.0 $mM^{-1}s^{-1}$ and r_1 = 6.4 $mM^{-1}s^{-1}$ for **[Gd.L36]**$^-$ and **[Gd.L37]**$^-$ respectively, which are much higher than the parent [Gd-DOTMA]$^-$ complex at r_1 = 3.8 $mM^{-1}s^{-1}$, attributed to the increased rotational

correlation time of the complexes due to the added hydrophobic moieties (20 MHz, 25^{o}C). Binding affinities, *K*, determined using relaxation rate enhancement, were measured as K = 2,700 M^{-1} and K = 95,000 M^{-1} with maximum relaxivity values of r_1 = 35 $mM^{-1}s^{-1}$ and r_1 = 43.5 $mM^{-1}s^{-1}$ for **[Gd.L36]**$^{-}$ and **[Gd.L37]**$^{-}$ respectively.

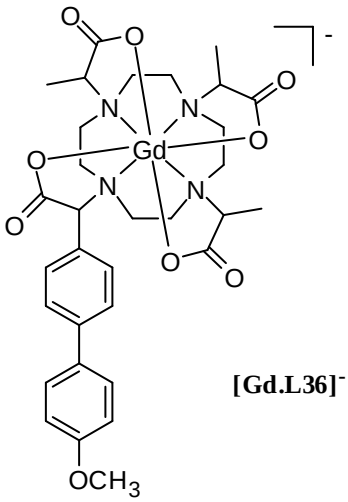

[Gd.L36]$^{-}$

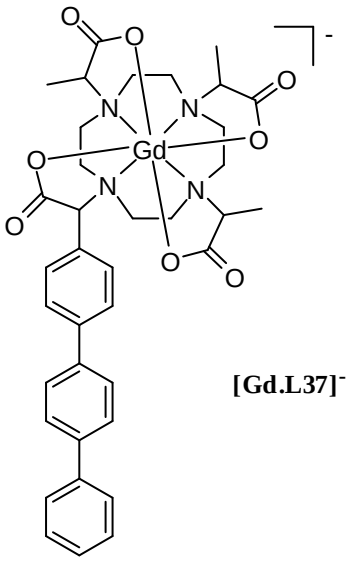

[Gd.L37]$^{-}$

Fluorescent probe displacement studies suggested that both complexes bind to site II of the proton and, following molecular modelling studies of the complex to protein docking interactions, the differences in relaxivity between each species is attributed to the orientations in which each complex binds to HSA. The shorter hydrophobic moiety incorporated into **[Gd.L36]**$^{-}$ causes the paramagnetic chelate to be in closer proximity to the protein. Hydrogen bond formation between residual groups on the protein with Gd(III) coordinated water molecules, as well as water displacement due to residual group ligation to Gd(III) centre results in lengthening of the water exchange lifetime and, hence, lower relaxivities. Molecular modelling of **[Gd.L37]**$^{-}$ demonstrated that the longer hydrophobic moiety held the Gd(III) chelate further from the protein, preventing protein residue interactions. Variable temperature ^{17}O NMR experiments were difficult to carry out due to poor solubility of the complexes, however the studies demonstrate the potential scope in relaxivity enhancement of HSA bound Gd(III) chelates in terms of improving water exchange processes.

3.3 Non-Covalent binding of Dpp Complex to HSA

The pH responsive dpp-containing complexes discussed in Chapter 2 showed that at physiological pH 7.4, the dpp moiety is mostly remote from the Ln(III) centre in the q = 2 form (Chapter 2, Sections 2.5 and 2.7). It was therefore hypothesised that the pendant hydrophobic dpp group would bind non-covalently to Human Serum Albumin (HSA). Such attachment would be expected to result in the lengthening of the rotational correlation time, τ_R, of the Gd(III) contrast agent, enhancing relaxivity, r_1, and MR image intensity.

The structure of the dpp moiety, containing two phenyl groups, is similar to that of the commercially available blood pool contrast agent MS-325 (Vasovist®), which has a high affinity for site II of HSA with a binding constant measured as K = 11.0 ± 2.7 mM^{-1} (0.1 mM MS-325, pH 7.4, 37°C). The site II hydrophobic pocket is around 16 - 25 Å deep[179, 180], allowing the diphenylcyclohexyl moiety of MS-325 to bind to the protein, holding the Gd(III)-DTPA macrocycle outside on the surface, enabling water molecules to exchange with the Gd(III) centre. Due to the similarity in structure of the dpp containing complexes discussed in Chapter 2, similar HSA binding affinity was expected and the hypothesis was studied by both luminescent (Eu) and relaxometric (Gd) methods.

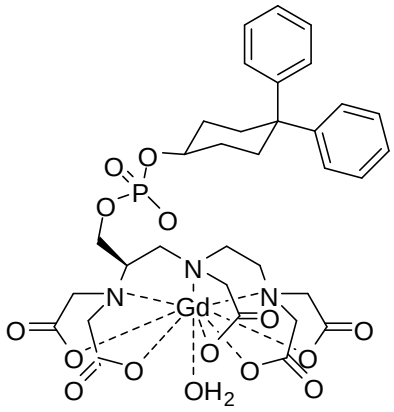

[MS-325]$^{3-}$

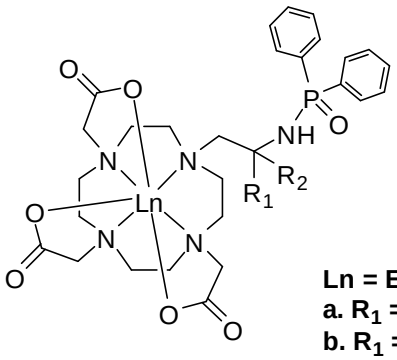

Ln = Eu(III), Gd(III)
a. R_1 = H, R_2 = CH_3
b. R_1 = R_2 = CH_3

Ln.4(a-b)

3.3.1 Ln(III)-dpp Ligation at Physiological pH 7.4

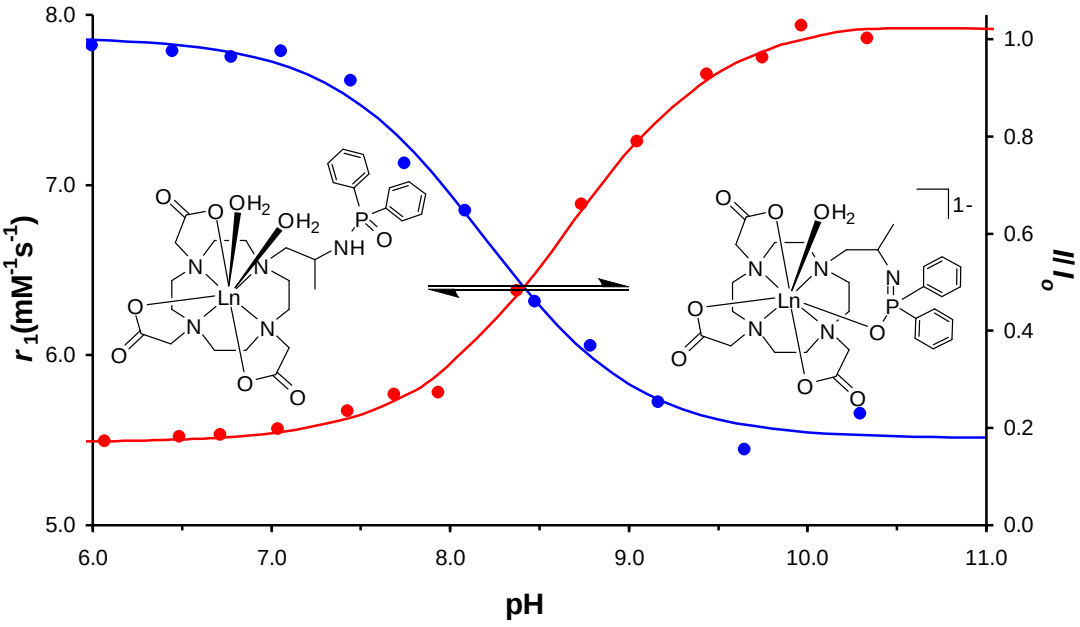

Figure 29. Eu(III) emission intensity *vs.* pH (blue) and Gd(III) relaxivity (r_1) *vs.* pH (red) for **Ln.4a**.

As mentioned in Section 3.2.2, if a compound contains a hydrophobic group then non-covalent binding at the hydrophobic binding sites of HSA can occur. The relaxivity, r_1, (Gd)

and emission intensity (Eu) *vs*. pH titrations of both the bis-methyl and mono-methyl Ln-dpp-DO3A complexes, discussed in Chapter 2, each show that the hydrophobic dpp moiety is mostly in the protonated form and not bound to the metal centre at pH, 7.4 (Figure 29).

The proportion of the unbound q = 2 dpp species, at pH 7.4 is determined by expansion of Equation 39 used in determining the first order rate of decay constants of the Eu(III) excited state from luminescent lifetime studies. At this pH emission intensity is comprised of both contributions from the dpp bound q = 1 species and the dpp free q = 2 species. The rate of decay constants for both species are known from previous lifetime studies conducted in acidic and basic media, shown in Chapter 2, Section 2.5.3. Therefore the proportion of q = 1 species in solution, x, is determined by lifetime measurements for both the mono-methyl **Eu.4a** and the bis-methyl **Eu.4b** at pH 7.4 and applying the data to Equation 40, where I_o is the initial intensity and k is the first order rate of decay constants of the Eu(III) excited state of both the q = 1 (pH 10) and q = 2 (pH 5) forms of the dpp complexes.

$$I_{obs} = I_o e^{-kt} + offset \tag{39}$$

$$I_{obs} = xI_o^{q=1} e^{-k^{q=1}t} + (1-x) I_o^{q=2} e^{-k^{q=2}t} + offset \tag{40}$$

	$k_{(H_2O)}$ (pH 7.4)	$k_{(D_2O)}$ (pH 7.4)	q (pH 7.4)	x	% q = 2 (pH 7.4)
Eu.4a	2.14	0.64	1.5	0.077	92.3
Eu.4b	2.67	1.18	1.5	0.043	95.7

Table 16. Measured x values at pH 7.4 for **Eu.4a** and **Eu.4b** and percentage of free dpp species present in solution. 0.1 mM **Eu.4(a-b)**, 0.1 M NaCl, 25°C. For full data analysis see Appendix **A5**.

The results shown in Table 16 show the vast majority of each compound to be in the dpp non-ligated, q = 2 form. Furthermore, they are consistent with the pK_a values observed for each of the dpp complexes; pK_a = 8.65 (± 0.09) and pK_a = 8.59 (± 0.14) respectively, calculated from emission intensity *vs*. pH titrations (Chapter 2, Section 2.5.2). Following Equations 41-44 it was determined that 94.7% and 93.9% of the dpp protonated, q = 2 species of **Eu.4a** and **Eu.4b** respectively was present in solution at pH 7.4, where Hdpp represents the protonated form of the dpp complex.

$$\mathrm{p}K_a = -\log_{10} K_a \tag{41}$$

$$\mathrm{pH} = -\log_{10}[\mathrm{H}^+] \tag{42}$$

$$K_a = \frac{[\mathrm{H}^+][\mathrm{dpp}^-]}{[\mathrm{Hdpp}]} \tag{43}$$

$$\%\,\mathrm{Hdpp} = \left[1 + \frac{K_a}{[\mathrm{H}^+]}\right]^{-1} \times 100 \tag{44}$$

The vast majority of each of the dpp complexes are present in the protonated, q = 2 form, potentially allowing non-covalent binding to HSA to occur. As discussed in Chapter 1, Section 1.4.2, attachment of an MRI contrast agent to a large, slowly tumbling molecule is expected to increase relaxivity and, therefore, enhance image intensity. Binding studies were carried out with the Eu(III) and Gd(III) analogues to explore this phenomenon.

3.4 Luminescent Investigation of the Binding of Eu(III) dpp Complexes with HSA

*3.4.1 Eu(III) Emission Intensity vs. [HSA] for **Eu.4(a-b)***

As seen in Chapter 2, excitation of the dpp chromophore at λ_{ex} ~ 270 nm resulted in an increase in the emission intensity, resulting from energy transfer from the dpp triplet excited state to the ^5D_o excited state of Eu(III). A decrease in the degree of sensitization was observed as Eu(III) emission intensity decreased upon addition of HSA to the complex solution at pH 7.4. It was hypothesised that the reduction of emission intensity was due to binding of the dpp moiety to HSA, reducing the efficiency of the energy transfer to Eu(III). As concentrations of HSA increase, more complex is bound to the protein and a result the Eu(III) emission decreases.

Eu(III) emission studies of fixed concentrations of around 0.2 mM of **Eu.4a** and **Eu.4b** with varying concentrations of HSA were carried out in order to see the effect on energy transfer from the chromophore's triplet excited state to the Eu(III) excited state. The complexes were excited indirectly, *via* the chromophore, at λ_{ex} ~ 270 nm and the variations in intensity of the ΔJ = 2 band (~ 615 nm) were observed. The titrations of **Eu.4a** and **Eu.4b** (fixed concentration 0.2 mM) *vs*. [HSA] were carried out at pH 7.4, buffered by PBS. The data is shown in Figure 41. The HSA binding affinity constant, *K*, was determined from the data in Figure 41 (Table 17).

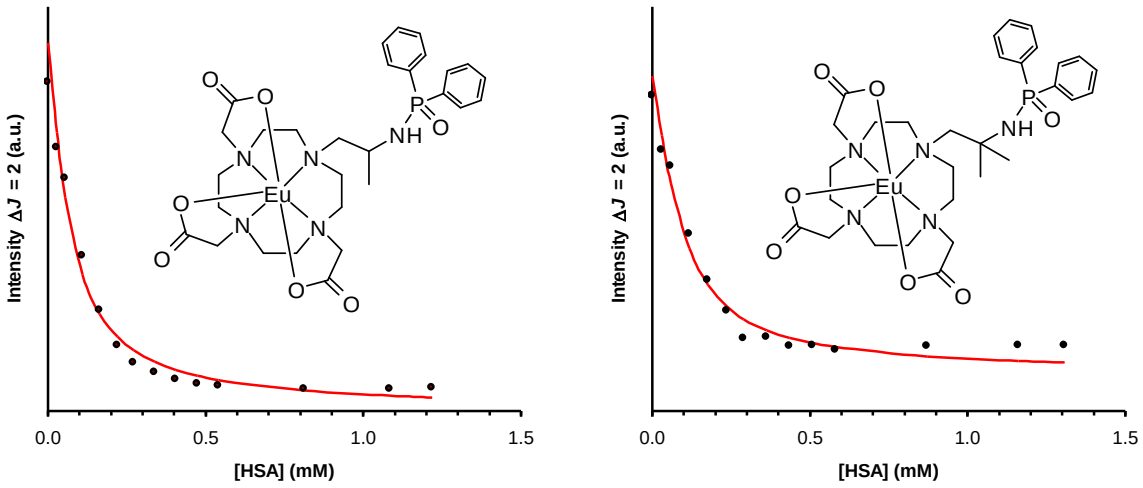

Figure 41. Plot of ΔJ = 2 Eu(III) emission intensity *vs.* [HSA] for **Eu.4a** (left) and **Eu.4b** (right) showing the experimental data (black dots) and the calculated data (red line). ~ 0.1 mM **Eu.4(a-b)**, 0.1 M NaCl, pH 7.4 (0.2 M PBS), 25°C.

	K (M^{-1})	% Bound
Eu.4a	22,268 (± 12%)	92.8
Eu.4b	20,059 (± 14%)	92.1

Table 17. HSA affinity constants, *K*, for **Eu.4a** and **Eu.4b** and calculated percentage of compound bound to HSA at imaging concentrations (0.67 mM HSA, 0.1 mM **Eu.4(a-b)**) at pH 7.4 (0.2 M PBS).

The equilibrium (Equation 45) was assumed for both **Eu.4a** and **Eu.4b**, where Ln represents the Ln(III) ligand complex. The concentration of bound lanthanide complex, [LnHSA], is determined by expansion of Equation 45, where $[HSA]_T$ and $[Ln]_T$ are the total concentrations of HSA and the Ln(III) complex (Ln = Eu(III) here and Gd(III), discussed in Section 3.5.1, (Equation 46).[197] The Ln(III) concentrations can be substituted for of Eu(III) emission intensity as shown in Equation 47, where I_{calc} is the theoretical Eu(III) emission intensity (to be compared with the experimentally observed Eu(III) emission intensity), I_{Eu} is the intensity of the Eu(III) complex when not bound to HSA (i.e. at the start of the titration) and I_{EuHSA} is the intensity of the Eu(III) complex when entirely bound to HSA (i.e. at the end of the titration).

$$[HSA] + [Ln] \overset{K}{\rightleftharpoons} [LnHSA] \tag{45}$$

$$[\mathrm{LnHSA}] = \frac{\left([\mathrm{HSA}]_T + [\mathrm{Ln}]_T + 1/K\right) - \sqrt{\left([\mathrm{HSA}]_T + [\mathrm{Ln}]_T + 1/K\right)^2 - 4[\mathrm{HSA}]_T[\mathrm{Ln}]_T}}{2} \tag{46}$$

$$I_{calc} = \frac{1}{[\mathrm{Eu}]_T}\left([\mathrm{Eu}]_T I_{Eu} + \left(I_{EuHSA} - I_{Eu}\right)[\mathrm{EuHSA}]\right) \tag{47}$$

*3.4.2 Determination of the HSA bound **Eu4(a-b)** Hydration State, q*

The relatively high values of the affinity constants are a result of the neutral charge of the dpp complexes, which allows for potential ligation of residual carboxylate groups of the protein to coordinate.[198] In Section 3.3.1 it was determined that the hydration state was $q = 2$ at pH 7.4 for both **Eu.4a** and **Eu.4b**, with the dpp moiety free from the metal centre for ~ 95% of each complex in solution. Therefore, bidentate coordination of such residual carboxylate groups could occur, which would have an effect of the water exchange dynamics of the protein bound chelate following displacement of Gd(III) coordinated water molecules. Lower q values and, therefore, lower relaxivity values of the Gd(III) analogue would be observed.[199, 200]

Luminescent lifetime studies were carried out for both **Eu.4a** and **Eu.4b** in the presence of HSA. The results of which are shown in Table 18. When comparing q values with those of the complex when no HSA is present at pH 7.4, determined as $q = 1.5$ for both **Eu.4a** and **Eu.4b** (Table 16), it is clear to see that inner sphere waters are being displaced by the presence of the protein.

	$k_{(H_2O)}$ (ms^{-1})	$\tau_{(H_2O)}$ (ms)	$k_{(D_2O)}$ (ms^{-1})	$\tau_{(D_2O)}$ (ms)	q
Eu.4a	1.34	0.75	0.75	1.33	0.4
Eu.4b	1.83	0.55	1.05	0.95	0.6

Table 18. First order rate constants, k, excited state lifetime, τ, and measured hydration state values, q, for **Eu.4a** and **Eu.4b** in the presence of HSA (0.7 mM). For full data analysis see Appendix **A6**.

*3.4.3 Competitive Anion Binding Investigations for **Eu.(4a-b)***

Carbonate is the second most abundant anion (~ 20-30 mM) found in human serum after chloride (0.1 M).[201] The anion is known to bind in a bidentate manner to $q = 2$ DO3A-based lanthanide complexes. As both **Eu.4a** and **Eu.4b** have two available coordination sites at pH 7.4 binding to the Eu(III) centre was anticipated (Figure 42).[202] The expected displacement of the inner-sphere waters leads to higher emission intensities and longer excited state lifetimes.

	$k_{(H_2O)}$ (ms^{-1})	$\tau_{(H_2O)}$ (ms)	$k_{(D_2O)}$ (ms^{-1})	$\tau_{(D_2O)}$ (ms)	q
Eu.4a	1.55	0.65	0.63	1.59	0.8
Eu.4b	2.26	0.44	1.26	0.79	0.9

Table 19. First order rate constants, k, excited state lifetime, τ, and measured hydration state values, q, for **Eu.4a** and **Eu.4b** in the presence of carbonate (30 mM) at pH 7.4. For full data analysis see Appendix **A7**.

Table 19 shows the data from lifetime studies in the presence of carbonate at pH 7.4. It can be clearly seen that as the hydration number decreases from q = 1.5 for both **Eu.4a** and **Eu.4b** (Table 16) upon addition of carbonate as coordinated water molecules are being displaced as anionic binding occurs.

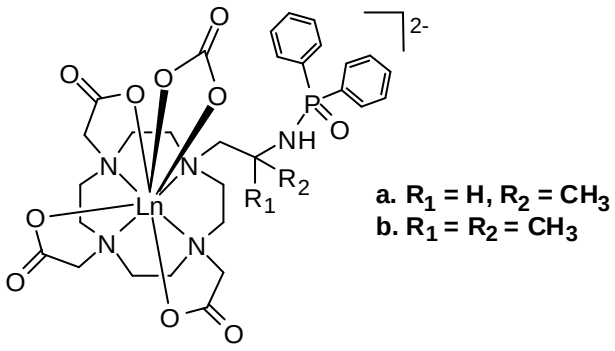

q = 0

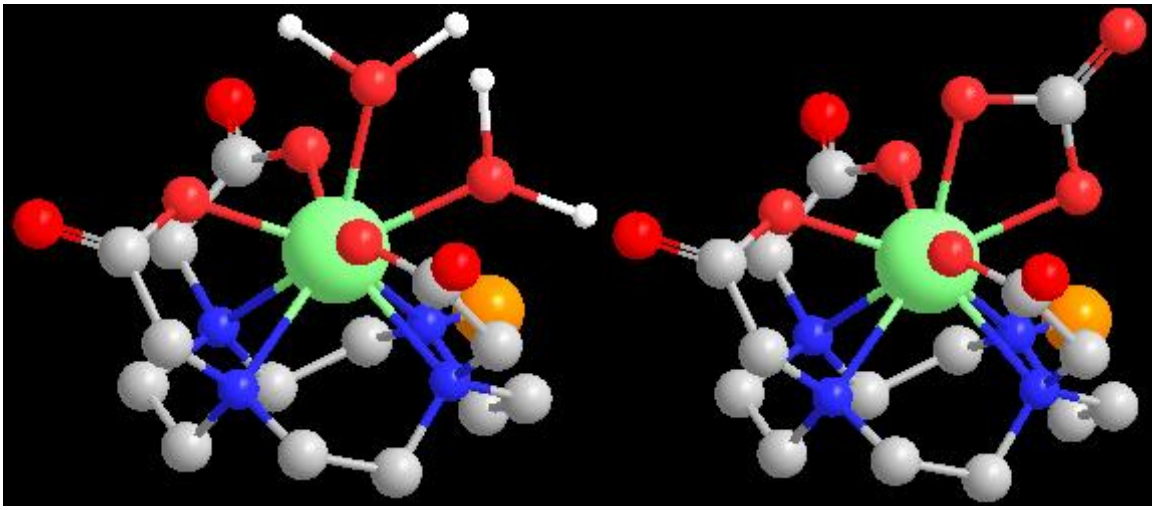

Figure 42. Top: bidentate anion binding of carbonate to **Ln.4(a-b)** complexes. Bottom: three dimensional view of **Ln.4(a-b)** showing coordination of two water molecules (left) and carbonate (right) to the two vacant coordination sites. The dpp moiety is represented by the orange R group.

In order for further investigate the affect of anion binding Eu(III) luminescent emission spectra were recorded in the presence of 30 mM sodium hydrogen carbonate at pH 7.4 (Figures 43 and 44). The spectra clearly show displacement of the coordinated inner-sphere water molecules by anion binding. Eu(III) emission intensity, particularly evident in the ΔJ = 2 band at ~ 615 nm, is increased in the presence of carbonate. Quenching water molecules of the q = 2 complexes are therefore being displaced at pH 7.4 by carbonate, resulting in fewer O–H oscillators bound the Eu(III) centre and therefore reduced vibrational quenching of the Eu(III) excited states, hence greater Eu(III) emission intensity.

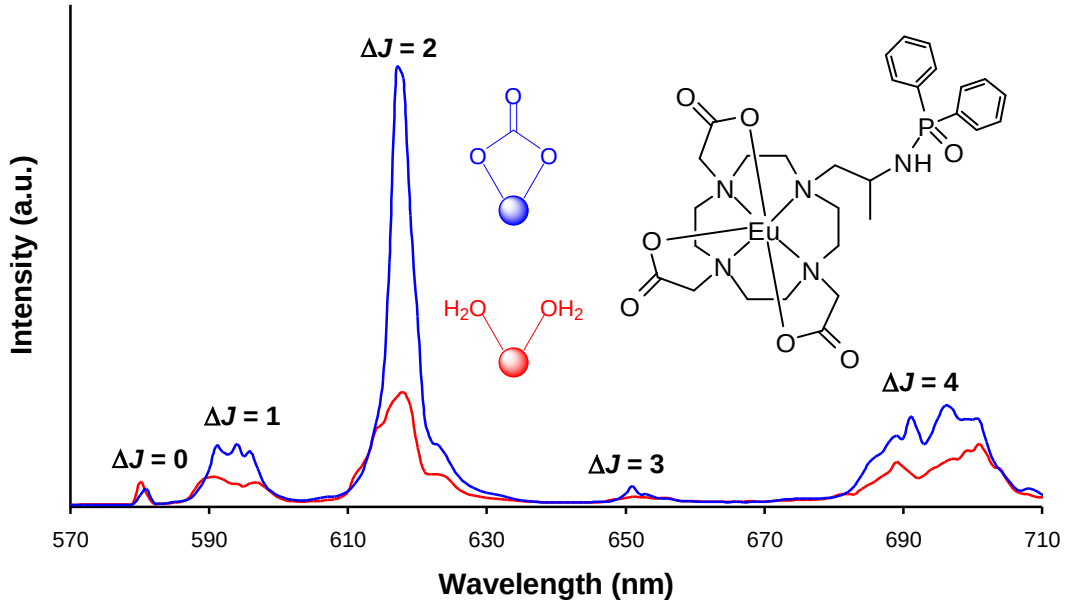

Figure 43. Eu(III) emission spectra for **Eu.4a** in the presence (blue) and absence (red) of carbonate. 1.0 mM **Eu.4a**, 0.1 M NaCl, 30 mM $NaHCO_3$ λ_{ex} = 271 nm, pH 7.4, 25°C.

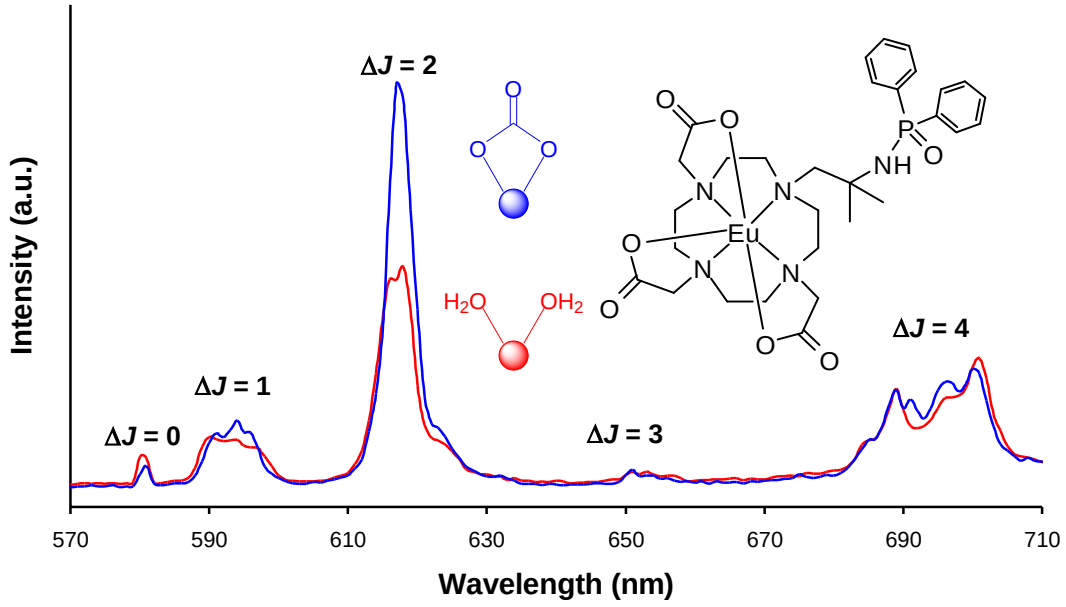

Figure 44. Eu(III) emission spectra for **Eu.4b** in the presence (blue) and absence (red) of carbonate. 1.0 mM **Eu.4b**, 0.1 M NaCl, 30 mM $NaHCO_3$ λ_{ex} = 271 nm, pH 7.4, 25°C.

*3.4.4 Eu(III) Emission Intensity vs. pH for **Eu.(4a-b)** in the Presence of Carbonate*

The Eu(III) emission *vs.* pH plots show a shift in the apparent pK_a of the dpp complexes towards more acidic values in the presence of carbonate (Figure 45 and Table 20). At physiological pH 7.4 it is clear that carbonate binding occurs, resulting in the displacement of quenching inner sphere water molecules, thus increasing Eu(III) emission intensity. The Eu(III) emission *vs.* pH profile comprises the reversible binding of the dpp moiety as well as

competition from carbonate. The equilibrium processes of carbonate are also intrinsic to the observed emission data. The solution pH determines the concentrations of HCO_3^-/CO_3^{2-} present. $[HCO_3^-]$ falls from ~ 90% at pH 8.9 to less < 2% at pH 4.9, and at pH > 9 there are significant quantities of CO_3^{2-} present. The pK_a of the H_2CO_3/HCO_3^- process is 6.4 while the HCO_3^-/CO_3^{2-} process is 10.2.[14]

$$H_2CO_3 \underset{H^+}{\overset{-H^+}{\rightleftharpoons}} HCO_3^- \underset{H^+}{\overset{-H^+}{\rightleftharpoons}} CO_3^{2-} \qquad (48)$$

$$Eu(H_2O)_2 \underset{H^+}{\overset{-H^+}{\rightleftharpoons}} [Eu(H_2O)(dpp)]^- \qquad (49)$$

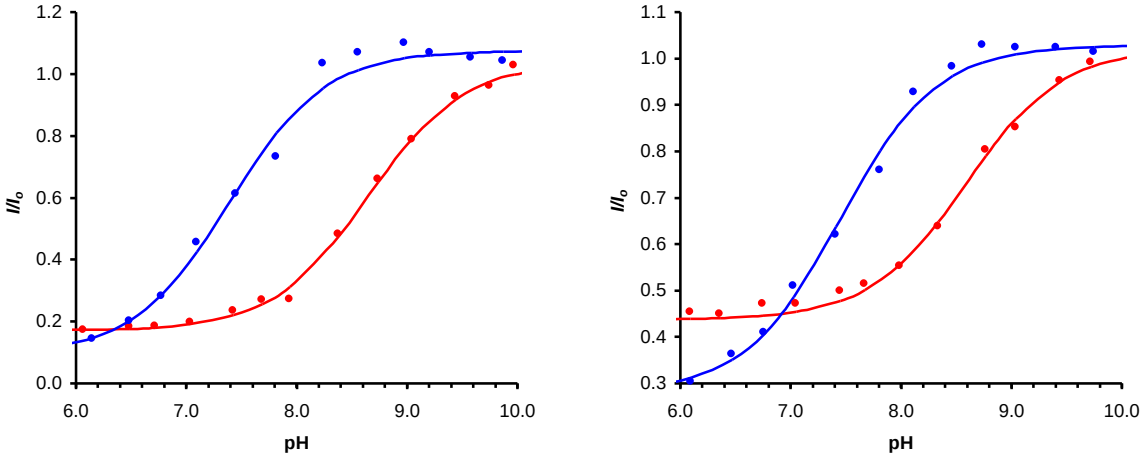

Figure 45. Eu(III) emission intensity (I/I_o $\Delta J = 2$) *vs.* pH for **Eu.4a** (left) and **Eu.4b** (right) showing the experimental data (dots) and the calculated data (line) in the presence (blue) and absence (red) of carbonate. 1.0 mM **Eu.4a**, 0.1 M NaCl, 30 mM $NaHCO_3$, λ_{ex} = 270 nm, 25°C.

	pK_a	Apparent pK_a in 30 mM $NaHCO_3$
Eu.4a	8.65 (± 0.09)	7.39 (± 0.19)
Eu.4b	8.59 (± 0.14)	7.45 (± 0.10)

Table 20. pK_a values in the absence of carbonate (Chapter 1) and the apparent pK_a values in the presence of carbonate for **Eu.4a** and **Eu.4b**

The apparent pK_a values from the $\Delta J = 2$ I/I_o profiles for both **Eu.4a** and **Eu.4b** in the presence of serum concentrations of carbonate are within the physiological pH range. The ratiometric $\Delta J = 2$ / $\Delta J = 1$ plots are shown in Figure 46, from which the apparent pK_as were

measured at 6.59 (± 0.07) and 7.09 (± 0.10) for both **Eu.4a** and **Eu.4b** respectively, allowing for concentration independent determination of pH in serum within the pH range ~ 6 – 8.

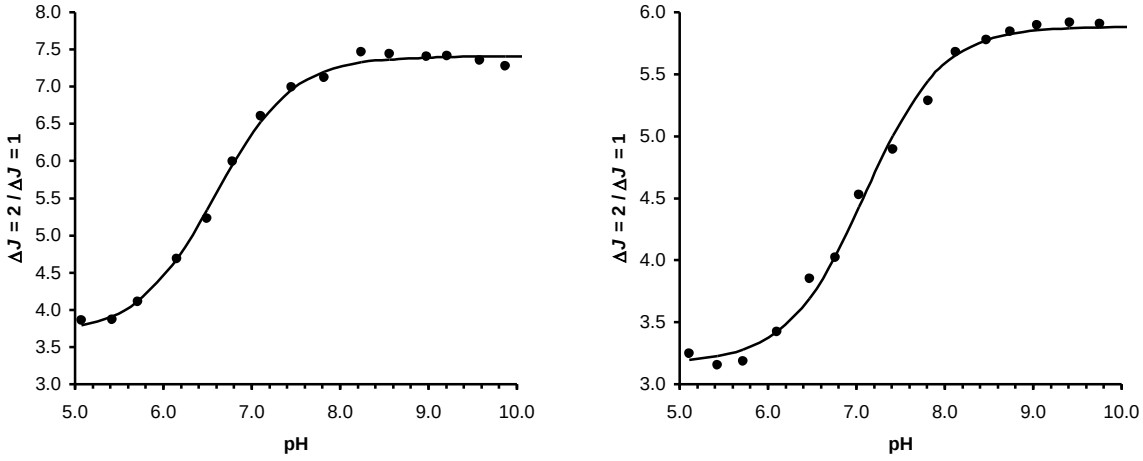

Figure 46. Eu(III) emission intensity ($\Delta J = 2/\Delta J = 1$) *vs.* pH for **Eu.4a** (left) and **Eu.4b** (right) in the presence of carbonate showing the experimental data (dots) and the calculated data (line). 0.1 mM **Eu.4(a-b)**, 0.1 M NaCl, 30 mM $NaHCO_3$ λ_{ex} ~ 270 nm, 25°C.

*3.4.5 Negatively Charged **[Ln.9]$^{3-}$**: A Dpp Complex that Suppress Anion Binding*

Anion binding can be suppressed by the generation of negatively charged Ln(III) complexes. The incorporation of negatively charged side chains to Ln-DO3A based chelates has been shown to inhibit water displacement from both anionic carbonate binding and HSA interaction.[77] In order to achieve this the [Ln-dpp-aDO3A]$^{3-}$ complex **[Ln.9]$^{3-}$** was prepared, which is negatively charged at pH 7.4.

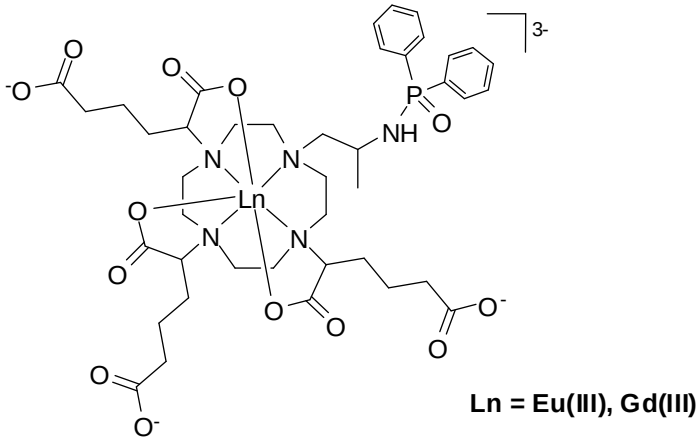

[Ln.9]$^{3-}$

*3.4.6 Preparation of the Negatively Charged Dpp Complex, **[Ln.9]$^{3-}$***

The synthesis of **9** was similar to that of the previous dpp pro-ligands (Chapter 2, Section 2.4.2), which involved aziridine ring opening.[157, 158] However, macrocycle **2** was replaced by the tris-adipate containing macrocycle **6**, which was prepared following literature

procedures (Scheme 12).[134] 2-Bromoadipic acid dimethyl ester, **5**, was also prepared following literature preparations and involved the reaction of adipic acid mono-methyl ester with thionyl chloride. Bromination and esterification was achieved by the addition of bromine under reflux, followed by methanol.[203] The reaction of cyclen with **5** yielded both the tris-adipate macrocycle, **6**, and the tetra-adipate containing macrocycle, **7**, the use of which is discussed in more detail in Chapter 4.

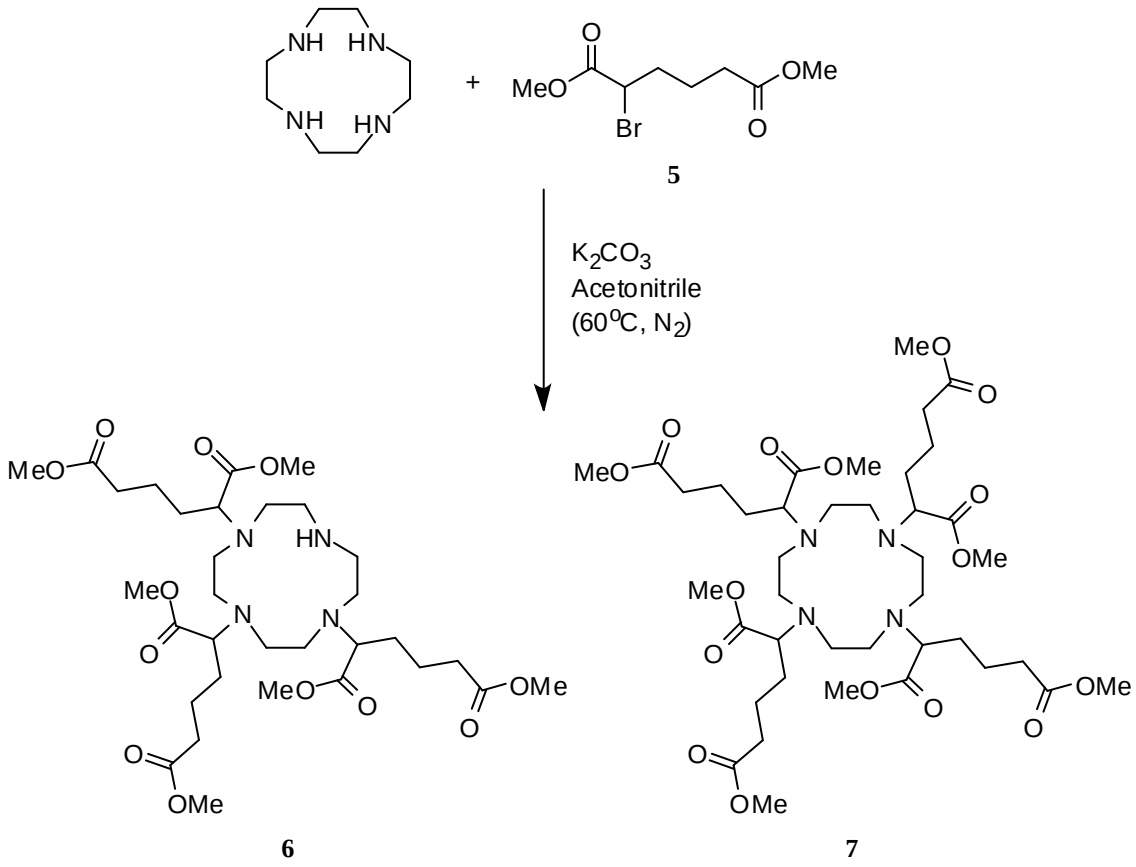

Scheme 12

The aziridine ring opening reactions were carried out in a similar manner to those for compounds **4a** although it was necessary for the reaction to be heated at reflux in acetonitrile, presumably due to increased steric hindrance around the macrocyclic ring. Poor yields (~ 14%) were obtained.

The preparation of the bis-methyl analogue *via* ring opening of aziridine **1b** was attempted. Despite carrying out the reaction in various solvents and at a range of temperatures, the ring-opening step proved difficult, with extremely poor yields obtained.

The lithium hydroxide deprotection and complexation steps were carried out in a similar fashion as previously (Scheme 13). Due to the multiple negative charge of the complex, monitoring of the reaction *via* ESMS proved to be difficult, therefore the reaction

was left at 80°C for 24 hours to ensure full complexation had taken place. The resulting Eu(III) and Gd(III) products were characterised by MALDI mass spectrometry once purified.

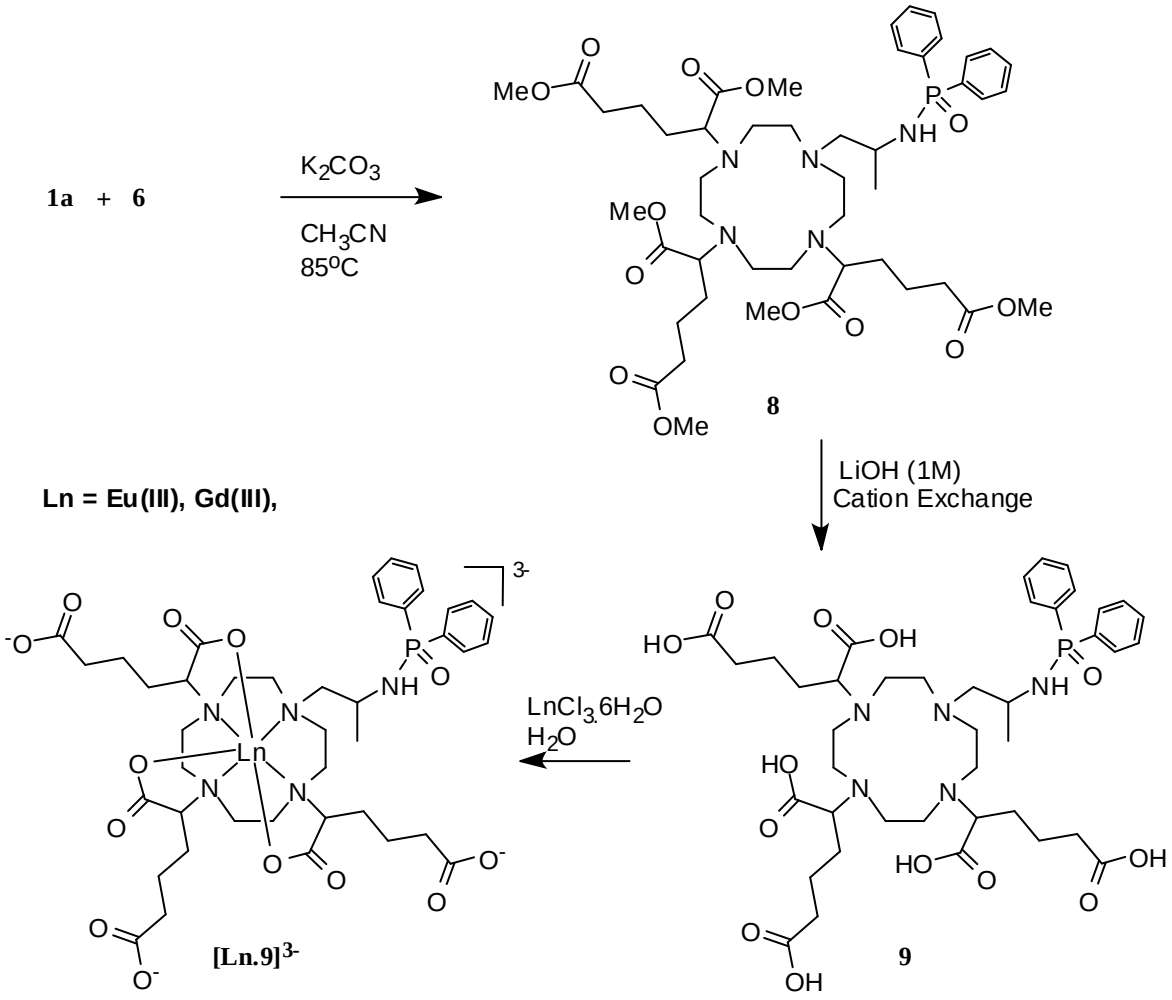

Scheme 13

3.4.7 Eu(III) Emission Intensity vs. pH for ***[Eu.9]$^{3-}$***

Luminescent emission spectra were recorded for the negatively charged **[Eu.9]$^{3-}$**. No pH dependence was observed following direct Eu(III) excitation at λ_{ex} = 395 nm. This is perhaps not surprising as the negatively charged adipates are likely to be suppressing reversible binding from the deprotonated dpp moiety. Sensitization following excitation of the dpp chromophore at λ_{ex} ~ 270 nm, therefore, was very poor as the chromophore remained free from the Eu(III) centre. However, an interesting observation was the pH dependence following sensitization *via* the dpp chromophore. A change in excitation spectra was observed between acidic and basic media. As the dpp oxygen becomes protonated in acidic media the change in electronic state of the chromophore causes a shift in the excitation wavelength maxima from λ_{ex} = 268 nm (pH 10) to λ_{ex} = 280 nm (pH 5), which was not observed for the neutral **Eu.4a** (Figure 47). The lowering of the chromophores singlet excited state energy as absorption shifts to longer wavelengths results in better overlap of the chromophore triplet

excited state with the ^5D_o excited state Eu(III), causing more efficient energy transfer and an increase in emission intensity.

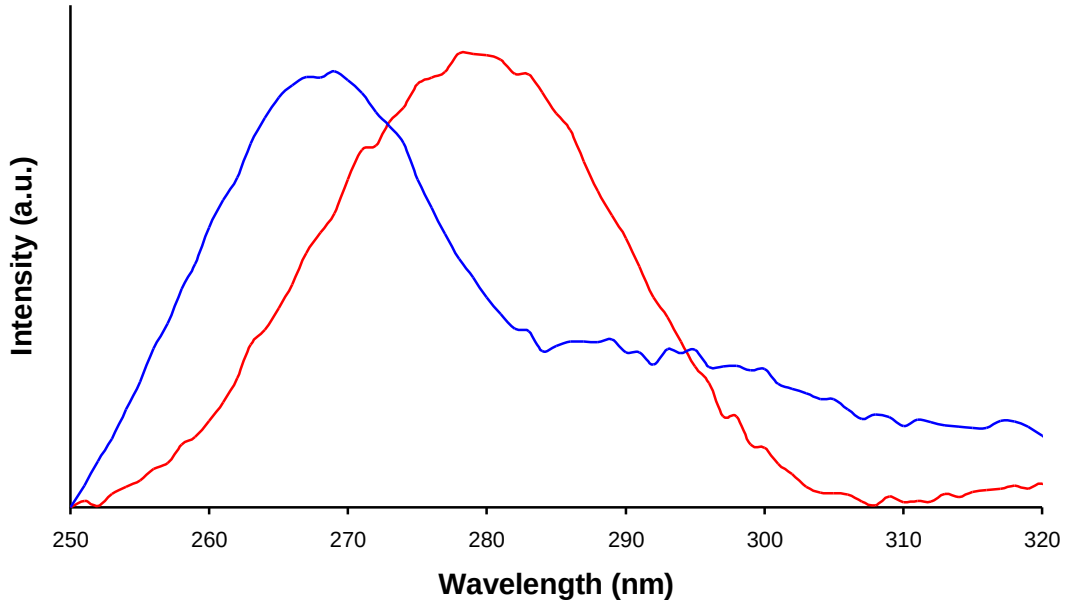

Figure 47. Excitation spectra for **[Eu.9]**$^{3-}$ at pH 10.23 (blue) and pH 5.01 (red). 1.0 mM **[Eu.9]**$^{3-}$, 0.1 M NaCl, 25°C.

Emission intensity *vs*. pH titrations were carried out with the excitation wavelength at both λ_{ex} = 395 nm (direct excitation of Eu(III)) and at λ_{ex} = 268 nm (sensitised *via* the dpp). The sensitised emission spectra showed an interesting trend as pH was lowered to acidic conditions (Figure 48).

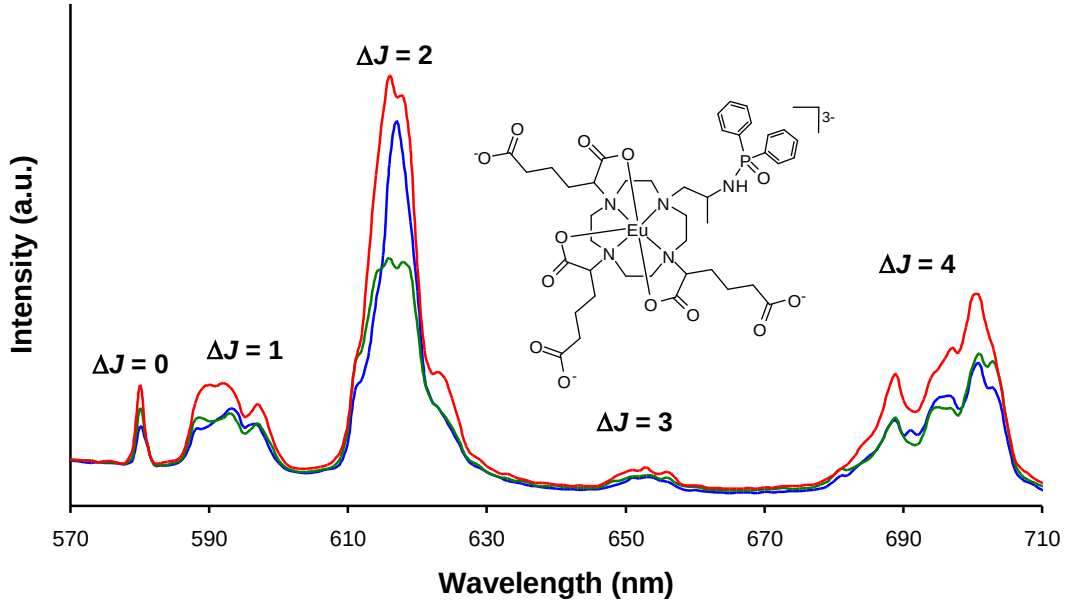

Figure 48. Eu(III) emission spectra for **[Eu.9]**$^{3-}$ at pH 10.23 (blue), pH 7.48 (green) and pH 5.01 (red). 1.0 mM **[Eu.9]**$^{3-}$, 0.1 M NaCl, λ_{ex} = 268 nm, 25°C.

An initial drop in the intensity of the $\Delta J = 2$ band (~ 616 nm) was observed at around pH 7.4, which then rose in more acidic conditions as the excitation maxima moved to higher wavelengths and more efficient energy transfer was achieved. The intensity and spectral form of the $\Delta J = 1$ band (~ 593 nm) also varied as pH was lowered. The $\Delta J = 1$ band is susceptible to variations in complex symmetry. Three bands are normally observed for complexes of low symmetry, with two observed for complexes possessing C_3 and C_4.[111] Complex geometry determination was not possible from ^{1}H NMR spectroscopy studies due to the fluxionality of the complex, which lead to spectral line broadening of the obtained ^{1}H NMR spectra. As the complex is DO3MA based it can be confidently hypothesised that the geometry would be in equilibrium between the SAP and TSAP, both of which posses C_4 symmetry through the cyclen nitrogens. There are two $\Delta J = 1$ bands for the major SAP isomer. The appearance of a third, central band is indicative to the presence the minor TSAP isomer.[111] The broadening of the ΔJ=1 band an acidic media suggests a variation in the isomeric composition of the complex in solution upon protonation of the dpp moiety.

The ratio of intensities for both the $\Delta J = 2$ / $\Delta J = 1$ and I/I_o of the $\Delta J = 2$ band *vs.* pH showed similar results arising form the variation in the spectral form following the protonation and deprotonation of the pendant dpp moiety. A dip was observed at pH ~ 8, presumably due to less efficient energy transfer from the dpp moiety to the Eu(III) excited state (Figure 49).

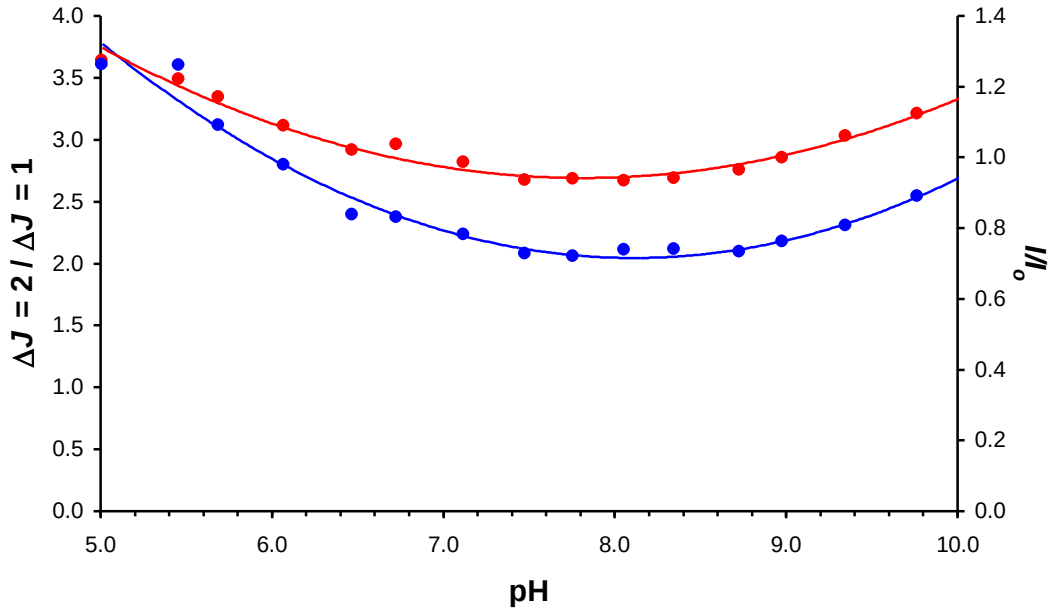

Figure 49. Eu(III) emission intensity *vs.* pH for **[Eu.9]$^{3-}$** showing the experimental data (dots) and the calculated data (line). $\Delta J = 2$ (616 nm) / $\Delta J = 1$ (592 nm) (red) and I/I_o ($\Delta J = 2$) (blue). 0.1 mM **[Eu.9]$^{3-}$**, 0.1 M NaCl, λ_{ex} = 268 nm, 25°C.

No such observations were made following direct excitation of the Eu(III) at λ_{ex} = 395 nm. The dominating factor controlling the Eu(III) emission is the number of quenching Eu(III) water molecules as the effects of sensitisation is now removed. The emission intensity of the ΔJ = 2 band remains the same throughout the titration suggesting that reversible dpp ligation is not occurring. Figure 50 shows the comparison of the I/I_o of the ΔJ = 2 band for both **[Eu.9]**$^{3-}$ and the neutral mono-methyl dpp complex **Eu.4a**. The sigmoidal curve observed for **Eu.4a** following excitation at λ_{ex} = 395 clearly shows the reversible binding nature of the dpp moiety, displacing quenching inner-sphere waters as ligation occurs at higher pH and leading to higher emission intensity in basic media. A slight increase in emission intensity is observed at pH > 9 for **[Eu.9]**$^{3-}$, which can be attributed to the coordination of OH^- in basic media resulting in fewer O–H oscillators present.

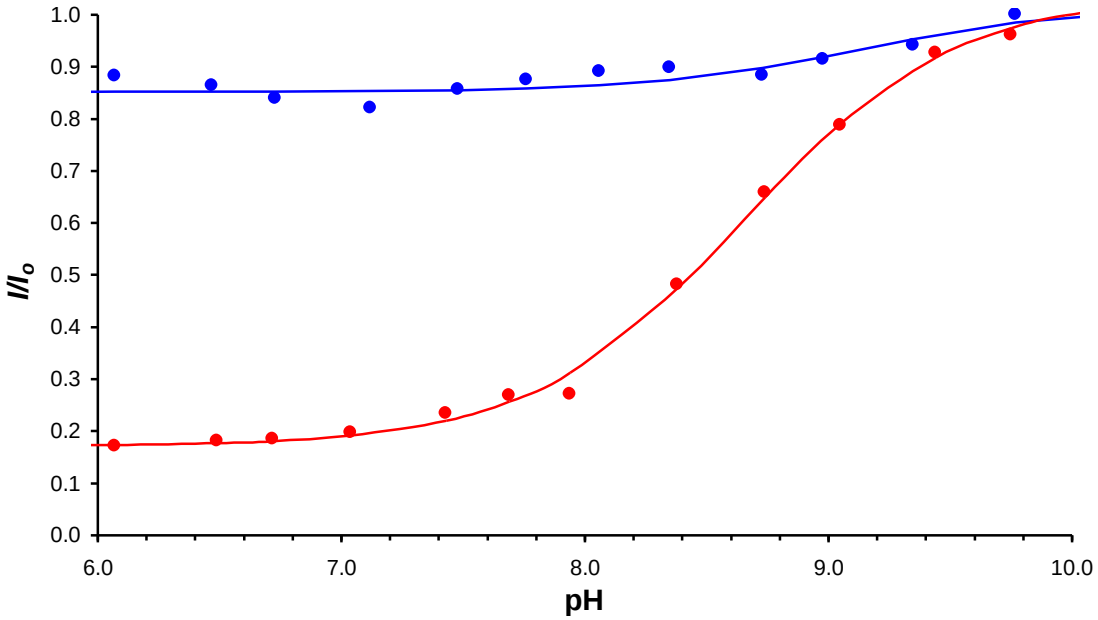

Figure 50. Eu(III) emission intensity (I/I_o $\Delta J = 2$) *vs.* pH for **[Eu.9]**$^{3-}$ (blue) and **Eu.4a** (red) showing the experimental data (dots) and the calculated data (line). 1.0 mM Eu, 0.1 M NaCl, λ_{ex} = 395 nm, 25°C.

3.4.8 Competitive Anion Binding Investigations for ***[Eu.9]***$^{3-}$

As for the neutral analogues, luminescence studies were carried out in the presence of 30 mM sodium hydrogen carbonate. Figure 51 shows that although there is a slight affinity for carbonate at pH 7.4 it is still much lower than for the neutral analogues as a small increase in the intensity of the ΔJ = 2 band is observed upon addition of carbonate. The equilibrium established at pH 7.4 must, therefore, lie more on the side of the q = 2 species as carbonate binding is suppressed by the negative charge of the complex.

Luminescent lifetime studies were carried out to determine the hydration state of **[Eu.9]**$^{3-}$ in both the presence and absence of carbonate at pH 7.4, as well as the measured q

value of the non dpp bearing complex **[Eu.10]**$^{3-}$, which was prepared by the addition of **6** to LiOH prior to the aziridine ring opening reaction, followed by complexation (the use of **[Eu.10]**$^{3-}$ is discussed in greater detail in Chapter 4. The data in Table 21 suggests there may be a slight affinity for carbonate at pH 7.4 as the hydration state values decrease slightly from q = 1.7 to q = 1.5 as carbonate is added. A similar trend was observed for **[Eu.10]**$^{3-}$ albeit to a lesser degree, which suggests that steric factors of the dpp moiety effect the coordination of both the inner-sphere water molecules and carbonate.

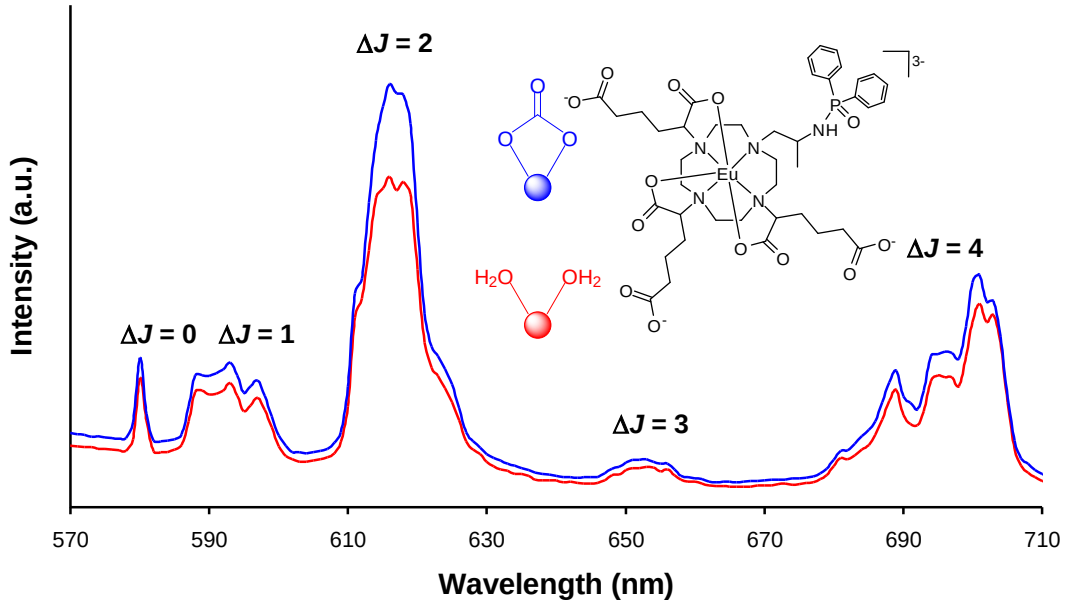

Figure 51. Eu(III) emission spectra for **[Eu.9]**$^{3-}$ in the presence (blue) and absence (red) of carbonate. 1.0 mM **[Eu.9]**$^{3-}$, 0.1 M NaCl, 30 mM $NaHCO_3$ λ_{ex} = 268 nm, pH 7.4, 25°C.

	$k_{(H_2O)}$ (ms^{-1})	$\tau_{(H_2O)}$ (ms)	$k_{(D_2O)}$ (ms^{-1})	$\tau_{(D_2O)}$ (ms)	q
[Eu.9]$^{3-}$ No $NaHCO_3$	2.41	0.42	0.74	1.3	1.7
[Eu.9]$^{3-}$ 30 mM $NaHCO_3$	2.19	0.46	0.74	1.36	1.5
[Eu.10]$^{3-}$ No $NaHCO_3$	3.34	0.30	1.38	0.73	2.1
[Eu.10]$^{3-}$ 30 mM $NaHCO_3$	3.26	0.31	1.38	0.72	2.0

Table 21. First order rate constants, k, excited state lifetime, τ, and measured hydration state values, q, for **[Eu.9]**$^{3-}$ and **[Eu.10]**$^{3-}$ in the presence and absence of carbonate (30 mM) at pH 7.4. For full data analysis see appendix **A8** and **A9**.

*3.4.9 Eu(III) Emission Intensity vs. pH for **[Eu.9]**$^{3-}$ in the Presence of Carbonate*

The Eu(III) emission *vs.* pH titration in the presence of carbonate shows the repulsion affect on carbonate when comparing the data with the neutral analogues (Figure 52). The

apparent pK_a in the presence of carbonate is calculated at a more basic value for the negatively charged complex **[Eu.9]$^{3-}$** (Table 22). At physiological pH 7.4 it is clear that carbonate binding is disfavoured due to the increase in the electrostatic repulsion, which occurs following the introduction of negative charge into the complex.

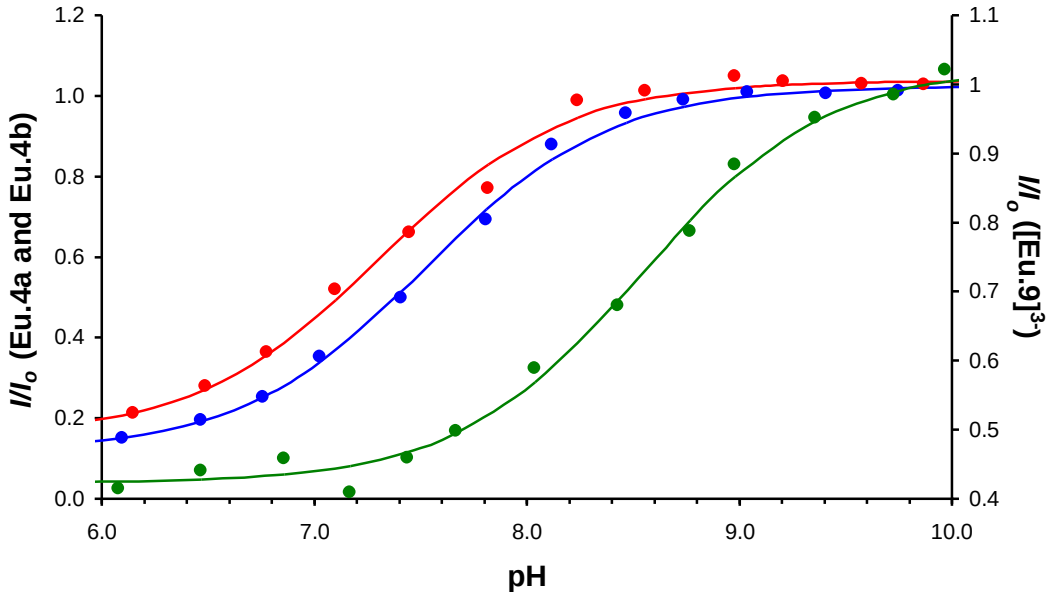

Figure 52. Eu(III) emission intensity (I/I_o $\Delta J = 2$) *vs*. pH for **[Eu.9]$^{3-}$** (green), **Eu.4a** (red) and **Eu.4b** (blue) showing the experimental data (dots) and the calculated data (line) in the presence of carbonate. 1.0 mM Eu, 0.1 M NaCl, 30 mM $NaHCO_3$, λ_{ex} = 271 nm, 25°C.

	pK_a	Apparent pK_a in 30 mM $NaHCO_3$
Eu.4a	8.65 (± 0.09)	7.39 (± 0.19)
Eu.4b	8.59 (± 0.14)	7.45 (± 0.10)
[Eu.9]$^{3-}$	-	8.53 (± 0.06)

Table 22. pK_a values in the absence of carbonate (Chapter 1, Section 2.5.2) and the apparent pK_a values in the presence of carbonate for **Eu.4a**, **Eu.4b** and **[Eu.9]$^{3-}$**.

*3.4.10 Eu(III) Emission Intensity vs. [HSA] for **[Eu.9]$^{3-}$***

The hydrophobic dpp moiety is always remote from the Eu(III) centre. The luminescence *vs*. pH titration shows this, therefore binding to HSA should occur in a similar manner to that of the neutral analogues. Greater protein binding affinities might be expected due to the presence of the anionic side chains encountering possible electrostatic interaction with the abundant positively charged lysine residues on the surface of the protein.[179]

Figure 53 shows the change in luminescence *vs*. [HSA]. As for the neutral analogues, the emission intensity of the ΔJ = 2 band decreased upon addition of HSA as the energy

transfer from the dpp moiety to the Eu(III) excited state was quenched. The data was then used to calculate a the affinity constant, *K*, as 17,915 ± 14% M^{-1}, which is slightly lower than the neutral analogues as now only 91.2% of complex is bound under imaging concentrations and physiological conditions (0.1 mM **[Eu.9]**$^{3-}$, 0.67 mM HSA, pH 7.4). The observed *K* is lower than what was expected and may be due to the increased size of the complex sterically hindering protein binding. A second possibility is that the coordination of residue carboxylate groups to the metal centres of both neutral complexes **Eu.4a** and **Eu.4b** is quite strong, which enhances their binding affinity, while no such carboxylate interaction occurs for **[Eu.9]**$^{3-}$.

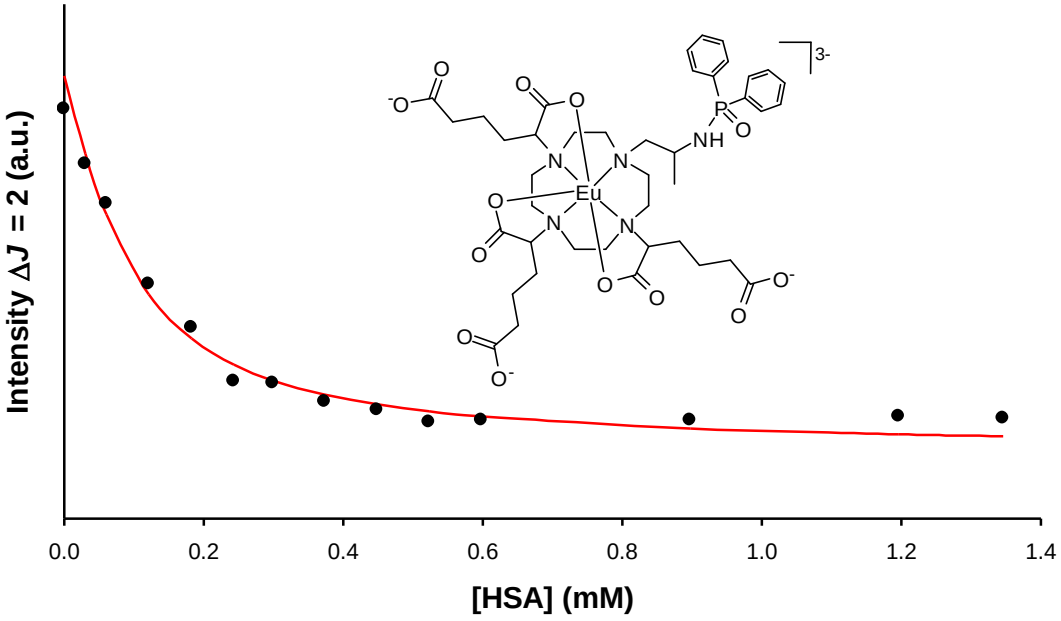

Figure 53. Plot of Δ*J* = 2 Eu(III) emission intensity *vs*. [HSA] for **[Eu.9]**$^{3-}$ showing the experimental data (black dots) and the calculated data (red line). ~ 0.1 mM **[Eu.9]**$^{3-}$, 0.1 M NaCl, pH 7.4 (0.2 M PBS), 25°C.

Luminescent lifetime measurements were carried out, which show that some water displacement is occurring as hydration state value was measured as q = 1.0 suggesting some carboxylate binding may be taking place. The short chain dpp moiety would be holding the Eu(III) chelate in close proximity with the protein, which may be causing hydrogen bonding interaction with the residual groups on the protein surface. This would affect the calculation q values as variations in the O–H oscillators coordinated to the Eu(III) centre would be present. (For full data analysis see Appendix **A10**).

3.5 Relaxometric Investigation of the Binding of Gd(III) dpp Complexes with HSA

*3.5.1 Relaxivity vs. [HSA] for **Gd.4(a-b)***

As MRI contrast agents bind to large slowly tumbling proteins, relaxivity is enhanced. A high affinity for HSA has been observed for the Eu(III) dpp containing complexes and, therefore, the Gd(III) analogues were also prepared to see if binding took place with a similar affinity and if so, to see the observed relaxivity enhancement.

Relaxivity *vs*. [HSA] titrations were carried out in the same manner as for the Eu(III) complexes, only now relaxation rate measurements were used instead of luminescent emission. The observed relaxation rates increased upon addition of HSA. This is as expected due to the increased rotational correlation time, τ_R, of the protein bound complex (Figure 54).

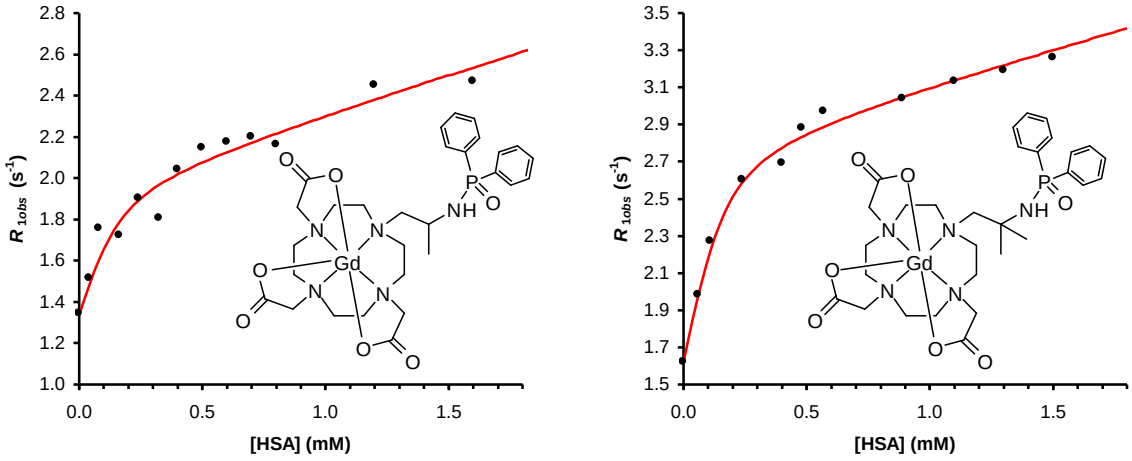

Figure 54. Plot of the observed longitudinal relaxation rate, R_{1obs}, *vs*. [HSA] for **Gd.4a** (left) and **Gd.4b** (right) showing the experimental data (black dots) and the calculated data (red line). ~ 0.1 mM **Gd.4(a-b)**, 0.1 M NaCl, pH 7.4 (0.2 M PBS), 20 MHz, 25°C.

The data analysis was carried out in a similar manner to that of the Eu(III) analogues (Table 23). In order to define the concentration of the HSA bound Gd(III) species in terms of its longitudinal relaxation rate, R_{1calc}, Equation 50 was used, where R_{1Gd} is the observed longitudinal relaxation rate of the Gd(III) complex in the absence of HSA (i.e. at the start of the titration) and R_{1GdHSA} is the observed longitudinal relaxation rate of the Gd(III) when entirely bound to HSA (i.e. at the end of the titration) and $[HSA]_T$ and $[Gd]_T$ are the total concentrations of HSA and the Gd(III) complex.[197]

$$R_{1calc} = \frac{1}{[\mathrm{Gd}]_T}\left([\mathrm{Gd}]_T R_{1Gd} + \left(R_{1GdHSA} - R_{1Gd}\right)[\mathrm{GdHSA}]\right) \qquad (50)$$

	K (M^{-1})	% Bound	r_1 unbound ($mM^{-1}s^{-1}$)	r_1 bound ($mM^{-1}s^{-1}$)
Gd.4a	21,000	92.4	7.1	11.7
Gd.4b	26,000	93.7	6.5	16.0

Table 23. HSA affinity constants, *K*, for **Gd.4a** and **Gd.4b** and percentage of compound bound to HSA at imaging concentrations (0.67 mM HSA, 0.1 mM Gd) at pH 7.4 (0.2 M PBS) as well as relaxivities, r_1, and of the bound of the unbound species (i.e. 1.8 mM HSA).

The affinity constants calculated from the relaxivity data in Figure 54 are similar to those calculated from luminescence, showing a relatively high affinity for HSA. The bis-methyl complex **Gd.4b** shows a higher relaxivity when bound to the protein, displaying ~ 146% increase in relaxivity compared to the unbound complex. It is likely that the independent rotation of the bis-methyl containing complex **Gd.4b** is lower the mono-methyl analogue **Gd.4b** due to the increased rigidity of the dpp moiety caused by the addition of the second methyl group, resulting in the greater relative enhancement in relaxivity.

*3.5.2 NMRD Profiles of **Gd.4(a-b)** in the Presence of HSA*

In order to fully see the effect protein binding has on relaxivity, NMRD profiles were recorded for each complex in both the presence and absence of HSA (Figures 55 and 56).

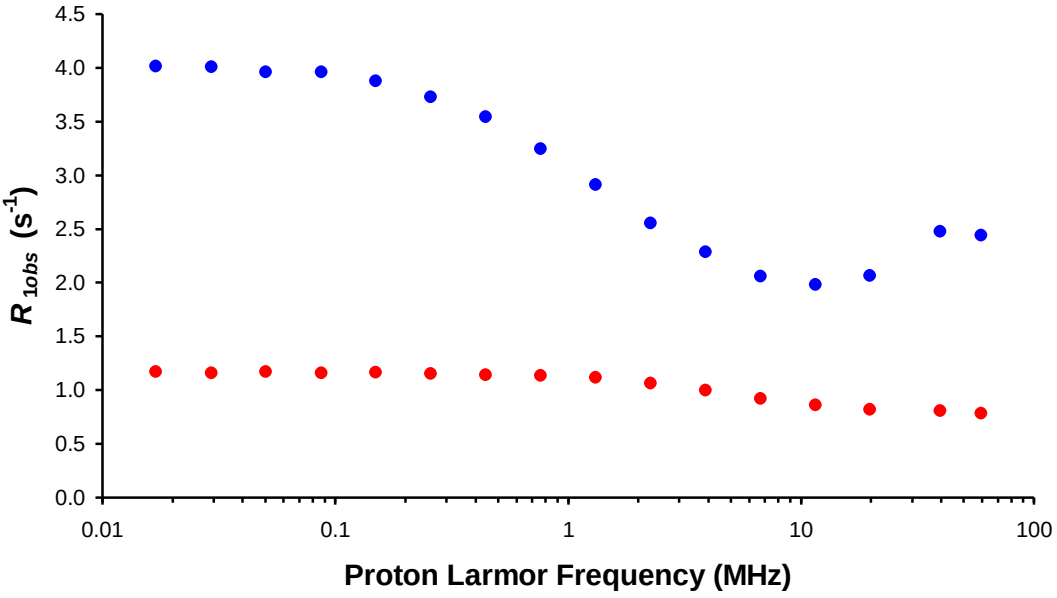

Figure 55. NMRD profiles of **Gd.4a** in the presence (blue) and absence (red) of HSA. 1.0 mM **Gd.4a**, 1.8 mM HSA, 0.1 M NaCl, pH 7.4 (0.2 M PBS), 25°C.

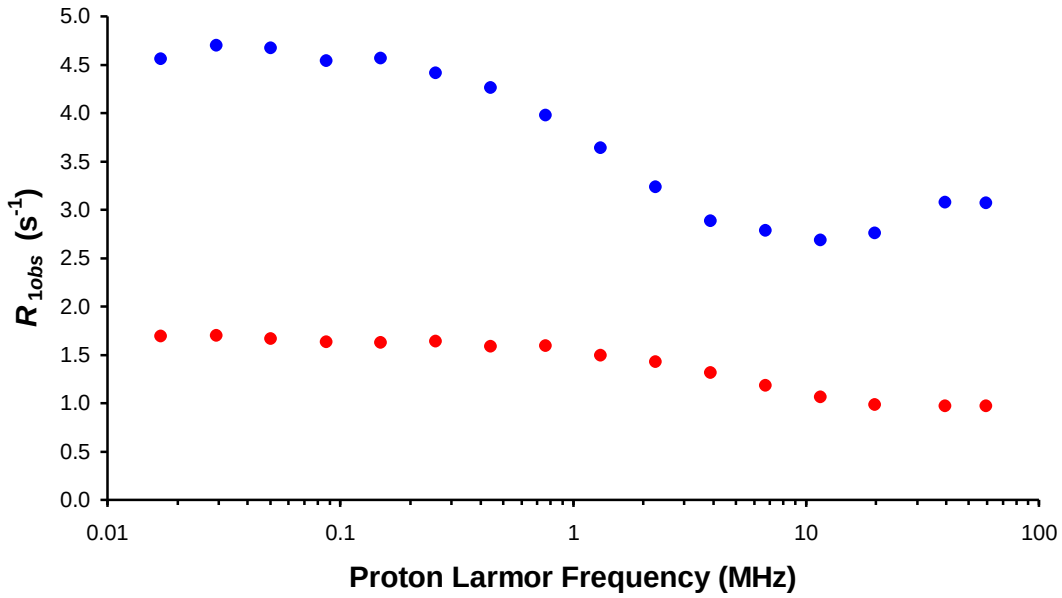

Figure 56. NMRD profiles of **Gd.4b** in the presence (blue) and absence (red) of HSA. 1.0 mM **Gd.4b**, 1.8 mM HSA, 0.1 M NaCl, pH 7.4 (0.2 M PBS), 25°C.

The profiles show there is an increase in observed relaxation rate upon addition to HSA, but most importantly, there is specific increase at between 20-60 MHz for the bound complexes, which is not apparent for the unbound species. This is indicative of a Gd(III) complex showing slow motional tumbling and, therefore, an increased rotational correlation time, τ_R. As discussed in Chapter 1, Section 1.3.7, at MRI operating frequencies 20-60 MHz T_1 is dominated by τ_R. Higher observed relaxation rates are therefore observed for the HSA bound complex as τ_R is increased following the reduction of the overall global motion of the Gd(III) complex.

3.5.3 Relaxivity vs. [HSA] for ***[Gd.9]$^{3-}$***

The relaxivities of the R and S-enantiomers of the dpp moiety of the negatively charged **[Gd.9]$^{3-}$** were measured in both the presence and absence of HSA (Table 24). (A more detailed description of the motives behind preparation of the dpp enantiomers of these complexes is discussed in Section 3.6).

	r_1 unbound ($mM^{-1}s^{-1}$)	r_1 bound ($mM^{-1}s^{-1}$)
[Gd.9(R)]$^{3-}$	9.6	15.8
[Gd.9(S)]$^{3-}$	9.5	16.0

Table 24. Measured relaxivities, r_1, of **[Gd.9(R)]$^{3-}$** and **[Gd.9(S)]$^{3-}$** both bound to and free from HSA**.** 0.1 mM Gd, 1.8 mM HSA, 0.1 M NaCl, 20 MHz, pH 7.4 (no buffer), 25°C.

A 68% increase in relaxivity was observed upon binding of the **[Gd.9]$^{3-}$** complex dpp enantiomers to HSA. This relative increase was not as great as was hoped, showing similar values to the HSA bound neutral bis-methyl complex, **Gd.4b**. The values are, however, ~ 36% greater than those observed for the neutral, mono-methyl analogue, **Gd.4a**. Independent rotation of the protein bound mono-methyl species results in a decrease in observed relaxivity. The high binding affinities of the complexes as well as the short chain hydrophobic dpp moieties may result in the Gd(III) chelate being in close proximity with the surface of the protein. Hydrogen bonding between residual protein groups and exchanging water molecules may be occurring as a result of this, which in turn would affect the water exchange dynamics of the Gd(III) complexes, reducing observed relaxivities.[196]

3.6 Luminescent Investigation of the Binding of Eu(III) dpp Complex Enantiomers to HSA

As the binding affinities and properties of both the bis-methyl and the mono-methyl dpp-containing neutral complexes varied, it was hypothesised that similar differences may occur for the R and S-enantiomers of the pendant dpp moieties of the mono-methyl dpp complexes **Ln.4aR/S** and **[Ln.9R/S]$^{3-}$**.

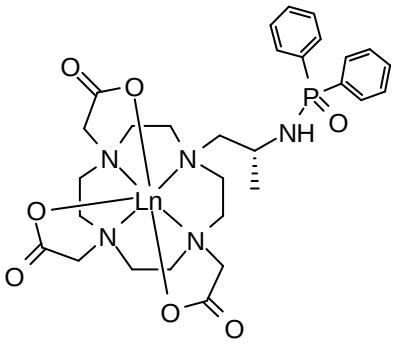

Ln.4a(R)

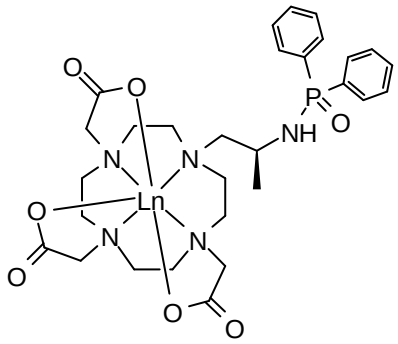

Ln.4a(S)

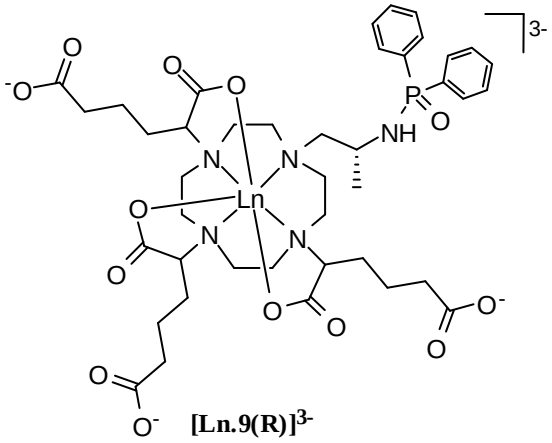

[Ln.9(R)]$^{3-}$

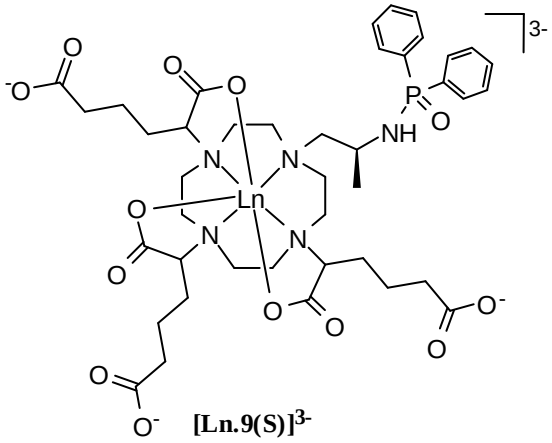

[Ln.9(S)]$^{3-}$

Ln = Eu(III), Gd(III)

Vander Elst and co-workers demonstrated the R and S-enantiomers of the HSA binding complex Gd-((R/S)-EOB-DTPA) possess differing binding affinities for HSA. The ligand incorporates an ethoxybenzyl (EOB) group in the C^5 position of the DTPA chelate, which becomes chiral upon addition of the pendant moiety. The S-enantiomer (Eovist®) has been shown to bind to HSA with a greater affinity than the R-enantiomer.[204]

Synthesis of each complex was conducted following the same methods as previously used, however, enatiomerically pure aziridines were prepared and employed in the ring opening steps. Commercially available R-2-amino-1-propanol and S-2-amino-1-propanol were used to form enantiomerically pure aziridines **1a(R)** and **1a(S)** in good yields following the methods described in Chapter 2.

*3.6.1 Eu(III) Emission Intensity vs. [HSA] for **Eu.4a(R/S)***

Luminescent emission *vs*. [HSA] titrations were carried out for the Eu(III) analogues of the neutral, enantiopure dpp complexes described in Section 3.4.1 in order to determine affinity constants, *K*, (Figure 57 and Table 25).

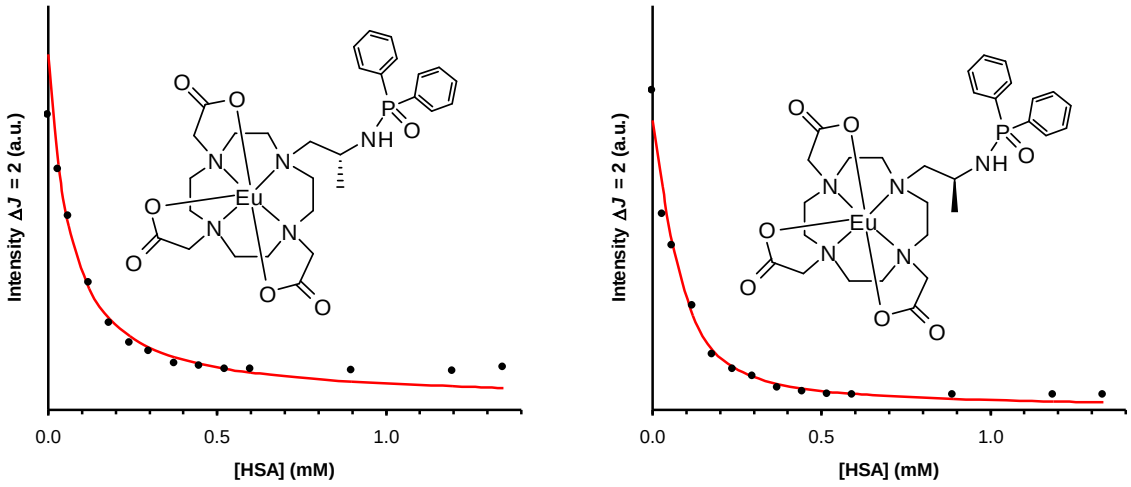

Figure 57. Plot of ΔJ = 2 Eu(III) emission intensity *vs*. [HSA] for **Eu.4a(R)** (left) and **Eu.4a(S)** (right) showing the experimental data (black dots) and the calculated data (red line). ~ 0.1 mM **Eu.4a(R/S)**, 0.1 M NaCl, pH 7.4 (0.2 M PBS), 25°C.

	K (M^{-1})	% Bound
Eu.4a(R)	19,432 (± 9%)	91.8
Eu.4b(S)	38,309 (± 15%)	96.5

Table 25. HSA affinity constants, *K*, for **Eu.4a(R)** and **Eu.4(S)** and percentage of compound bound to HSA at imaging concentrations (0.67 mM HSA, 0.1 mM Eu) at pH 7.4 (0.2 M PBS).

The calculated affinity constants show a much higher affinity to HSA for the S-enantiomer than for the R. As there are two main binding sites on the protein (denoted site I

and site II, Section 3.2.1)[177, 178] it was hypothesised that the S-enantiomer of the dpp moiety can bind to either site while the R only binds to one site. The existence of two enantiomeric species, each with differing affinities for HSA may explain the relatively poor data fit observed for the determination of *K* for the racemic complex **Eu.4a** (Section 3.4.1).

3.6.2 Binding Site Determination using Dansylsarcosine and Warfarin Fluorescent Probes

Warfarin and dansylsarcosine are fluorescent probes, which bind site specifically to HSA and whose fluorescence is enhanced upon binding. Warfarin binds exclusively to site I and displays an increase in emission intensity at λ_{max} = 385 nm upon biding when exciting at λ_{ex} = 320 nm.[178, 205] Dansylsarcosine, however, binds exclusively to site II. Upon excitation at 360 nm, dansylsarcosine emission occurs at λ_{max} = 565 nm in the absence of HSA.[177] Upon binding to site II, the emission wavelength shifts to λ_{max} = 480 nm. The probe's emission intensity is monitored at fixed concentrations in the presence of HSA. Upon addition of a HSA binding species, the emission intensity of the probe decreases due to the competition for the protein binding site.

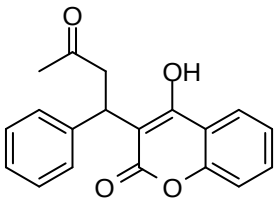

Warfarin

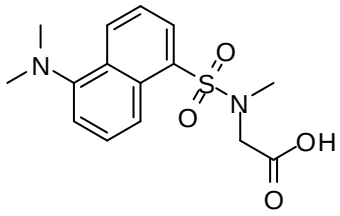

Dansylsarcosine

Competitive binding studies were carried out for both dpp enantiomer bearing complexes **Gd.4a(R)** and **Gd.4a(S)**. The emission spectra were recorded at fixed HSA and probe concentrations ([HSA] = [probe] = 5 μM ~ K_d) with [Gd] ranging from 1 μM to 1000 μM (Figures 58 and 59). The Gd(III) analogues were employed in these experiments to avoid the potential energy transfer processes that may occur between the probe and the Eu(III) analogues' excited states.

It is clear from the data plotted in Figures 58 and 59 that the R-enantiomer of the dpp pendant group binds exclusively to site II of the protein, while the S-enantiomer is binding to both sites, as both warfarin and dansylsarcosine are being displaced, resulting in a drop in their emission intensities. Table 26 shows the inhibition constants for each enantiomer, clearly showing the S-enantiomer to have a greater affinity for site II over site I as the measured K_i values are lower (i.e. less Gd(III) complex required to displace probe). There also is a greater affinity for the S-enantiomer over the R-enantiomer for site II binding. This fits with the overall higher affinity constants observed for this species. It is not surprising that site II is the

preferred binding site for such complexes as the binding affinity towards neutral charged, aromatic containing binding moieties is favoured, while site I tends to bind anionic, heterocyclic binding moieties.[179] The results are comparable to those reported for the site II binding MRI contrast agent MS-325 (Vasovist®), whose inhibition constant for dansylsarcosine was measured at K_i = 85 ± 3.0% μM.[187]

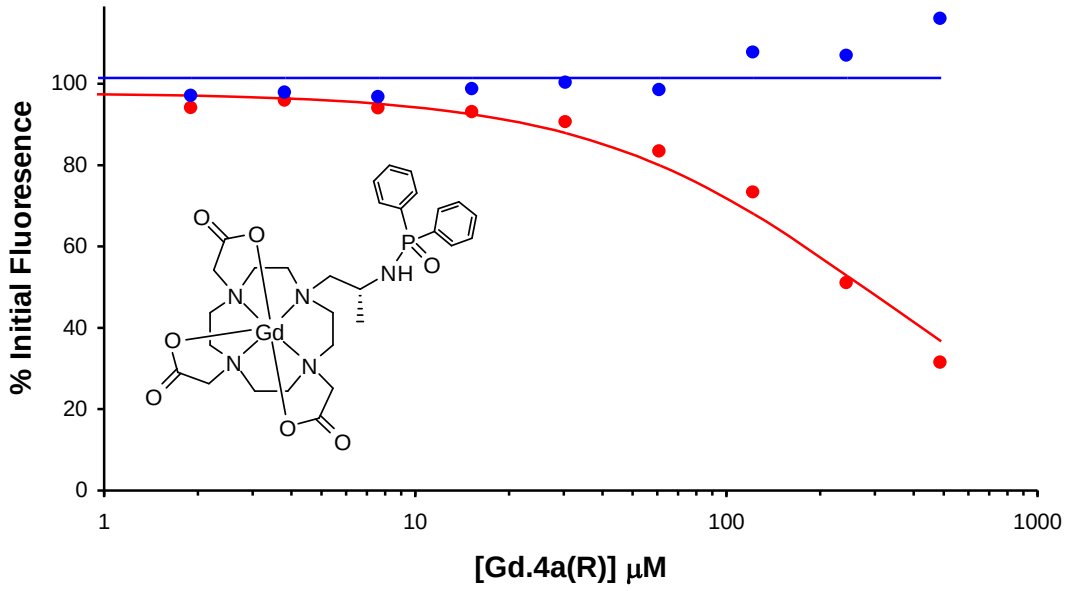

Figure 58. Fluorescent probe displacement curves for **Gd.4a(R)** showing the experimental data (dots) and the calculated data (lines) for dansylsarcosine (red) and warfarin (blue). 5 μM HSA, 5 μM probe, 0.1 M NaCl, pH 7.4 (50 mM HEPES), 25°C.

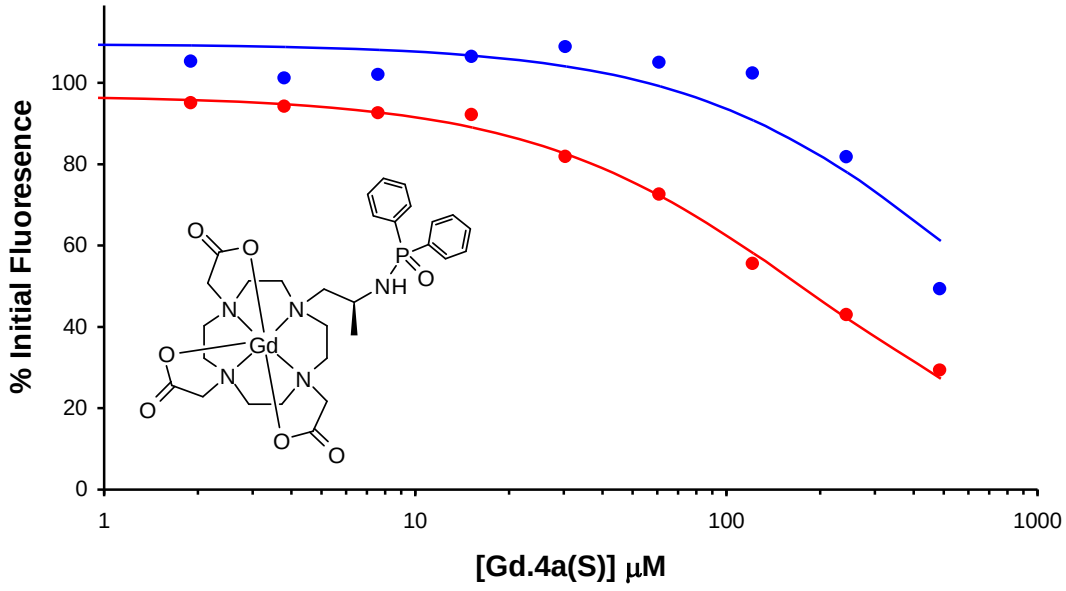

Figure 59. Fluorescent probe displacement curves for **Gd.4a(S)** showing the experimental data (dots) and the calculated data (lines) for dansylsarcosine (red) and warfarin (blue). 5 μM HSA, 5 μM probe, 0.1 M NaCl, pH 7.4 (50 mM HEPES), 25°C.

	K_i dansylsarcosine (μM)	K_i warfarin (μM)
Gd.4a(R)	118 (± 2.0%)	-
Gd.4a(S)	76 (± 1.8%)	252 (± 6.0%)

Table 26. Measured inhibition constants, K_i, for **Gd.4a(R)** and **Gd.4a(S)** for dansylsarcosine and warfarin displacement.

The titrations were repeated for the bis-methyl dpp compound **Gd.4b**, as well as for the R and S-enantiomers of the pendant dpp group of **[Gd.9]$^{3-}$**, none of which showed any warfarin displacement (Figure 60 and Table 27).

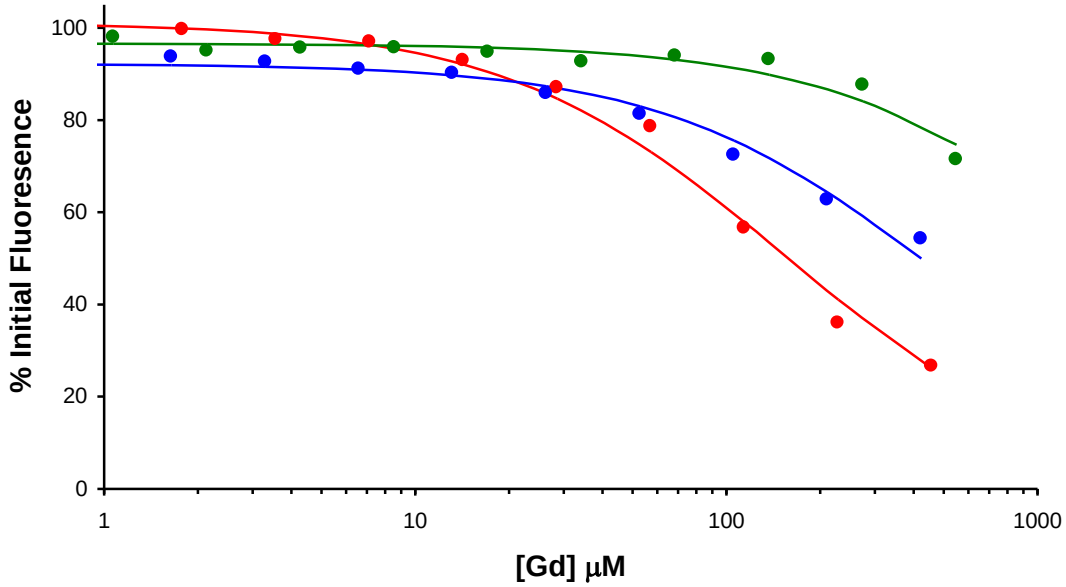

Figure 60. Dansylsarcosine displacement curves for **Gd.4b** (red), **[Gd.9(R)]$^{3-}$** (blue) and **[Gd.9(S)]$^{3-}$** (green) showing the experimental data (dots) and the calculated data (lines). 5 μM HSA, 5 μM dansylsarcosine, 0.1 M NaCl, pH 7.4 (50 mM HEPES), 25°C.

	K_i dansylsarcosine (μM)
Gd.4b	63 (± 1.6%)
[Gd.9(R)]$^{3-}$	207 (± 1.5%)
[Gd.9(S)]$^{3-}$	807 (± 3.8%)

Table 27. Measured inhibition constants, K_i, for **Gd.4b**, **[Gd.9(R)]$^{3-}$** and **[Gd.9(S)]$^{3-}$** for dansylsarcosine displacement. No warfarin displacement was observed.

It is not surprising that the bis-methyl dpp complex **Gd.4b** binds exclusively to site II given that only one enantiomer of the mono-methyl analogue displaces warfarin. The affinity is however, slightly higher for site II than for each of the R and S **Gd.4a** enantiomers. Interestingly, the R-enantiomer of the dpp moiety of the tris adipate complex **[Gd.9(R)]$^{3-}$** shows a higher affinity for site II than the S-enantiomer, **[Gd.9(S)]$^{3-}$**, which is the opposite to what was observed for the neutral acetate containing complexes. Neither enantiomer shows a

high affinity for site II, which is most likely due to steric hindrance, caused by the pendant adipate side groups.

3.7 Summary and Conclusions

pH responsive dpp bearing complexes have been prepared which show the hydrophobic dpp moiety to be 92.3% and 95.7% non-ligated to the metal centre at physiological pH 7.4 for both the racemic mono- and bis-methyl dpp derivatives respectively. This enabled non-covalent binding to HSA with high affinity, K = 22,268 ± 12 % M^{-1} (comprised of both the R and S-enantiomers of the monomethyl dpp, each with differing binding affinities) and K = 20,059 ± 14% M^{-1}, corresponding to 92.8% and 92.1% of complex bound to the protein at imaging concentrations and physiological conditions for both the racemic mono-methyl **Eu.4a** and bis-methyl **Eu.4b** respectively (0.1 mM complex, 0.67 mM HSA, pH 7.4). Similar binding affinities were observed from relaxometric studies of the Gd(III) analogues, showing maximum relaxivity values of r_1 = 11.7 $mM^{-1}s^{-1}$ and r_1 = 16.0 $mM^{-1}s^{-1}$ for both fully HSA bound **Gd.4a** and **Gd.4b** respectively. The higher value observed for the bis-methyl complex **Gd.4b** is attributed to the lower independent rotation of the more rigid complex when bound to the protein. Luminescent lifetime measurements of the Eu(III) analogues demonstrated that the two inner sphere waters were displaced, presumably by bidentate carboxylate residue groups upon binding to the protein. Eu(III) emission *vs*. pH titrations in the presence of carbonate determined the apparent pK_as to be 7.39 (± 0.19) and 7.45 (± 0.10) ($\Delta J = 2\ I/I_o$) and 6.59 (± 0.07) and 7.09 (± 0.10) ($\Delta J = 2$ / $\Delta J = 1$) for both **Eu.4a** and **Eu.4b** respectively; within the physiological pH range enabling possible use of the complexes as concentration independent pH sensors in serum. The negatively charged mono-methyl dpp complex **[Gd.9]$^{3-}$** was prepared in order to reduce anionic water displacement and, therefore, increase relaxivity of the HSA bound species. Relaxivity was enhanced by ~ 36% compared to the neutral mono-methyl analogue to r_1 = 15.8 $mM^{-1}s^{-1}$ and r_1 = 16.0 $mM^{-1}s^{-1}$ for the R and S-enantiomers of the dpp moiety respectively, while luminescent studies of the Eu(III) analogue measured the binding affinity, K = 17,915 (± 14%) M^{-1}. The R and S-enantiomers of the dpp group of each mono-methyl complex were prepared. Each neutral dpp complex showed high binding affinity to site II of the protein following displacement titrations with dansylsarcosine (K_i = 118 ± 2.0% **Gd.4a(R)**; K_i = 76 ± 1.8% **Gd.4a(S)**) while the S-enantiomer showed an affinity for site I following displacement titrations with warfarin (K_i = 252 ± 6.0%). Both the R and S-enantiomers of the dpp moiety of the negatively charged dpp complex **[Gd.9]$^{3-}$** as well as the neutral bis-methyl dpp complex **Gd.4b** displayed site II specific binding, as each displaced dansylsarcosine during competitive binding titrations, but did not displace warfarin (K_i = 63 ± 1.6 % **Gd.4b**; K_i = 207

± 1.5% **[Gd.9(R)]$^{3-}$**; K_i = 807 ± 3.8% **[Gd.9(S)]$^{3-}$**). The results are comparable to those observed for the site II specific MRA contrast agent MS-325 (Vasovist®), for which the binding constant of K = 11,000 M^{-1} (37°C) and an inhibition constant of K_i = 83 ± 3.0% (dansylsarcosine) were reported.[187]

The greatest relaxivity enhancement upon binding to HSA was observed for the neutral bis-methyl dpp complex **Gd.4b**. Relaxivity increased by 146% from r_1 = 6.5 $mM^{-1}s^{-1}$ to r_1 = 16.0 $mM^{-1}s^{-1}$ upon binding of **Gd.4b** to HSA, compared to the 64% increase from r_1 = 7.1 $mM^{-1}s^{-1}$ to r_1 = 11.7 $mM^{-1}s^{-1}$ observed for the mono-methyl dpp complex, **Gd.4a**. The greater relaxivity enhancement displayed by **Gd.4b** is presumably due to the increased rigidity of the bis-methyl dpp moiety compared to the mono-methyl dpp complex, **Gd.4a**. A reduction in the independent rotation of the HSA-bound **Gd.4b** complex is thus achieved, resulting in the greater relative enhancement of the observed relaxivity. The measured relaxivity of the R and S-enantiomers of the dpp groups of the HSA bound negatively charged mono-methyl dpp complex, **[Gd.9R/S]$^{3-}$** were both similar at r_1 ~ 16.0 $mM^{-1}s^{-1}$ showing an ~ 68% increase compared to the unbound complex; r_1 ~ 9.5 $mM^{-1}s^{-1}$. The observed relaxivity of the mono-methyl dpp negatively charged HSA bound complex was comparable to that observed for the bis-methyl dpp complex **Gd.4b**, presumably due in part to the increase in independent rotations of the bound **[Gd.9]$^{3-}$** complex caused by the reduction of rigidity of the mono-methyl dpp moiety as well as the increased molecular weight of the tris adipate bearing complex. Furthermore, the water exchange dynamics of the bound **[Gd.9]$^{3-}$** may have been affected by the close proximity of the adipate side chains with the protein, reducing the overall exchange rate of the inner-sphere water.

Greater enhancement of relaxivity may therefore be achieved by introducing negative charge into the bis-methyl dpp complex.

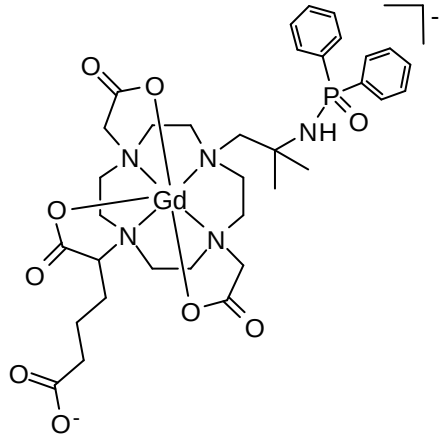

The incorporation of fewer adipate side chains would produce a lower molecular weight, more rigid complex that binds with high affinity to site II of HSA. Increased

relaxivity enhancement would therefore be achieved following the reduction of the independent rotations of the HSA bound complex. The introduction of a single adipate side chain may result in increased electrostatic repulsion of protein residue carboxylate groups, maintaining the $q = 2$ hydration state of the bound complex as well reducing the effect on the water exchange dynamics observed for the HSA bound tris-adipate analogue.

Chapter 4

Enzyme Activated Contrast Agents

4.1 Introduction

There has been great interest in the development of contrast agents that respond to the presence of an enzyme, which may be associated with particular disease state. Several contrast agents have been designed which contain the substrate for a given enzyme. Such substrates are incorporated into the molecule and mask the relaxometric properties of the contrast agent, causing low MR image intensity. Enzymatic cleavage of the masking groups results in increased relaxivity of the contrast agent and an increase in the MR image intensity, effectively "switching on" the contrast agent.

M^{c}Murry and co-workers developed Gd-DTPA based contrast agents incorporating either a diphenylalanine or a 3,5-diiodotyrosine group, **Gd.L38**, both of which have a high affinity for human serum albumin (HSA).[206]

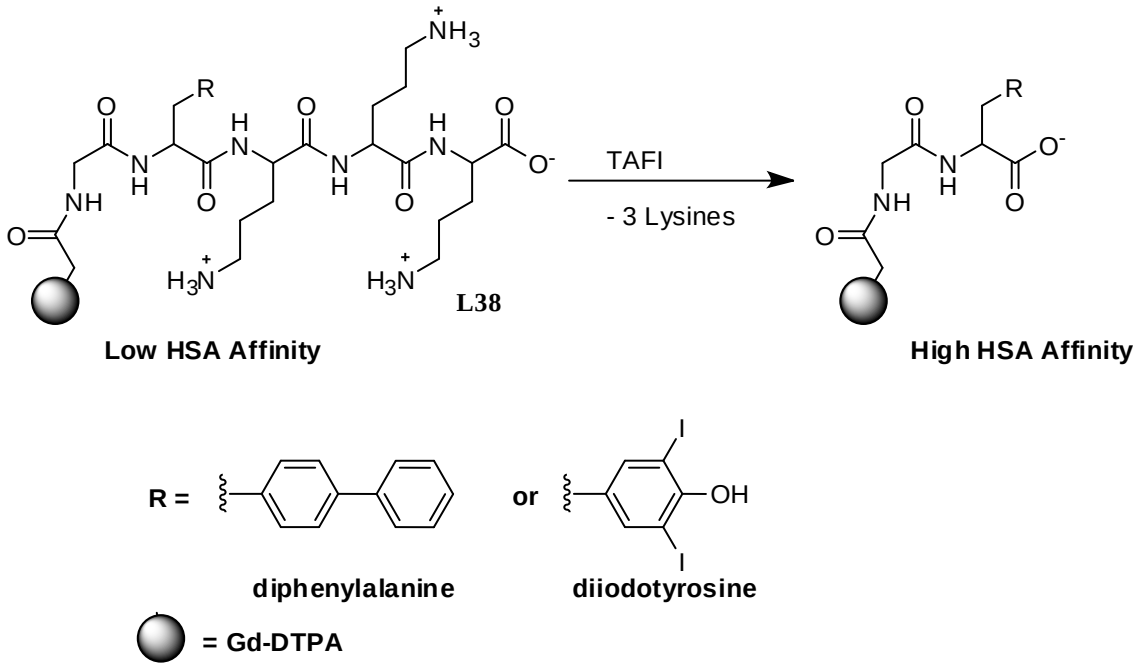

Scheme 14

Protein binding was suppressed by the incorporation of a trilysine peptide chain, known for its low affinity for HSA. Furthermore, lysine residues are cleaved by carboxypeptidase B, thrombin-activatable fibrinolysis inhibitor (TAFI), which has been implicated in thrombotic disease. Enzymatic cleavage of the trilysine masking group results in the exposure of the moiety with an affinity for HSA binding. This leads to non-covalent

attachment of the contrast agent to the slowly tumbling protein, resulting in a reduction of the rotational correlation time, τ_R, and enhancement of relaxivity and thus MR image intensity (Scheme 14). Relaxivity was enhanced from r_1 = 11.1 $mM^{-1}s^{-1}$ to r_1 = 24.5 $mM^{-1}s^{-1}$ for the diphenylalanine derivative (~ 120% increase) and from r_1 = 9.8 $mM^{-1}s^{-1}$ to r_1 = 26.5 $mM^{-1}s^{-1}$ for the diiodotyrosine derivative (~ 170% increase) (4.5% w/v HSA, 20 MHz, pH 7.4 (PBS), 37°C). Despite the greater percentage increase for the diiodotyrosine derivative, enzymatic cleavage was achieved to a greater extent for the diphenylalanine species with complete conversion occurring within one hour (230 μM complex, 75 nM TAFI). Under the same conditions only 5% of the resulting solution contained the completely converted diiodotyrosine complex with 83% of the monolysine intermediate present. Complete cleavage was only achieved upon addition of micromolar quantities of TAFI, therefore the diphenylalanine derivative shows more promise for *in vivo* use in the detection of TAFI.

Another approach was taken by Meade and co-workers who devised a system for the *in vivo* visualisation of gene expression.[207, 208] The modulation of the hydration state, *q*, of a Gd-DO3A based contrast agent was achieved by the enzymatic cleavage of a galactopyranose, which was incorporated into the molecule to block the ninth Gd(III) coordination site from exchanging waters. The q = 0 species will, therefore, have low relaxivity and hence low MR image intensity. The galactopyranose residue is a substrate for β-galactosidase enzyme (β-gal), a commonly used marker for monitoring gene expression. Enzymatic cleavage of the galactopyranose results in the exposure of the final Gd(III) coordination site, which allows water exchange at the metal centre. Initial results showed a 20% increase in observed relaxivity upon β-gal activation.[209] The results were improved, however, by the addition of a α-methyl to the sugar linkage arm, resulting in increased rigidity and steric hindrance to water exchange in the non-cleaved complex, **Gd.L39**, (Scheme 15).

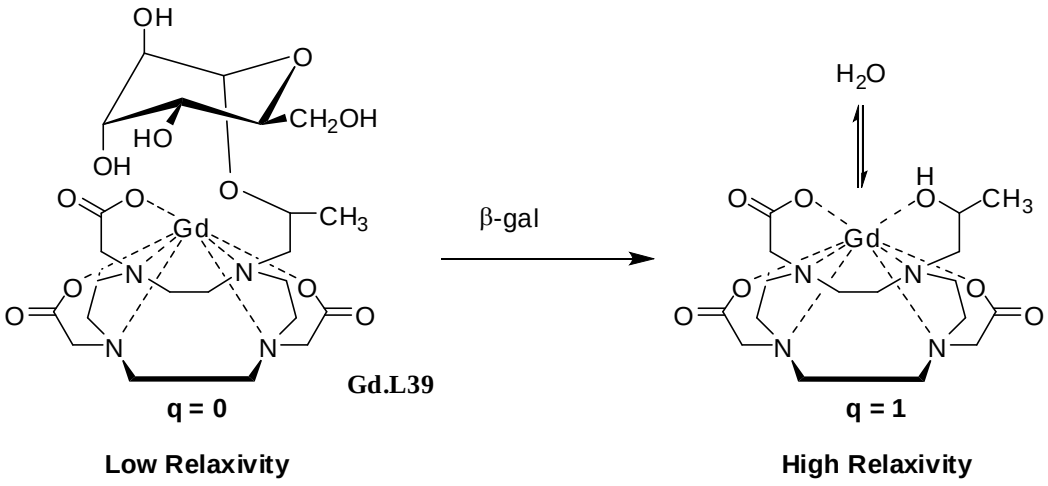

Scheme 15

The contrast agent has been used to detect *in vivo* transcription and translation in *Xenopus Laevis* embryos. One **Gd.L39** labelled embryo was injected with a DNA construct carrying the lacZ gene, which encodes for β-gal, at the two-cell stage. The subsequent MR image detected β-gal expression showing areas of enhanced MR image intensity, particularly in the eye, head and ventral regions. Initial experiments detected a 45-65% increase in relaxivity for embryos containing **Gd.L39** than for those that did not.

More recently the same group has adopted a similar strategy, incorporating a β-glucuronic acid moiety, a substrate for enzymatic cleavage by β-glucuronidase, which is found in high concentration near cancer tumours.[210] Enzymatic hydrolysis of the pendant moiety lead to the self-imolative generation of an eight coordinate species, **Gd.L40**. (Scheme 16).

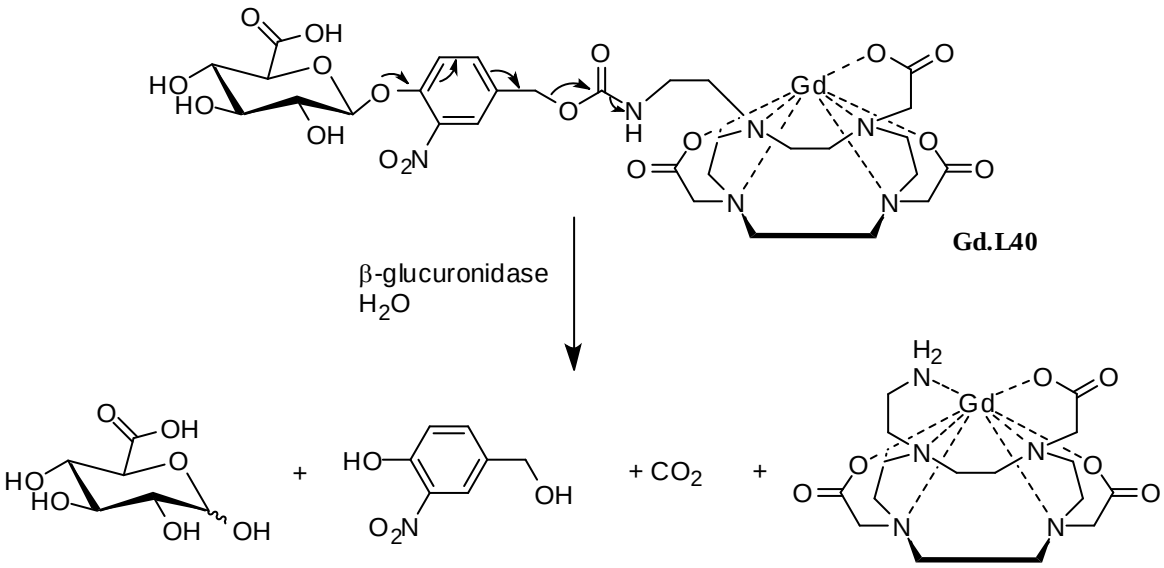

Scheme 16

In vitro studies showed of non-cleaved species and the independently prepared cleaved species showed relaxivities of r_1 = 3.68 $mM^{-1}s^{-1}$ versus r_1 = 2.65 $mM^{-1}s^{-1}$ (pH 7.4, 10 mM MOPS buffer, 60 MHz, 37°C) respectively. The values were measured in a series of buffers and it was found that there was ~ 20% difference in relaxivity between the two species. This was attributed to the higher hydration state of the non-cleaved complex. Upon addition of physiologically relevant carbonate concentrations (24 mM $NaHCO_3$) to the buffered solutions a 20-30% drop in relaxivity was observed for the non-cleaved compound, while the cleaved species remained the same within error at r_1 = 2.64 $mM^{-1}s^{-1}$ and r_1 = 2.58 $mM^{-1}s^{-1}$ respectively (10 mM MOPS buffer, 60 MHz, 37°C). The seven coordinate non-cleaved species, containing two vacant coordination sites, demonstrated almost an eight-fold higher affinity for carbonate binding than the eight coordinate cleaved species. This displaces the inner sphere waters and lowers relaxivity. Enzymatic hydrolysis using bovine

liver β-glucuronidase was monitored *via* a continuous UV-visible assay, measuring the increased absorption of the 4-hydroxy nitrobenzyl alcohol product. k_{cat}/K_m was measured as 74.0 ± 10.9 $M^{-1}s^{-1}$ using *p*-nitrophenyl-β-D-glucuronide as a standard (1.0 mg/ml enzyme, 100 mM sodium phosphate, 0.01% (w/v) bovine serum albumin, pH 7.4, 37^{o}C. In human serum a 14% increase in relaxivity was observed after one hour in the presence of β-gluronidase enzyme (60 MHz, 37^{o}C, pH 7.4).

4.1.1 MRI Contrast Agents for Molecular Imaging Applications

Molecular imaging is defined as "the *in vivo* characterization and measurement of biological processes at the cellular and molecular level".[211] Current MRI contrast agents are administered at around 0.1 mmol/kg range (approx 5.0 g for an average male). Relatively high concentrations are required to overcome the inherent low sensitivity of the MRI scanner. Concentrations of ~ 5 μM contrast agent are administered in order to sufficiently observe image enhancement. At such high concentrations, however, increased background signals make it impossible to use MRI for molecular imaging purposes as cell surface receptor concentrations are somewhat lower than the administered contrast agent dose.

Cellular imaging has been the focus of a great deal of recent interest. The addition of a targeting moiety to Gd(III) chelates has been highly successful for the *in vitro* and *in vivo* imaging of tumour cells. The increased glutamine transporting system in tumour cells has been exploited by the addition of a glutamine residue to a Gd-DOTA chelate, leading to an accumulation of contrast agent within tumour masses of mice.[212] Tumour angiogenesis has also been visualised both *in vitro* and *in vivo* by incorporation of a target peptide moiety to a Gd(III) loaded apoferritin probe.[213]

Aime and co-workers developed an insoluble Gd(III) chelate based contrast agent bearing long aliphatic side chains for uptake into dendritic cells, **Gd.L41**.[101, 214] The insoluble contrast agent would display low relaxivity. Enzymatic cleavage of the aliphatic side chains by intracellular lipase resulted in the enhanced solubility of the Gd(III) chelate and consequentially an increase in relaxivity and image intensity (Scheme 17). *In vitro* studies demonstrated an immediate enhancement in the observed relaxation rate, R_{1obs}, upon uptake into the dendritic cells. Cells (50,000 cells μl^{-1}) were incubated for three hours with **Gd.L41** present, after which they were washed with PBS and continuously incubated in culture medium in the absence of **Gd.L41**. Maximum cellular uptake was achieved after only a few hours. Detectability limits were determined by *in vitro* phantom experiments in various concentrations of dendritic cells, incubated with differing concentrations of **Gd.L41**. *In vivo* experiments have been carried out in order to validate cell detectability in an animal model.

Gd.L41 labelled dendritic cells were implanted into rat brains immediately after labelling. The minimum number of cells detected was 20,000 μl^{-1} by MRI for up to 72 hours after implantation. 50,000 cells μl^{-1} were detectable for up to eight days after implantation. The model shows great scope for future development as contrast agents for functional cellular imaging as the pendant aliphatic side chains can be easily modified into specific substrates to monitor varying target enzymes.

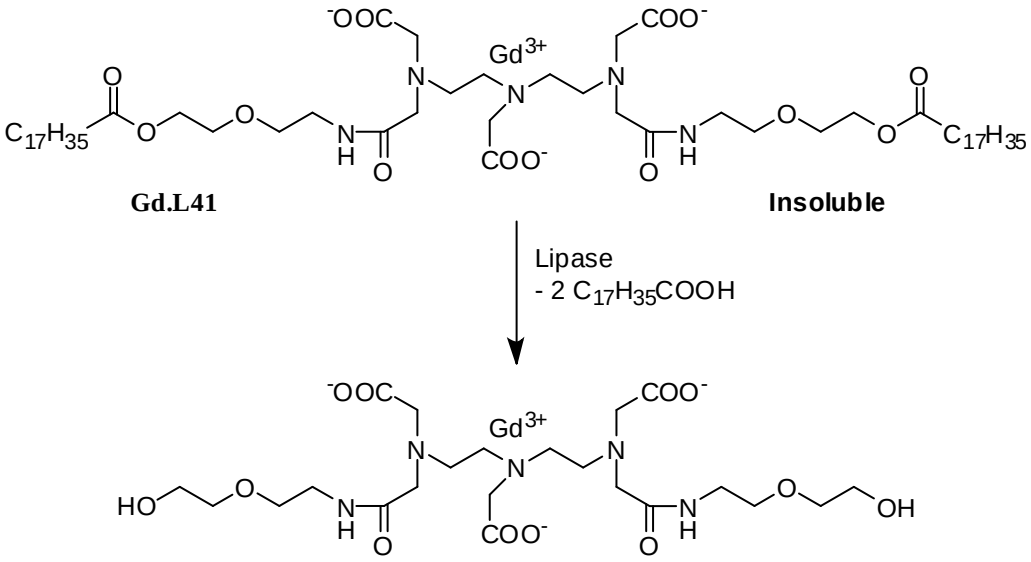

Scheme 17

4.2 Esterase Activated Contrast Agents for Molecular Imaging Applications

Research into increasing a contrast agent's hydration state, *q*, following enzyme activation has been of considerable interest, as shown in Section 4.1. The result is an enhancement of relaxivity, r_1, and MR image intensity. Here, binding affinities of endogenous anions for neutral and charged contrast agents have been exploited in order to modulate the hydration state of Gd(III) complexes.

Neutral, q = 2 Gd(III) DO3MA based complexes bearing acetoxymethyl esters have been prepared. Endogenous anions, such as carbonate, were expected to coordinate to the Gd(III) centre, displacing inner sphere water molecules, lowering the observed relaxivity. The acetoxymethyl ester groups would be expected to be hydrolysed by the enzyme esterase. The negatively charged complex that is generated should then disfavour the coordination of anions, allowing water molecules to exchange with the Gd(III) centre, thus enhancing relaxivity following enzyme activation (here pig liver esterase is used to demonstrate the hypothesis as acetoxymethyl ester hydrolysis is well documented.[215])

An accumulation and activation strategy has been proposed in which the charge-neutral contrast agent (as the acetoxymethyl ester) should be able to pass through cell

membranes and localise within cells. Following activation from non-specific intracellular esterases (increased levels of which have been associated with diseases such as leukaemia.[216]) a negatively charged species will be generated, the outflow from the cell should be slowed, thus the agent is accumulated. In addition to this, the relaxivity should be enhanced as binding of endogenous anions is suppressed.

4.2.1 Accumulation and Activation Strategy

In order to prepare a contrast agent that will be activated by a biological event it is important to remember the fundamental factors that enhance contrast agent sensitivity. By referring to Equation 21 (Chapter 1) we see that the most important factors, that as chemists we have control over, are the hydration number, q, the rotational correlation time, τ_R (which has the largest contribution towards the water proton longitudinal relaxation time of the inner sphere waters, T_{1M}, at MRI operating frequencies (Chapter 1)), and water exchange lifetime, τ_m.

It has already been shown in Chapter 3 that attachment of a contrast agent to a large protein such as HSA slows down tumbling, enhancing relaxivity. Another aspect that was alluded to in Chapter 3 was the concept of anion binding, which was seen to be a problem when designing neutral contrast agents that bind to HSA. As anions such as carbonate bind to a neutral q = 2 complex, they displace exchanging water molecules, lowering the hydration number, q, and therefore decrease relaxation efficiency and image intensity.[202, 217] However, anion binding can be suppressed by the preparation of negatively charged contrast agents. Electrostatic repulsion prevents anion binding allowing waters to exchange with the Gd(III) centre.[77]

Anions are extremely abundant in serum, with chloride being the most prominent (0.1 M). The anions carbonate (~ 20-30 mM), citrate (0.13 mM), lactate (2.3 mM) and phosphate (0.9 mM)[201] are also present in serum. These can all bind in a bidentate manner to a q = 2 neutral contrast agent.[202] This displacement of inner sphere waters by endogenous anions has generally been a problem when designing contrast agents in the past. Herein the concept of anion binding has been embraced and was exploited in order to prepare contrast agents where anion binding is disfavoured as a result of enzyme activation.

Scheme 18 shows the model that was hypothesised. The neutral q = 2 complex bearing acetoxymethyl esters is expected to be in equilibrium with the anion bound q = 0 complex in serum. If this equilibrium lies to the right it is hypothesised that the contrast agent will have a lower hydration state and, consequently, lower relaxivity. As the contrast agent is neutral diffusion, through cell walls would be possible (e.g. by endocytosis, pinocytosis or pressure

transport).[218] Once inside the cell, the intracellular anion binding equilibrium would be re-established, displacing exchanging waters and lower the contrast agent's efficiency. The equilibrium would be short lived, however, as intracellular esterases are expected to hydrolyse the acteoxymethyl ester groups, unmasking a negatively charged complex. It is also expected to result in a slowing down of the outflow from the cell.[219, 220] Indeed, such acetoxymethyl ester hydrolysis strategies have been used in many aspects of drug development for cellular drug delivery and compartmentalisation.[221, 222]

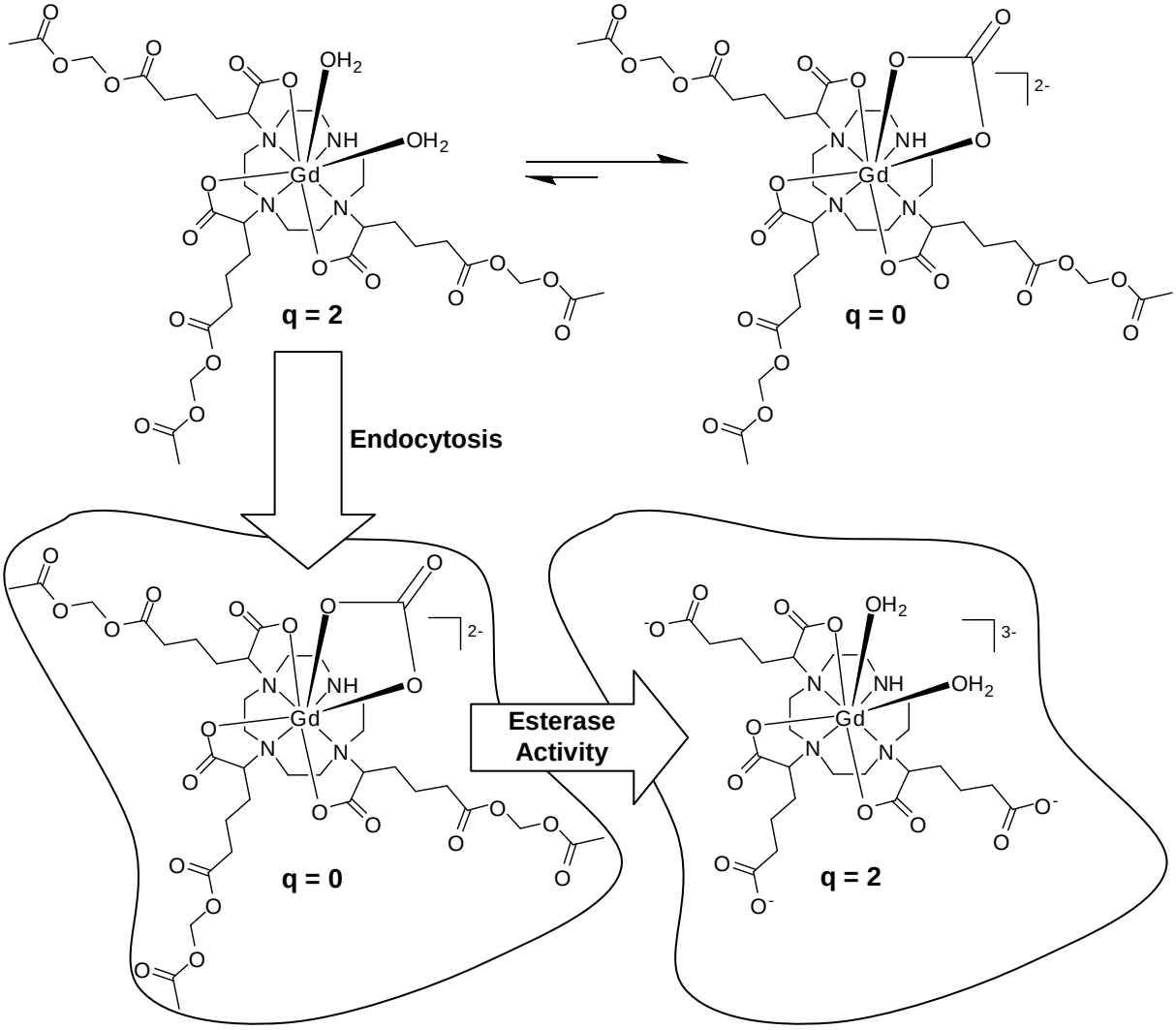

Scheme 18

The now negatively charged species would disfavour anionic binding and allow waters to exchange with the metal centre. The hydration state would be increased upon enzyme activation and the relaxivity of the contrast agent would be therefore enhanced, leading to higher MR image intensity. The contrast agent is both accumulated *and* activated inside the cell by enzymatic hydrolysis.

4.2.2 Models for Enzyme Activation

The complexes are based on the Gd-DO3MA structure, known for its sufficiently high stability for use *in vivo*.[223] The aliphatic adipate side chains containing six carbons are incorporated into the complex in the place of the DO3MA methyl groups at the α-carbon position to avoid ligation of the enzymatically generated free acid to the Gd(III) centre, which is known to occur for the five carbon-containing glutamate analogue.[77] The acetoxymethyl esters are readily hydrolysed by esterase enzymes, and are frequently used in the drug industry as masking groups for negative charge. These were the substrates of choice for enzyme activation in this work.

Two model compounds were prepared and used in initial luminescent (Eu) and relaxometric (Gd) studies to probe the feasibility of the enzyme activation hypothesis. A negatively charged post-hydrolysis, free acid complex, **[Ln.10]$^{3-}$**, was prepared as well as a neutral pre-hydrolysis complex, **Ln.14**.

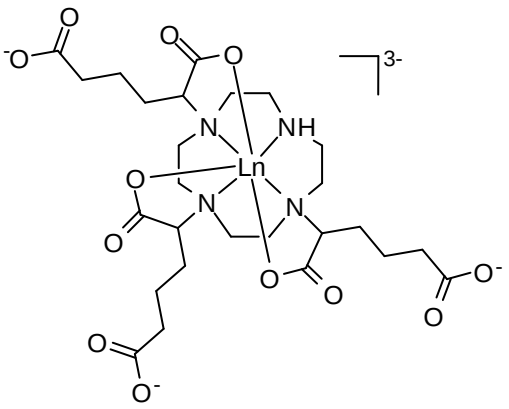

[Ln.10]$^{3-}$

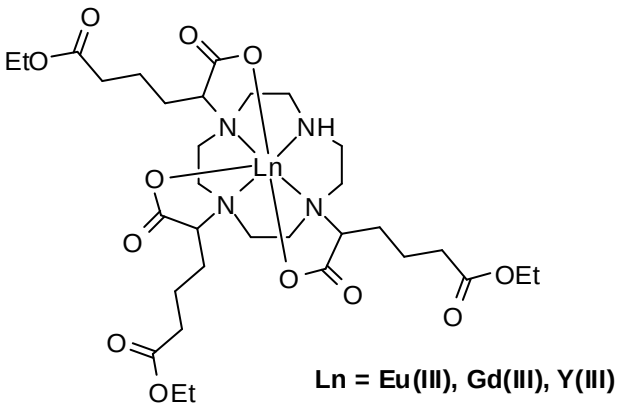

Ln.14

*4.2.3 Post-Hydrolysis Model Complex Preparation, **[Ln.10]$^{3-}$***

The post-hydrolysis, carboxylic acid-containing complex **[Ln.10]$^{3-}$** was prepared as a control compound in order to monitor the anion binding affinity of both the pre- and post-enzyme activated complexes prior to esterase hydrolysis tests being carried out.

The complex was prepared by simple hydrolysis of the methyl ester groups of **6** (Chapter 3, Section 3.4.6) using 1 M LiOH, followed by cation exchange chromatography. Complexation was carried out in water at 90^{o}C, adjusted to pH 6 (Scheme 19).[134]

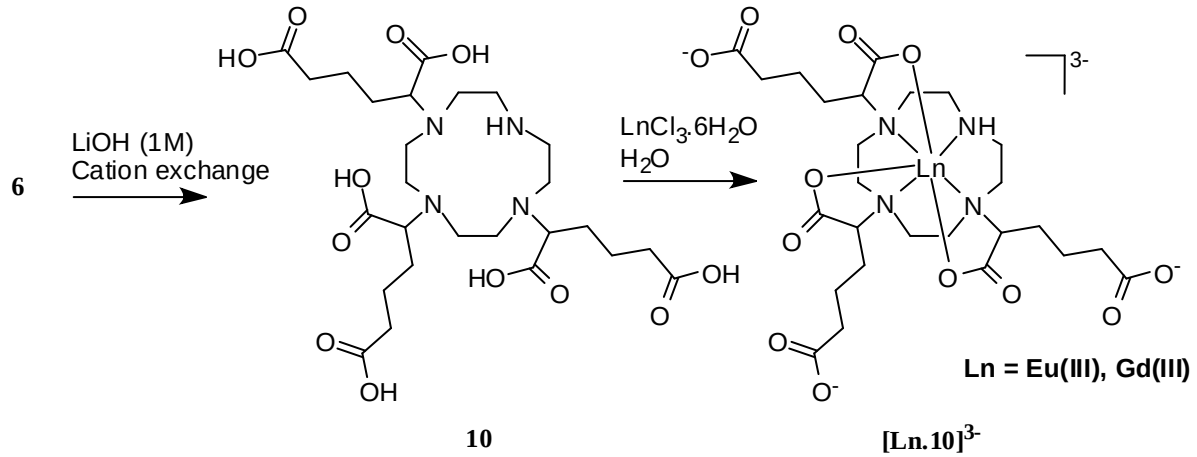

10 **[Ln.10]$^{3-}$**

Scheme 19

*4.2.4 Pre-Hydrolysis Model Complex Preparation, **Ln.14***

Ethyl esters were chosen for the neutral model compound due to their relative synthetic ease and stability in comparison with the acetoxymethyl ester derivative. The tris-substituted macrocyclic compound, **12**, was prepared by addition of 2-bromoadipic acid 1-*tert*-butyl ester 6-ethyl ester, **11**, to cyclen (3:1 ratio) in the presence of potassium carbonate (Scheme 20).[134]

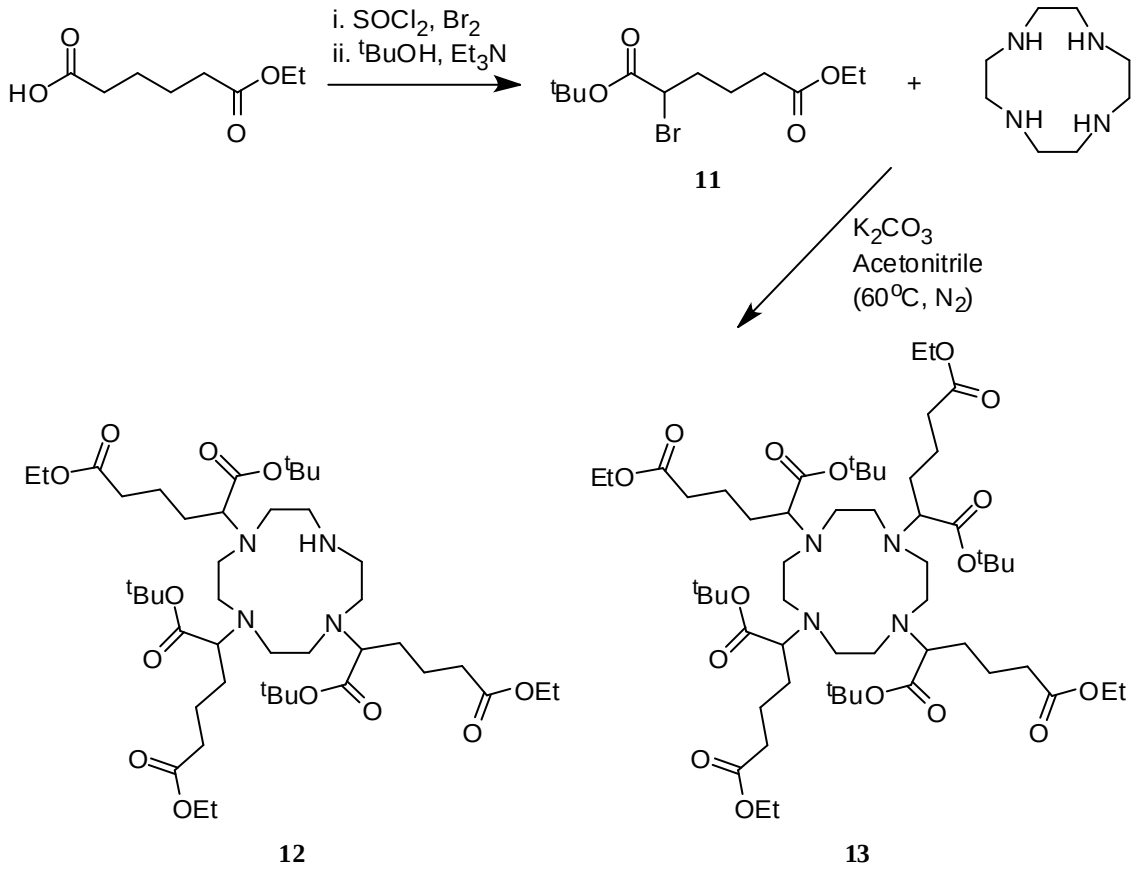

12 **13**

Scheme 20

The reaction was carried out in acetonitrile under mild conditions (60°C) in order to avoid the formation of large quantities of the tetra-substituted macrocycle, **13**, which was produced in greater abundance when the reaction temperature was raised to 85°C. Despite this, some tetra-substituted macrocycle was isolated following purification by silica-column chromatography. This was used to prepare the Eu(III) complexes, which could be studied by ^{1}H NMR spectroscopy in order to investigate the complex geometry, discussed later (Section 4.2.6). Synthesis of **11** involved much the same procedure as for **5** (Chapter 3, Section 3.4.6), employing adipic acid monoethyl ester following literature preparation.[203] Following the bromination of the adipic acid chloride ethyl ester, *tert*-butanol and triethylamine were added to the residue to generate **11** (under anhydrous conditions to avoid the acid hydrolysis of the *tert*-butyl esters that were to be formed). Yields were improved by allowing the reaction mixture to stir in bromine at 65°C whilst monitoring the C*H*Br chemical shift at δ = 4.1 ppm using ^{1}H NMR spectroscopy. The product was purified by column chromatography using DCM as eluent with yields typically ~ 44%.

Scheme 21 shows the synthetic route for producing the neutral ethyl ester complex **Ln.14**. The acid hydrolysis of the tert-butyl ester groups of **12** using trifluoroacetic acid (TFA) followed by complexation. The solution was adjusted to pH 6, as for preparation of **[Ln.10]$^{3-}$**. Due to poor solubility, addition of ~ 5% methanol was necessary.[134]

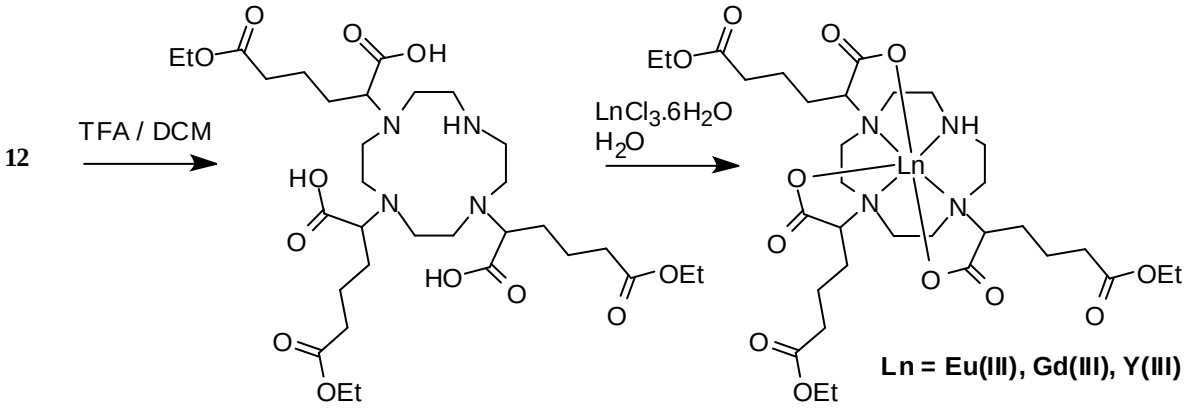

14 **Ln.14**

Scheme 21

*4.2.5 Pre-Hydrolysis, Acetoxymethyl Ester Complex Preparation, **Ln.18***

Several steps were necessary in the preparation of **Ln.18**. The free ring nitrogen of **12** was BOC-protected by addition of di-*tert*-butyl-dicarbonate and triethylamine in dry DCM to give **15**. After the solvent was removed and the product purified by chromatography, a 1:1 solution of 1M sodium hydroxide/ethanol was added, which resulted in base hydrolysis of the ethyl ester groups, leaving the *tert*-butyl esters intact.[224] The pH was carefully lowered to ~ 4

at 0°C then the solution was lyophilised. The product was extracted from the salt residues with 20% dry methanol/DCM solutions (Scheme 22).

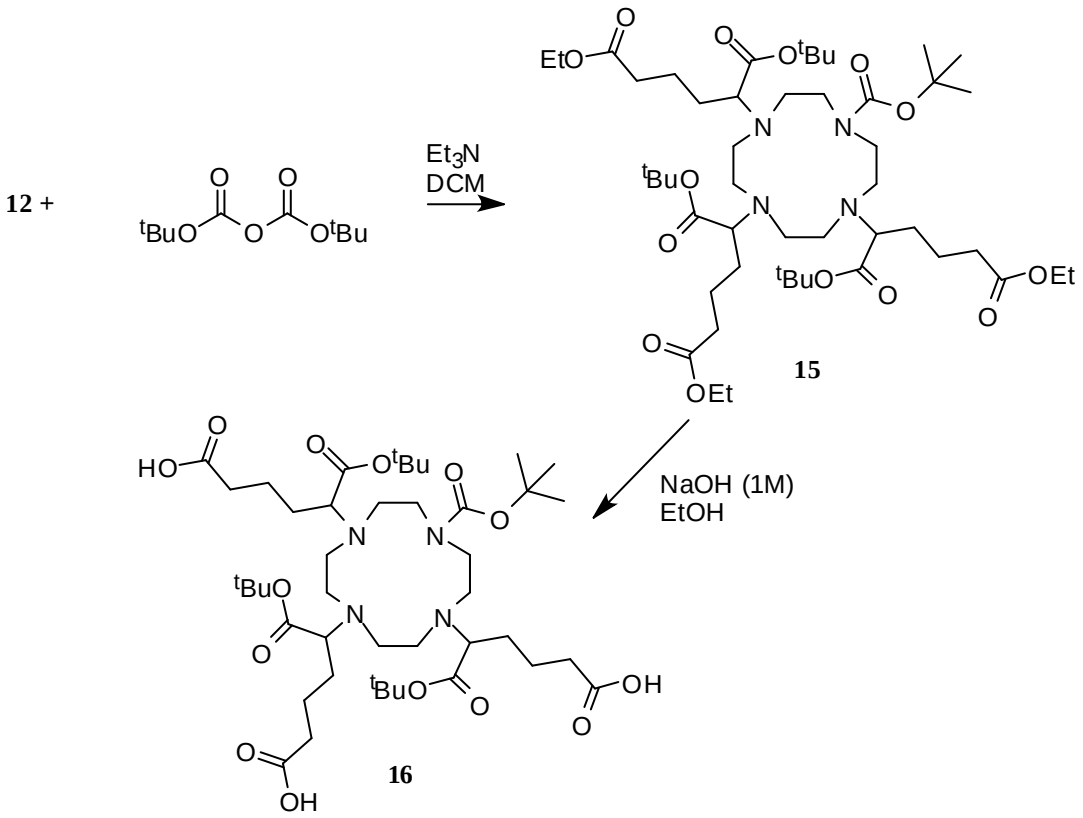

Scheme 22

The acetoxymethyl esterification step was carried out under anhydrous conditions with the addition bromomethyl acetate and DIPEA in DCM, monitored by ESMS.[225] Once addition was complete, the solvent was removed and both the BOC-protecting group and *tert*-butyl ester groups were hydrolysed with TFA/DCM solution to give **18**. Complexation was achieved in dry methanol at 55°C for two hours (reactions carried out in water may have resulted in hydrolysis of the far less robust acetoxymethyl ester groups) (Scheme 23). In solution, **[Ln.10]$^{3-}$**, **Ln.14** and **Ln.18** will exist in the square antiprismatic (SAP) and twisted square antiprismatic (TSAP) equilibrium isomeric geometries (Chapter 1, Section 1.4.1). The aliphatic side chains will also be present in six stereoisomeric forms defined by the absolute configuration at the α-carbon[74]; *RRR*, *SSS*, *RRS*, *SSR*, *RSR* and *SRS*. The precise equilibrium composition of the complexes is not known. Therefore, it is assumed that each isomeric form is present in solution and contributes to both luminescent and relaxometric observations that were carried out with each complex.

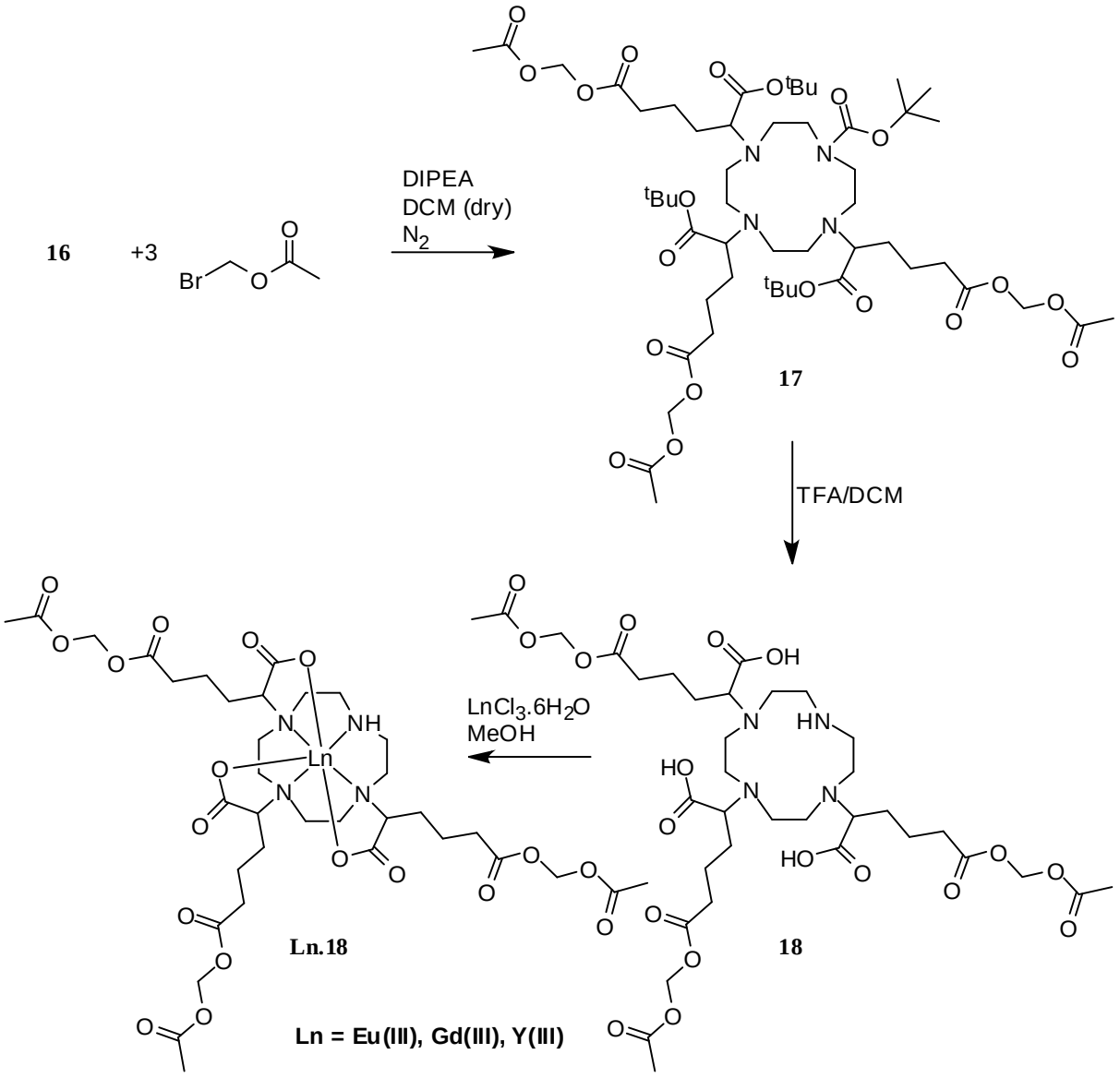

Scheme 23

4.2.6 Preparation of Eu(III) Complexes of Tetra-Substituted ***[Eu.19]***$^{5-}$ *and* ***[Eu.20]***$^{-}$ *for Structural Investigation with* ^{1}*H NMR Spectroscopy*

^{1}H NMR studies to determine the complex structure using the *tris*-substituted Eu(III) analogues proved inconclusive due to the fluxionality of the pendant arm and the macrocycle. Broad, featureless resonances were observed even upon cooling to 0^{o}C. The more rigid tetra-substituted species were therefore synthesised and studied by ^{1}H NMR spectroscopy. **7** and **13** were deprotected using LiOH and TFA respectively and the Eu(III) complexes were prepared following the same methods as their *tri*-substituted analogues (Scheme 24).

^{1}H NMR spectra were recorded on a 400 MHz NMR spectrometer at 27^{o}C with D_2O as solvent. The observed resonances for the tetra free acid **[Eu.19]**$^{5-}$ complex suggested that the complex is present in both the square antiprismatic (SAP) and twisted square antiprismatic (TSAP) isomeric forms. Peaks were present at δ = 19.1, 20.5, 22.8 and 25.9 ppm

corresponding to the axial ring protons of the twisted square antiprismatic geometry (TSAP) as well as a series of eight peaks at δ = 37.1, 38.5, 42.5, 42.9, 44.4, 49.3, 47.7 and 48.7 ppm corresponding to the axial ring protons of the square antiprismatic (SAP) geometry about the Eu(III) centre. The multiplets observed in the ^{1}H NMR spectrum are present due to the existence of the complex in the *RRRR, (SSSS), RSSS, (SRRR), RRSS* and *RSRS* isomeric forms with respect to the adipic acid side arms in solution. The integration of the peaks show the major isomers to be SAP at ~ 4:1. Similar results were observed for the ethyl ester bearing **[Eu.20]**$^{-}$ complex with resonances at δ = 19.4 and 26.2 ppm (TSAP) and δ = 38.4 and 48.8 ppm (SAP) observed. The integrations show the SAP geometry to be the major isomer in solution at ~ 5:1.[111]

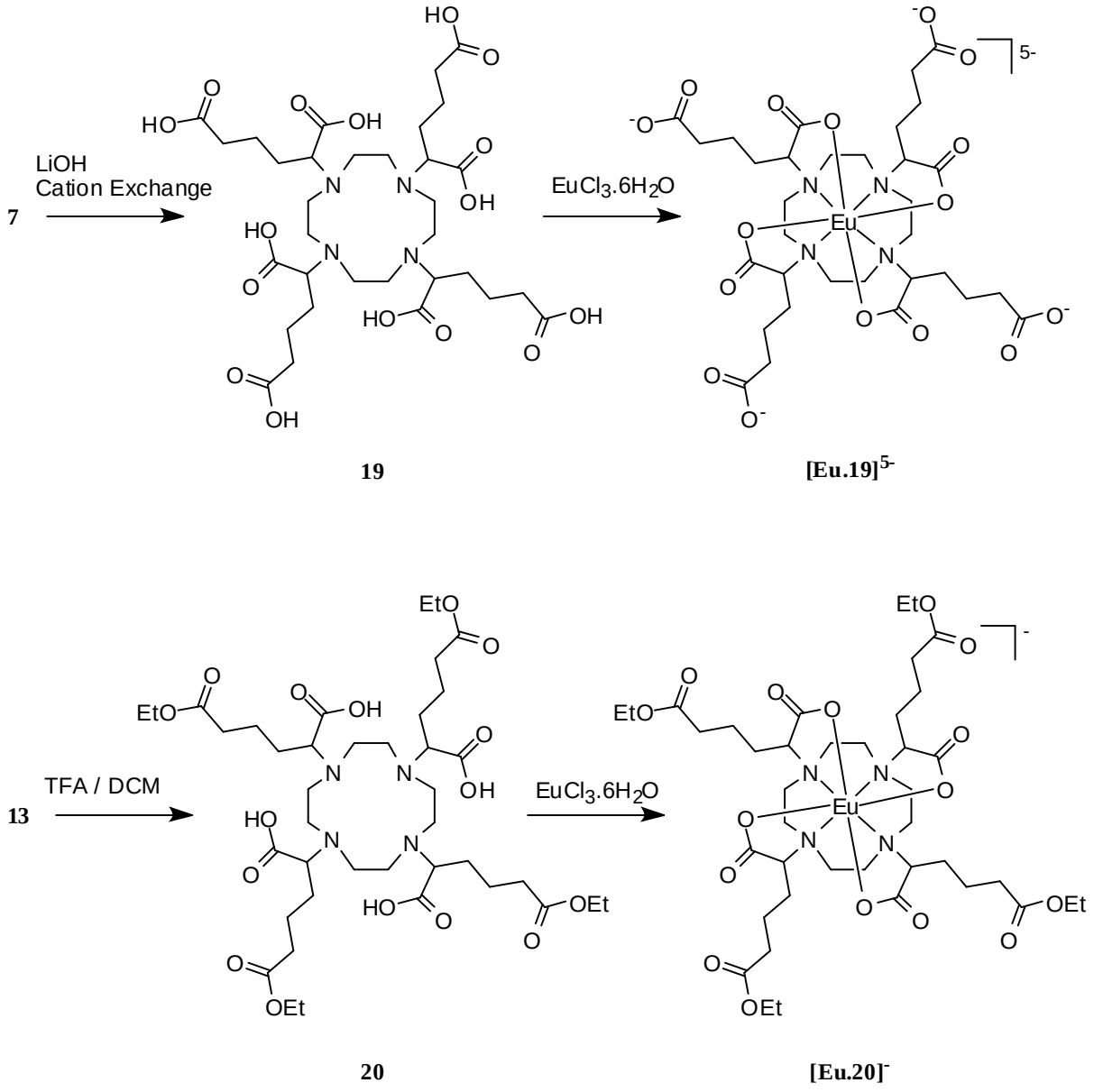

Scheme 24

4.2.7 Complex Purification

Any unreacted lanthanide ions were detected for each of the complexation reactions using the xylenol orange test. If solutions remained orange in colour there are no free Ln(III) ions present. If the colour turned pink, then free Ln(III) ions were present in the solutions.[160] In order to remove these free ions, a method using Dowex MAC-3 weak acid-cation exchange resin was employed. A weakly acidic exchange resin was necessary as more strongly acidic resins result in decomplexation. The resin was prepared with 1% HCl solution followed by washing with H_2O and the complex solutions were added. It was very important to ensure pH of the solution was ~ 7 before addition to the resin. Addition of a solution containing metal ions lowers the pH as protons from the resin exchange with the metal ions in solution, therefore it was essential pH was sufficiently high to avoid decomplexation. Upon addition, the pH of the solution would drop to ~ 4, which is both within the operating range of the resin, and high enough to ensure the complex remained intact. Solutions were stirred for around ten minutes and monitored by addition of 200 μl aliquots to 800 μl of 0.1 M xylenol orange solution (Chapter 6, Section 6.1.14). The solutions were then decanted from the resin and lyophilised to yield white powders, free of uncomplexed Ln(III) ions.

4.3 Luminescence and Relaxometric Studies of Model Complexes

Due to the relative ease of preparation and robustness of the model ethyl ester compounds, luminescence (Eu) and relaxometric (Gd) studies on both the model pre-enzyme activated complex, **Ln.14**, and the model post-enzyme activated complex, **[Ln.10]$^{3-}$**, were carried out prior to preparation of the acetoxymethyl ester compounds.

*4.3.1 Determination of Hydration State, q, for **[Eu.10]$^{3-}$** and **Eu.14***

The model pro-ligands **10** and **14** are both seven coordinate, leaving two coordination sites vacant for coordination of water molecules to Eu(III) or Gd(III). The presence of these two vacant sites is essential for bidentate anion binding to occur. In order to confirm the hydration number, *q*, and therefore the number of readily available coordination sites luminescent lifetime studies were carried out (Table 28).

	k_{H_2O} (ms^{-1})	τ_{H_2O} (ms)	k_{D_2O} (ms^{-1})	τ_{D_2O} (ms)	q
[Eu.10]$^{3-}$	3.30	0.30	1.33	0.75	2.1
Eu.14	3.32	0.30	1.36	0.74	2.1

Table 28. First order rate constants, *k*, excited state lifetime, τ, and measured hydration state values, *q*, for **[Eu.10]$^{3-}$** and **Eu.14** at pH 7.4. For full data analysis see Appendix **A9** and **A11**.

The rate constants, *k*, were determined from the decay of Eu(III) emission intensity *vs.* time plots in both H_2O and D_2O. The hydration state values, *q*, were calculated using Equation 33 (Chapter 1)[115, 116] and showed there to be two waters binding to the Eu(III). Therefore it is possible for these waters to be displaced by binding of bidentate anions.

4.3.2 Eu(III) Emission Intensity vs. pH for ***[Eu.10]$^{3-}$*** *and* ***Eu.14*** *in the Presence of Carbonate*

Carbonate is the most abundant bidentate anion in human serum, with concentrations around 20-30 mM. It is also abundant inside cells at around 10 mM.[226] pH titrations monitoring the Eu(III) emission intensity in the presence of carbonate were carried out in order to determine the extent and the optimum pH of binding to the model compounds. Figures 61 and 62 show the Eu(III) emission spectra for both **[Eu.10]$^{3-}$** and **Eu.14** in the presence and absence of carbonate at pH 7.4. It is clear that there is a lower affinity for carbonate resulting from a much higher degree of anionic repulsion for the negatively charged, free acid compound **[Eu.10]$^{3-}$** in comparison to its neutral analogue **Eu.14** at physiological pH.

As the O–H oscillators of water quench the Eu(III) excited state it is clear to see from the spectra in Figure 61 that little or no water displacement occurs upon addition of carbonate to **[Eu.10]$^{3-}$**. There is little change in emission intensity and spectral form. Addition of carbonate to the neutral complex **Eu.14** results in an increase in emission intensity and a change in spectral form. Quenching water molecules are displaced as a carbonate binding competes with water for ligation to the Eu(III) centre. There is a shift in the emission maxima and intensity of the hypersensitive $\Delta J = 2$ band from λ_{em} = 615 nm to λ_{em} = 617 nm upon addition of carbonate. Furthermore, the form of the $\Delta J = 1$ band at ~ 590 nm changes as three distinct sharp peaks are observed in the absence of carbonate, which change to two broad peaks upon addition. The $\Delta J = 1$ band is sensitive to variations in the complex symmetry. Three bands are observed for complexes with low symmetry while two are observed for those possessing C_3 and C_4 symmetry. Both the major SAP and the minor TSAP isomers each possess C_4 symmetry through the four ring nitrogens. Two $\Delta J = 1$ bands are observed for the major SAP isomer, with a third central band present for the minor TSAP isomer. As carbonate coordinates with the Eu(III) complex the helicity about the Eu(III) centre is reduced, leading to a reduction of the SAP isomer present in solution,[202] resulting in the broadening of the $\Delta J = 1$ band. At pH 7.4 in the presence of carbonate a larger equilibrium concentration of the TSAP isomer is present in solution for the neutral **Ln.14**. The observed spectrum is therefore composed from a greater contribution from the TSAP isomer, resulting in the observed spectral changes. These observations were exploited further when studying the effects of

esterase addition, discussed in Sections 4.4 and 4.5. No spectral change is observed at pH 7.4 with the negatively charged **[Eu.10]**$^{3-}$ complex as minimal carbonate binding occurs.

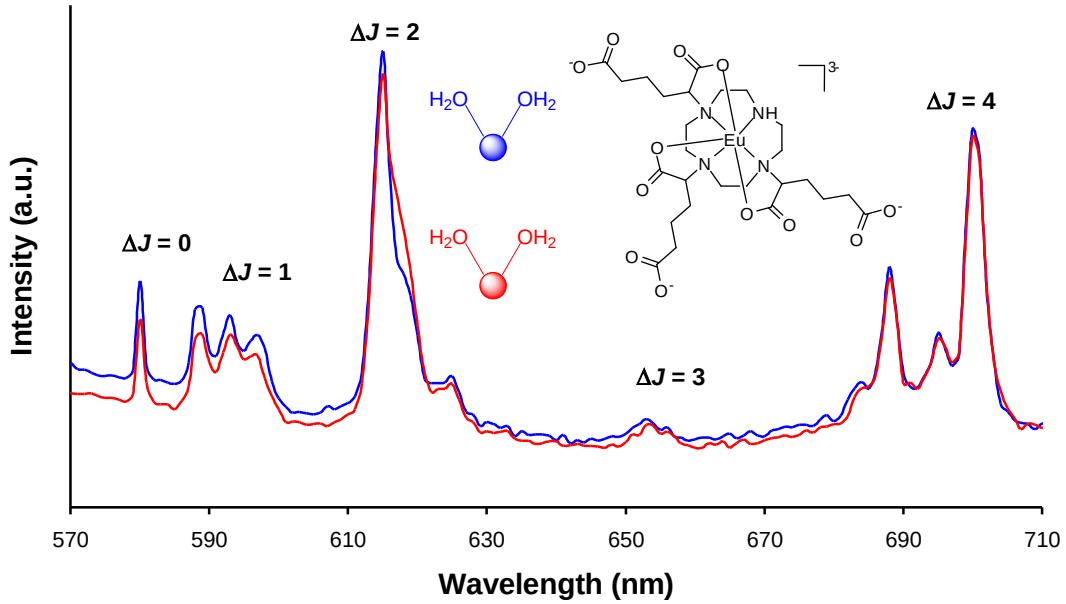

Figure 61. Eu(III) emission spectra for **[Eu.10]**$^{3-}$ in the presence (blue) and absence (red) of carbonate. 1.0 mM **[Eu.10]**$^{3-}$, 0.1 M NaCl, 30 mM $NaHCO_3$ λ_{ex} = 395 nm, pH 7.4, 25°C.

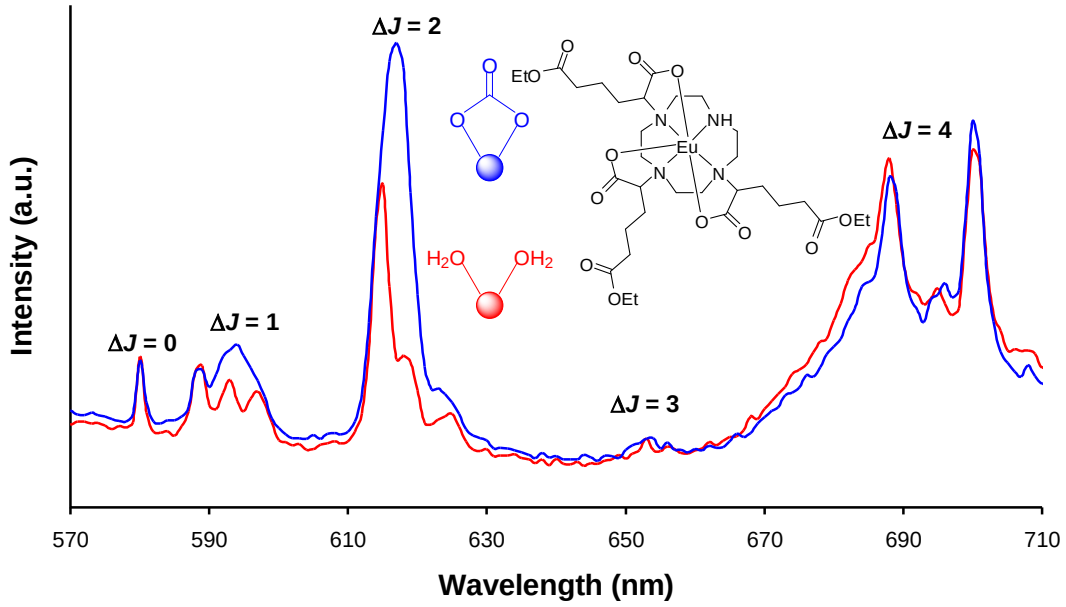

Figure 62. Eu(III) emission spectra for **Eu.14** in the presence (blue) and absence (red) of carbonate. 1.0 mM **Eu.14**, 0.1 M NaCl, 30 mM $NaHCO_3$ λ_{ex} = 395 nm, pH 7.4, 25°C.

Table 29 shows the calculated hydration state values for both the pre- and post-enzyme activated species in the presence of 30 mM sodium hydrogen carbonate at pH 7.4. By comparison of the data in Table 29 and the spectra in Figures 61 and 62, the minor change in

hydration state of the free acid complex **[Eu.10]$^{3-}$** suggests there may be a small quantity of the carbonate bound species present at pH 7.4.

	k_{H_2O} (ms^{-1})	τ_{H_2O} (ms)	k_{D_2O} (ms^{-1})	τ_{D_2O} (ms)	q
[Eu.10]$^{3-}$	3.26	0.31	1.38	0.72	2.0
Eu.14	2.83	0.35	1.61	0.62	1.2

Table 29. First order rate constants, k, excited state lifetime, τ, and measured hydration state values, q, for **[Eu.10]$^{3-}$** and **Eu.14** at pH 7.4, in the presence of carbonate (30 mM $NaHCO_3$). For full data analysis see Appendix **A9** and **A11**.

The change in hydration state is much greater for the neutral complex **Eu.14**; however, water molecules are not completely displaced. The hydration state value of q = 1.2 suggests that an equilibrium is reached between the q = 0 carbonate bound and q = 2 water bound species. This can be clearly seen from the titration of Eu(III) emission intensity *vs*. pH in the presence of carbonate (Figure 63).

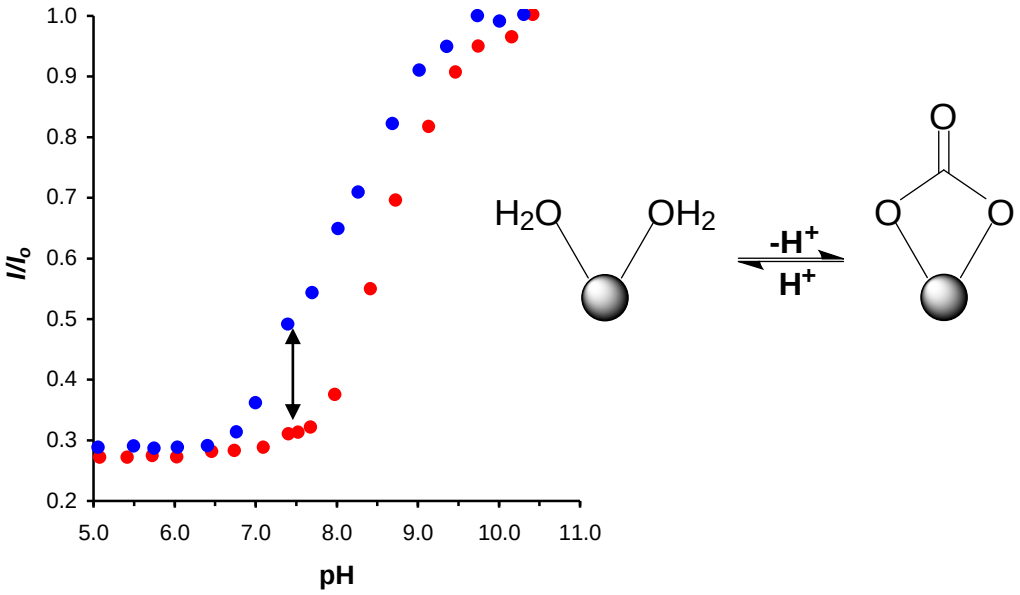

Figure 63. Eu(III) emission intensity (I/I_o $\Delta J = 2$) *vs*. pH for **Eu.14** (blue) and **[Eu.10]$^{3-}$** (red) in the presence of carbonate. 1.0 mM Eu, 0.1 M NaCl, 30 mM $NaHCO_3$, λ_{ex} = 395 nm, 25°C.

The plotted data incorporates the pH dependant speciation of carbonate in aqueous solution, as well as the coordination equilibrium established with the Eu(III) complex and the deprotonation of coordinated water molecules (Equations 48, 51 and 52).[227] The solution pH determines the concentrations of HCO_3^-/CO_3^{2-} present. [HCO_3^-] falls from ~ 90% at pH 8.9 to less < 2% at pH 4.9, and at pH > 9 there are significant quantities of CO_3^{2-} present. The pK_a for the H_2CO_3/HCO_3^- equilibria is 6.4 while the HCO_3^-/CO_3^{2-} equilibria is 10.2.[14]

$$H_2CO_3 \underset{H^+}{\overset{-H^+}{\rightleftharpoons}} HCO_3^- \underset{H^+}{\overset{-H^+}{\rightleftharpoons}} CO_3^{2-} \quad (48)$$

$$Eu(H_2O)_2 \underset{H^+}{\overset{-H^+}{\rightleftharpoons}} [Eu(H_2O)(OH)]^- \quad (51)$$

$$Eu(H_2O)_2 \underset{H^+}{\overset{-H^+ + HCO_3^-}{\rightleftharpoons}} [Eu(CO_3]^- \quad (52)$$

The affinity for carbonate binding at pH 7.4 has been observed by Parker and co-workers to decrease with increasing overall negative charge of q = 2 complexes for a series of heptadentate tri-amide or polycarboxylate ligands.[202] Higher carbonate binding affinities were recorded for the positively charged tris amide, [Eu-DO3AMPh]$^{3+}$ derivatives; K = ~ 400 M^{-1} and ~ 5,600 M^{-1} where R = H or Me respectively. The affinity decreased sequentially for the neutral Eu-DO3MA complex followed by the negatively charged [Eu-gDO3A]$^{3-}$ species as the Eu(III) emission intensity *vs*. pH curves in the presence of carbonate shifted towards more basic pH values.

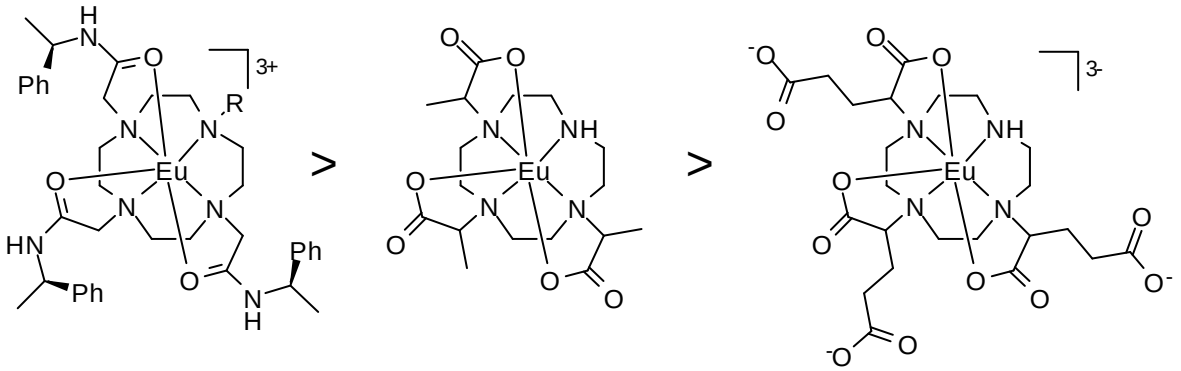

[Eu-DO3AMPh]$^{3+}$ **[Eu-DO3MA]** **[Eu-gDO3A]$^{3-}$**

R = Me, H

A similar trend is observed in this work as carbonate binding affinity at pH 7.4 decreases with increasing negative charge from **Eu.14** to **[Eu.10]$^{3-}$**. In strongly basic media, carbonate is clearly coordinated to both the neutral, **Eu.14**, and the negatively charged, **[Eu.10]$^{3-}$**, species. Quenching water molecules are displaced leading to more intense emission. Similar spectral form for each compound is observed with the ΔJ = 1 band adopting two broad peaks corresponding to the favoured TSAP isomer of the carbonate bound complex

(for full spectra see Appendix **A12**). Hydration states are calculated as q = 0.4 for both **[Eu.10]$^{3-}$** and **Eu.14**. As pH is lowered an equilibrium is established for both of the complexes. Water molecules compete with carbonate for coordination to the Eu(III) centres. Due to the electrostatic repulsive effects of the negatively charged, free acid species **[Eu.10]$^{3-}$**, carbonate binding does not occur to the same extent of neutral analogue, **Eu.14**. At physiological pH (7.4) Figure 63 clearly shows carbonate is binding to a much lesser degree for the post-enzyme model, **[Eu.10]$^{3-}$**, than for the pre-enzyme, **Eu.14**, with the calculated hydration state values q = 2.0 and q = 1.2 for **[Eu.10]$^{3-}$** and **Eu.14** respectively. In acidic media hydration states were calculated as q = 2.1 for both **[Eu.10]$^{3-}$** and **Eu.14**. (For full data analysis see Appendix **A13** and **A14**)

Eu(III) emission spectra observed at pH 7.4 in the presence of carbonate, are comprised of the equilibrium contributions from both the carbonate bound and water bound species. Equation 53 was applied to the lifetime data, recorded at pH 7.4 in the presence of carbonate, to calculate the mole fraction of carbonate bound complex present in solution, x, where $I_o^{CO_3^{2-}}$ and $k^{CO_3^{2-}}$ are the initial Eu(III) emission intensity and the calculated rate constant of the Eu(III) excited state decay of the carbonate bound species (i.e. measured at pH 10 where maximum carbonate binding occurs), $I_o^{H_20}$ and k^{H_2O} are the initial emission intensity and the calculated rate constant of the water bound species (i.e. measured at pH 5 where no carbonate binding occurs).

$$I_{obs} = xI_o^{CO_3^{2-}} e^{-k^{CO_3^{2-}}t} + (1-x)I_o^{H_2O} e^{-k^{H_2O}t} + offset \qquad (53)$$

Table 30 shows the measured the first order rate of decay constants, k, of the Eu(III) excited states of both **[Eu.10]$^{3-}$** and **Eu.14** in both acidic and basic media as well as the calculated percentage of the carbonate bound complex present.

	$k_{q=0.4}$ (ms^{-1}, pH 10)	$k_{q=2.1}$ (ms^{-1}, pH 5)	*q (pH 7.4)*	*x*	%
[Eu.10]$^{3-}$	2.14	3.36	2.0	0.05	5.0
Eu.14	2.20	3.67	1.2	0.42	42.0

Table 30. Measured x and hydration state, q, values at pH 7.4 for **[Eu.10]$^{3-}$** and **Eu.14** and percentage of carbonate bound species present in solution. 1.0 mM Eu, 0.1 M NaCl, pH 7.4, 25^{o}C. For full data analysis see Appendix **A9**, **A11**, **A13** and **A14**).

The calculated values for both **[Eu.10]$^{3-}$** and **Eu.14** were q = 2.1 and q = 0.4 in acidic and basic media respectively. The apparent q value at pH 7.4 in the presence of carbonate for

[Eu.10]$^{3-}$ comprises 95% of the q = 2.1 species and 5% of the q = 0.4 species, which is consistent with the observed value of q = 2.0. Likewise, the apparent q value for **Eu.14** comprises 58% of the q = 2.1 species and 42% of the q = 0.4 species, which is once again consistent with the observed value of q = 1.2 in the presence of carbonate at pH 7.4. There is over an eight-fold difference in the proportion of bound carbonate to the neutral, ester bearing complex than for the negatively charged free acid at pH 7.4, highlighting the repulsive effects of the unmasked post enzyme activated complex.

*4.3.3 Relaxivity vs. pH for **[Gd.10]**$^{3-}$ and **Gd.14** in the Presence of Carbonate*

As there is a clear difference in hydration states between the pre- and post-enzyme activated Eu(III) models in the presence of carbonate, relaxometric studies were carried out to see if the differences in relaxivities and, therefore, hypothetical changes in MR image intensity occur upon enzyme activation.

The relaxivity *vs*. pH titrations in the presence of carbonate were carried out for the Gd(III) analogues (Figure 64).

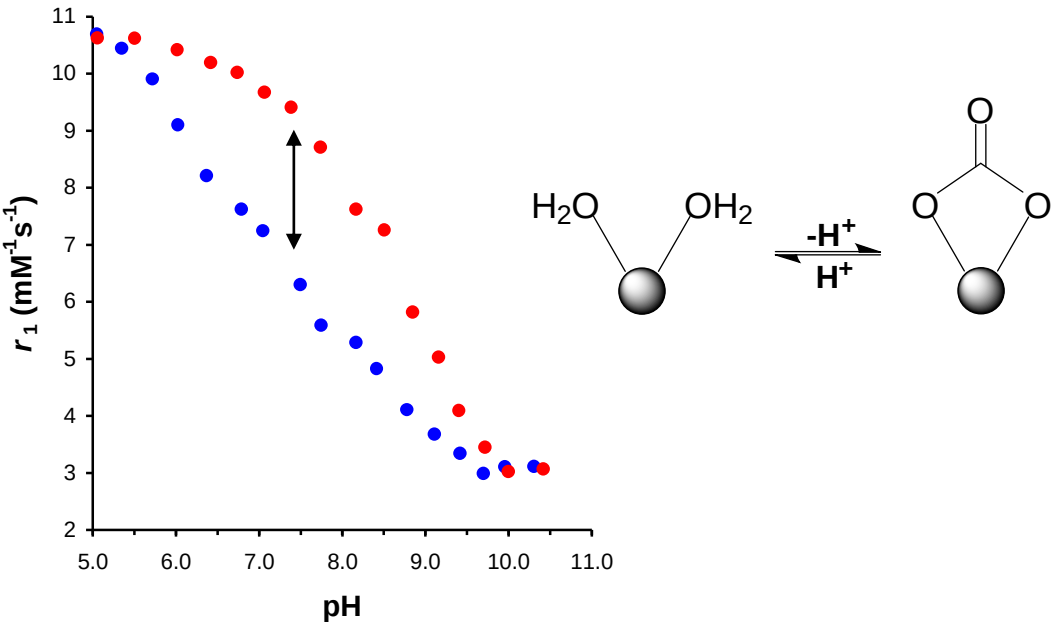

Figure 64. Relaxivity (r_1) *vs*. pH for **Gd.14** (blue) and **[Gd.10]**$^{3-}$ (red) in the presence of carbonate. 1.0 mM Gd, 0.1 M NaCl, 30 mM $NaHCO_3$, 20 MHz, 25°C.

The Gd(III) complexes behave in a similar manner to the Eu(III) complexes; however displacement of inner sphere water molecules has an opposite effect on the measured relaxivity of the Gd(III) analogue to that of the emission intensity of Eu(III). Gd(III) relaxivity is enhanced by the presence of inner sphere water molecules, whereas Eu(III) emission is quenched. As carbonate displaces water molecules in basic media, relaxivity decreases as the hydration state q decreases. At physiological pH there is a clear difference in

observed relaxivity for the pre- and post-enzyme complexes as carbonate has less affinity for the free acid species, **[Gd.10]$^{3-}$**. This is similar behaviour to that seen for the Eu(III) analogues. In the presence of carbonate relaxivity at physiological pH was measured at r_1 ~ 10 mM^{-1}s^{-1} and r_1 ~ 6 mM^{-1}s^{-1} for **[Gd.10]$^{3-}$** and **Gd.14** respectively, suggesting a potential increase in MR image intensity of ~ 60% upon enzyme activation.

The relaxivities measured in the absence of carbonate at pH 7.4 were r_1 = 11.3 mM^{-1}s^{-1} and r_1 = 10.2 mM^{-1}s^{-1} for **[Gd.10]$^{3-}$** and **Gd.14** respectively, which are considerably higher than for other q = 2 complexes, such as Gd-DO3A (r_1 = 5.7 mM^{-1}s^{-1}, 20 MHz, 25^{o}C).[51] As the hydration states are the same, the difference may arise from changes in water exchange lifetime, $\tau_{m,}$ or rotational correlation time, $\tau_{R,}$

*4.3.4 NMRD: Rotational Correlation Time, τ_R, for **[Gd.10]$^{3-}$** and **Gd.14***

As previously discussed in Chapter 1, Section 1.3.7, NMRD profiles are recorded in order to determine the rotational correlation time of a Gd(III) containing species. Figures 65 and 66 show the NMRD profiles for both **[Gd.10]$^{3-}$** and **Gd.14** with calculated data from Equations 22, 26 and 27 (Chapter 1) using the fitting parameters in Table 31. The increased molecular weight of the complexes results in an increase in τ_R with respect to Gd-DO3A, τ_R = 66 ps (25^{o}C).[51] The rotational correlation times calculated for both **[Gd.10]$^{3-}$** and **Gd.14** were identical, which is not surprising given the similar size and geometry of each complex.

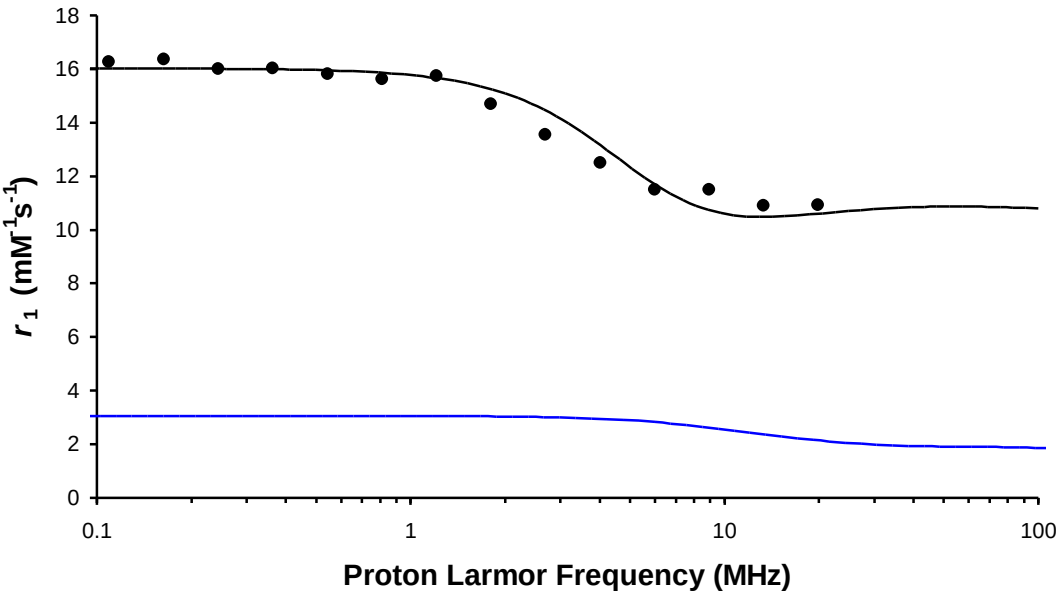

Figure 65. NMRD profile of **[Gd.10]$^{3-}$** showing the experimental data (black dots) and the calculated data (black line). The outer sphere contribution is shown as a blue line. 1.0 mM **[Gd.10]$^{3-}$** 0.1 M NaCl, pH 7.0, 25^{o}C.

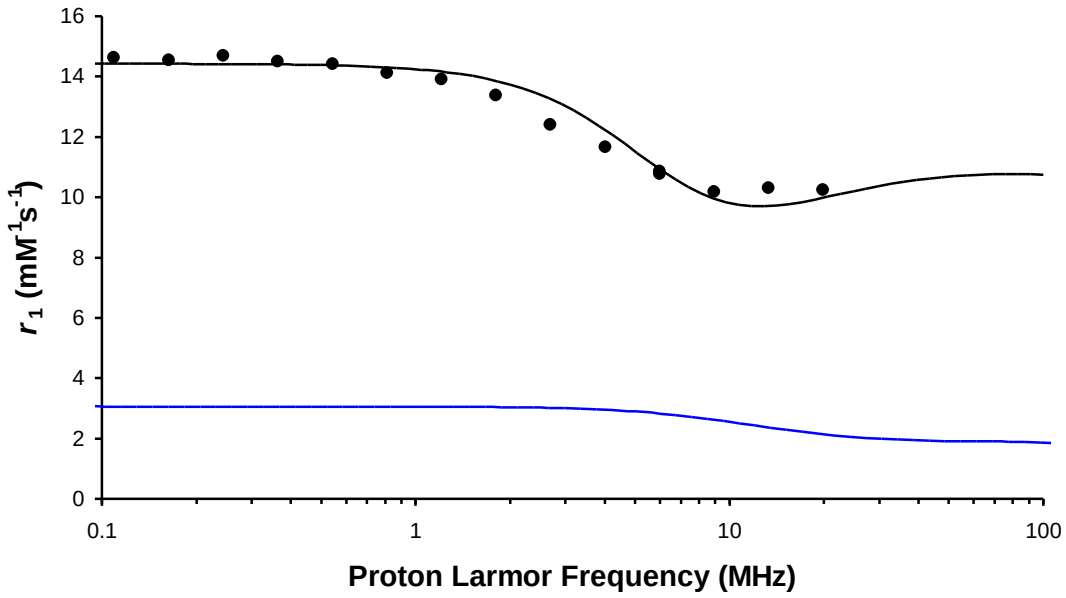

Figure 66. NMRD profile of **Gd.14** showing the experimental data (black dots) and the calculated data (black line). The outer sphere contribution is shown as a blue line. 1.0 mM **Gd.14** 0.1 M NaCl, pH 7.0, 25°C.

	τ_R (ps)	τ_v(ps)	τ_m (ns)	q	Δ^2 (s^{-2} x 10^{19})	r (Å)	a (Å)	D (cm^2 sec^{-1} x 10^{-5})
[Gd.10]$^{3-}$	120.0	22.98	20*	2	4.231	3.0	4.0	2.24
Gd.14	120.0	19.12	20*	2	6.173	3.0	4.0	2.24

Table 31. Fitting parameters for NMRD profiles of **[Gd.10]$^{3-}$** and **Gd.14** where τ_m is the water exchange lifetime (*estimated as calculations were made independent from VT ^{17}O NMR measurements), Δ^2 is the mean square zero field splitting energy and τ_v is the correlation time for its modulation, r is the Gd-H water distance, a is the shortest distance of approach and D is the diffusion coefficient. Data was collected using 1.0 mM complex, 0.1 M NaCl, pH 7.4 at 25°C.

*4.3.5 Variable Temperature ^{17}O NMR: Water Exchange Lifetime, τ_m, for **Gd.14***

An extremely short water exchange lifetime was measured for **Gd.14** at τ_m = 7.9 ns using variable temperature ^{17}O NMR. The data from Figure 67 was applied to Equations 29-32 (Chapter 1) using the fitting parameters in Table 32. A 20-fold increase in the water exchange rate was observed with respect to Gd-DO3A; τ_m = 160 ns (2.1 T),[51] and 3-fold increase with respect to **[Gd.10]$^{3-}$**; τ_m = 30 ns (0.5 T, reported by Parker and co-workers[77]) which is comparable to the highest water exchange rate ever measured for a Gd(III) chelate, recently reported by Tóth and co-workers in which the eight coordinate *N*,*N*'-bis(6-carboxy-2-pyridylmethyl)ethylendiamine-*N*,*N*'-methylenephosphoric acid chelate was incorporated, where the water exchange lifetime was measured as τ_m = 1.14 ns, which is similar to $[Gd(H_2O)_8]^{3+}$, τ_m = 1.24 ns (7.05 T).[228]

The non-bell shaped curve obtained from the ^{17}O data (Figure 67) corresponding to the extremely fast water exchange rate observed for **Gd.14**, is attributed to the presence of the

hydrophobic, ethyl ester containing side chains causing a higher degree of organisation of the second sphere water molecules, creating a greater network of H-bonding between the ligated and bulk water molecules resulting in the enhancement of the water exchange rate.[78] This fast exchange accounts for the relatively high observed relaxivity of the complex.

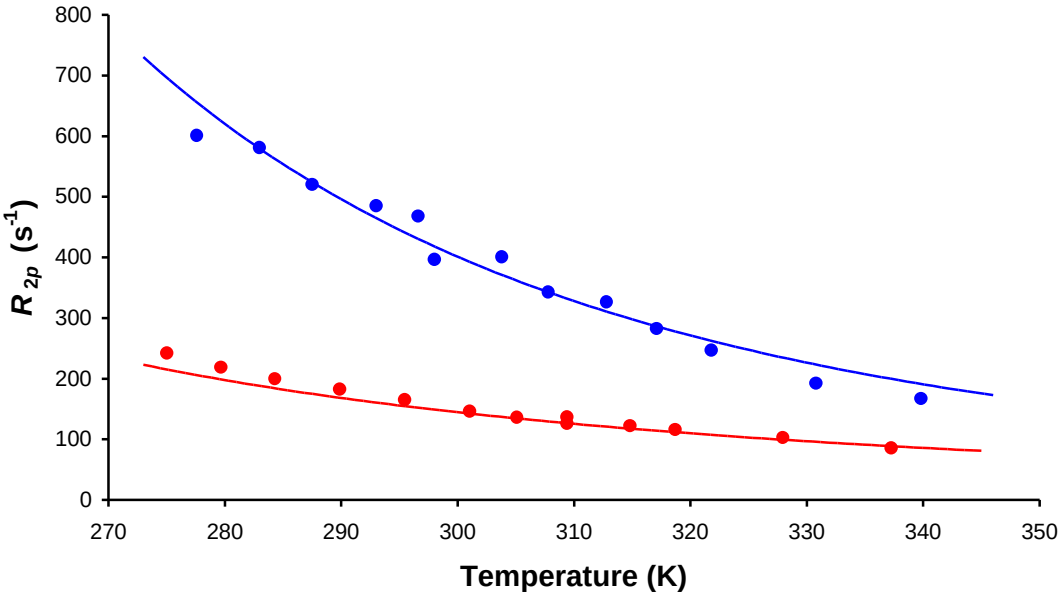

Figure 67. Variation of ^{17}O transverse relaxation rate, R_{2p}, with temperature for **Gd.14** showing the experimental data (dots) and the calculated data (lines). (Red = 2.1 T, blue = 9.4 T). 20.0 mM **Gd.14**, pH 6.

	Gd.14
τ_m (ns)	7.9
τ_v(ps)	10
ΔH_m (kJ mol^{-1})	13.7
ΔH_v (kJ mol^{-1})	5
$A/\hbar$ (x10^6 rad s^{-1})	-3.6
Δ^2 (s^{-2} x 10^{19})	9.0

Table 32. **Gd.14** fitting parameters for ^{17}O NMR where Δ^2 is the mean square zero field splitting energy and τ_v is the correlation time for its modulation, ΔH_m is activation enthalpy of water exchange, ΔH_v is the activation enthalpy for the modulation of the zero field splitting (ZFS) and $A/\hbar$ is the Gd-O scalar coupling constant. 10.2 mM complex, pH 5.5, 2.1 T.

4.4 Esterase Hydrolysis Experiments using Model Complexes

*4.4.1 ^1H NMR Investigation of Esterase Hydrolysis of **Y.14***

Ethyl ester hydrolysis results in the formation of ethanol (Scheme 25). ^1H NMR spectroscopy can be used to show the production of ethanol as a result of esterase hydrolysis as resonances appear at δ = 1.0 and 3.5 ppm, corresponding to the methyl and CH_2 protons of

ethanol respectively. At the same time, ethyl ester resonances at δ = 1.1 and 4.0 ppm disappear upon hydrolysis, once again corresponding to the methyl and CH_2 protons.

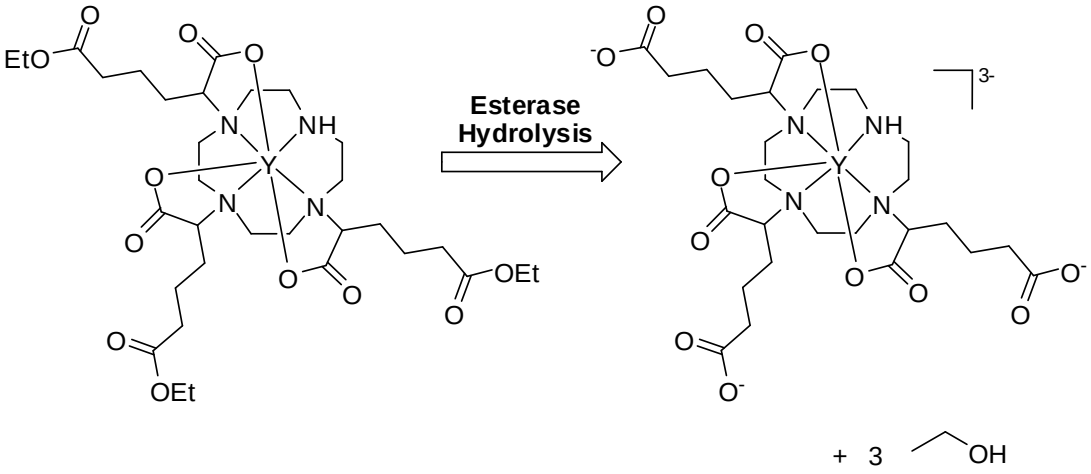

Scheme 25

In order to determine the effect of esterase on the ethyl ester model complex, the yttrium analogue **Y.14** was prepared. Yttrium is non-paramagnetic, and therefore ^{1}H NMR spectra can be easily studied as chemical shift values and line widths are not affected as they are for the paramagnetic Eu(III) analogues; these display increased spectral line broadening due to the inherent paramagnetism. The ionic radius of Y(III) is similar to Ho(III) at r = 1.02 Å; it is the most similar sized non-paramagnetic ion to Gd(III) (r = 1.05 Å). La(III) and Lu(III) ions are also non-paramagnetic but posses ionic radii too dissimilar to Gd(III) at r = 1.16 Å and r = 0.97 Å respectively.[25, 26] Two solutions were prepared in D_2O, each containing ~ 6 mg **Y.14** (equating to ~ 15 mM). 100 units of pig liver esterase, chosen for its known ability to hydrolyse ethyl[229] and acetoxymethyl esters,[230] was added to one solution. Both were then incubated at 37^{o}C at pD 7.4 for 72 hours. The resulting ^{1}H NMR spectra are shown (Figure 68).

The broad resonances which span δ ~ 1.4 to 2.3 ppm correspond to the aliphatic carbon CH_2s. The remaining resonances from δ ~ 2.4 to δ ~ 3.4 ppm are those of the 16 ring protons and the NC*H*(CO_2)CH_2. The spectral line broadening occurs as a result of the fluxionality of the complex. Sharper resonances could have been observed upon cooling to reduce the degree of fluxionality and increase complex rigidity. This was not necessary, however, as the ethanol and ethyl ester resonances could clearly be observed in the room temperature ^{1}H NMR spectra. The spectrum recorded in the absence of esterase shows that no ethanol is formed. This proves that the compound is stable in solution at 37^{o}C at pD 7.4. The integration of the spectra shows the ethyl ester resonances at δ = 1.1 ppm and δ = 4.0 ppm to be in a 3:2 ratio with each other, as expected for the CH_3 and CH_2 protons, and in a 1:6 ratio to the remaining resonances, which correspond to the remaining 37 protons of the complex.

The spectrum recorded in the presence of esterase shows the generation of ethanol as peaks at δ = 1.0 and 3.5 ppm are present following incubation at pD 7.4. The ratio of the ethyl ester to the remaining complex proton peaks is now 1:9, clearly demonstrating the production of ethanol as the ethyl esters are hydrolysed. The samples were left for a further 7 days in order to see if the ethyl ester peaks disappeared entirely and, therefore, complete hydrolysis occurred. No further ethanol production was seen, however, suggesting that the enzyme had de-natured. Relatively high concentrations of **Y.14** were necessary in order to obtain clear ^{1}H NMR spectra. 100 units of esterase should be sufficient for the catalytic process, but clearly this amount is only able to process ~ 10% of the sample. When 1000 units of pig liver esterase were used, very poor, unclear spectra with extremely high background noise were observed.

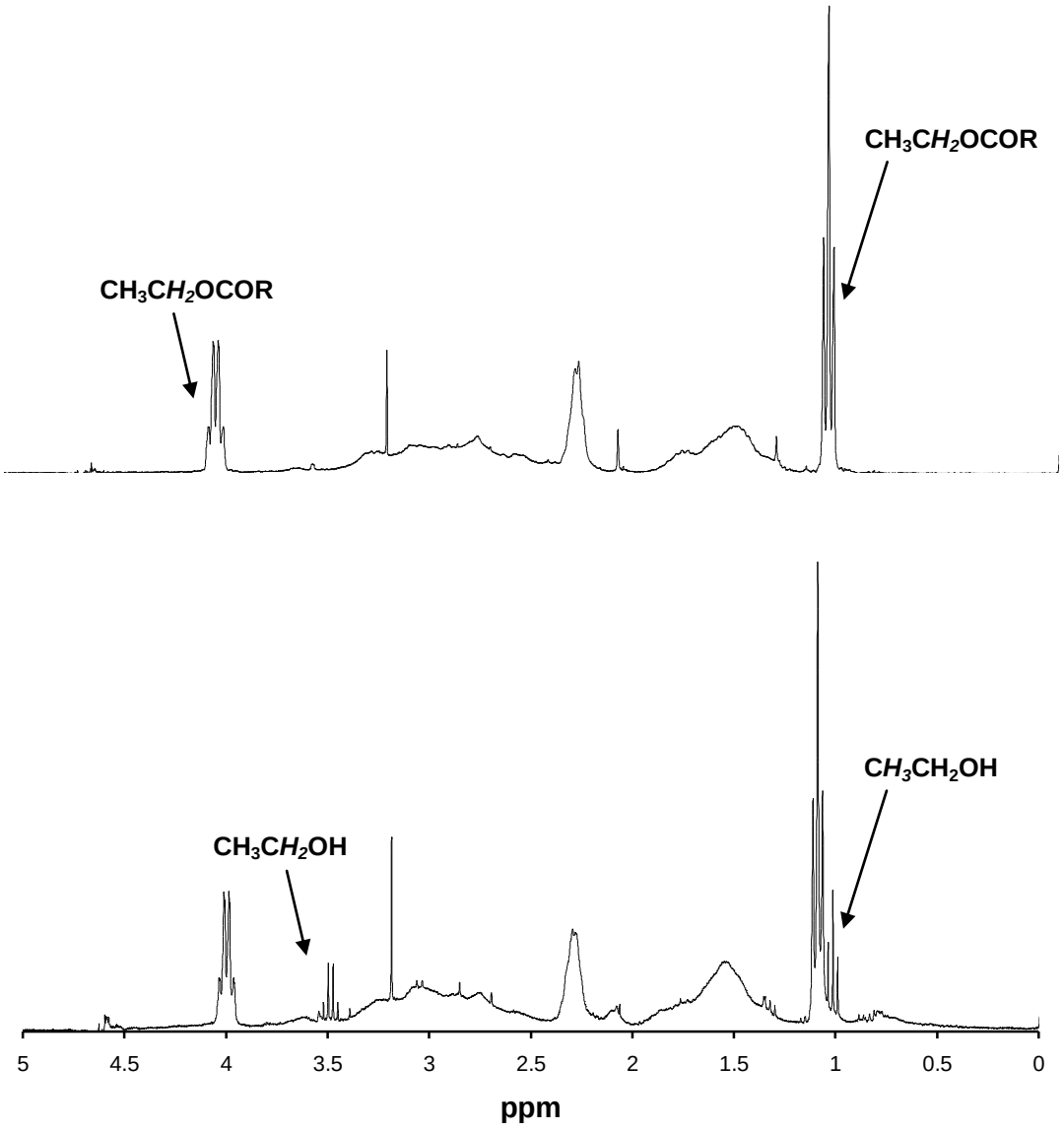

Figure 68. ^{1}H NMR spectra of **Y.14** (15 mM) after 72 hours incubation (37^{o}C) in the absence (above) and presence (below) of pig liver esterase (100 units). pD 7.4, 27^{o}C.

The ^{1}H NMR data does, nevertheless, show hydrolysis has occurred. This lead to further studies using both luminescence (Eu) and relaxometric (Gd) methods. In order to be certain of complete ethyl ester hydrolysis, higher ratios of enzyme:complex were employed.

*4.4.2 Relaxometric Investigation of **[Gd.10]$^{3-}$** and **Gd.14** in the Presence of Esterase.*

Solutions containing esterase were prepared using both the pre-enzyme activated ethyl ester model, **Gd.14**, and the post-enzyme activated model, **[Gd.10]$^{3-}$**, as a control. Four solutions were prepared, each containing 0.1 M NaCl and adjusted to pH 7.4 by addition of small aliquots of HCl or NaOH; 1. ~ 0.5 mM Gd; 2. ~ 0.5 mM Gd, 10 mM $NaHCO_3$; 3. ~ 0.5 mM Gd, 100 units esterase; 4. ~ 0.5 mM Gd, 10 mM $NaHCO_3$, 100 units esterase. Gd(III) concentrations were determined from mineralization of the samples using nitric acid (Chapter 6, Section 6.1.11). Tables 33 and 34 show the ^{1}H relaxation data measured after the solutions were incubated at 37^{o}C for two hours, where T_{1obs} is the observed longitudinal water proton relaxation time measured from standard inversion recovery experiments (Chapter 6, Section 6.1.6), R_{1obs} is the observed water proton longitudinal relaxation rate ($1/T_{1obs}$), R_{1p} is the paramagnetic water proton relaxation rate (R_{1obs} – 0.38, the diamagnetic contribution of the bulk water molecules) and r_1 is relaxivity (R_{1p}/[Gd]).

Solution	T_{1obs} (s)	R_{1obs} (s^{-1})	R_{1p} (s^{-1})	r_1 ($mM^{-1}s^{-1}$)
1. Gd Alone	0.43	2.32	1.94	10.2
2. Gd + $NaHCO_3$	0.68	1.47	1.09	5.7
3. Gd + Esterase	0.41	2.44	2.06	10.8
4. Gd + $NaHCO_3$ + Esterase	0.41	2.44	2.06	10.8

Table 33. ^{1}H relaxation data of **Gd.14** solutions 1 to 4 following incubation (2 hours at 37^{o}C). 0.19 mM **Gd.14**, 20 MHz, 25^{o}C.

Solution	T_{1obs} (s)	R_{1obs} (s^{-1})	R_{1p} (s^{-1})	r_1 ($mM^{-1}s^{-1}$)
1. Gd Alone	0.35	2.86	2.48	11.3
2. Gd + $NaHCO_3$	0.36	2.77	2.39	10.8
3. Gd + Esterase	0.36	2.77	2.39	10.8
4. Gd + $NaHCO_3$ + Esterase	0.36	2.77	2.39	10.8

Table 34. ^{1}H relaxation data of **[Gd.10]$^{3-}$** solutions 1 to 4 following incubation (2 hours at 37^{o}C). 0.22 mM **[Gd.10]$^{3-}$**, 20 MHz, 25^{o}C.

The results successfully proved the ester hydrolysis of the ethyl esters of **Gd.14**. An 89% difference in the observed relaxivity following incubation at 37^{o}C was observed for the solutions in the presence of carbonate; r_1 = 5.7 $mM^{-1}s^{-1}$ (solution 2) and r_1 = 10.8 $mM^{-1}s^{-1}$ (solution 4), thus proving hydrolysis of the ethyl ester groups to be occurring in solution 4 to

which, 100 units of esterase were added. This follows the generation of the negatively charged species upon esterase hydrolysis, which disfavours carbonate binding and in turn allows waters to exchange with the Gd(III) centre, raising the observed relaxivity (Table 33). As relaxivity remained low for solution 2 it can be concluded that the complex remained intact and the ethyl esters did not hydrolyse under the experimental conditions.

The equivalent experiments using the negatively charged post-enzyme activated model **[Gd.10]$^{3-}$** (Table 34) showed important parallels to those observed for **Gd.14**. These control experiments demonstrate that the presence of esterase has no great overall effect on the observed relaxivity of **[Gd.10]$^{3-}$**. The resulting relaxivity upon addition of esterase to **Gd.14** in the presence of carbonate is the same as that observed for **[Gd.10]$^{3-}$** (i.e. solution 4), thus proving conversion from **Gd.14** to **[Gd.10]$^{3-}$** upon esterase hydrolysis. The slight decrease between solutions 1 and 2 is due to the low binding affinity for carbonate of **[Gd.10]$^{3-}$**. The Eu(III) emission lifetime measurements suggested a small quantity of the carbonate bound species to be present in solution, which would result in an overall decrease in the observed relaxivity upon addition of carbonate. The difference in the overall relaxivity of the both complexes (i.e. solution 1; the complex alone in 0.1 M saline solution), showed the negatively charged species **[Gd.10]$^{3-}$** to have higher relaxivity than the neutral species **Gd.14** (r_1 = 11.3 $mM^{-1}s^{-1}$ and r_1 = 10.2 $mM^{-1}s^{-1}$ respectively). The negative charge may facilitate faster water exchange and enhance the outer sphere and second sphere water proton contribution resulting in higher relaxivities of the **[Gd.10]$^{3-}$** complex. This results in the observed increase in relaxivity from solution 1 to solutions 3 and 4 of the ethyl ester model complex, i.e. the relaxivity measured for solutions 3 and 4 are now of **[Gd.10]$^{3-}$**. This once again proves the complete conversion of **Gd.14** to **[Gd.10]$^{3-}$** upon addition of esterase.

*4.4.3 Luminescence Investigation of **[Eu.10]$^{3-}$** and **Eu.14** in the Presence of Esterase*

Hydrolysis of the ethyl ester groups and the consequential inhibition of carbonate anion binding has been successfully demonstrated by both ^{1}H NMR spectroscopy (Y) and relaxometric (Gd) studies; the later showed a large increase in observed relaxivities upon enzyme activation. Recalling Section 4.3.2 it was hypothesised that enzyme activation could be monitored *via* the luminescent properties of the Eu(III) analogues. Upon addition of carbonate to the neutral complex **Eu.14** at pH 7.4 the emission intensity of the ΔJ = 2 band increased, while the emission maxima shifted from λ_{max} = 615 nm to λ_{max} = 617 nm. The spectral form of the ΔJ = 1 band also altered upon addition as the three sharp peaks observed when no carbonate was present was replaced by two broad peaks as carbonate was added. Such spectral changes were attributed to the change in isomeric distribution in solution between the SAP and TSAP geometries about the Eu(III) centre at pH 7.4. The carbonate

bound complex formed upon displacement of the inner sphere water molecules favours the TSAP isomer.[202] At pH 10 in the presence of carbonate the spectra for both **[Eu.10]**$^{3-}$ and **Eu.14** show two ΔJ = 1 peaks, corresponding to the favoured TSAP of the carbonate bound complex (See Appendix **A12**). Therefore, at pH 7.4 the observed spectrum for **Eu.14** in the presence of carbonate is composed of contributions from a greater equilibrium concentration of the carbonate bound TSAP isomer, i.e. an overlay of the spectra observed at pH 5 and at pH 10. No such spectral change was observed at pH 7.4 for the negatively charged **[Eu.10]**$^{3-}$ model as little carbonate was seen to be binding to the Eu(III) centre.

Four solutions were prepared in the same manner as for the relaxometric investigations of the Gd(III) analogues, each containing 0.1 M NaCl and adjusted to pH 7.4; 1. ~ 1.0 mM Eu; 2. ~ 1.0 mM Eu, 30 mM $NaHCO_3$; 3. ~ 1.0 mM Eu, 100 units esterase; 4. ~ 1.0 mM Eu, 30 mM $NaHCO_3$, 100 units esterase. Eu(III) emission spectra were recorded both before and after incubation in the presence and absence of esterase. In order eliminate the complication of background fluorescence from esterase, a 0.1 ms delay was incorporated prior to emission being recorded, i.e. the samples were excited at 395 nm and the delay was imposed, during which, all background organic fluorescence decayed, thus only the longer lived emission of Eu(III) was observed. Lifetime studies were also conducted to determine any change in hydration state upon addition of esterase.

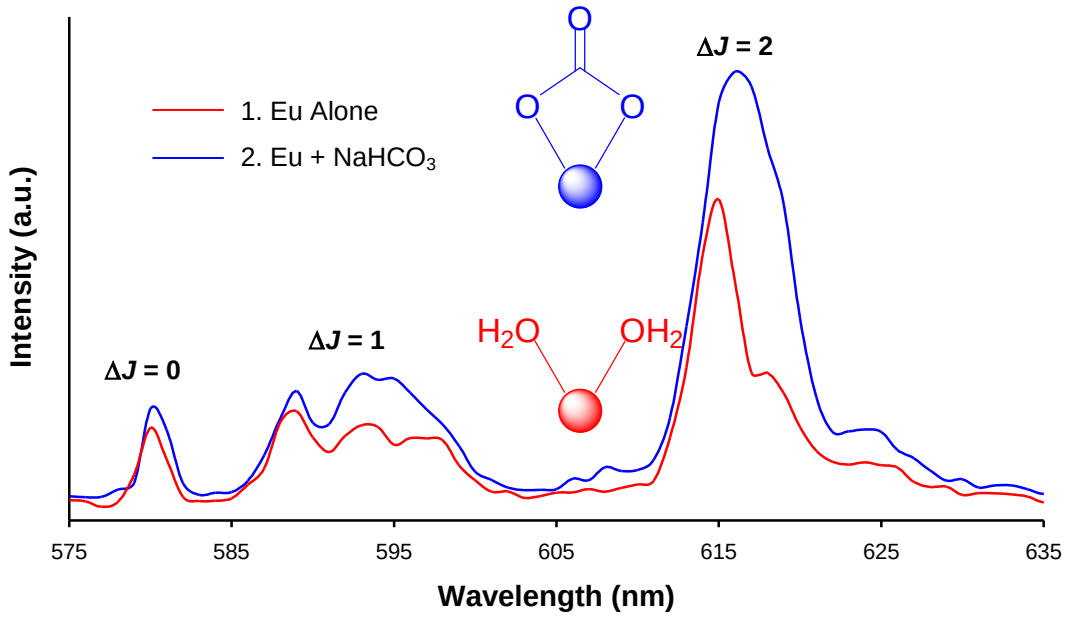

Figure 69. Eu(III) emission spectra for **Eu.14** solutions 1 (red) and 2 (blue) prior to incubation at 37°C. λ_{ex} = 395 nm, 0.1 ms delay, pH7.4, 25°C.

Figure 69 shows the resulting spectra of solutions 1 and 2 prior to incubation at 37°C at pH 7.4 for the neutral complex **Eu.14**. The change in intensity of the ΔJ = 2 band is clearly

observed, as well as the expected spectral change of the $\Delta J = 1$ band, indicating that carbonate displaces the quenching water molecules as the carbonate binding equilibrium is established.

All four solutions were incubated at 37°C for two hours. The resulting spectra are shown in Figure 70. Once again, the emission spectrum of the carbonate containing solution 2 remained unchanged following incubation, showing the Eu(III) complex remained intact and that the ester groups not hydrolysed under the experimental conditions; the $\Delta J = 2$ emission intensity is still high at λ_{max} = 617 nm and the $\Delta J = 1$ band is still quite broad. Hydrolysis of the ethyl ester groups occurs for the esterase and carbonate containing solution 4 as the $\Delta J = 2$ band shifts to λ_{max} = 615 nm, less intense and is similar to that of solutions 1 and 3 where no carbonate is present. Furthermore, the appearance of the $\Delta J = 1$ band has also changed, now containing three peaks, similar to the non-carbonate containing solutions 1 and 3. This suggests a complete hydrolysis of the ethyl ester groups has occurred as little or no carbonate appears to be binding to the complex in solution 4. The similarity in spectral forms of both solutions 3 and 4 demonstrates that the presence of esterase has little effect on the Eu(III) emission properties of the complex.

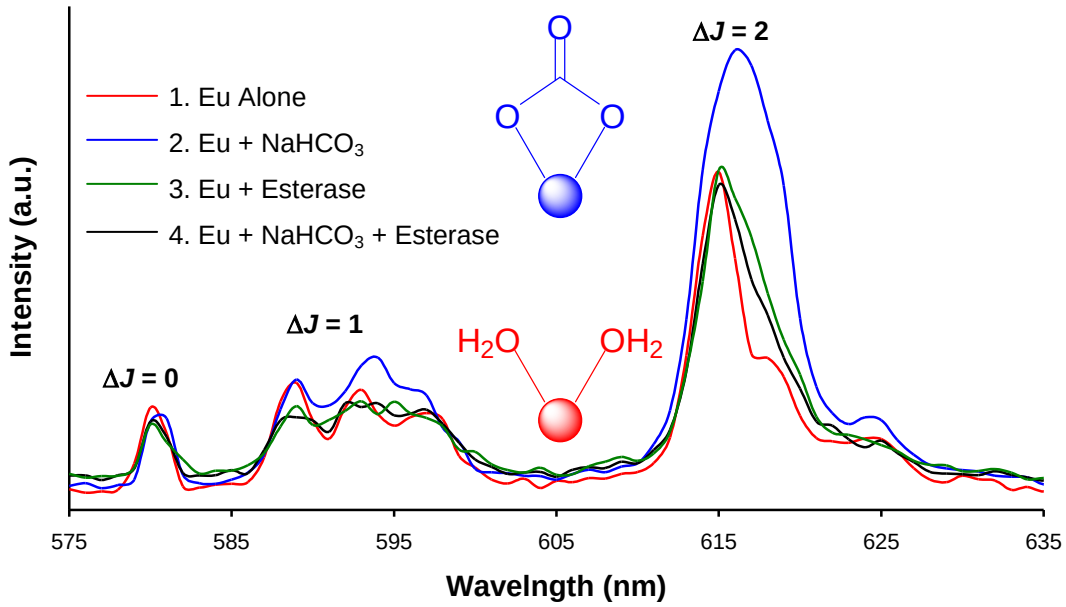

Figure 70. Eu(III) emission spectra for **Eu.14** solutions 1 (red), 2 (blue), 3 (green) and 4 (black) following 2 hours incubation at 37°C. λ_{ex} = 395 nm, 0.1 ms delay, pH 7.4, 25°C.

As a control, the same solution compositions of the post-enzyme activated model, **[Eu.10]$^{3-}$**, were also prepared and their Eu(III) emissive properties were investigated following incubation at 37°C (Figure 71). As there is very little difference between the spectral forms and intensities of each of the four solutions of **[Eu.10]$^{3-}$** it can be concluded that the presence of esterase has no effect on the nature of the Eu(III) emission observed.

Likewise, as the emission spectra of the esterase hydrolysed **Eu.14** are very similar to those seen for the post-enzyme hydrolysed model complex **[Eu.10]$^{3-}$**, it can be confidently concluded that the species is indeed being converted to from **Eu.14** to form **[Eu.10]$^{3-}$** upon enzyme activity.

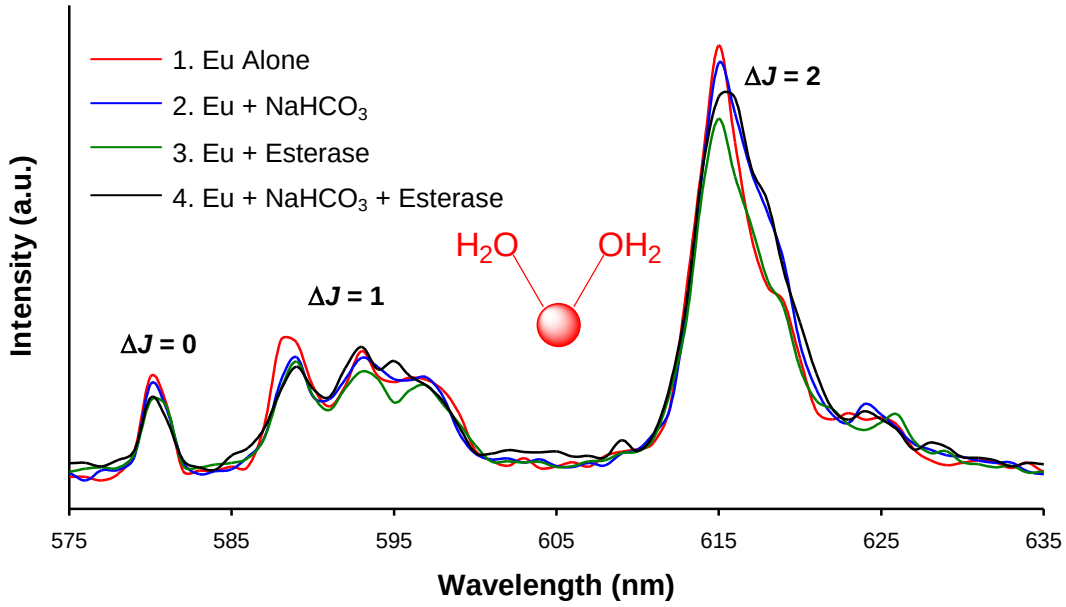

Figure 71. Eu(III) emission spectra for **[Eu.10]$^{3-}$** solutions 1 (red), 2 (blue), 3 (green) and 4 (black) following 2 hours incubation at 37°C. λ_{ex} = 395 nm, 0.1 ms delay, pH 7.4, 25°C.

Luminescent lifetime studies were carried out for each of the four solutions of both **Eu.14** and **[Eu.10]$^{3-}$** to determine the hydration states of the complexes for each of the experimental solutions. The results are summarised in Tables 35 and 36.

Solution	k_{H_2O} (ms^{-1}) (initial)	k_{D_2O} (ms^{-1}) (initial)	q	k_{H_2O} (ms^{-1}) (incubated)	k_{D_2O} (ms^{-1}) (incubated)	q
1. Eu Alone	3.32	1.36	2.1	3.30	1.31	2.1
2. Eu + $NaHCO_3$	2.83	1.61	1.2	2.82	1.54	1.2
3. Eu + Esterase	-	-	-	3.24	1.49	1.8
4. Eu + $NaHCO_3$ + Esterase	-	-	-	3.13	1.47	1.7

Table 35. Measured hydration state values, q, **Eu.14** solutions 1 to 4 at pH 7.4, where k is the experimentally determined rate constant for the decay of the Eu(III) excited state. Incubation was at 37°C for 2 hours. pH 7.4, 25°C. For full data analysis see Appendix **A15 and A16**.

The hydration state variations shown in Table 35 are consistent with previously observed luminescent lifetime data. A decrease in the calculated hydration state, q, is observed upon the addition of carbonate (solution 1 c.f. 2) as an equilibrium is established between the **Eu.14(H$_2$O)$_2$** and **[Eu.14CO$_3$]$^{2-}$** complexes at pH 7.4, resulting in the

equilibrium hydration state value of q = 1.2. Upon addition of esterase there is an overall decrease in observed hydration state, (solution 3 and 4 c.f. solution 1). This may be due to a change in the outer sphere water proton effects, which in turn would lower the observed calculated q values. The calculated q value of the carbonate containing solution 4 is lower than that of 3 where no carbonate is present. This is consistent with the slight carbonate affinity of the ethyl ester hydrolysed complex **[Eu.10]$^{3-}$**, which is now present in both solution 3 and 4. The higher q value of solution 4 with respect to solution 2 indicates that the negatively charged species has been generated upon esterase hydrolysis as carbonate binding is disfavoured, resulting in a higher hydration state of the complex as inner sphere waters are no longer displaced.

The hydration state calculations were also carried out for the post-enzyme model, **[Eu.10]$^{3-}$**, as a control (Table 36). The decrease in q values between solution 1 and 2 once again confirms a small proportion of the carbonate bound species to be present in solution pH 7.4. The similarity between solution 3 and 4 for both **[Eu.10]$^{3-}$** and **Eu.14** experiments confirms that conversion of **Eu.14** to **[Eu.10]$^{3-}$** occurs following ethyl ester hydrolysis upon addition of esterase.

Solution	k_{H_2O} (ms^{-1}) (initial)	k_{D_2O} (ms^{-1}) (initial)	q	k_{H_2O} (ms^{-1}) (incubated)	k_{D_2O} (ms^{-1}) (incubated)	q
1. Eu Alone	3.30	1.33	2.1	3.34	1.38	2.1
2. Eu + $NaHCO_3$	3.26	1.38	2.0	3.33	1.42	2.0
3. Eu + Esterase	-	-	-	3.29	1.50	1.8
4. Eu + $NaHCO_3$ + Esterase	-	-	-	3.12	1.44	1.7

Table 36. Measured hydration state values, q, **[Eu.10]$^{3-}$** solutions 1 to 4 at pH 7.4, where k is the experimentally determined rate constant for the decay of the Eu(III) excited state. Incubation was at 37°C for 2 hours. pH 7.4, 25°C. For full data analysis see Appendix **A17 and A18**.

4.5 Esterase Hydrolysis Experiments using Acetoxymethyl Ester Complexes

Enzyme activation has been observed for the ethyl ester model complex and, as such, similar results were expected with the acetoxymethyl ester equivalent. Due to the much more base sensitive hydrolysis of acetoxymethyl esters, however, neither relaxivity (Gd) or emission intensity (Eu) *vs.* pH titrations could be carried out as acetoxymethyl esters readily hydrolyse above pH 8.

*4.5.1 ^{1}H NMR Investigation of Esterase Hydrolysis of **Y.18***

Esterase hydrolysis of acetoxymethyl ester groups results in the formation of ethanoic acid and formaldehyde (Scheme 26).

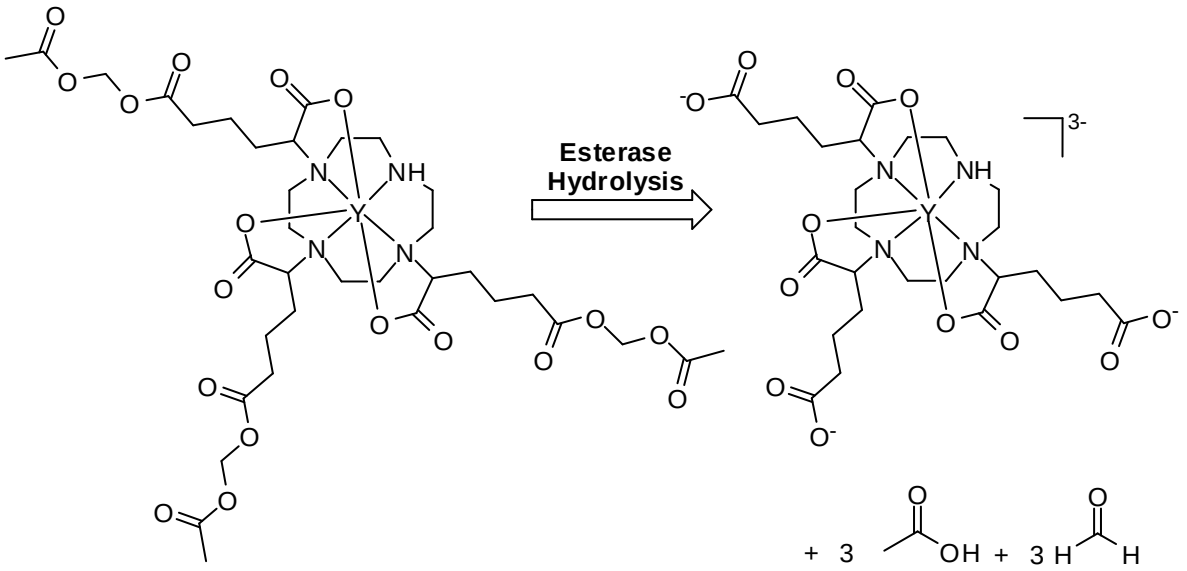

Scheme 26

^{1}H NMR spectroscopy was employed to monitor this reaction in the same way as for the Y(III) ethyl ester analogue (Section 4.4.1). Hydrolysis is observed by monitoring the disappearance of the ~OC*H*$_2$O~ resonances of the acetoxymethyl ester groups at δ = 5.7 ppm upon the addition of esterase.

Two solutions were prepared containing ~ 5 mg **Y.18** (equal to ~ 13 mM) in D_2O. 100 units of esterase were added to one of the samples and they were both incubated at 37^{o}C at pD 7.4. The complex proved to be more robust than was previously anticipated, requiring incubation for 24 hours before hydrolysis took place. The ^{1}H NMR spectrum following incubation of the sample in the presence of esterase shows loss of the resonance at δ = 5.7 ppm, proving hydrolysis takes place (Figure 72).

The extent to which the peak was lost in comparison to results observed for the ethyl ester analogue suggests the expected more facile hydrolysis of the acetytoxymethyl ester group. The ^{1}H NMR spectrum for the solution in the absence of esterase following incubation proves the complex to be stable under these conditions for 24 hours as the resonance at δ = 5.7 ppm was still present. The solutions were left for a further night resulting in the expected complete hydrolysis of the acetoxymethyl ester groups in both samples.

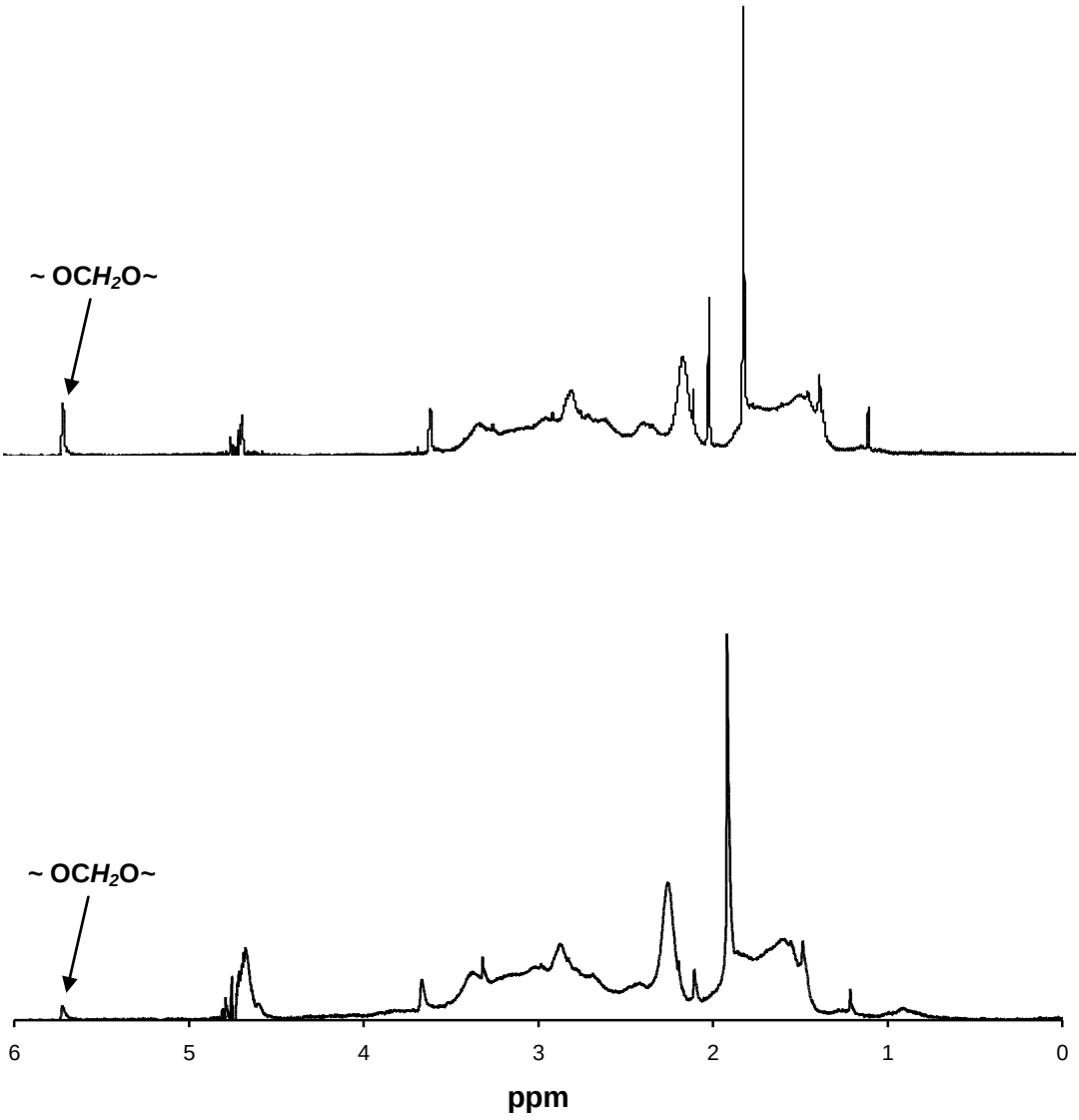

Figure 72. ^{1}H NMR spectrum of **Y.18** (15 mM) after 24 hours incubation (37^{o}C) in the absence (above) and presence (below) of 100 units pig liver esterase. 300 MHz; D_2O; pD 7.4, 27^{o}C.

*4.5.2 Luminescence Investigation of **Eu.18** in the presence of Esterase*

Following the same procedures outlined in Section 4.4.3 for the ethyl ester analogue **Eu.14**, four solutions containing **Eu.18** were prepared in 0.1 M NaCl and adjusted to pH 7.4; 1. ~ 1.0 mM Eu; 2. ~ 1.0 mM Eu, 30 mM $NaHCO_3$; 3. ~ 1.0 mM Eu, 100 units esterase; 4. ~ 1.0 mM Eu, 30 mM $NaHCO_3$, 100 units esterase.

Figure 73 shows the emission spectra of solutions 1 and 2 prior to incubation (no delay incorporated into the spectral scan).

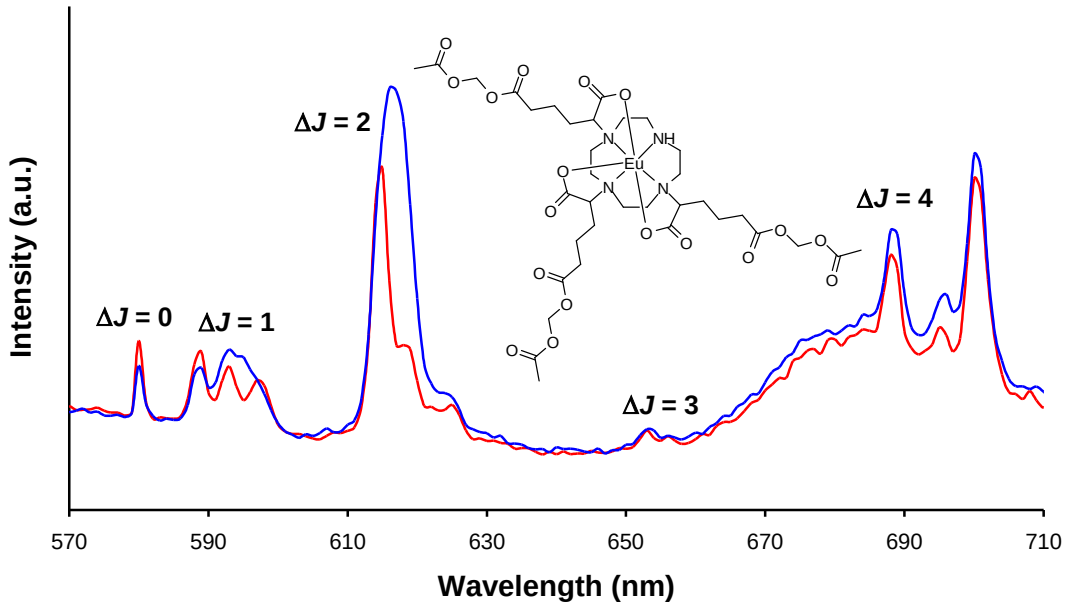

Figure 73. Eu(III) emission spectra for **Eu.18** in the presence (blue) and absence (red) of carbonate. 1.0 mM **Eu.18**, 0.1 M NaCl, 30 mM $NaHCO_3$ λ_{ex} = 395 nm, pH 7.4, 25°C.

The observed spectra are consistent with those obtained for the model complex **Eu.14**. Emission intensity of the ΔJ = 2 band increased upon addition of carbonate and shifted from λ_{max} = 615 nm to λ_{max} = 617 nm, while the form of the spectra at the ΔJ = 1 band varied in similar way to that observed for the **Eu.14** analogue. The four samples were incubated at 37°C and at pH 7.4; the resulting spectra were measured incorporating a 0.1 ms delay to allow for the decay of the esterase background fluorescence (Figure 74).

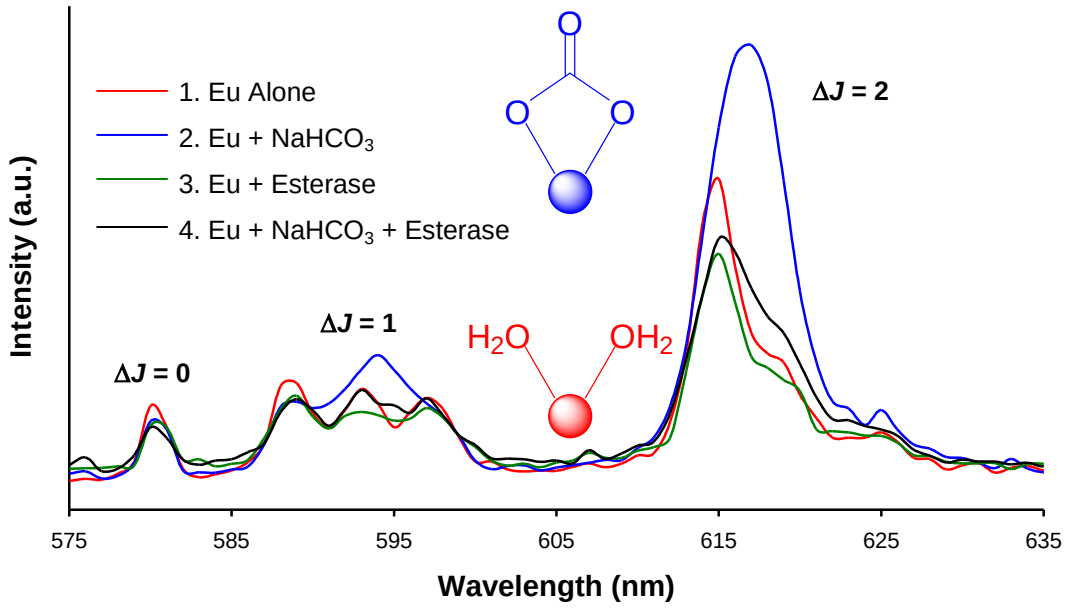

Figure 74. Eu(III) emission spectra for **Eu.18** solutions 1 (red), 2 (blue) , 3 (green) and 4 (black) following 2 hours incubation at 37°C. λ_{ex} = 395 nm, 0.1 ms delay, pH 7.4, 25°C.

The observed data is consistent with predicted results, mirroring tests with the ethyl ester analogue. Higher Eu(III) emission intensity of the $\Delta J = 2$ band is observed in the presence of carbonate (solution 2) than in its absence (solution 1) of carbonate as quenching inner sphere waters are displaced. Furthermore, the spectral form of the $\Delta J = 1$ band is consistent with the increase of carbonate bound complex present in solution. The spectral form of solution 2 does not change following incubation, which confirms the acetoxymethyl ester groups have remained intact and have not hydrolysed under experimental conditions. The similarity in intensity and spectral form of solutions 3 and 4 c.f. solution 1 suggest that complete hydrolysis of the acetoxymethyl ester groups has occurred. The reduction in emission intensity of the $\Delta J = 2$ band and the presence of three sharp peaks of the $\Delta J = 1$ band suggest that carbonate binding is disfavoured as the negatively charged species is generated. Furthermore, the spectral forms are similar to those observed during the equivalent control experiments with **[Eu.10]**$^{3-}$ (Section 4.4.3), suggesting complete conversion form **Eu.18** to **[Eu.10]**$^{3-}$ following esterase hydrolyses of the acetoxymethyl ester groups.

Lifetime studies were also carried out in order to confirm full hydrolysis had taken place and to show consistency with each of the previous Eu(III) models (Table 37).

Solution	k_{H_2O} (ms^{-1}) (initial)	k_{D_2O} (ms^{-1}) (initial)	q	k_{H_2O} (ms^{-1}) (incubated)	k_{D_2O} (ms^{-1}) (incubated)	q
1. Eu Alone	3.26	1.22	2.1	3.40	1.44	2.1
2. Eu + $NaHCO_3$	2.75	1.46	1.2	2.76	1.47	1.2
3. Eu + Esterase	-	-	-	3.14	1.42	1.8
4. Eu + $NaHCO_3$ + Esterase	-	-	-	3.17	1.51	1.7

Table 37. Measured hydration state values, q, **Eu.18** solutions 1 to 4 at pH 7.4, where k is the experimentally determined rate constant for the decay of the Eu(III) excited state. Incubation was at 37°C for 2 hours. pH 7.4, 25°C. For full data analysis see Appendix **A19, A20 and A21**.

Lifetime studies indicate the complex has a hydration state $q = 2.1$ (solution 1), thus carbonate binding is possible. The hydration state is reduced to $q = 1.2$ upon the addition of carbonate (solution 2), which is identical to that observed for the ethyl ester model **Eu.14**. It can therefore be hypothesised that the carbonate binding equilibrium established at pH 7.4 would be similar to that of the **Eu.14** model, where it was estimated that ~ 42% of the carbonate bound species was present in solution. Following incubation at 37°C for 2 hours the hydration state value remained the same for solution 2, which confirms the acetoxymethyl ester groups have not hydrolysed under experimental conditions. Overall hydration state values are reduced upon the addition of esterase (solutions 3 and 4 c.f. solution 1), possibly due to changes in the outer and second sphere water molecules effecting the observed q value.

The q values of solutions 3 and 4 are identical to the negatively charged model complex **[Eu.10]$^{3-}$** in the presence of esterase, showing a slight affinity for carbonate as the q value is lower for solution 4 than for solution 3. The similarity confirms complete conversion from **Eu.18** to **[Eu.10]$^{3-}$** occurs upon addition of esterase. The higher q value of solution 4 with respect to solution 2 indicates that esterase hydrolysis of the acetoxymethyl ester groups has occurred. The negatively charged species has been generated, which disfavours carbonate binding. Higher q values are therefore observed for solution 4 with respect to solution 2, as inner sphere waters are no longer displaced.

*4.5.3 Relaxometric Investigation of **Gd.18** in the Presence of Esterase*

The four solutions of **Gd.18** were prepared in 0.1 NaCl solution and adjusted to pH 7.4 by addition of small aliquots of HCl or NaOH in the same manner as previously conducted for the model complexes **Gd.14** and **[Gd.10]$^{3-}$**; 1. ~ 0.5 mM Gd; 2. ~ 0.5 mM Gd, 10 mM $NaHCO_3$; 3. ~ 0.5 mM Gd, 100 units esterase; 4. ~ 0.5 mM Gd, 10 mM $NaHCO_3$, 100 units esterase. Table 38 shows the observed relaxometric data following incubation for 2.5 hours at 37^{o}C, where T_{1obs} is the observed longitudinal relaxation time, R_{1obs} is the observed water proton longitudinal relaxation rate ($1/T_{1obs}$) and R_{1p} is the paramagnetic water proton relaxation rate ($R_{1obs} - 0.38$, the diamagnetic contribution of the bulk water molecules).

Solution	T_{1obs} (s)	R_{1obs} (s^{-1})	R_{1p} (s^{-1})	r_1 ($mM^{-1}s^{-1}$)
1. Gd Alone	0.39	2.56	2.18	9.9
2. Gd + $NaHCO_3$	0.61	1.64	1.26	5.7
3. Gd + Esterase	0.37	2.70	2.32	10.5
4. Gd + $NaHCO_3$ + Esterase	0.37	2.70	2.32	10.5

Table 38. ^{1}H relaxation data of **Gd.18** solutions 1 to 4 following incubation (2 hours at 37^{o}C). 0.22 mM **Gd.18**, 20 MHz, 25^{o}C.

The observed relaxivities, r_1 (R_{1p}/[Gd**]**), of the four solutions following incubation mirror those observed for the equivalent experiments with the model complexes **Gd.14** and **[Gd.10]$^{3-}$**. An 84% difference in relaxivities is observed between the carbonate containing solutions 2 (r_1 = 5.7 $mM^{-1}s^{-1}$) and 4 (r_1 = 10.5 $mM^{-1}s^{-1}$), thus proving hydrolysis of the acteoxymethyl ester groups to occur in solution 4 as 100 units of esterase are added. The stability towards hydrolysis of the acetoxymethyl ester groups during experimental conditions is confirmed as the relaxivity solution 2 remains low following incubation. The overall relaxivity of the complex was recorded at r_1 = 9.9 $mM^{-1}s^{-1}$ (solution 1), which is marginally lower than observed for the model ethyl ester complex, **Gd.14** (r_1 = 10.2 $mM^{-1}s^{-1}$). It however remains within the 5% error range of the spectrometer. Solutions 3 and 4 displayed higher relaxivities with respect to solution 1, which results from the generation of the negatively

charged complex **[Gd.10]**$^{3-}$ following hydrolysis of the acetoxymethyl ester groups, which possesses a greater overall relaxivity (r_1 = 11.3 $mM^{-1}s^{-1}$). The comparison between solutions 3 and 4 (r_1 = 10.5 $mM^{-1}s^{-1}$) with those observed during control experiments with the negatively charged model complex **[Gd.10]**$^{3-}$ (r_1 = 10.8 $mM^{-1}s^{-1}$) are again within the 5% error range of the spectrometer with the similarity confirming that the presence of esterase has no great overall effect on the observed relaxivity. It can therefore be concluded the complete conversion of **Gd.18** to **[Gd.10]**$^{3-}$ has occurred following esterase hydrolysis of the acteoxymethyl ester groups, resulting in a higher observed relaxivity due to the increased electrostatic repulsion of carbonate.

4.6 Summary and Conclusions

It has been demonstrated that neutral q = 2 Gd(III) complexes show decreased relaxivity in the presence of serum concentrations of carbonate due to the inner sphere water molecule displacement by bidentate anionic binding. This decrease in relaxivity is not as great for the negatively charged analogues of such complexes, presumably due to increased electrostatic repulsion and hence a lower affinity for anionic binding a pH 7.4. High relaxivities were observed in the absence of carbonate, attributed to the rapid water exchange exhibited by the ethyl ester containing complex **Gd.14**. This was confirmed by variable temperature ^{17}O NMR. The conversion of neutral, carboxylic ester containing complexes into free acid forms by enzymatic hydrolysis using pig liver esterase has been demonstrated by ^{1}H NMR spectroscopy (Y), luminescence (Eu) and relaxometric (Gd) investigations. The studies have demonstrated the concept of inhibition of anion binding as a result of enzyme activation works. Further, *in vitro* cellular imaging must be carried out in order to determine the rate of endocytosis and the degree of intracellular compartmentalisation of the hydrolysed product, as well as the degree of increase in relaxivity upon intracellular activation.

The model shows great scope for future development, firstly by modification of the aliphatic side chains, incorporating more enzyme-specific substrates for monitoring enzyme activities associated with specific disease sites. Secondly, the addition of a targeting vector to the non-substituted cyclen ring nitrogen would lead to accumulation at a specific disease site prior to activation. Preliminary work has been carried out in this area following the addition of a nitrobenzyl moiety to the model macrocyclic pro-ligands, **6** and **12** (Scheme 27). The nitrobenzyl moiety is a pre-cursor to the addition of targeting groups, such as antibody fragments.[231] As the hydration state is q = 2 in the presence of the nitrobenzyl group it would be expected that similar relaxometric and luminescent results would be observed once the targeting vector is attached.

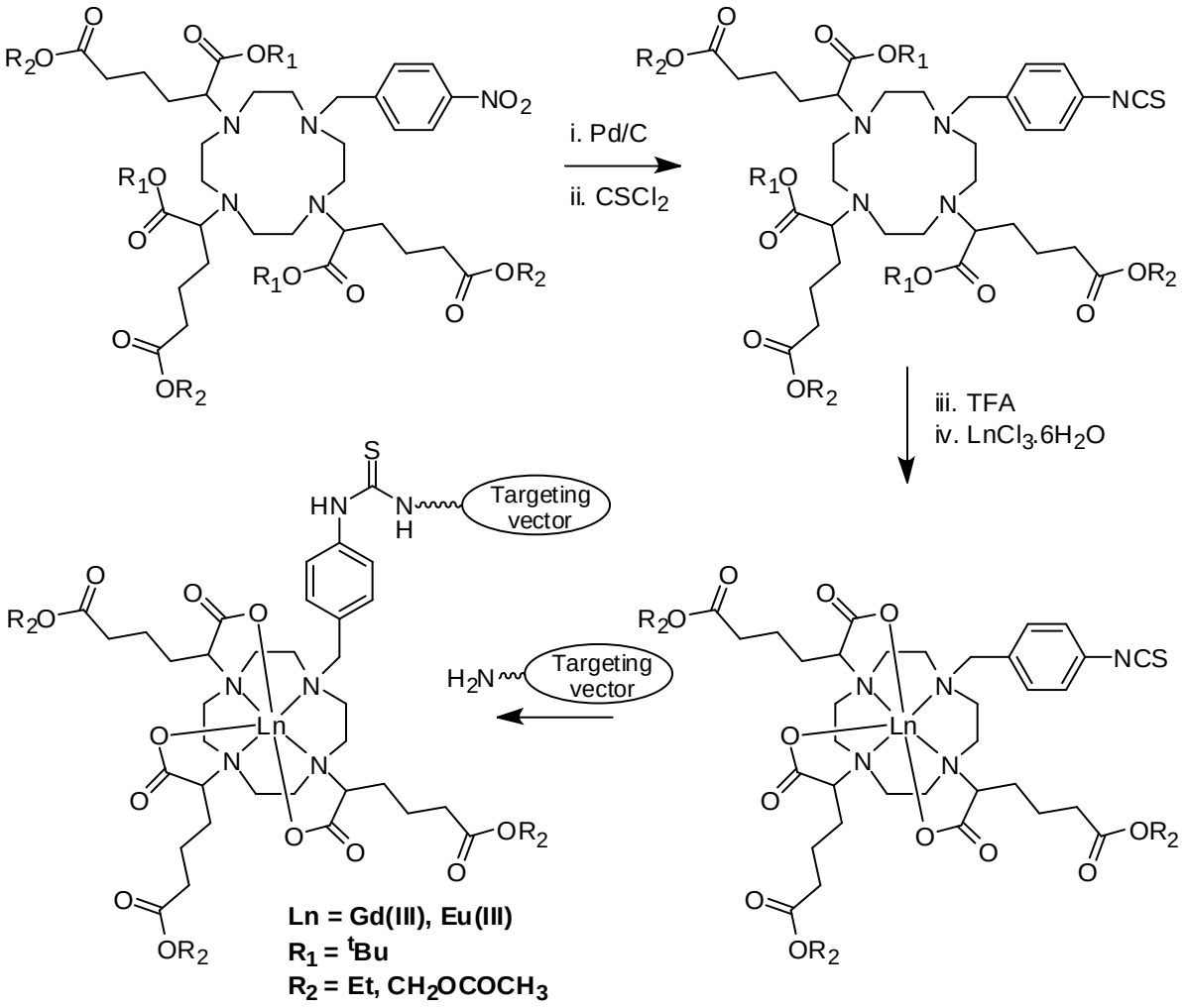

Scheme 27

Increasing the affinity for anion binding of the pre-enzyme activated species is also an area for future research. An increase in the carbonate binding affinity would lead to a larger difference in relaxivity prior to and following enzyme activity, increasing contrast between labelled and non-labelled cells. Such an increase in affinity could be made possible by the incorporation of amide donor side chains to the Gd(III) chelate.

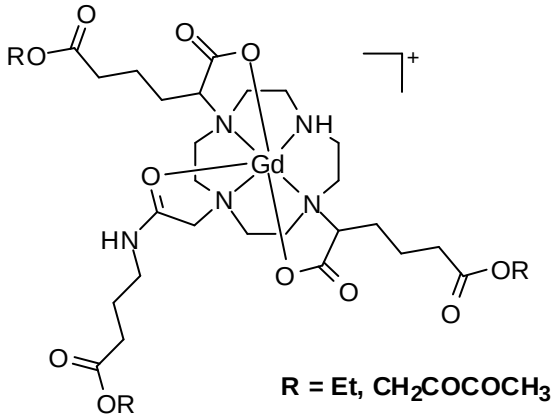

Similar complexes have shown an increase in anionic affinity as a result of the variation of complex geometry about the Gd(III) centre as well increasing the overall positive

charge of the complex, enhancing the electrostatic attraction towards carbonate.[202] The incorporation of amide donors has, however, been observed to decrease the water exchange rate, k_{ex} ($1/\tau_m$), of the Gd(III) complex, reducing relaxivity. The hypothesis may be worth pursuing as the percentage change in relaxivity between the pre- and post-enzymatically activated complexes may be considerably large, showing significant relative contrast prior to and following enzyme activation.

Chapter 5

Summary and Future Work

5.1 Dpp Bearing Complexes

The mono- and bis-methyl analogues of dppDO3A-based Ln(III) complexes were prepared. These demonstrated sensitised emission when Ln(III) = Eu, Tb, Dy and Sm, following excitation of the dpp antenna at λ_{ex} ~ 270 nm. pH responsive reversible ligation of the dpp pendant moiety was observed for both the Gd(III) and Eu(III) analogues, which is not the case for the other lanthanide analogues. This is attributed to the variation in ionic radii across the lanthanide series. pH responsive behaviour has been studied by both luminescence (Eu) and relaxometric methods (Gd). The hydration state values of the Eu(III) analogues were measured at q = 1 and q = 2 in basic and acidic media respectively. Furthermore, the ratio of emission intensities of the ΔJ = 1 and ΔJ = 2 bands demonstrates the potential application of such dpp compounds as ratiometric probes for concentration independent determination of pH. Relaxivities of the Gd(III) analogues were measured as r_1 = 7.9 $mM^{-1}s^{-1}$ (mono-methyl, **Gd.4a**) and r_1 = 8.2 $mM^{-1}s^{-1}$ (bis-methyl, **Gd.4b**) in acidic media with the complex in its q = 2 form. Dpp ligation (likely *via* the oxygen) occurs in basic media following deprotonation of the dpp moiety. The complex hydration state is q = 1 and the measured relaxivity values are r_1 = 5.4 $mM^{-1}s^{-1}$ (**Gd.4a**) and r_1 = 4.4 $mM^{-1}s^{-1}$ (**Gd.4b**).

The pK_a values were determined as 8.65 (± 0.09) and 8.59 (± 0.14) for the **Eu.4a** and **Eu.4b** respectively, calculated from luminescent studies. These values fall somewhat higher than physiological pH conditions (pH 7.4). The hydrophobic dpp moiety was thus only 7.7% and 4.3% bound to the metal centre at physiological pH 7.4 for both the racemic mono- and bis-methyl dpp derivatives respectively. This allows non-covalent binding to HSA with high affinity, K = 22,268 ± 12 % M^{-1} (92.8% HSA-bound **Eu.4a**) and K = 20,059 ± 14% M^{-1} (92.1% HSA-bound, **Eu.4b**), under physiological conditions and imaging concentrations (0.1 mM complex, 0.67 mM HSA, pH 7.4). Relaxometric studies of the Gd(III) analogues gave similar binding affinities. Maximum relaxivity values of r_1 = 11.7 $mM^{-1}s^{-1}$ and r_1 = 16.0 $mM^{-1}s^{-1}$ were observed for HSA-bound **Gd.4a** and **Gd.4b** respectively. The higher relaxivity value observed for the bis-methyl complex **Gd.4b** is attributed to less independent rotation of this more rigid complex when bound to the protein. Eu(III) luminescent lifetime measurements showed that on binding to HSA, the two inner sphere water molecules were displaced, presumably by bidentate carboxylate residue groups. Eu(III) emission *vs.* pH

titrations in the presence of carbonate gave the apparent measured pK_as of 7.39 (± 0.19) and 7.45 (± 0.10) ($\Delta J = 2\ I/I_o$) and 6.59 (± 0.07) and 7.09 (± 0.10) ($\Delta J = 2$ / $\Delta J = 1$) for both **Eu.4a** and **Eu.4b** respectively. These values are now within the physiological pH range, suggesting the possible use of such complexes as concentration independent pH sensors in serum. In order to reduce anionic water displacement by residual carboxylate groups, thus increasing the relaxivity of the HSA bound species, the negatively charged mono-methyl dpp complex **[Gd.9]$^{3-}$** was prepared. Relaxivity was enhanced by ~ 36% compared to the neutral mono-methyl analogue to r_1 = 15.8 $mM^{-1}s^{-1}$ and r_1 = 16.0 $mM^{-1}s^{-1}$ for the Gd(III) complexes of the R and S-enantiomers of the ligand **9** respectively, while luminescent studies of the Eu(III) analogue measured the binding affinity, K = 17,915 (± 14%) M^{-1}.

The R and S-enantiomers of the mono-methyl ligand **4a** were prepared. Following displacement titrations with dansylsarcosine it was demonstrated that each neutral dpp complex showed high binding affinity to site II of the protein (inhibition constants for dansylsarcosine: K_i = 118 ± 2.0% **Gd.4a(R)**; K_i = 76 ± 1.8% **Gd.4a(S)**) while the Gd(III) complex of the S-enantiomer showed an affinity for site I following displacement titrations with warfarin (K_i = 252 ± 6.0%). Site II-specific binding was also observed for the Gd(III) complexes of both the R and S-enantiomers of the dpp moiety of the negatively charged dpp complex **[Gd.9]$^{3-}$** as well as the neutral bis-methyl dpp complex **Gd.4b**, each displacing dansylsarcosine (inhibition constants for dansylsarcosine: K_i = 63 ± 1.6 % **Gd.4b**; K_i = 207 ± 1.5% [**Gd.9(R)]$^{3-}$**; K_i = 807 ± 3.8% **[Gd.9(S)]$^{3-}$**). None of these complexes displaced warfarin, and are thus unable to bind to site I. The results are comparable to those observed for the site II-specific MRA contrast agent MS-325 (Vasovist®), for which the binding constant of K = 11,000 M^{-1} (37°C) and an inhibition constant of K_i = 83 ± 3.0% (dansylsarcosine) were reported.[187]

Relaxivity increased from r_1 = 6.5 $mM^{-1}s^{-1}$ to r_1 = 16.0 $mM^{-1}s^{-1}$ upon binding of **Gd.4b** to HSA (146% increase), compared to the increase from r_1 = 7.1 $mM^{-1}s^{-1}$ to r_1 = 11.7 $mM^{-1}s^{-1}$ observed for the mono-methyl dpp complex, **Gd.4a** (64% increase). The greater relaxivity enhancement displayed by **Gd.4b** was attributed to the expected increased rigidity in the binding site of the bis-methyl dpp moiety compared to the mono-methyl dpp complex, **Gd.4a**, causing a reduction in the independent rotation of the HSA-bound **Gd.4b** complex. This resulted in greater relative enhancement of the observed relaxivity. The relaxivities of the Gd(III) complexes of the R and S-enantiomers of the dpp moiety of the HSA-bound negatively charged mono-methyl dpp complex, **[Gd.9R/S]$^{3-}$** were both measured at r_1 ~ 16.0 $mM^{-1}s^{-1}$ each, demonstrating an ~ 68% increase compared to the unbound complex; r_1 ~ 9.5 $mM^{-1}s^{-1}$. The relaxivity observations are comparable those of the bis-methyl dpp complex

Gd.4b. This may be due to both the increase in independent rotations of the bound **[Gd.9]$^{3-}$** complex caused by the reduction of rigidity of the mono-methyl dpp moiety as well as the increased molecular weight of the tris adipate-bearing complex. The overall exchange rate of the inner-sphere waters may also have been reduced as the water exchange dynamics of the bound **[Gd.9]$^{3-}$** may have been affected by the close proximity of the adipate side chains to the protein.

There are therefore three main areas for future development of the dpp bearing Ln-DO3A complexes. Firstly, continuation of the preparation of multi-Gd(III) containing dendrimeric compounds following TFA deprotection of the dpp protecting groups, as discussed in Chapter 2, Section 2.4.

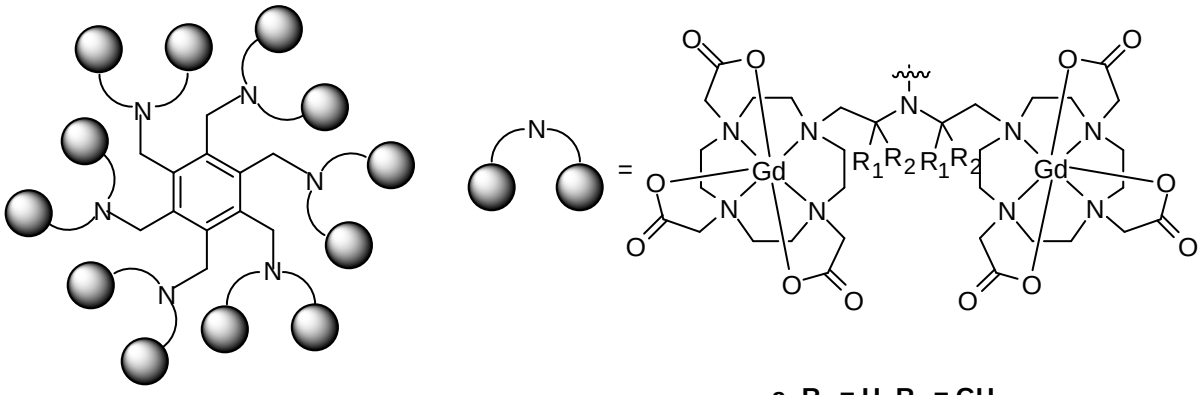

a. R_1 = H, R_2 = CH_3
b. R_1 = R_2 = CH_3

Secondly, although it was observed that the dpp complexes demonstrated lower apparent pK_a values within the physiological pH range in the presence of serum concentrations of carbonate, the incorporation of more electron withdrawing groups, such as CF_3, in place of the dpp methyl groups may result in further lowering of the pK_a values enabling use of such dpp complexes as concentration independent pH probes in biological systems.

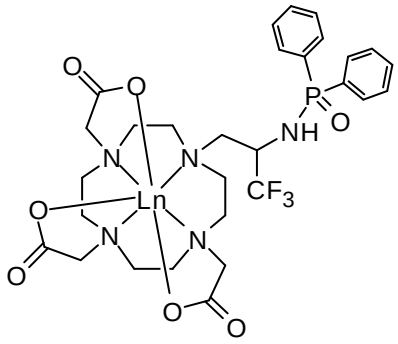

Finally, greater enhancement of relaxivity observed upon binding dpp complexes to HSA may be achieved by preparing a negatively charged bis-methyl dpp complex incorporating fewer adipate side chains. This would result in a low molecular weight complex

that binds with high affinity to site II of HSA. Relaxivity enhancement would be achieved as a reduction of the independent rotations of the HSA bound complex is expected. The q = 2 hydration state of the bound complex should be maintained through the introduction of a single adipate side chain. This may result in increased electrostatic repulsion of protein residue carboxylate groups as well reducing the effect on the water exchange dynamics as fewer adipate interactions with protein residue groups would be expected.

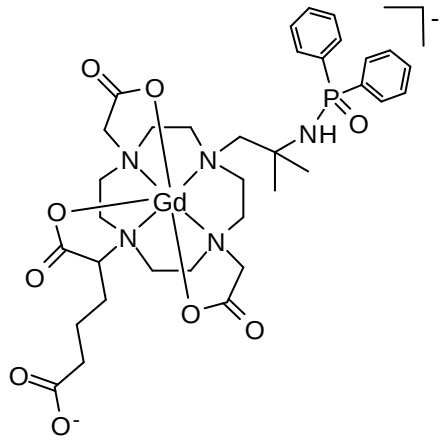

5.2 Enzyme Activated Complexes

In the presence of serum concentrations of carbonate, a greater affinity for anion binding was demonstrated for neutral q = 2 Gd(III) complexes compared to the negatively charged analogue. This was manifested as a larger reduction in the observed relaxivity due to the inner-sphere water molecule displacement by bidentate carbonate binding. The negative charge increases electrostatic repulsion and hence a lower affinity for carbonate binding a pH 7.4. The rapid water exchange exhibited by the ethyl ester containing complex **Gd.14** (confirmed by variable temperature ^{17}O NMR), lead to high relaxivities being observed in the absence of carbonate. Conversion of neutral, carboxylic ester containing complexes into free acid forms by enzymatic hydrolysis using pig liver esterase has been demonstrated by ^{1}H NMR spectroscopy (Y), luminescence (Eu) and relaxometric (Gd) investigations. The concept of inhibition of anion binding *via* enzyme activation has been proven to work as a strategy to developing enzyme activated contrast agents.

Luminescent lifetime measurements of the Eu(III) pre- and post-enzymatically hydrolysed q = 2 model complexes **Eu.14** and **[Eu.10]$^{3-}$** respectively determined the carbonate binding affinity to be greater for the neutral ethyl ester bearing complex **Eu.14** compared to the negatively charged **[Eu.10]$^{3-}$**, with hydration state values measured as q = 1.2 and q = 2.0 for **Eu.14** and **[Eu.10]$^{3-}$** respectively at pH 7.4 in the presence of 30 mM $NaHCO_3$ (1.0 mM complex, 0.1 M NaCl). This corresponded to ~ 42% of the carbonate bound, q = 0 species present in solution for the neutral **Eu.14** compared to ~5% for the

negatively charged **[Eu.10]$^{3-}$**. The greater carbonate binding affinity for the neutral complex was further demonstrated by Eu(III) emission *vs*. pH titrations, which showed higher emission intensities at pH 7.4 for the neutral **Eu.14** compared to the negatively charged **[Eu.10]$^{3-}$** as quenching water molecules were more efficiently displaced by anion binding at the Eu(III) centre. The results mirrored the equivalent relaxivity (Gd) *vs*. pH titrations, which showed ~ 60% greater relaxivity at pH 7.4 for the negatively charged **[Eu.10]$^{3-}$** compared to the neutral **Eu.14** as carbonate binding was suppressed, allowing more water molecules to exchange with the Gd(III) centre, enhancing relaxivity.

Hydrolysis of the ethyl esters by pig liver esterase was first demonstrated by ^{1}H NMR of the non-paramagnetic **Y.14**, which clearly showed loss of the ethyl ester resonances with a concomitant increase in ethanol resonances. Secondly, luminescence studies in the presence of carbonate, showed higher emission intensity for the $\Delta J = 2$ band in the absence of esterase than in the presence, i.e. the ethyl ester is hydrolysed by esterase, inhibiting carbonate binding. Furthermore, the appearance of the spectra were different; the $\Delta J = 2$ peak was not only less intense but shifted from 617 nm in the absence of to 615 nm in the presence of esterase. Three distinct $\Delta J = 1$ bands were also observed in the presence of esterase as opposed to the broad $\Delta J = 1$ band observed in the absence. The spectral differences were attributed to the conformational changes of the complex as carbonate binding occurred. Hydration state values were recorded as $q = 1.2$ in the absence and $q = 1.7$ in the presence of esterase following incubation at 37^{o}C for 2 hours. The emission spectra and hydration state values of **Eu.14** in the presence of esterase were identical to those observed for the equivalent solution of the model post-enzyme activated negatively charged complex **[Eu.10]$^{3-}$**, therefore confirming complete hydrolysis of **Eu.14** into **[Eu.10]$^{3-}$** to be occurring upon incubation in the presence of esterase. Equivalent relaxometric studies were carried out with the Gd(III) model complex analogues. **Gd.14** in the presence of carbonate gave a relaxivity of $r_1 = 10.8$ mM^{-1}s^{-1} in the presence of esterase compared to $r_1 = 5.7$ mM^{-1}s^{-1} in the absence. This corresponded to an 89% increase in relaxivity following enzymatic hydrolysis of the ethyl ester groups resulting in suppression of carbonate binding and inner sphere water displacement. The relaxivity observed for **Gd.14** in the presence of esterase and carbonate following incubation is identical to that observed for the negatively charged **[Gd.10]$^{3-}$**, once again confirming complete hydrolysis of **Gd.14** to **[Gd.10]$^{3-}$** to be occurring following esterase activity.

The pH studies carried out for the model ethyl ester-bearing complex were inaccessible to the acetoxymethyl ester complex **Ln.18** due to the instability of these esters in basic media. However, as the hydration states of **Eu.18** were determined as $q = 1.2$ in the

presence and q = 2.1 in the absence of carbonate (identical to those observed for the neutral model complex **Eu.14**) it was hypothesised that similar luminescent (Eu) and relaxometric (Gd) observations would be made following addition of esterase to **Ln.18** in the presence of carbonate. Hydrolysis was firstly confirmed by ^{1}H NMR of **Y.18**, showing the disappearance of the acetoxymethyl ester resonances upon addition of pig liver esterase. Luminescence studies of **Eu.18** showed identical results to those observed for the negatively charged model complex **[Eu.10]$^{3-}$** and showing the same trend as for the neutral model complex **Eu.14**, i.e. spectral differences such as decreased ΔJ = 2 emission and three distinct ΔJ = 1 bands in the presence of carbonate following the addition of esterase and incubation at 37^{o}C. Relaxivities in the presence of carbonate following incubation at 37^{o}C for 2 hours were determined as r_1 = 5.7 mM^{-1}s^{-1} in the absence and r_1 = 10.5 mM^{-1}s^{-1} in the presence of esterase, once again confirming the complete hydrolysis of **Gd.18** to **[Gd.10]$^{3-}$** and corresponding to an 84% increase in relaxivity. This is a result of greater electrostatic repulsion, inhibiting carbonate binding to the now negatively charged species, allowing more waters to exchange with the Gd(III) centre. Furthermore, as the relaxivity value remains low at r_1 = 5.7 mM^{-1}s^{-1} following incubation at 37^{o}C in the absence of esterase it can therefore be concluded that the acetoxymethyl ester complex has not hydrolysed under these experimental conditions.

Future development of such complexes must involve *in vitro* cellular imaging to determine the rate of endocytosis and the degree of intracellular compartmentalisation of the hydrolysed product, as well as the percentage increase in relaxivity upon intracellular activation.

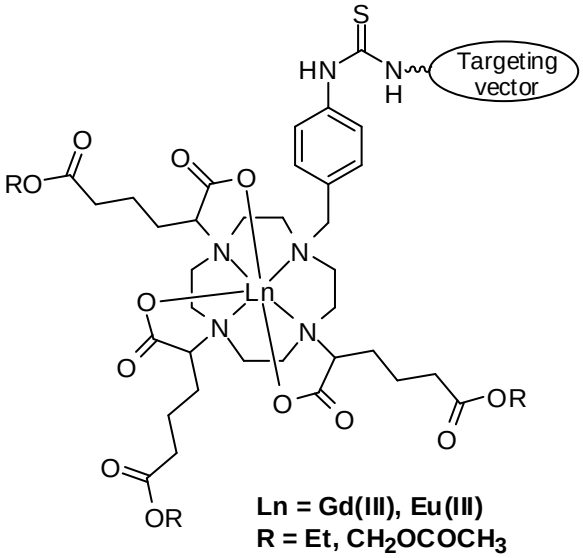

Modification of the aliphatic side chains to incorporate more enzyme-specific substrates could potentially enable monitoring of enzyme activities associated with specific

diseases, which may be further achieved by the addition of a targeting vector to the non-substituted cyclen ring nitrogen allowing accumulation at a location prior to activation.

The affinity for anion binding of the pre-enzyme activated species is also an area for future research. A larger difference in relaxivity prior to and following enzyme activity could be achieved by increasing the affinity for carbonate binding. This would increase the contrast between pre- and post-activated complex. The incorporation of amide donor side chains to the Gd(III) chelate is likely to show an increase in anion binding affinity as a result of the introduction of overall positive charge on the complex, enhancing the electrostatic attraction for carbonate. The incorporation of amide donors has, however, been observed to decrease the water exchange rate, k_{ex} $(1/\tau_m)$, of Gd(III) complexes, reducing relaxivity. [202] However, in such cases the percentage change in relaxivity between pre- and post-enzymatically activated complexes is of most importance rather than the absolute value of relaxivity. This suggests the future development of such complexes may be worth pursuing.

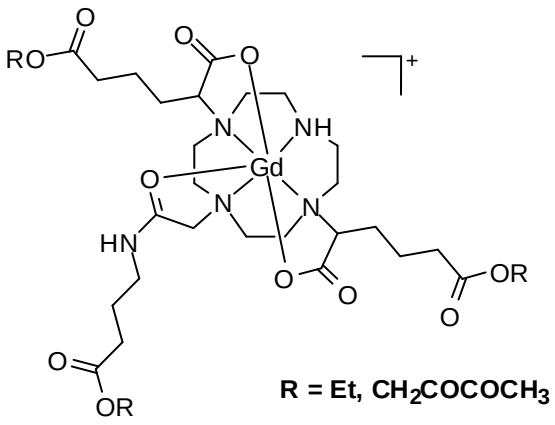

Chapter 6

Experimental

6.1 Materials and Methods

6.1.1 Reagents

All reagents and solvents were purchased from Alfa Aesar, Strem, Acros or Sigma Aldrich. Dichloromethane and acetonitrile were dried over calcium hydride using an Inovative Technology inc. PureSolv solvent purification system. THF was dried over sodium benzophenone. Methanol was preliminarily dried over magnesium and distilled onto 3 Å sieves. Triethylamine was preliminarily dried over calcium hydride and distilled onto 4 Å sieves. Human serum albumin (HSA), product number A-1653 (fraction V powder 96-99% albumin, containing fatty acids) and Porcine Liver Esterase, product number E3019 (lyophilised powder, 20 units per mg solid) were purchased from Sigma Aldrich.

6.1.2 Chromatography

Flash column chromatography was carried out using silica gel 60. Cation exchange chromatography was carried out using Dowex 50W 50 x 4 – 200 strong ion-exchange resin, prepared with 5 M HCl and Dowex MAC-3 weak acid-cation exchange resin, prepared with 1% HCl, where stated.

6.1.3 Spectroscopy

^{1}H, ^{13}C and ^{31}P NMR spectra were recorded using Bruker 250 MHz, 300 MHz and 400 MHz spectrometers using deuterated chloroform ($CDCl_3$), deuterated methanol (CD_3OD) and deuterium oxide (D_2O) where stated, referenced to residual solvent peaks. All chemical shifts are recorded in ppm. Electrospray mass spectra (ESMS) were recorded using a Micromass Quatro mass spectrometer using MeOH as solvent. FAB mass spectra were recorded using a Kratos Concept mass spectrometer with a NBA matrix. MALDI mass spectra were recorded on a Voyager DE-Str instrument from Applied Biosciences Ltd. on a stainless steel plate with 100 wells. The matrices were various or none and an average of 100 laser shots were used to generate the spectrum. ICP-MS were carried out using an Agilent Technologies 7500ce inductively coupled plasma mass spectrometer. Accurate masses were determined at the EPSRC National MS Service at Swansea. IR measurements were carried out using a Perkin Elmer Spectrum One FT-IR spectrometer. Electronic absorption spectra

were measured with a Shimadzu UV 180 spectrometer using a 10x10 mm or 10x2 mm quartz Hellma cuvette.

6.1.4 Luminescence Spectroscopy

Luminescence data was recorded using a Jobin Yvon Horiba FluoroMax-P spectrometer (using DataMax for Windows v2.2). Samples were held in a 10x10 nm or 10x2 nm quartz Hellma cuvette and cut-off filter (550 nm Eu, 500 nm Sm, 450 nm Tb and Dy) was used to avoid second-order diffraction effects. Excitation and emission slits were typically 10:1 nm for emission spectra. Eu(III) excitation was either direct (λ_{ex} = 395 nm) or sensitised *via* the dpp chromophore (λ_{ex} ~ 270 nm). Eu(III) excitation spectra monitored the $\Delta J = 2$ band. Excitation and emission slits were 1:1 nm with a 1.0 s integration time. Phosphorimer emission spectra obtained in phosphorimeter mode (for esterase hydrolysis tests) used excitation and emission slits of 20:1.5 nm with a 0.1 ms delay. Flash time was 50 ms with 150 flashes per point. The sample window was 2 ms with an increment of 1 nm. Excitation was λ_{ex} = 395 nm (direct Eu) with a 550 nm cut-off filter.

6.1.5 Hydration State, q, Determination

Lifetimes were measured by excitation (395 nm direct unless stated) of the sample with a short 40 ms pulse of light (500 pulses per point) followed by monitoring the integrated intensity of light ($\Delta J = 2$) emitted during a fixed gate time of 0.1 ms, at a delay time later. Delay times were set at 0.1 ms intervals, covering 4 or more lifetimes. Excitation and emission slits were set to 5:5 nm. The data is the applied to the standard first order decay Equation 39, minimised in terms of *k* by iterative least-square fitting operation in Microsoft Excel, where I_{obs} is the observed intensity, I_o is the initial intensity of the excited state Eu(III) and *t* is the time (ms). The calculated *k* values are then applied to Equation 33 to calculate the hydration state, *q*.[115, 116]

$$I_{obs} = I_o e^{-kt} + offset \tag{39}$$

$$q = 1.2[(k_{H_2O} - k_{D_2O}) - 0.25] \tag{33}$$

6.1.6 ^{1}H Relaxation Data

The observed longitudinal water proton relaxation times (T_{1obs}) were measured on a Stelar Spinmaster spectrometer (Stelar, Mede (PV) Italy) operating at 20 MHz, by means of

the standard inversion-recovery technique (16 experiments, 2 scans). A typical 90° pulse width was 3.5 μs and the reproducibility of the T_{1obs} data was ±0.5%. The paramagnetic water proton relaxation rate, R_{1p} and relaxivity, r_1 were determined following Equations 20, 54 and 55, where 0.38 is the diamagnetic contribution of the bulk water molecules.[232] Complex concentrations were estimated *via* mineralization with nitric acid or by Evan's method.

$$R_{1obs} = \frac{1}{T_{1obs}} \tag{54}$$

$$R_{1p} = R_{1obs} - 0.38 \tag{55}$$

$$r_1 = R_{1p} / [\mathrm{Gd}] \tag{20}$$

The $1/T_1$ nuclear magnetic relaxation dispersion (NMRD) profiles of water protons were measured over a continuum of magnetic field strength from 0.00024 to 0.7 T (corresponding to 0.01 – 30 MHz proton Larmor frequency) on a fast field-cycling Stelar Spinmaster FFC 2000 relaxometer equipped with a silver magnet. The relaxometer operates under complete computer control with an absolute uncertainty in the $1/T_1$ values of ±1%. The typical field sequences used were the NP sequence between 30 and 8 MHz and the PP sequence between 8 and 0.01MHz. The observation field was set at 13 MHz. 16 experiments of 2 scans were used for the observed longitudinal relaxation time T_1 determination at each field.

Variable-temperature ^{17}O NMR measurements were recorded on a JEOL EX-90 (2.1 T and 9.4 T) spectrometer, equipped with a 5 mm probe, by using D_2O as external lock. Experimental settings were: spectral width 10,000 Hz, pulse width 7 μs, acquisition time 10 ms, 1,200 scans and no sample spinning. Solutions containing 2.6% of ^{17}O isotope (Yeda, Israel) were used. The observed transverse relaxation rates, R^{O}_{2obs}, were calculated from the signal width at half height.

6.1.7 pH Titrations

pH measurements were recorded using a Jenway 3510 pH meter with a BDH probe, model 309-1025-02 calibrated at pH 4, 7 and 10. Both luminescence and relaxivity pH titrations were carried out in a background of constant ionic strength (I = 0.1 NaCl, 298 K). Aqueous solutions were made basic by addition of 1 M or 0.1 M NaOH and titrated to acid

pH by addition of small aliquots of 1 M or 0.1 M HCl. For each titration 20-25 points were recorded. Equation 56 and 57 were minimized in terms of K_a, where I_{obs} is the observed I/I_o ratio (ΔJ = 2) of Eu(III) emission intensity and I_{Hdpp} and I_{dpp}- are the I/I_o (ΔJ = 2) Eu(III) emission intensity ratios of the fully protonated and fully deprotonated dpp. Data analysis was performed using an iterative least-squares fitting procedure, operating in Microsoft Excel.

$$I_{obs} = \frac{[\mathrm{H}^+]I_{Hdpp} + K_a I_{dpp^-}}{[\mathrm{H}^+] + K_a} \tag{56}$$

The same methods were used in order to determine pK_a using relaxivity *vs.* pH titrations, where r_{1obs} is the observed relaxivity (Gd(III)) and r_{1Hdpp} and r_{1dpp}- are the relaxivities of the fully protonated and fully deprotonated dpp.

$$r_{1obs} = \frac{[\mathrm{H}^+]r_{1Hdpp} + K_a r_{1dpp^-}}{[\mathrm{H}^+] + K_a} \tag{57}$$

For derivation of equations see Appendix Section 7.2.

6.1.8 HSA Binding Studies

For both luminescence and relaxivity studies, aqueous solutions were buffered to pH 7.4 using phosphate buffered saline solution (PBS, 150 mM NaCl). Titrations were run at fixed complex concentration (0.2 mM) with varied [HSA] at 25^{o}C. 14 points were recorded for each titration. The Eu(III) complexes were excited indirectly, *via* the dpp chromophore, at λ_{ex} ~ 270 nm and the variations in intensity of the ΔJ = 2 band was recorded. The concentrations of each of the Eu(III) solutions was determined by ICP-MS while the exact concentration of HSA was determined by electronic absorption spectroscopy using the Beer Lambert law (Equation 58), where A = absorption at 280 nm, ε = extinction coefficient of HSA and l = path length (1 cm).[187] Equation 59 was used to determine [HSA], where 2.2645x10^{-7} is a correction factor from the calibration accounting for the residual background fluorescence of the HSA sample.

$$[\mathrm{HSA}] = \frac{A_{(280nm)}}{\varepsilon l} \tag{58}$$

$$[\mathrm{HSA}] = 2.462\times10^{-5} \times A_{(280nm)} + 2.2645\times10^{-7} \tag{59}$$

The equilibrium Equation 45 was assumed, where K is the affinity constant and [Ln] represents the Ln-dpp complex. The concentration of bound complex, [LnHSA], is determined from Equation 46, where $[HSA]_T$ and $[Ln]_T$ are the total concentrations of HSA and the Ln-dpp complex.[197]

$$[HSA]+[Ln] \quad \overset{K}{} \quad [LnHSA] \tag{45}$$

$$[LnHSA]=\frac{([HSA]_T+[Ln]_T+1/K)-\sqrt{([HSA]_T+[Ln]_T+1/K)^2-4[HSA]_T[Ln]_T}}{2} \tag{46}$$

Concentrations were substituted for Eu(III) emission intensity as in Equation 47, where I_{calc} is the calculated Eu(III) emission intensity (to be compared with the experimentally observed intensity), I_{Eu} is the intensity of the Eu(III) complex when in the absence of HSA (i.e. at the start of the titration) and I_{EuHSA} is the intensity of the Eu(III) complex when entirely bound to HSA (i.e. at the end of the titration).

$$I_{calc}=\frac{1}{[Eu]_T}([Eu]_T I_{Eu}+(I_{EuHSA}-I_{Eu})[EuHSA]) \tag{47}$$

Equations 46 and 47 and were combined to give Equation 60, which was minimized in terms of K. Data analysis was performed using an iterative least-squares fitting procedure, assuming a 1:1 binding stoichiometry, operating in Microsoft Excel.

$$I_{calc}=\frac{1}{[Eu]_T}\left(\begin{pmatrix}(I_{Eu}\times[Eu]_T)+\\(I_{EuHSA}-I_{Eu})\end{pmatrix}\left(\begin{pmatrix}([HSA]_T+[Eu]_T+1/K)-\\\sqrt{([HSA]_T+[Eu]_T+1/K)^2-4[HSA]_T[Eu]_T}\end{pmatrix}/2\right)\right) \tag{60}$$

Relaxometric data analysis of the Gd-dpp complexes was carried out in a similar manner to that of the Eu(III) analogues, using an iterative least-squares fitting procedure, assuming a 1:1 binding stoichiometry, operating in Microcal Origin. In order to define the concentration of the HSA bound Gd species in terms of its relaxation rate, R_{1calc}, Equation 50 was used, which was combined with Equation 46 to give Equation 61, where R_{1Gd} is the observed longitudinal relaxation rate of the Gd(III) complex in the absence of HSA (i.e. at the

start of the titration) and R_{1GdHSA} is the observed longitudinal relaxation rate of the Gd(III) when entirely bound to HSA (i.e. at the end of the titration) and $[HSA]_T$ and $[Gd]_T$ are the total concentrations of HSA and the Gd(III) complex. [Gd(III)] was determined by mineralisation of the complex stock solution with nitric acid.

$$R_{1calc} = \frac{1}{[Gd]_T}\left([Gd]_T R_{1Gd} + \left(R_{1GdHSA} - R_{1Gd}\right)[GdHSA]\right) \tag{50}$$

$$R_{1calc} = \frac{1}{[Gd]_T}\left(\left(\left(I_{Gd} \times [Gd]_T\right) + \left(R_{1GdHSA} - R_{1Gd}\right)\right)\left(\left([HSA]_T + [Gd]_T + 1/K\right) - \sqrt{\left([HSA]_T + [Gd]_T + 1/K\right)^2 - 4[HSA]_T[Gd]_T}\right)/2\right) \tag{61}$$

For derivation of equations see Appendix Section 7.3.

6.1.9 Competitive Binding Studies for HSA using Fluorescent Probes

The dissociation constants, K_d ($1/K$) are ~ 5 μM for both warfarin and dansylsarcosine,[187] therefore the concentration of bound probe, $[P]_{bound}$, at the start of the titration is known. A stock solution of 5 μM probe and 5 μM HSA were prepared. A second solution of 1.0 mM of the Gd(III) complex, 5 μM probe and 5 μM HSA was also prepared (each solution pH 7.4 (50 mM HEPES). [Gd(III)] was determined by mineralisation of the complex stock solution with nitric acid. The probe's emission spectrum was recorded following excitation at the relevant wavelength, after which continuous 50:50 dilution of the complex solution using the probe/HSA stock was carried out, with emission spectra recorded after each dilution. 11 points were recorded for each titration. The complex concentration was, therefore, decreased while the probe and HSA concentrations remained the same throughout, resulting in an observed increase in probe emission throughout the titration. Dansylsarcosine spectra were recorded using λ_{ex} = 360 nm, λ_{em} = 480 nm using a 400 nm cut-off filter and excitation and emission slits 10:1 nm. Warfarin spectra were recorded using λ_{ex} = 320 nm, λ_{em} = 385nm, with no filter and excitation and emission slits 8:1 nm. Equations 62 and 63 were used to determine the inhibition constant, K_i, for the Gd complex,[187] where I_{bound} is the emission intensity of the bound probe, K_d is the dissociation constant of the florescent probe, K_d^{app} is the apparent K_d in the presence of the Gd-dpp complex, $[HSA]_T$ and $[P]_T$ are the initial concentrations of HSA and probe respectively, $[Gd]_{free}$ is the concentration of the unbound Gd-dpp complex (i.e. the total concentration of added Gd-dpp complex minus the concentration of the displaced probe, calculated from the observed intensity) and I_{PHSA} is the

initial emission intensity of the fully bound probe. The data was minimised in terms of K_i with the analysis performed using an iterative least-squares fitting procedure operating in Microsoft Excel.

$$I_{bound} = \left(\frac{1}{[\mathrm{P}]_{bound}} \left(\left(\left([\mathrm{HSA}]_T + [\mathrm{P}]_T + K_d^{app} \right) - \sqrt{\left([\mathrm{HSA}]_T + [\mathrm{P}]_T + K_d^{app} \right)^2 - 4[\mathrm{HSA}]_T [\mathrm{P}]_T} \right) / 2 \right) \right) I_{PHSA} \quad (62)$$

$$K_d^{app} = Kd \left(1 + \frac{[\mathrm{Gd}]_{free}}{K_i} \right) \quad (63)$$

6.1.10 Esterase Hydrolysis Studies

For both luminescence (Eu) and relaxivity (Gd) studies, four aqueous solutions were prepared, each containing 0.1 M NaCl and adjusted to pH 7.4 with small aliquots of HCl and NaOH; Solution 1 contains 0.5 mM Gd or 1.0 mM Eu**;** Solution 2 contains 0.5 mM Gd or 1.0 mM Eu, 10 mM (Gd) or 30 mM (Eu) $NaHCO_3$; Solution 3 contains 0.5 mM Gd or 1.0 mM Eu, 100 units pig liver esterase; Solution 4 contains 0.5 mM Gd or 1.0 mM Eu, 10 mM (Gd) or 30 mM (Eu) $NaHCO_3$, 100 units pig liver esterase. Luminescence and relaxometric studies were conducted prior to and following incubation for ~ 2 hours at 37^{o}C.

6.1.11 Concentration Determination via Mineralisation with Nitric Acid

In order to estimate the concentration of the Gd(III) in solution, complexes were dissolved in water and 70% nitric acid in a 1:1 ratio and left in a sealed ampule at 120^{o}C overnight, destroying the complex leaving free Gd(III) in solution. The observed relaxation rates for this solution were measured and applied to Equation 64 (determined from previous calibrations using atomic absorption standard solutions, 1005 μg ml^{-1} Gd in 1 wt. % HNO_3), where 0.4 is the corrected diamagnetic contribution of nitric acid and 13.99 mM^{-1}s^{-1} is the relaxivity of Gd(III) in 45% HNO_3. Note: values are multiplied by two as solutions were diluted 50:50.

$$[Gd] = 2 \times \left(\frac{R_{1obs} - 0.40}{13.99} \right) \quad (64)$$

6.1.12 Concentration Determination via Evan's method

Concentration of lanthanide containing complexes can be estimated by exploiting their ^{1}H NMR chemical shift properties. The bulk magnetic susceptibility shift, Δ_x, of an inert compound (*tert*-butanol) caused by the presence of a paramagnetic solute is measured and used in Equation 65, where c is the molar concentration of paramagnetic complex, T is absolute temperature (K) and μ_{eff} is the effective magnetic moment of a particular lanthanide (Table 39). The factor s is dependant on the NMR magnet in use; 1/3 for cryomagnets and –1/6 for electromagnets.[233]

$$\Delta_x = \frac{4000\pi cs}{T}\left(\frac{\mu_{eff}}{2.84}\right)^2 \tag{65}$$

Lanthanide	μ_{eff} (B.M.)
Ce	2.56
Pr	3.62
Nd	3.68
Sm	1.55-1.65
Eu	3.40-3.51
Gd	7.94
Tb	9.70
Dy	10.60
Ho	10.60
Er	9.60
Tm	7.60
Yb	4.50

Table 39. Effective magnetic moment for the lanthanide series.

Concentration determination was carried out using a 400 MHz NMR spectrometer. 10 μl of *tert*-butanol was added to 190 μl of the lanthanide complex containing sample in a 5 mm NMR tube. Into this was inserted a coaxial NMR tube containing the reference solution; D_2O with 10% *tert*-butanol. The spectrometer was shimmed and locked onto the D_2O signal and a proton NMR spectrum was recorded. The observed chemical shift difference between the sample and reference *tert*-butanol signals equates to the shift in bulk magnetic susceptibility, Δ_x, and was used in Equation 65 to determine the concentration of paramagnetic complex.[234]

6.1.13 Concentration Determination via ICP-MS

200 μl of complex experimental stock solutions were diluted with 70% nitric acid in a 1:1 ratio and left in a sealed ampule at 120°C overnight, destroying the complex leaving free Ln(III) in solution. After cooling the solutions were further diluted 1:35 with water; ~ 4×10^{-3} gl^{-1} Eu(III), ~ 1% HNO_3. Note: experimental stock solutions may contain 0.1 M NaCl, 50 mM HEPES or 150 mM PBS, therefore identical solutions were prepared without containing Ln(III) for use as blanks. The measurements were calibrated using known concentrations of atomic absorption standard solutions (999 μg ml^{-1} Eu in 1 wt. % HNO_3, 1005 μg ml^{-1} Gd in 1 wt. % HNO_3).

6.1.14 Xylenol Orange Calibrations

Xylenol orange is used as a metal ion indicator not only for the lanthanides but for various other metal ions including lead, aluminium and zinc.[235] In acidic conditions the solutions of xylenol orange are yellow as phenolic oxygen remains protonated. Deprotonation of the hydroxyl group in basic media results in an extended electronic delocalisation, resulting in an increase of the absorption wavelength at λ_{max} ~ 580 nm with the solution colour changing to purple.[236] Metal ion coordination occurs through both the iminodiacetic moiety and the phenolic hydroxyl group, resulting in its deprotonation. The presence of metal ions has, therefore, the same resulting colour change effects as variation of pH. When the solutions are buffered to pH 5, colour change can be entirely attributed to the presence of metal ions in solution.

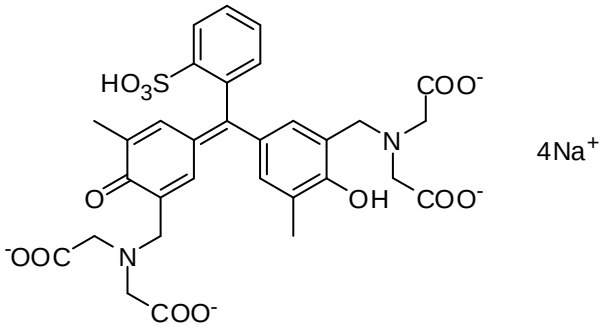

Xylenol Orange

A solution of 0.1 mM xylenol orange solution, buffered to pH 5 by addition of urotropine buffer (0.15 mM) was prepared. Aqueous solutions of Eu(III) and Gd(III) were prepared at known concentrations using atomic absorption standard solutions (999 μg ml^{-1} Eu in 1 wt. % HNO_3, 1005 μg ml^{-1} Gd in 1 wt. % HNO_3). Electronic absorption spectral analysis revealed that at higher concentrations of the free lanthanide ion the absorption at λ_{max} = 580 increased as the solutions changed from orange to bright purple in colour. To use the calibration, a solution of the Ln(III) containing complex must be prepared and the

concentration of the solution recorded. 200 μl was added to 800 μl of the xylenol orange solution and an electronic absorption spectrum recorded. The absorption at $\lambda_{max} = 580$ nm was fit to Equations 66 and 67. This gives the concentration of free Ln(III) ions present in the complex solution that has been prepared. The calibration plots in Figure 75 shows the range between [Ln(III)] 0.02-0.18 mM. If a 1.0 mM complex solution is prepared this equates to the 2-18% range of free Ln(III) in solution.

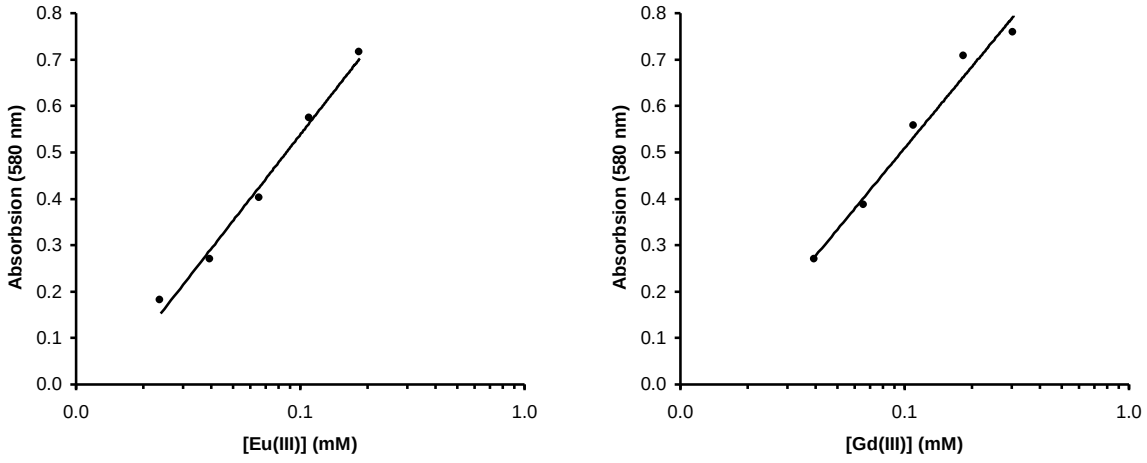

Figure 75. The variation of xylenol orange absorption at λ_{max} = 580 nm with [Eu(III)] (left) and [Gd(III)] (right). 0.1 mM xylenol orange, pH 5.5 (urotropine buffer, 0.15 mM), 25°C.

$$[\mathrm{Eu(III)}] = e^{\left(\frac{Abs(580nm) - 1.1577}{0.269}\right)} \tag{66}$$

$$[\mathrm{Gd(III)}] = e^{\left(\frac{Abs(580nm) - 1.1012}{0.254}\right)} \tag{67}$$

6.2 Aziridine Synthesis

General Synthesis: to a solution of the appropriate amino alcohol in dry THF (300 ml) at 0°C, under nitrogen, was added two equivalents of diphenylphosphinic chloride and three equivalents of triethylamine. A white precipitate of triethylamine hydrochloride was formed. The suspension was stirred at 0°C to room temperature for 20 hours. The solution was then cooled to 0°C, five equivalents of sodium hydride were added and the solution was left to stir at room temperature for a further 20 hours. Five equivalents of water were then carefully added to neutralise the NaH. The solution was then filtered on anhydrous magnesium sulfate and the resulting filter cake was washed with ether. The solvent was removed under reduced

pressure to leave a gum, purified by silica column chromatography with ethyl acetate as eluent.

6.2.1 (±)-1-(Diphenyl-phosphinoyl)-2-methyl-aziridine, ***1a***

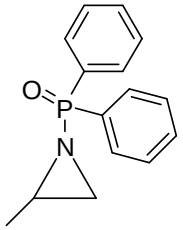

2-amino-1-propanol (1.00 g, 13.31 mmol), diphenylphosphinic chloride (6.30 g, 26.63 mmol), triethylamine (4.04 g, 39.94 mmol), sodium hydride (1.59 g (2.6 g including oil), 66.25 mmol) and water (1.99 ml). **1a** (2.97 g, 86%) was obtained as a white powder. R_f = 0.61 (100% ethyl acetate), λ_{max} (DCM)/nm 259; ν_{max} cm^{-1} 3057, 2986, 2961, 2926 (CH), 1443,1336 1199, 1122 (P=O), 1110, 961, 847; δ_H (300 MHz; $CDCl_3$) 1.3 (3 H, d, $^3J_{HH}$ 5.3 Hz, Me), 1.9 (1 H, m, ring CH_2), 2.6 (1 H, m, ring CH_2), 2.8 (1 H, m, ring CH), 7.5 (6H, m, phenyl H), 7.9 (4H, m, phenyl H); δ_C (75 MHz; $CDCl_3$) 18.0 (methyl C), 30.3 (ring CH_2), 31.2 (ring *C*H), 128.4 (phenyl C), 131.6 (phenyl C), 132.4 (phenyl C), 134.1 (phenyl C); δ_P (121 MHz; $CDCl_3$) 32.0; *m/z* (FAB+) 258 $[M+H]^+$.

6.2.2 (R)-1-(Diphenyl-phosphinoyl)-2-methyl-aziridine, ***1a(R)***

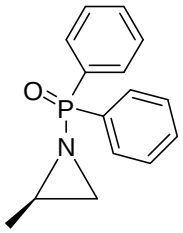

R-2-amino-1-propanol (0.32 g, 4.32 mmol), diphenylphosphinic chloride (2.05 g, 8.66 mmol), triethylamine (1.42 g, 14.03 mmol), sodium hydride (0.48 g (0.77 g including oil), 20.00 mmol) and water (0.6 ml). **1a(R)** (0.32 g, 29%) white powder. R_f = 0.61 (100% ethyl acetate), λ_{max} (DCM)/nm 269; ν_{max} cm^{-1} 3056, 2982, 2962, 2926 (CH), 1440, 1368, 1198, 1125 (P=O), 1110, 992, 873; δ_H (300 MHz; $CDCl_3$) 1.2 (3 H, d, $^3J_{HH}$ 5.5 Hz, Me), 1.8 (1 H, ring CH_2), 2.5 (1 H, m, ring CH_2), 2.7 (1 H, m, ring CH), 7.4 (6H, m, phenyl H), 7.9 (4H, m, phenyl H); δ_C (64 MHz; $CDCl_3$) 18.4 (methyl C), 30.8 (ring CH_2), 31.7 (ring *C*H), 128.8 (phenyl C), 132.0 (phenyl C), 132.9 (phenyl C),134.8 (phenyl C); δ_P (121 MHz; $CDCl_3$) 32.1; *m/z* (HR-FAB+) $[M+H]^+$ calcd for $C_{15}H_{17}NOP$; 258.10478, found; 258.10481.

6.2.3 (S)-1-(Diphenyl-phosphinoyl)-2-methyl-aziridine, ***1a(S)***

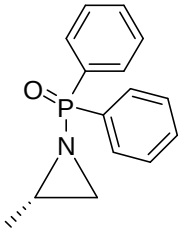

S-2-amino-1-propanol (0.32 g, 4.27 mmol), diphenylphosphinic chloride (2.07 g, 8.74 mmol), triethylamine (1.31 g, 12.94 mmol), sodium hydride (0.48 g (0.77 g including oil), 20.00 mmol) and water (0.6 ml) was carefully added. **1a(S)** (0.34 g, 31%) was obtained as a white powder. R_f = 0.60 (100% ethyl acetate); λ_{max} (DCM)/nm 255; ν_{max} cm^{-1} 3057, 2985, 2961, 2925 (CH), 1443, 1336, 1199, 1133 (P=O), 1110, 961, 847; δ_H (300 MHz; $CDCl_3$) 1.2 (3 H, d, $^3J_{HH}$ 5.2 Hz, Me), 1.8 (1 H, m, ring CH_2), 2.5 (1 H, m, ring CH_2), 2.7 (1 H, m, ring CH), 7.4 (6H, m, phenyl H), 7.8 (4H, m, phenyl H); δ_C (64 MHz; $CDCl_3$) 18.4 (methyl C), 30.8 (ring CH_2), 31.7 (ring CH), 128.8 (phenyl C), 131.9 (phenyl C), 132.4 (phenyl C), 134.6 (phenyl C); δ_P (121 MHz; $CDCl_3$) 32.0; *m/z* (FAB+) 258 $[M+H]^+$.

6.2.4 1-(Diphenyl-phosphinoyl)-2-2-dimethyl-aziridine, ***1b***

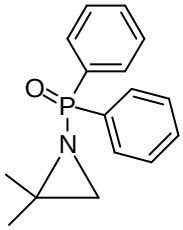

2-amino-2-methyl-1-propanol (3.05 g, 34.22 mmol), diphenylphosphinic chloride (16.20 g, 68.46 mmol), triethylamine (10.39 g, 102.67 mmol), sodium hydride (4.13 g (6.88 g including oil), 172.1 mmol) and water (5.2 ml). **1b** (1.96 g, 21%) was obtained as a white powder. R_f = 0.44 (100% ethyl acetate); λ_{max} (DCM)/nm 258; ν_{max} cm^{-1} 3058, 2987, 2960, 2927 (CH), 1443, 1201, 1134, 1121 (P=O), 1111, 1058, 961, 847; δ_H ($CDCl_3$; 300 MHz) 1.4 (6 H, s, Me), 2.6 (1 H, s, ring H), 3.3 (1 H, s, ring H), 7.5 (6 H, m, phenyl H), 7.9 (4 H, m, phenyl H); δ_C (75 MHz; $CDCl_3$) 23.6 (methyl C), 35.7 (ring CH_2), 42.5 (ring C), 128.3 (phenyl C), 131.5 (phenyl C), 133.7 (phenyl C), 135.5 (phenyl C), δ_P (121 MHz; $CDCl_3$) 28.1. *m/z* (FAB+) 272 $[M+H]^+$.

6.2.5 2-(Diphenylphosphinoylamino)ethyl diphenylphosphinate, ***1d***

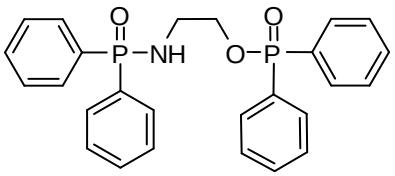

To a solution of 2-aminoethanol (1.04 g, 17.09 mmol) in dry THF (300 ml) at 0^{o}C, under nitrogen, was added diphenylphosphinic chloride (8.09 g, 34.18 mmol) and triethylamine (5.19 g, 51.27 mmol. The solvent was removed under reduced pressure and the product was purified using column chromatography; R_f = 0.31 (5% MeOH, 95% ethyl acetate) to give **1d** (7.87 g, 25%) as a hygroscopic white powder. δ_H (300 MHz; $CDCl_3$) 3.2 (2 H, br m, NHC*H*$_2$), 4.0 (2 H, m, OC*H*$_2$), 7.4 (12H, m, phenyl H), 7.8 (8 H, m, phenyl H); δ_C (75 MHz; $CDCl_3$) 41.2 (NC), 66.6 (OC), 128.6 (phenyl C), 132.0 (phenyl C); δ_P (121 MHz; $CDCl_3$) 24.4, 33.6; *m/z* (ESMS+) 462 $[M+H]^+$.

6.3 Bromo Adipic Acid Ester Derivative Synthesis

6.3.1 2-Bromoadipic acid dimethyl ester, ***5***

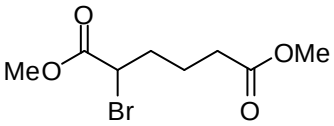

Adipic acid monomethylester (10.07 g, 62.87 mmol) was added to thionyl chloride (32.17 g, 0.27 mol) and the mixture was heated at reflux for 24 hours. Bromine (10.05 g, 62.88 mmol) was then added drop wise over 3 hours. Gentle reflux was maintained throughout and the solution was left at 75^{o}C for two nights, monitored periodically by ^{1}H NMR spectrometry observing the C*H*Br peak at 4.2 ppm. Once the integration showed a 1:3ratio with the methyl peak at 3.7 ppm the mixture was then added cautiously to cold methanol (80 ml). The resulting alcoholic mixture was maintained at 20 ^{o}C for 20 hours then poured into water and extracted with (3 x 100 ml) ether. The combined extracts were washed with water, dilute sodium carbonate solution and again with water. After drying over sodium sulfate the ether was removed under reduced pressure. The pure product was collected following distillation under reduced pressure (bp = 68 ^{o}C 0.06 mmHg) to give **5** (9.89 g, 62%) as a pale yellow oil. ν_{max} cm^{-1} 2954 (CH), 1732 (C=O), 1436, 1258, 1195, 1152 (C-O); δ_H (300 MHz; $CDCl_3$) 1.7 (2 H, m, ~$CH_2CH_2CH_2$~), 1.8 (2 H, m, ~CHBrC*H*$_2$$CH_2$~), 2.4 (2 H, t, $^3J_{HH}$ 7.3 Hz, ~$CH_2CH_2CO_2CH_3$), 3.7 (3 H, s, ~$CH_2O_2CH_3$), 3.8 (3 H, s, ~CHBrO_2C*H*$_3$) 4.2 (1 H, m, ~CBr*H*), δ_C (75 MHz; $CDCl_3$) 22.6 (~$CH_2CH_2CH_2$~), 33.0 (~$CH_2CH_2CO_2CH_3$), 34.1

(~CHBr*C*H_2CH_2~), 45.0 (~*C*BrH), 51.6 (~CHBrCO_2*C*H_3), 53.0 (~CH_2CO_2*C*H_3), 170.0 (carbonyl ~CHBr*C*O_2CH_3), 173.2 (carbonyl ~CH_2*C*O_2CH_3); *m/z* (FAB+) 253 $[M+H]^+$.

6.3.2 2-Bromoadipic acid 1-tert-butyl ester 6-ethyl ester, ***11***

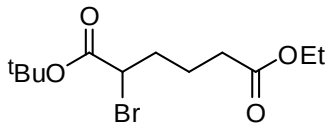

Adipic acid monoethyl ester (10.55 g, 60.56 mmol) was added to thionyl chloride (27.25 g, 0.23 mol) and the mixture was heated at reflux for 24 hours. Bromine (9.98 g, 62.44 mmol) was added drop wise over 3 hours. Gentle reflux was maintained throughout and the solution was left at 75°C for 48 hours, monitored periodically by ^{1}H NMR spectroscopy observing the C*H*Br peak at 4.5 ppm (peaks at 3.2 ppm corresponding to the ClOC*H*$_2$~ acid chloride intermediate were also observed). Once the integration showed a 1:3 with the methyl peak at 1.26 ppm the thionyl chloride was then removed under reduced pressure and the residue was dissolved in dry ether (50 ml) and evaporated three times. The residue was then re-dissolved in dry ether (50 ml) and added very slowly (as HCl gas is evolved) to dry *tert*-butanol (6.97 g, 94.00) and triethylamine (8.71 g, 86.10 mmol) under nitrogen and at room temperature. The solution was then left to stir for 72 hours. The mixture was then poured into water and extracted with (3 x 100 ml) ether. The combined extracts were washed with water, dilute sodium carbonate solution and again with water. After drying over sodium sulfate the ether was removed under reduced pressure. The pure product was collected following distillation under reduced pressure (bp = 68 °C 0.06 mmHg) to give **11** (7.91 g, 44%) as a pale yellow oil. ν_{max} cm^{-1} 2954 (CH), 1732 (C=O), 1436, 1364, 1258, 1195, 1152 (C-O); δ_H (300 MHz; $CDCl_3$) 1.3 (3 H, t, $^3J_{HH}$ 7.0 Hz, ~$CO_2CH_2CH_3$), 1.5 (9 H, s, ^{t}Bu), 1.7 (2 H, m, ~$CH_2CH_2CH_2$~), 2.0 (2 H, m, ~CHBrCH_2CH_2~), 2.4 (2 H, t, $^3J_{HH}$ 7.3 Hz, ~$CH_2CH_2CO_2CH_3$), 4.1 (3 H, m, ~CBr*H* and ~$CO_2CH_2CH_3$ overlap as bromine peak shifts from 4.5 ppm following addition of *tert*-butyl group); δ_C (75 MHz; $CDCl_3$) 13.2 (~$CO_2CH_2CH_3$), 21.7 (~$CH_2CH_2CH_2$~), 26.7 (~$CO_2C(CH_3)_3$), 32.4 (~$CH_2CH_2CO_2CH_2CH_3$), 33.1 (~CHBrCH_2CH_2~), 45.2 (~*C*BrH), 59.4 (~$CO_2CH_2CH_3$), 81.4 (~$CO_2C(CH_3)_3$), 167.6 (carbonyl ~CHBr$CO_2C(CH_3)_3$), 171.8 (carbonyl ~$CH_2CO_2CH_2CH_3$); *m/z* (FAB+) 309 $[M+H]^+$.

6.4 Macrocycle Synthesis

*6.4.1 1,4,7-Tris(methoxycarbonylmethyl)-1,4,7,10-tetraazacyclododecane, **2***

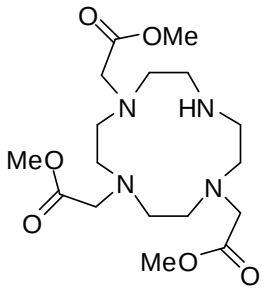

Methyl 2-bromoacetate (5.55 g, 36.28 mmol) in chloroform (100 ml) was added drop wise over 4 hours to a stirred solution of 1,4,7,10-tetracyclododecane (2.08 g. 12.08 mmol) in chloroform (300 ml) in the presence of K_2CO_3 (1.74 g, 12.60 mmol) under nitrogen. After addition was complete the solution was left to stir at room temperature for 72 hours. Inorganic salts were then removed by filtration and the solvent removed under reduced pressure. The product was purified using silica column chromatography with solvent gradient elution from 100% DCM to 6% MeOH, 1% ammonia and 93% DCM. R_f = 0.54 (10% MeOH, 1% NH_3, 90% DCM) to give **2** (1.71 g, 36%) as a hygroscopic white powder. ν_{max} cm^{-1} 2953, 2846, 1729 (C=O), 1436, 1380, 1311, 1200, 1116 (C–O); δ_H (300 MHz; $CDCl_3$) 2.9 (4 H, br s, ring H), 3.0 (8 H, br s, ring H), 3.1 (4 H, br s, ring H), 3.5 (6 H, s, ~OCC*H*$_2$N~), 3.7 (9 H, s, ~OC*H*$_3$); δ_C (75 MHz; $CDCl_3$) 47.3, 48.5, 49.3, 51.3 (ring CH_2), 51.7 (~CO_2*C*H_3), 56.9 (~OC*C*H_2N~), 170.7, 171.6 (CO_2); *m/z* (HR-FAB+) $[M+H]^+$ calcd for $C_{17}H_{33}N_4O_6$, 389.24001; found, 389.24003.

*6.4.2 1,4,7-Tris[(4'-methoxycarbonyl)-1'-methoxycarbonylbutyl]-1,4,7,10-tetraazacyclododedane, **6***

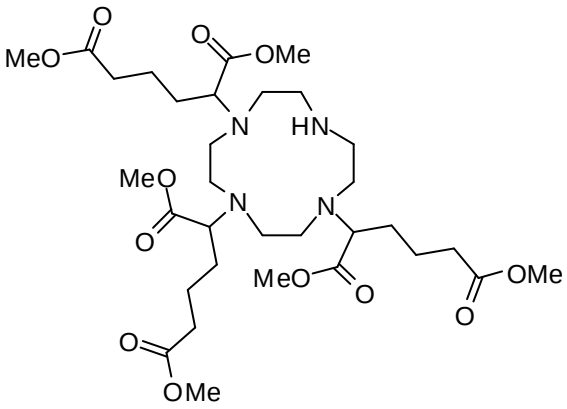

1,4,7,10-tetracyclododecane (0.35 g, 2.05 mmol) and **5** (1.56 g, 6.16 mmol) in the presence of K_2CO_3 (0.68 g, 4.92 mmol) were heated in dry acetonitrile (10 ml) at 60 ^oC under nitrogen for 2 days. The solution was then filtered through celite and the solvent was removed

under reduced pressure. The product was purified by silica column chromatography with solvent gradient elution from 100% DCM to 60% THF, 5% MeOH, 5% NH_3, 30% DCM. R_f = 0.53 (70% THF, 30% DCM) to give **5** (0.47 g, 33%, 6 possible stereoisomers) as a yellow oil. ν_{max} cm^{-1} 2953, 2847 (CH), 1726 (C=O), 1435, 1365, 1195, 1155 (C–O); δ_H (300 MHz; $CDCl_3$) 1.5 (6 H, br, ~$CH_2CH_2CH_2$~), 1.7 (6 H, br, ~$CHBrCH_2CH_2$~), 2.2 (6 H, br, ~$CH_2CH_2CO_2CH_3$) 2.3 – 3.2 (16 H, br, ring H), 3.6 (3 H, br, ~CN*H*), 3.5 – 3.7 (18 H, 3 x s, ~CO_2CH_3); δ_C (75 MHz; $CDCl_3$) 22.1 (~$CH_2CH_2CH_2$~), 25.6 (~$CHNCH_2CH_2$~), 33.4 (~$CH_2CH_2CO_2CH_3$), 46.1, 49.6, 51.0 (ring CH_2), 51.2 (~CO_2CH_3), 60.6 (~*C*NH), 172.1, 172.6, 173.4 (CO_2); *m/z* (ESMS+) 689 $[M+H]^+$.

*6.4.3 1,4,7,10-Tetra[(4'-methoxycarbonyl)-1'-methoxycarbonylbutyl]-1,4,7,10-tetraazacyclododedane, **7***

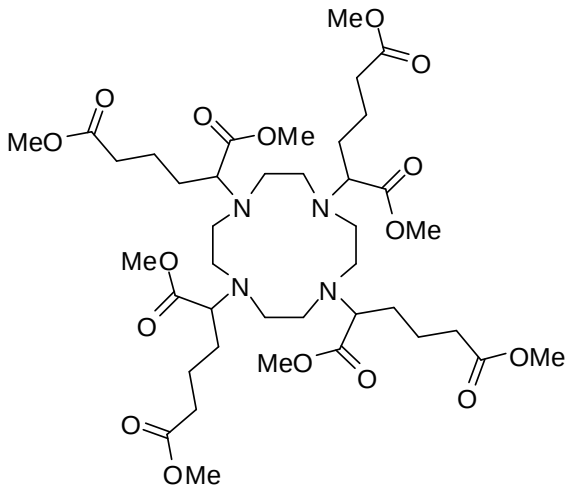

1,4,7,10-tetracyclododecane (1.14 g, 6.63 mmol) and **5** (5.02 g, 19.84 mmol) in the presence of K_2CO_3 (0.93 g, 6.70 mmol) were heated in dry acetonitrile (10 ml) at 85 ^oC under nitrogen for 48 hours. The solution was then filtered through celite and the solvent was removed under reduced pressure. The product was purified by silica column chromatography with solvent gradient elution from 100% DCM to 30% THF, 70% DCM. R_f = 0.75 (70% THF, 30% DCM) to give **7** (1.02 g, 21%, 6 possible stereoisomers) as a yellow oil. ν_{max} cm^{-1} 2954 (CH), 1731 (C=O), 1436, 1153; δ_H (300 MHz; $CDCl_3$) 1.4 – 2.0 (24 H, br, aliphatic CH_2), 2.1 – 2.2 (16 H, br, ring H), 3.4 – 3.5 (24 H, 2 x s, ~CO_2CH_3), 3.6 (4H, br, ~CN*H*); δ_C (75 MHz; $CDCl_3$) 22.18, 24.4, 27.2, 28.7, 34.0 (aliphatic CH_2), 50.1, 50.2, 50.5, 50.6 (ring CH_2), 51.5 (~CO_2CH_3), 62.6 (~*C*NH), 173.2 (carbonyl ~$CHNCO_2CH_3$), 173.7 (carbonyl ~$CH_2CO_2CH_3$); *m/z* (HR-FAB+) $[M+H]^+$ calcd for $C_{40}H_{69}N_4O_{16}$; 861.47086, found; 861.47089.

6.4.4 *1,4,7-Tris[(4'-ethoxycarbonyl)-1'-tert-butoxycarbonylbutyl]-1,4,7,10-tetraazacyclododecane,* ***12***

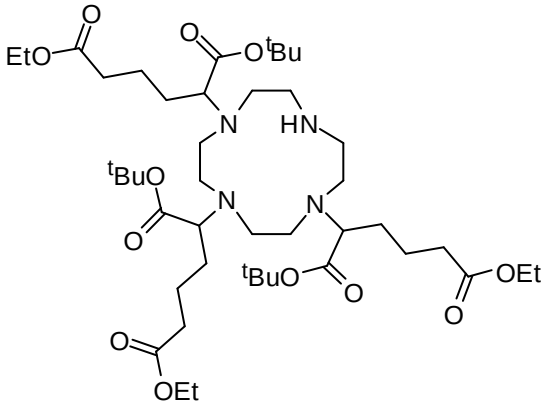

1,4,7,10-tetracyclododecane (0.18 g, 1.05 mmol) and **11** (1.01 g, 3.27 mmol) in the presence of K_2CO_3 (0.15 g, 1.09 mmol) were heated in dry MeCN (10 ml) at 60 ^oC under nitrogen for 5 days. The solution was then filtered through celite and the solvent was removed under reduced pressure. The product was purified by column chromatography with solvent gradient elution from 100% DCM to 20% THF, 80% DCM. R_f = 0.58 (70% THF, 30% DCM) to give **12** (0.44 mg, 48%, 6 possible stereoisomers) as a yellow oil. ν_{max} cm^{-1} 3642, 2964, 1727 (C=O), 1146; δ_H (300 MHz; $CDCl_3$) 1.2 (9 H, t, $^3J_{HH}$ 7.3 Hz, ~$CO_2CH_2CH_3$), 1.4 (27 H, 3 x s, ^{t}Bu), 1.5 – 1.8 (12 H, br, ~$CHNCH_2CH_2$~ and ~$CH_2CH_2CH_2$~), 2.3 (6H, br, ~$CH_2CH_2CO_2CH_2CH_3$), 2.4 –3.3 (16 H, br, ring H), 3.7 (3H, br, ~CNH), 4.0 (6 H, q, $^3J_{HH}$ 7.0 Hz, ~$CO_2CH_2CH_3$); δ_C (75 MHz; $CDCl_3$) 13.2 (~$CO_2CH_2CH_3$), 21.3 (~$CH_2CH_2CH_2$~), 24.6 (~$CHNCH_2CH_2$~), 27.2 (~$CO_2C(CH_3)_3$), 29.3 (~$CO_2C(CH_3)_3$), 32.7 (~$CH_2CH_2CO_2CH_2CH_3$), 44.8, 45.5, 47.5, 49.0, 50.2, 50.6, 51.1 (ring CH_2), 59.3 (~$CO_2CH_2CH_3$), 66.9 (~CNH), 81.0 (~$CO_2C(CH_3)_3$), 170.5 (carbonyl ~$CHNCO_2C(CH_3)_3$), 172.0 (carbonyl ~$CH_2CO_2CH_2CH_3$); *m/z* (HR-ESMS+) $[M+H]^+$ calcd for $C_{44}H_{81}N_4O_{12}$; 857.5846, found; 857.5846.

6.4.5 1,4,7,10-Tetra[(4'-ethoxycarbonyl)-1'-tert-butoxycarbonylbutyl]-1,4,7,10-tetraazacyclododecane, ***13***

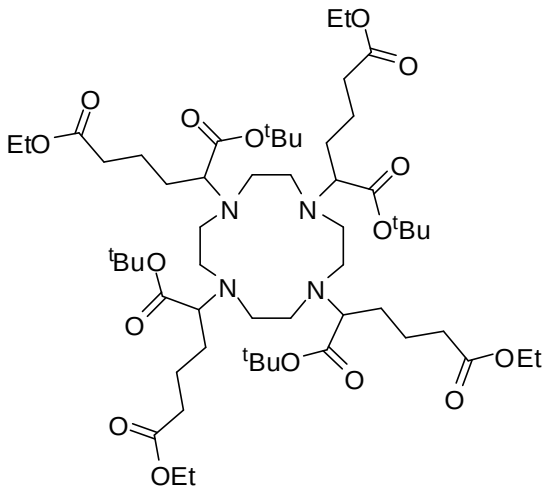

1,4,7,10-tetracyclododecane (0.41 mg, 2.37 mmol) and **11** (2.94 g, 9.51 mmol) in the presence of K_2CO_3 (1.32 g, 9.55 mmol) were heated in dry acetonitrile (10 ml) at 85 ^oC under nitrogen for 5 days. The solution was then filtered through celite and the solvent was removed under reduced pressure. The product was purified by silica column chromatography with solvent gradient elution from 100% DCM to 6% THF, 94% DCM. R_f = 0.73 (70% THF, 30% DCM). to give **13** (0.43 g, 16%, 6 possible stereoisomers) as a yellow oil. ν_{max} cm^{-1} 2859, 1537 (C=O), 1394; δ_H (300 MHz; $CDCl_3$) 1.2 (12 H, t, $^3J_{HH}$ 6.4 Hz, ~$CO_2CH_2CH_3$), 1.4 (36 H, 2 x s, ^{t}Bu), 1.4 – 2.0 (24 H, br, aliphatic CH_2), 2.2 – 2.4 (20 H, br, ring H (16 H) and ~CN*H* (4 H)), 4.0 (8 H, br q, $^3J_{HH}$ 7.0 Hz, ~$CO_2CH_2CH_3$); δ_C (75 MHz; $CDCl_3$) 14.1 (~$CO_2CH_2CH_3$), 22.5, 24.4, 32.4, 35.0, 38.0 (aliphatic CH_2), 27.8, 30.2 (~$CO_2C(CH_3)_3$), 50.5 (ring CH_2) 60.1 (~$CO_2CH_2CH_3$), 70.1 (~*C*NH), 81.1 (~$CO_2OC(CH_3)_3$), 169.7, 172.5, 173.2 (CO_2); *m/z* (FAB+) 1086 $[M+H]^+$.

6.4.6 1-Tert-butoxycarbonyl-4,7,10-tris[(4'-ethoxycarbonyl)-1'-tert-butoxycarbonylbutyl]-1,4,7,10-tetraazacyclododecane, ***15***

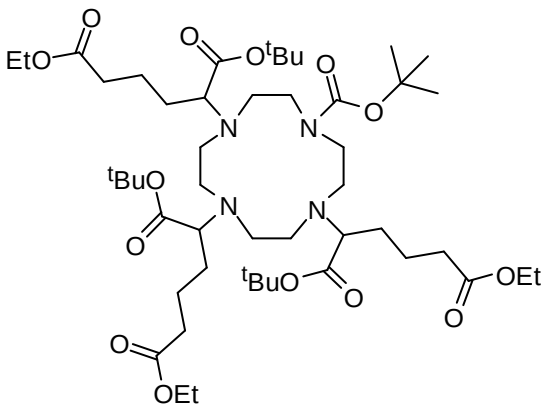

To a solution of **12** (0.162 g, 0.189 mmol) and triethylamine (0.019 g, 0.189 mmol) in dry DCM (10ml) at 0^{o}C was added di-*tert*-buytyl-dicarbonate (0.041, 0.189 mmol) in 10 ml DCM drop wise under nitrogen and was left to stir for 24 hours. The solvent was then removed under reduced pressure and the product was purified by silica column chromatography with solvent gradient elution from 100% DCM to 10% MeOH, 90% DCM. R_f = 0.60 (10% THF, 90% DCM) to give **15** (145.02 mg, 80%, 6 possible stereoisomers) as a yellow oil. ν_{max} cm^{-1} 2976, 2934, 1726 (C=O), 1689 (C=O), 1366, 1143; δ_H (300 MHz; $CDCl_3$) 1.3 (9 H, t, $^3J_{HH}$ 6.7 Hz, ~$CO_2CH_2CH_3$), 1.5 (36 H, 2 x s, ^{t}Bu), 1.5 – 1.9 (12 H, br, ~CHNCH_2CH_2~ and ~$CH_2CH_2CH_2$~), 2.3 –2.4 (6 H, br, ~$CH_2CH_2CO_2CH_2CH_3$), 2.4 – 3.6 (19 H, br, ring H (16 H) and ~CN*H* (3 H) overlap), 4.1 (6 H, q, $^3J_{HH}$ 7.0 Hz, ~$CO_2CH_2CH_3$); δ_C (75 MHz; $CDCl_3$) 14.2 (~$CO_2OCH_2CH_3$), 22.1 (~$CH_2CH_2CH_2$~), 28.2 (~$CO_2C(CH_3)_3$), 28.4 (~$CO_2C(CH_3)_3$), 29.3 (~CHNCH_2CH_2~), 34.0 (~$CH_2CH_2CO_2CH_2CH_3$), 46.3, 47.2, 47.6, 48.8, 49.5, 50.0, 51.0, 51.4 (ring CH_2), 60.1 (~$CO_2CH_2CH_3$), 61.7 (~*C*NH), 80.7 (BOC ~$CO_2C(CH_3)_3$), 80.9 (~$CO_2OC(CH_3)_3$), 155.7 (BOC, CO_2), 171.6 (carbonyl ~CHN$CO_2C(CH_3)_3$), 173.1 (carbonyl ~$CH_2CO_2CH_2CH_3$); *m/z* (ESMS+) 957 $[M+H]^+$.

6.4.7 1-Tert-butoxycarbonyl-4,7,10-tris[(4'-carboxyl)-1'-tert-butoxycarbonylbutyl]-1,4,7,10-tetraazacyclododecane, ***16***

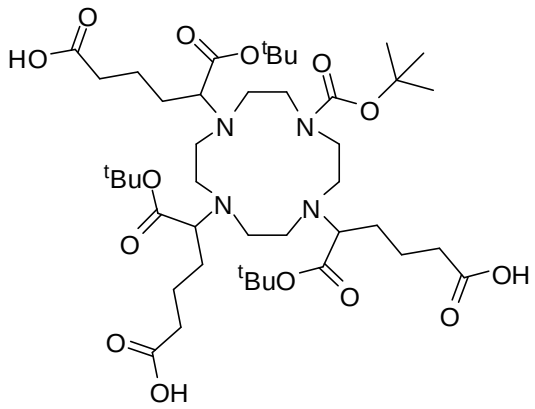

15 (0.145 g, 0.151 mmol), was dissolved in 10 ml EtOH and 10 ml 1M NaOH and stirred overnight. The ethanol was then removed under reduced pressure and the solution pH was lowered to 5 (carefully at 0^{o}C) and was lyophilised. The product was then extracted from the salt residue with 20% dry MeOH/DCM solution which was then removed under reduced pressure to yield **16** as a pale oil (0.129 g, 97%, 6 possible stereoisomers). ν_{max} cm^{-1} 2975, 2932, 1719 (C=O), 1367, 1144; δ_H (300 MHz; $CDCl_3$), 1.5 (36 H, 2 x s, ^{t}Bu), 1.5 – 1.9 (18 H, br, ~CHNCH_2CH_2~ and ~$CH_2CH_2CH_2$~), 2.4 (6 H, br, ~$CH_2CH_2CO_2H$), 2.5 – 3.9 (19 H, br, ring H (16 H) and ~CN*H* H (3 H)); *m/z* (ESMS+) 873 $[M+H]^+$.

*6.4.8 1-Tert-butoxycarbonyl-4,7,10-tris[(4'-(acetoxymethoxycarbonyl)-1'-tert-butoxycarbonylbutyl]-1,4,7,10-tetraazacyclododecane, **17***

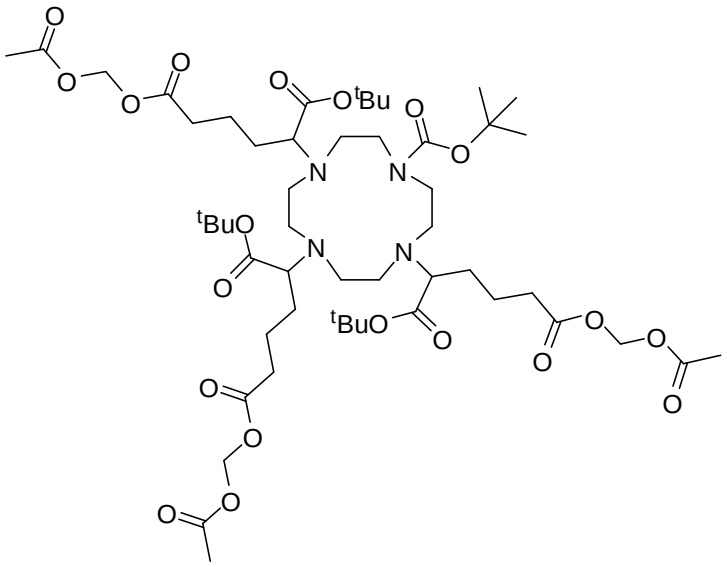

To a solution of **16** (0.131 g, 0.106 mmol) in dry DCM was added DIPEA (0.058 g, 0.451 mmol) and bromomethyl acetate (0.072 g, 0.451 mmol) under nitrogen and was left to stir for 24 hours. The solvents were removed under reduced pressure and the product was purified by column chromatography using ethyl acetate as eluent to yield **17** as a pale oil (74.9 mg, 45%, 6 possible stereoisomers). R_f = 0.79 (ethyl acetate). ν_{max} cm^{-1} 2975, 1763, 1720, 1688 (C=O), 1367, 1143; δ_H (300 MHz; $CDCl_3$) 1.4 (36 H, s, ^tBu), 1.5 – 1.8 (16 H, br, ~CHNC$H_2$$CH_2$~ and ~$CH_2CH_2$$CH_2$~), 2.0 (9H, s, ~$CO_2CCH_3$), 2.2 –2.4 (6 H, br, ~$CH_2CH_2CO_2CH_2$~), 2.5 – 3.7 (19 H, br, ring H (16 H) and ~CN*H* (3 H)), 5.7 (6H, s, ~OCH_2O~); δ_C (75 MHz; $CDCl_3$) 19.7 (~CO_2CCH_3), 20.7 (~$CH_2$$CH_2CH_2$~) 27.5 (~$CO_2$C($CH_3$)$_3$), 28.8 (~CHN$CH_2CH_2$~), 34.0 (~$CH_2$$CH_2CO_2CH_2$~), 45.4, 46.3, 46.9, 47.4, 49.1, 50.0 (ring CH_2), 60.8 (~*C*NH), 78.1 (~OCH_2O~), 80.1 (~CO_2*C*(CH_3)$_3$), 154.7 (BOC CO_2), 168.6 (carbonyl ~CHNCO_2C(CH_3)$_3$), 170.9 (carbonyl ~*C*$O_2$$CCH_3$), 171.38 (carbonyl ~CHN$CO_2CH_2$~); *m/z* (ESMS+) 1089 $[M+H]^+$.

6.5 Dpp Ring Opening Synthesis

General synthesis; the appropriate macrocycle and aziridine were dissolved in dry MeCN (or DMF, **3b**). K_2CO_3 was added. The solution was then stirred under nitrogen for up to 72 hours at 85°C (or 120°C in DMF, **3b**), monitored by ESMS. The solution was then allowed to cool and was filtered through celite and the solvent removed under reduced pressure. The product was purified by silica column chromatography with solvent gradient elution from 100% DCM to 8% MeOH, 1% ammonia and 91% DCM.

6.5.1 1-[2'-(Diphenylphosphinylamino)-propyl]-4,7,10-tris(methoxycarbonylmethyl)-1,4,7,10-tetraazacyclododecane, ***3a***

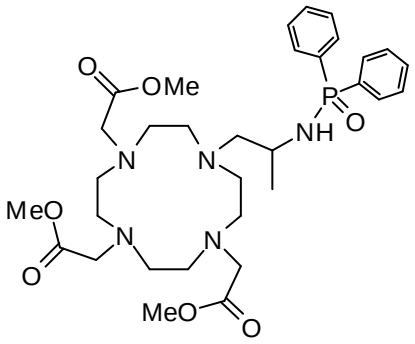

2 (0.311 g, 0.78 mmol), K_2CO_3 (0.11 g, 0.79 mmol) and **1a** (0.21 g, 0.82 mmol). **3a** (121.1 mg, 23%) was obtained as a yellow oil. R_f = 0.60 (10% MeOH, 1% NH_3, 90% DCM); λ_{max} (DCM)/nm 269; ν_{max} cm^{-1} 3352 (br), 2951, 2825 (CH), 1733 (C=O), 1667, 1438, 1308, 1196 (P=O), 1112; δ_H (300 MHz; $CDCl_3$) 1.1 (3 H, d, dpp CH_3) 1.9 – 4.4 (25 H, br, (ring H (16 H), ~OCC*H*$_2$N~ (6 H), dpp ~NC*H*$_2$C~ (2 H), dpp ~C*H*CH_3 (1 H)), 3.7 (9 H, 2 x s, ~CO_2*C*H_3) 7.4 (6 H, m, phenyl H), 7.9 (4 H, m, phenyl H); δ_C (75 MHz; $CDCl_3$) 23.5 (dpp CH_3), 43.4 (dpp ~*C*HCH_3), 48.4, 50.4, 51.4, 53.5 (ring CH_2), 51.7, 52.0, 52.5 (~CO_2*C*H_3), 55.0, 55.3, 55.9 (~OC*C*H_2N~), 66.2 (dpp ~NC*H*$_2$C~), 129.8 (phenyl C), 132.1 (phenyl C), 133.3 (phenyl C), 134.4 (phenyl C), 172.0 (CO_2), 173.5 (CO_2), 174.3 (CO_2); δ_P (121 MHz; $CDCl_3$) 24.1; *m/z* (HR-FAB+) $[M+H]^+$ calcd for $C_{32}H_{49}N_5O_7P$; 646.33696, found; 646.33703.

6.5.2 1-[(R)-2'-(Diphenylphosphinylamino)-propyl]-4,7,10-tris(methoxycarbonylmethyl)-1,4,7,10-tetraazacyclododecane, ***3a(R)***

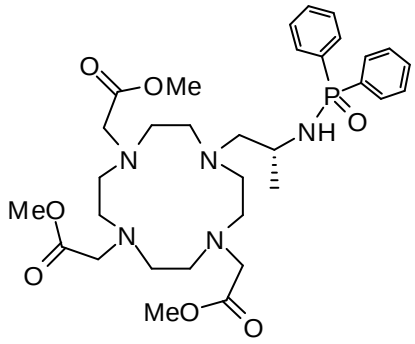

2 (0.051 g, 0.13 mmol), K_2CO_3 (0.018 g, 0.13 mmol) and **1a(R)** (0.033 g, 0.13 mmol). **3a(R)** (0.026 g, 32%) was obtained as a yellow oil. R_f = 0.60 (10% MeOH, 1% NH_3, 90% DCM); λ_{max} (DCM)/nm 269; ν_{max} cm^{-1} 3349 (br), 2952, 2831 (CH), 1732 (C=O), 1666, 1438,

1308, 1197 (P=O), 1112; δ_H (300 MHz; $CDCl_3$) 1.1 (3 H, d, dpp CH_3) 1.2 – 4.2 (25 H, br, (ring H (16 H), ~OCCH_2N~ (6 H), dpp ~NCH_2C~ (2 H), dpp ~CHCH_3 (1 H)) 3.7 (9 H, m, 3 x s, OCH_3) 7.4 (6 H, m, phenyl H), 7.9 (4 H, m, phenyl H); δ_C (75 MHz; $CDCl_3$) 23.5 (dpp CH_3), 43.4 (dpp ~CHCH_3), 47.3, 48.3, 49.5, 50.6, 51.2 (ring CH_2), 51.4, 51.6, 52.0 (OCH_3), 53.1, 55.0, 55.3, 55.9, 60.3 (~OCCH$_2$N~), 66.2 (dpp ~NCH_2C~), 128.3 (phenyl C), 132.1 (phenyl C), 133.2 (phenyl C), 134.3 (phenyl C), 163.6 (phenyl C), 171.6, 172.0, 173.4, 174.4 (CO_2); δ_P (121 MHz; $CDCl_3$) 24.1; *m/z* (ESMS+) 646 $[M+H]^+$.

6.5.3 1-[(S)-2'-(Diphenylphosphinylamino)-propyl]-4,7,10-tris(methoxycarbonylmethyl)-1,4,7,10-tetraazacyclododecane, ***3a(S)***

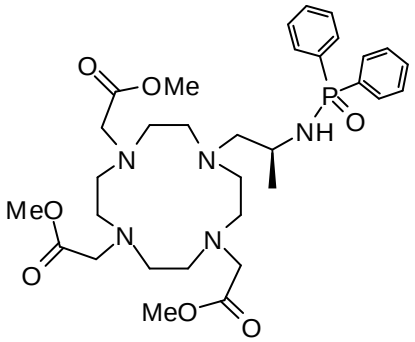

2 (0.066 g, 0.17 mmol), **1a(S)** (0.044 g, 0.17 mmol) and K_2CO_3 (0.02 g, 0.17 mmol). **3a(S)** (0.045 g, 41%) was obtained as a yellow oil. R_f = 0.60 (10% MeOH, 1% NH_3, 90% DCM); λ_{max} (DCM)/nm 269; ν_{max} cm^{-1} 3351 (br), 2952, 2830 (CH), 1733 (C=O), 1666, 1438, 1308, 1196 (P=O), 1112; δ_H (300 MHz; $CDCl_3$) 1.1 (3 H, d, dpp CH_3), 1.4 – 4.1 (25 H, br, (ring H (16 H), ~OCCH_2N~ (6 H), dpp ~NCH_2C~ (2 H), dpp ~CHCH_3 (1 H)), 3.7 (9 H, m, 2 x s, OCH_3), 7.4 (6 H, m, phenyl H), 7.9 (4 H, m, phenyl H); δ_C (75 MHz; $CDCl_3$) 21.0 (dpp CH_3), 43.5 (dpp ~CHCH_3), 48.4, 49.4, 50.6, (ring CH_2), 51.4, 51.6, 52.0 (~CO_2CH$_3$), 53.2, 53.5, 55.1, 55.9 (~OCCH$_2$N~), 66.3 (dpp ~NCH_2C~), 128.3 (phenyl C), 132.0 (phenyl C), 172.0, 173.5, 174.3 (CO_2); δ_P (121 MHz; $CDCl_3$) 24.0; *m/z* (ESMS+) 646 $[M+H]^+$.

6.5.4 1-[2-(Diphenylphosphinylamino)-2-(methyl)-propyl -4,7,10-tris(methoxycarbonylmethyl)-1,4,7,10-tetraazacyclododecane, ***3b***

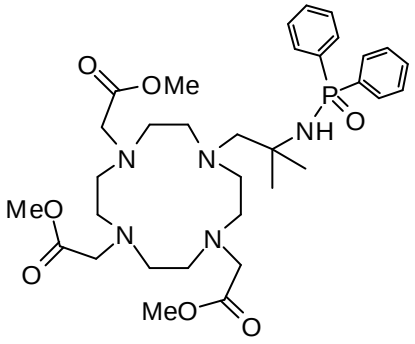

2 (0.305 g, 0.79 mmol), **1b** (0.217 g, 0.80 mmol) and K_2CO_3 (0.112 g, 0.81 mmol). **3b** (0.102 g, 19%) was obtained as a yellow oil. R_f = 0.70 (10% MeOH, 1% NH_3, 90% DCM); λ_{max} (DCM)/nm 269; ν_{max} cm^{-1} 3370 (br), 2926, 2852 (CH), 1732 (C=O), 1655, 1378, 1438, 1215 (P=O), 1110; δ_H (300 MHz; $CDCl_3$) 1.2 (6 H, br s, dpp CH_3), 2.2 – 3.5 (24 H, br, (ring H (16 H), ~OCC*H*$_2$N~ (6 H), dpp ~NC*H*$_2$C~ (2 H)), 3.6, 3.6, 3.7 (9 H, 3 x s, OCH_3), 7.4 (6 H, m, phenyl H) 7.8, (4 H, m, phenyl H); δ_C (75 MHz; $CDCl_3$) 29.0 (dpp CH_3), 38.4 (~*C*$(CH_3)_2$), 51.0 (ring CH_2), 54.2, 54.8 (~OC*C*H_2N~), 69.3 (dpp ~NC*H*$_2$C~), 127.4 (phenyl C), 130.5 (phenyl C), 172.4, 172.8 (CO_2); δ_P (121 MHz; $CDCl_3$) 19.4 (s); *m/z* (HR-FAB+) $[M+H]^+$ calcd for $C_{33}H_{51}N_5O_7P$; 660.35261, found; 660.35262.

6.5.5 *1-[2-(Diphenylphosphinylamino)propyl]-4,7,10-tris[(4'-methoxycarbonyl)-1'-methoxycarbonylbutyl]-1,4,7,10-tetraazacyclododecane,* ***8***

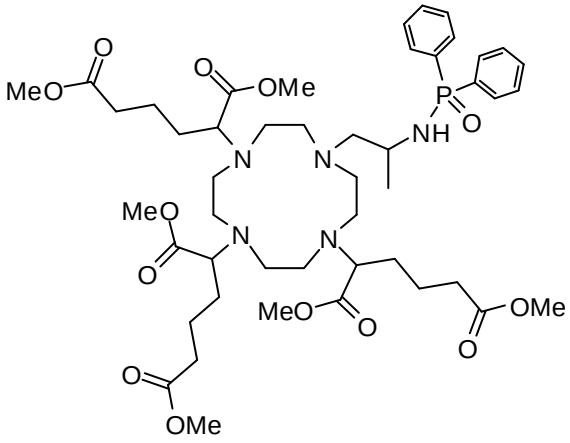

6 (0.171 g, 0.25 mmol), **1a** (0.064 g, 0.25 mmol) and K_2CO_3 (0.035 g, 0.25 mmol). **8** (0.033 g, 14%, 12 possible stereoisomers) was obtained as a as a yellow oil. R_f = 0.40 (10% MeOH, 1% NH_3, 90% DCM); λ_{max} (DCM)/nm 266; ν_{max} cm^{-1} 3285 (br), 2952, (CH), 1727 (C=O), 1637, 1436, 1155, (P=O); δ_H (300 MHz; $CDCl_3$) 1.3 (3 H, m, dpp CH_3), 1.5 – 2.1 (12 H, br, ~CHNC*H*$_2$CH_2~ and ~CH_2C*H*$_2$CH_2~), 2.4 (6 H, br, ~CH_2C*H*$_2$CO_2CH_3), 2.5 – 3.3 (22 H, br, ring H (16 H), ~CN*H* (3H), dpp ~NC*H*$_2$C~ (2 H), dpp ~C*H*CH_3 (1 H)), 3.7 (18H, 4 x s, ~CO_2C*H*$_3$) 7.5 (6 H, m, phenyl H), 7.9 (4 H, m, phenyl H); δ_C (100 MHz; $CDCl_3$) 21.0 (dpp CH_3), 22.1 (~CH_2*C*H_2CH_2~), 28.5 (~CHNCH_2CH_2~), 33.5 (~CH_2*C*H_2CO_2CH_3), 45.8 (dpp ~*C*HCH_3), 46.2, 49.8 (ring CH_2), 51.5 (~CO_2*C*H_3), 53.4 (dpp ~NCH_2C~), 63.1 (~*C*NH), 128.6 (phenyl C), 132.2 (phenyl C), 172.9 (carbonyl ~CHN*C*O_2CH_3), 173.5 (carbonyl ~CH_2*C*O_2CH_3); δ_P (121 MHz; $CDCl_3$) 27.8; *m/z* (HR-ESMS+) $[M+H]^+$ calcd for $C_{47}H_{73}N_5O_{13}P$; 946.4937, found; 946.4935.

6.5.6 1-[(R)-2-(Diphenylphosphinylamino)propyl]-4,7,10-tris[(4'-methoxycarbonyl)-1'-methoxycarbonylbutyl]-1,4,7,10-tetraazacyclododecane, ***8(R)***

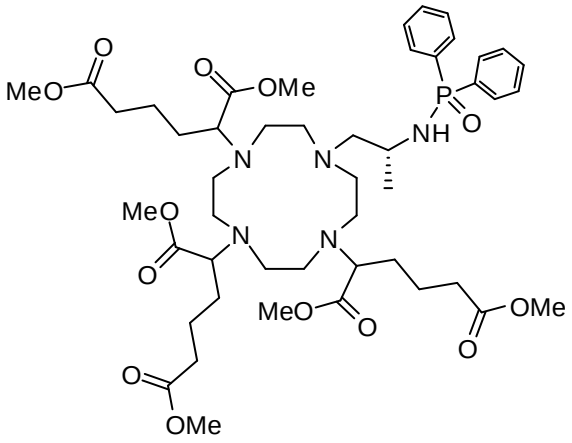

6 (0.180 g, 0.26 mmol), **1a(R)** (0.067 g, 0.26 mmol) and K_2CO_3 (0.036 g, 0.26 mmol). **8(R)** (18.9 mg, 7%, 6 possible stereoisomers) was obtained as a yellow oil. R_f = 0.40 (10% MeOH, 1% NH_3, 90% DCM); λ_{max} (DCM)/nm 264; ν_{max} cm^{-1} 2954 (br), (CH), 1728 (C=O), 1688, 1436, 1196, 1154, (P=O), 1122; δ_H (300 MHz; $CDCl_3$) 1.3 (3 H, m, dpp CH_3) 1.5 – 1.9 (12 H, br, ~CHNCH_2CH_2~ and ~CH_2CH_2CH_2~) 2.3 (6 H, m, ~CH_2CH_2CO_2CH_3), 2.5 – 3.5 (22 H, br, ring H (16 H), ~CNH (3H), dpp ~NCH_2C~ (2 H), dpp ~C$H$$CH_3$ (1 H), 3.7 (18H, 4 x s, ~CO_2CH_3), 7.5 (6 H, m, phenyl H), 7.9 (4 H, m, phenyl H); δ_C (100 MHz; $CDCl_3$) 21.0 (dpp CH_3), 22.2, 22.6, 28.4, 29.3, 33.5 (aliphatic CH_2), 43.7 (dpp ~CHCH_3), 45.8, 49.7 (ring CH_2), 51.5 (~$CO_2C$$H_3$), 61.4 (dpp ~N$CH_2$C~), 63.1 (~$C$NH), 128.5 (phenyl C), 132.4 (phenyl C), 172.9 (carbonyl ~CHNCO_2CH_3), 173.6 (carbonyl ~$CH_2CO_2CH_3$); δ_P (121 MHz; $CDCl_3$) 27.1; *m/z* (ESMS+) 946 $[M+H]^+$.

6.5.7 1-[(S)-2-(Diphenylphosphinylamino)propyl -4,7,10-tris[(4'-methoxycarbonyl)-1'-methoxycarbonylbutyl]-1,4,7,10-tetraazacyclododecane, ***8(S)***

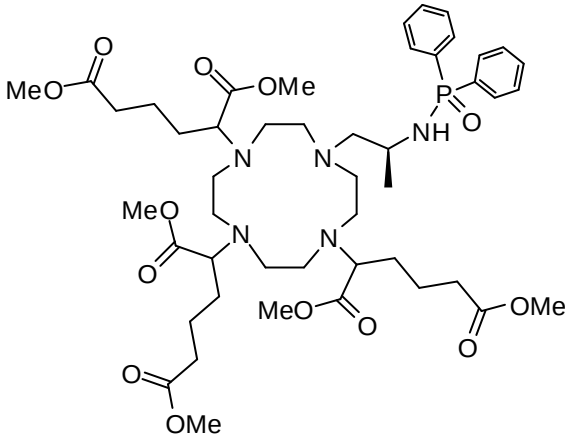

6 (0.18 g, 0.26 mmol), **1a(S)** (0.067 g, 0.26 mmol) and K_2CO_3 (0.036 g, 0.26 mmol). **8(S)** (0.029 mg, 11%, 6 possible stereoisomers) was obtained as a yellow oil. R_f = 0.40 (10%

MeOH, 1% NH_3, 90% DCM); λ_{max} (DCM)/nm 263; ν_{max} cm^{-1} 2961 (br), (CH), 1730 (C=O), 1688, 1436, 1259, 1155 (P=O), 1094, 1017; δ_H (300 MHz; $CDCl_3$) 1.3 (3 H, dpp CH_3) 1.6 (6 H, br, ~$CH_2CH_2CH_2$~), 1.7 (6H, br, ~$CHNCH_2CH_2$~), 2.3 (6 H, br, ~$CH_2CH_2CO_2CH_3$), 2.4 – 3.4 (22 H, br, ring H (16 H), ~CN*H* (3H), dpp ~NCH_2C~ (2 H), dpp ~$CHCH_3$ (1 H)), 3.7 (18H, 4 x s, ~CO_2CH_3), 7.5 (6 H, m, phenyl H), 7.9 (4 H, m, phenyl H); δ_C (100 MHz; $CDCl_3$) 20.6 (dpp CH_3), 22.2 (~$CH_2CH_2CH_2$~), 29.0 (~$CHNCH_2CH_2$~), 33.6 (~$CH_2CH_2CO_2CH_3$), 44.6 (dpp ~$CHCH_3$), 48.1, 49.7, 50.2, (ring CH_2), 51.5 (~CO_2CH_3), 53.4 (dpp ~NCH_2C~), 63.1 (~CNH), 128.5 (phenyl C), 132.2 (phenyl C), 173.7 (carbonyl ~$CHNCO_2CH_3$), 174.6 (carbonyl ~$CH_2CO_2CH_3$); δ_P (121 MHz; $CDCl_3$) 27.2; *m/z* (ESMS+) 946 $[M+H]^+$.

6.6 Pro-Ligand Synthesis

General synthesis for the base hydrolysis of methyl ester protected macrocycles, **4a**, **4a(R)**, **4a(S)**, **4b**, **9**, **9(R)**, **9(S)**, **10** and **19**. The methyl ester protected macrocycles were dissolved in 1 M LiOH (5ml) and heated at 80°C for 24 hours. The resulting solution was loaded onto a Dowex 50 W strong acid-cation exchange column (H^+ form), washed with water and eluted with 12% ammonia solution. The solvent was then removed under reduced pressure and the residue taken up in water and lyophilized to give the product.

General synthesis for the acid hydrolysis of *tert*-butyl ester protected macrocycles, **14**, **18**, and **20**. The *tert*-butyl ester protected macrocycles were dissolved in dichloromethane (2.5ml) and TFA (2.5 ml) was carefully added. The mixture was stirred at room temperature for 3 hours under nitrogen. The solvent was then removed under reduced pressure. Two portions of dichloromethane (5ml) were added and removed under reduced pressure, followed by 2 portions of ether (5ml), which were also removed under reduced pressure to yield the product.

*6.6.1 1-[2-(Diphenylphosphinylamino)propyl]-4,7,10-tris(carboxymethyl)-1,4,7,10-tetraazacyclododecane, **4a***

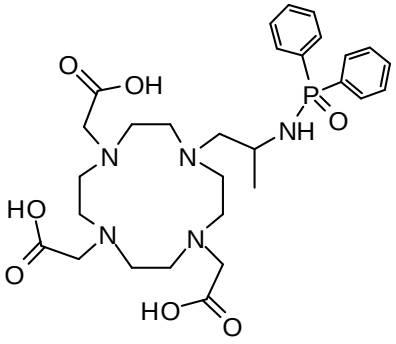

3a (0.121 g, 0.19 mmol). **4a** (0.075 g, 58%) was obtained as a white hygroscopic powder. λ_{max} (H_2O)/nm 269; ν_{max} cm^{-1} 3335 (OH), 1583 (C=O), 1410, 1175 (P=O), 1094.24, 996, 862; δ_H (300 MHz; D_2O) 1.9 (3H, s, CH_3), 1.2 – 4.0 (25 H, br, (ring H (16 H), ~OCC*H*$_2$N~ (6 H), dpp ~NC*H*$_2$C~ (2 H), dpp ~C*H*CH_3 (1 H)), 7.6 (6 H, m, phenyl H), 7.9 (4 H, m, phenyl H); δ_C (75 MHz; D_2O) 24.7 (CH_3), 46.0 (~*C*HCH_3), 50.9, 51.3, 51.7, 52.1, 53.0, 53.7 (ring CH_2), 58.3, 59.2 (~OC*C*H$_2$N~), 62.4 (dpp ~NC*H*$_2$C~), 131.5 (phenyl C), 134.3 (phenyl C), 135.4 (phenyl C), 174.0, 178.7, 180.7 (CO_2); δ_P (121 MHz; D_2O) 28.1; *m/z* (HR-FAB+) $[M+H]^+$ calcd for $C_{29}H_{43}N_5O_7P$; 604.29001, found; 604.29002.

6.6.2 1-[(R)-2-(Diphenylphosphinylamino)propyl -4,7,10-tris(carboxymethyl)-1,4,7,10-tetraazacyclododecane, ***4a(R)***

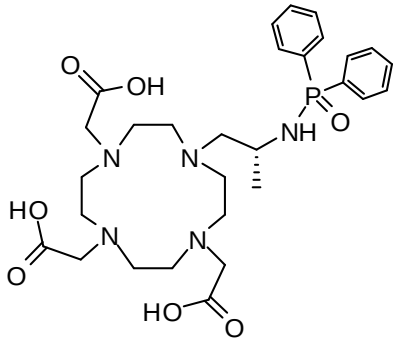

3a(R) (0.026 g, 0.04 mmol). **4a(R)** (0.026 g, 96%) was obtained as a white hygroscopic powder. λ_{max} (H_2O)/nm 268; ν_{max} cm^{-1} 3049 (OH), 1592 (C=O), 1402, 1009 (br, P–O); δ_H (300 MHz; D_2O) 1.2 (3H, d, CH_3), 1.9 – 3.9 (25 H, br, (ring H (16 H), ~OCC*H*$_2$N~ (6 H), dpp ~NC*H*$_2$C~ (2 H), ~C*H*CH_3 (1 H)), 7.5 (6 H, m, phenyl H), 7.8 (4 H, m, phenyl H); δ_P (121 MHz; D_2O) 28.4; *m/z* (ESMS+) 604 $[M+H]^+$.

6.6.3 1-[(S)-2-(Diphenylphosphinylamino)propyl]-4,7,10-tris(carboxymethyl)-1,4,7,10-tetraazacyclododecane, ***4a(S)***

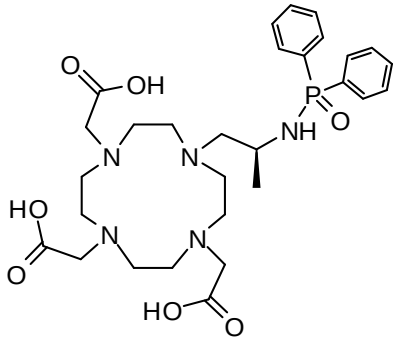

3a(S) (0.045 g, 0.07 mmol). **4a(S)** (0.039 g, 83%) was obtained as a white hygroscopic powder. λ_{max} (H_2O)/nm 269; ν_{max} cm^{-1} 2966 (OH), 1582 (C=O), 1399, 1011 (br, P–O); δ_H (300 MHz; D_2O) 1.2 (3H, d, CH_3), 2.2 – 3.9 (25 H, br, (ring H (16 H), ~OCC*H*$_2$N~

(6 H), dpp ~NCH_2C~ (2 H), ~CHCH$_3$ (1 H)), 7.5 (6 H, m, phenyl H), 7.8 (4 H, m, phenyl H); δ_P (121 MHz; D_2O) 28.3; *m/z* (ESMS+) 604 $[M+H]^+$.

6.6.4 1-[2'-(Diphenylphosphinylamino)-2-(methyl)-propyl]-4,7,10-tris(carboxymethyl)-1,4,7,10-tetraazacyclododecane, ***4b***

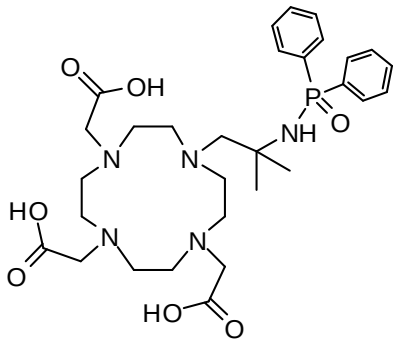

3b (0.102 g, 0.16 mmol). **4b** (0.079 g, 71%) was obtained as a white hygroscopic powder. λ_{max} (H_2O)/nm 270; ν_{max} cm^{-1} 2970, 1738 (C=O), 1586, 1379, 1203 (P=O), 1088; δ_H (300 MHz; D_2O) 1.5 (6 H, s, CH_3), 2.5 – 3.7 (24 H, br, (ring H (16 H), ~OCCH_2N~ (6 H), dpp ~NCH_2C~ (2 H)) 7.5 (6 H, m, phenyl H), 7.7 (4 H, m, phenyl H); δ_C (100 MHz; D_2O) 21.6 (CH_3), 42.8 (~*C*(CH_3)$_2$), 48.8, 49.6, 51.8, 55.7, 56.5 (ring CH_2), 58.8, 61.2 (~OC*C*H_2N~), 66.6 (dpp ~N*C*H_2C~), 128.5 (m, phenyl C), 131.4 (m, phenyl C), 132.9 (s, phenyl C), 137.9 (s, phenyl C), 171.0, 178.1, 180.2 (CO_2); δ_P (121 MHz; D_2O) 26.4; *m/z* (ESMS+) 618 $[M+H]^+$.

6.6.5 1-[2-(Diphenylphosphinylamino)propyl]-4,7,10-tris[(4'-(carboxyl)-1'-carboxybutyl]-1,4,7,10-tetraazacyclododecane, ***9***

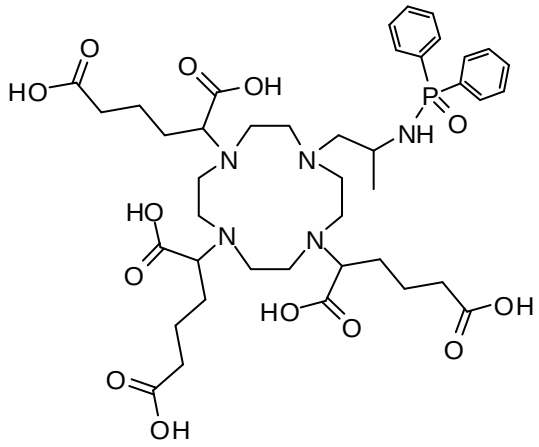

8 (0.032 g, 0.03 mmol). **9** (0.032 g, 99%, 12 possible stereoisomers) was obtained as a white hygroscopic powder. λ_{max} (H_2O)/nm 266; ν_{max} cm^{-1} 3039 (OH), 1403, 1042 (P–O); δ_H (300 MHz; D_2O) 1.2 (3H, br, dpp CH_3), 1.4 – 1.8 (12 H, br, ~CHNCH_2CH_2~ and ~CH_2CH_2CH_2~), 2.1 (6H, br, ~CH_2CH_2CO_2H), 2.5 – 3.9 (22 H, br, ring H (16 H), ~CN*H* (3H), dpp ~NCH_2C~ (2 H), ~CHCH$_3$ (1 H)), 7.5 (6 H, m, phenyl H), 7.8 (4 H, m, phenyl H);

δ_P (121 MHz; D_2O) 23.7; *m/z* (HR-FAB+) $[M+H]^+$ calcd for $C_{41}H_{61}N_5O_{13}P$; 862.3998, found; 862.3994.

6.6.6 *1-[(R)-2-(Diphenylphosphinylamino)propyl]-4,7,10-tris[(4'-(carboxyl)-1'-carboxybutyl]-1,4,7,10-tetraazacyclododecane,* ***9(R)***

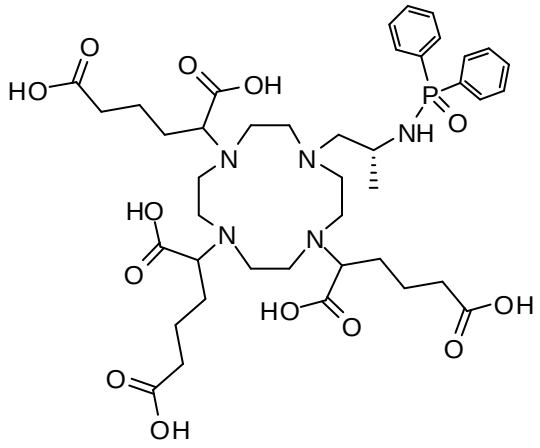

8(R) (0.019 g, 0.02 mmol). **9(R)** (0.019 g, 98%, 6 possible stereoisomers) was obtained as a white hygroscopic powder. λ_{max} (H_2O)/nm 263; ν_{max} cm^{-1} 2971 (OH), 1551, 1398, 993 (P–O); δ_H (300 MHz; D_2O) 1.2 (6H, br, ~$CH_2CH_2CH_2$~), 1.5 (6H, br, ~$CHNCH_2CH_2$~), 2.2 (6H, br, ~$CH_2CH_2CO_2H$), 2.3 – 3.6 (22 H, br, ring H (16 H), ~CN*H* (3H), dpp ~NCH_2C~ (2 H), ~$CHCH_3$ (1 H)), 7.5 (6 H, m, phenyl H), 7.8 (4 H, m, phenyl H); δ_P (121 MHz; D_2O) 23.7; *m/z* (FAB+) 862 $[M+H]^+$.

6.6.7 *1-[(S)-2-(Diphenylphosphinylamino)propyl]-4,7,10-tris[(4'-(carboxyl)-1'-carboxybutyl]-1,4,7,10-tetraazacyclododecane,* ***9(S)***

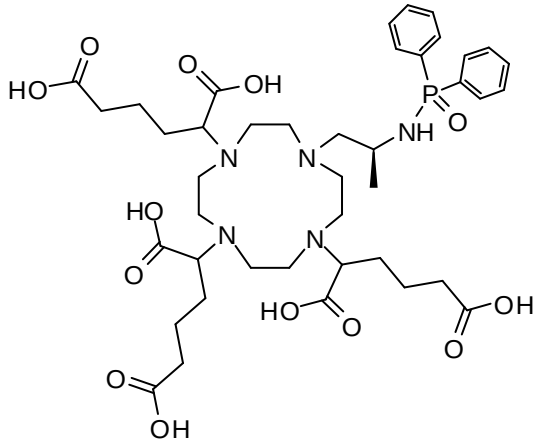

8(S) (0.029 g, 0.03 mmol). **9(S)** (0.027 g, 95%, 6 possible stereoisomers) was obtained as a white hygroscopic powder. λ_{max} (H_2O)/nm 264; ν_{max} cm^{-1} 2971 (OH), 1551, 1398, 994 (P–O); δ_H (300 MHz; D_2O) 1.2 (6H, br, ~$CH_2CH_2CH_2$~), 1.6 (6H, br, ~$CHNCH_2CH_2$~), 2.2 (6H, br, ~$CH_2CH_2CO_2H$), 2.5 – 3.7 (22 H, br, ring H (16 H), ~CN*H* (3H), dpp ~NCH_2C~ (2

H), ~C*H*CH_3 (1 H)), 7.5 (6 H, m, phenyl H), 7.8 (4 H, m, phenyl H); δ_P (121 MHz; D_2O) 23.7; *m/z* (FAB+) 862 $[M+H]^+$.

6.6.8 1,4,7-Tris[(4'-(carboxyl)-1'-carboxybutyl]-1,4,7,10-tetraazacyclododecane, ***10***

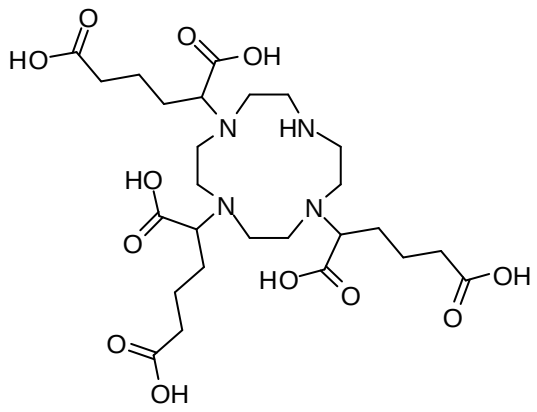

6 (0.209 g, 0.30 mmol). **10** (0.141 g, 68%, 6 possible stereoisomers) was obtained as a white hygroscopic powder. ν_{max} cm^{-1} 3045 (OH), 1554 (C=O), 1402, 1071; δ_H (300 MHz; D_2O) 1.4 – 2.0 (12H, br, aliphatic CH_2), 2.0 (6H, br, aliphatic CH_2), 2.7 – 3.8 (19 H, br, ring H (16 H) and ~CN*H* (3 H)); δ_C (75 MHz; D_2O) 23.6 (~CH_2*C*H_2CH_2~), 24.2 (~CHN*C*H_2CH_2~), 37.1 (~CH_2*C*H_2CO_2H), 45.3, 45.9, 50.4 (ring CH_2), 63.0 (~*C*NH), 182.2 (carbonyl ~CHN*C*O_2H), 182.6 (carbonyl ~CH_2*C*O_2H); *m/z* (ESMS+) 605 $[M+H]^+$.

6.6.9 1,4,7-Tris[(4'-(ethoxycarbonyl)-1'-carboxybutyl]-1,4,7,10-tetraazacyclododecane, ***14***

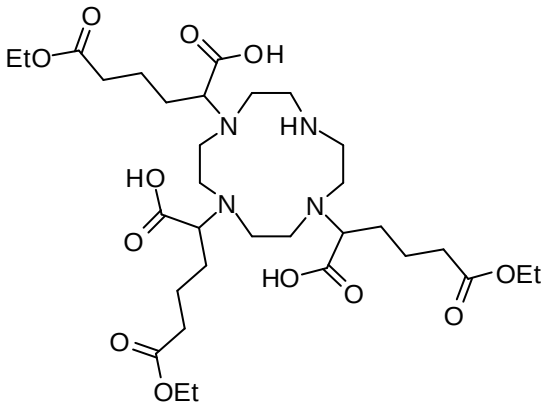

12 (0.451 g, 0.54 mmol). **14** (0.140 g, 38%, 6 possible stereoisomers) was obtained as a white hygroscopic powder. ν_{max} cm^{-1} 2930, 1719 (C=O), 1674, 1375, 1177, 1130; δ_H (300 MHz; CD_3OD) 1.1 (9H, t, $^3J_{HH}$ 7.0 Hz, ~CO_2CH_2C*H*$_3$), 1.5 – 2.0 (12 H, br, ~CHNC*H*$_2CH_2$~ and ~CH_2C*H*$_2CH_2$~), 2.3 – 2.4 (6 H, br, ~CH_2C*H*$_2CO_2H$), 2.9 – 3.7 (16 H, br, ring H), 3.8 (6 H, br q, $^3J_{HH}$ 6.5 Hz ~CO_2C*H*$_2CH_3$); *m/z* (FAB+) 689 $[M+H]^+$.

6.6.10 1,4,7-Tris[(4'-(acetoxymethoxycarbonyl)-1'-carboxybutyl]-1,4,7,10-tetraazacyclododecane, ***18***

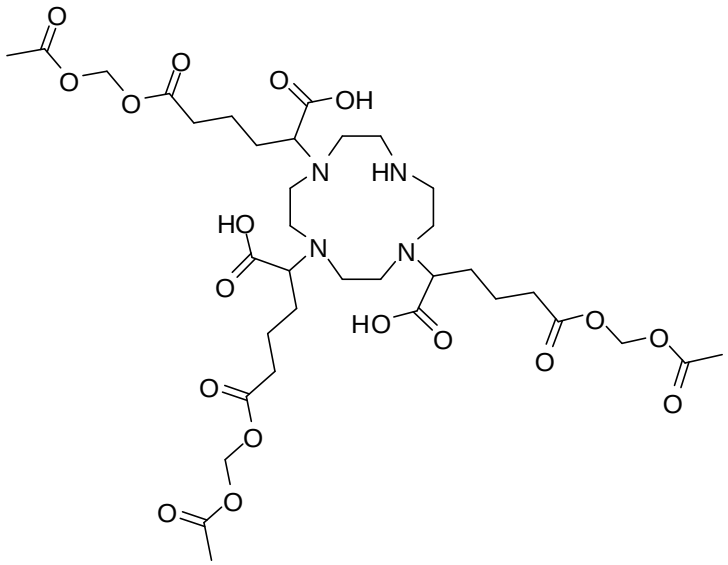

17 (0.075 g, 0.069 mmol). **18** (0.057 g, 99%, 6 possible stereoisomers) was obtained as a white hygroscopic powder. ν_{max} cm^{-1} 2962, 1755 (C=O), 1668, 1181, 1138, 977; δ_H (300 MHz; CD_3OD); 1.6 – 1.9 (12H, br, ~CHNC*H*$_2$CH$_2$~ and ~CH$_2$C*H*$_2$CH$_2$~), 2.0 (9H, s, ~CO$_2$CC*H*$_3$), 2.3 – 2.5 (6H, br, ~CH$_2$C*H*$_2$CO$_2$H), 2.6 – 3.6 (19 H, br, ring H (16 H) and ~CN*H* (3 H)), 5.7 (6H, s, ~OC*H*$_2$O~); *m/z* (ESMS+) 821 $[M+H]^+$.

6.6.11 1,4,7,10-Tetra[(4'-(carboxyl)-1'-carboxybutyl]-1,4,7,10-tetraazacyclododecane, ***19***

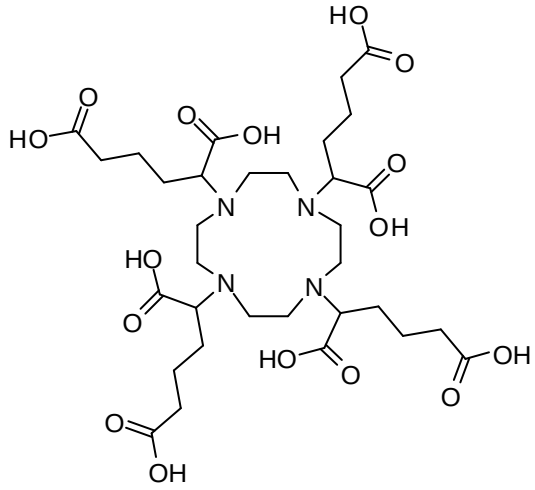

7 (0.361 g, 0.49 mmol). **19** (0.276 g, 68%, 6 possible stereoisomers) was obtained as a white hygroscopic powder. ν_{max} cm^{-1} 2857 (OH), 1535 (C=O), 1394; δ_H (300 MHz; D_2O) 1.4 – 1.8 (18H, br, ~CHNC*H*$_2$CH$_2$~ and ~CH$_2$C*H*$_2$CH$_2$~), 2.0 – 2.1 (8H, br, ~CH$_2$C*H*$_2$CO$_2$H), 2.1 – 3.8 (16H, br, ring H), 3.9 (4H, br, ~CN*H*): δ_C (75 MHz; D_2O) 21.5 (~CH$_2$*C*H$_2$CH$_2$~), 25.6 (~CHNCH$_2$CH$_2$~), 33.7 (~CH$_2$*C*H$_2$CO$_2$H), 37.1 (ring C), 71.9 (~*C*N*H*), 181.4, 183.1, 183.4 (CO_2); *m/z* (ESMS+) 749 $[M+H]^+$.

6.6.12 1,4,7,10-Tetra[(4'-(carboxyl)-1'-carboxybutyl]-1,4,7,10-tetraazacyclododecane, ***20***

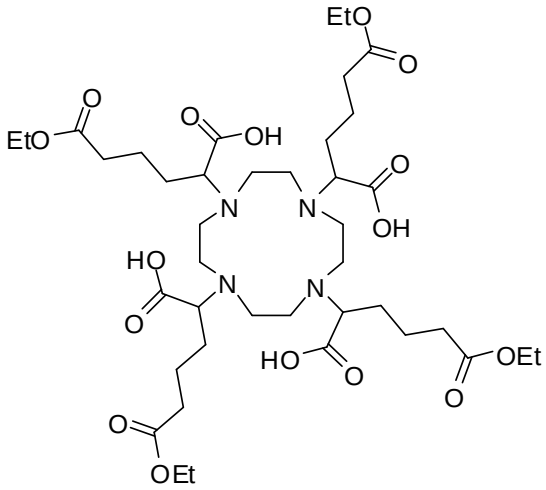

13 (0.107 mg, 0.098 mmol). **20** (0.79 mg, 93%, 6 possible stereoisomers) was obtained as a white hygroscopic powder. δ_H (300 MHz; CD_3OD) 1.2 (12H, br, ~$CO_2CH_2CH_3$), 1.5 – 1.9 (16 H, br, ~CHNCH_2CH_2~ and ~$CH_2CH_2CH_2$~), 1.6 – 3.3 (16H, very broad, ring H), 2.3 (8 H, br, ~$CH_2CH_2CO_2H$) 4.0 (8 H, br, ~$CO_2CH_2CH_3$); δ_C (75 MHz; CD_3OD) 14.5 (~$CO_2CH_2CH_3$), 25.4 (~$CH_2CH_2CH_2$~), 34.2 (~CHNCH_2CH_2~), 34.7 (~$CH_2CH_2CO_2H$), 61.4 (~$CO_2CH_2CH_3$), 49.2 (ring CH_2 (under CD_3OD solvent peak), 61.5 (~CNH), 174.8 (carbonyl ~CHNCO_2H), 175.2 (carbonyl ~$CH_2CO_2CH_2CH_3$); *m/z* (FAB+) 861 $[M+H]^+$.

6.7 Dpp Complex Synthesis

General synthesis; two separate solutions of the appropriate pro-ligand and $LnCl_3.6H_2O$ (slight excess to ensure all ligand used in complexation) in water (5 ml) were prepared and were each adjusted to pH 7 by addition of NaOH. The two solutions were added together and the pH fell to ~ 5, due to release of protons on complexation. The solution was adjusted to pH 6 using NaOH and was heated at 90 ^oC for 2 hours. On cooling the pH was raised to 10 and filtered through a celite plug to remove any precipitated $Ln(OH)_3$. The solution was then lowered to pH 5.5 and lyophilised. The product was extracted from the salt residue with 20% dry MeOH/DCM solution which was then removed under reduced pressure. The residue was taken up in water lyophilised once more to give the Ln(dpp) complex.

6.7.1 Dysprosium(III) 1-[2-(diphenylphosphinylamino)propyl]-4,7,10-tris(carboxymethyl)-1,4,7,10-tetraazacyclododecane, ***Dy.4a***

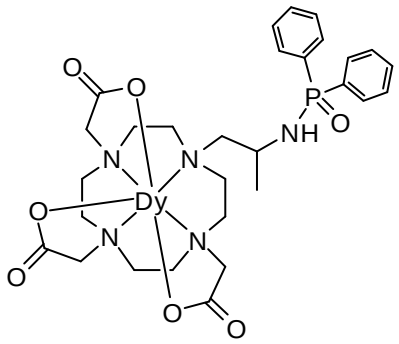

4a (8.3 mg, 13.7 μmol) and $DyCl_3.6H_2O$ (5.2 mg, 13.7 μmol). **Dy.4a** (8.3 mg, 79%) was obtained as a white powder, *m/z* HR-ESMS+ $[M+H]^+$ calcd for $C_{29}H_{40}N_5O_7PDy$; 765.1952, found; 765.1962 (^{164}Dy).

6.7.2 Europium(III) 1-[2-(diphenylphosphinylamino)propyl]-4,7,10-tris(carboxymethyl)-1,4,7,10-tetraazacyclododecane, ***Eu.4a***

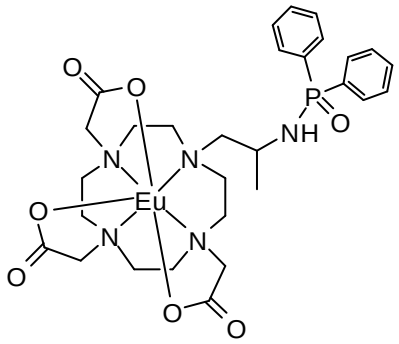

4a (20.8 mg, 35.0 μmol) and $EuCl_3.6H_2O$ (15.4 mg, 42.0 μmol). **Eu.4a** (25.7 mg, 99%) was obtained as a white powder. λ_{max} (H_2O)/nm 273; ν_{max} cm^{-1} 3368, 2984, 1594 (C=O), 1437, 1396, 1083 (P–O); δ_H (400 MHz; D_2O; 4 ^oC) selected resonances: 25.7 (1H, s, ring CH axial), 33.0 (1H, s, ring CH axial), 34.7 (1H, s, ring CH axial), 34.9 (1H, s, ring CH axial), typical of a square-anti prismatic (SAP) geometry about Eu, the remaining resonances span –17.4 to 7.65 ppm; *m/z* (HR-ESMS+) $[M+H]^+$ calcd for $C_{29}H_{40}N_5O_7PEu$; 754.1872, found; 754.1876 (^{153}Eu).

6.7.3 *Europium(III) 1-[(R)-2-(diphenylphosphinylamino)propyl -4,7,10-tris(carboxymethyl)-1,4,7,10-tetraazacyclododecane,* ***Eu.4a(R)***

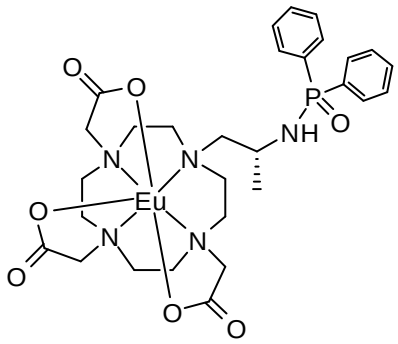

4a(R) (12.7 mg, 21.0 μmol) and $EuCl_3.6H_2O$ (7.7 mg, 21.0 μmol). **Eu.4a(R)** (5.9 mg, 37%.) was obtained as a white powder. λ_{max} (H_2O)/nm 273; ν_{max} cm^{-1} 3350, 1579 (C=O), 1438, 1405, 1083 (P–O); δ_H (400 MHz; D_2O; 4 ^oC) selected resonances: 21.5 (1H, s, ring CH axial), 31.6 (1H, s, ring CH axial), 32.8(1H, s, ring CH axial), 33.6 (1H, s, ring CH axial), typical of a square-anti prismatic geometry (SAP) about Eu, the remaining resonances span –25.2 to 17.1 ppm; *m/z* (ESMS+) 754 $[M+H]^+$ (^{153}Eu).

6.7.4 *Europium(III) 1-[(S)-2-(diphenylphosphinylamino)propyl -4,7,10-tris(carboxymethyl)-1,4,7,10-tetraazacyclododecane,* ***Eu.4a(S)***

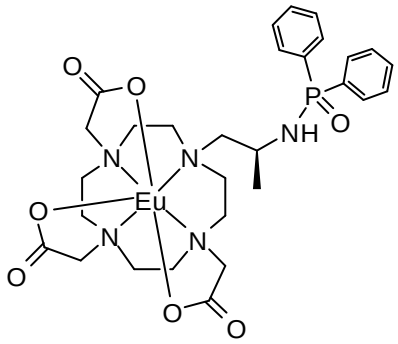

4a(S) (10.3 mg, 17.0 μmol) and $EuCl_3.6H_2O$ (6.25 mg, 17.1 μmol). **Eu.4a(S)** (5.1 mg, 40%) was obtained as a white powder. λ_{max} (H_2O)/nm 273; ν_{max} cm^{-1} 3160, 1582 (C=O), 1438, 1404, 1084 (P–O); δ_H (400 MHz; D_2O; 4 ^oC) 21.9 (1H, s, ring CH axial), 25.9 (1H, s, ring CH axial), 31.2 (1H, s, ring CH axial), 41.8 (1H, s, ring CH axial), typical of a square-anti prismatic geometry (SAP) about Eu, the remaining resonances span –25.2 to 15.1 ppm; *m/z* (ESMS+) 754 $[M+H]^+$ (^{153}Eu).

6.7.5 Gadolinium(III) 1-[2-(diphenylphosphinylamino)propyl]-4,7,10-tris(carboxymethyl)-1,4,7,10-tetraazacyclododecane, ***Gd.4a***

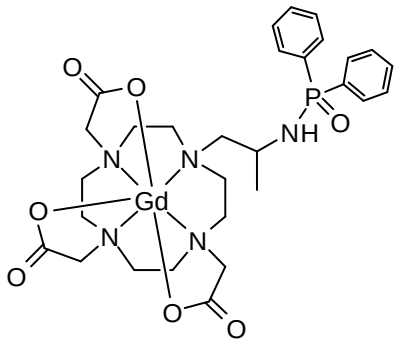

4a (12.0 mg, 20.0 μmol) and $GdCl_3.6H_2O$ (10.7 mg, 29.0 μmol). **Gd.4a** (15.0 mg, 99%.) was obtained as a white powder. λ_{max} (H_2O)/nm 270; ν_{max} cm^{-1} 2819, 1587 (C=O), 1426, 1330, 1109 (P–O); *m/z* (HR-ESMS+) $[M+H]^+$ calcd for $C_{29}H_{40}N_5O_7PGd$; 756.1886, found; 756.1885 (^{155}Gd).

6.7.6 Gadolinium(III) 1-[(R)-2-(diphenylphosphinylamino)propyl -4,7,10-tris(carboxymethyl)-1,4,7,10-tetraazacyclododecane, ***Gd.4a(R)***

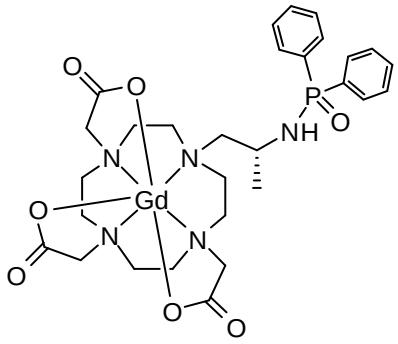

4a(R) (11.4 mg, 19.0 μmol) and $GdCl_3.6H_2O$ (7.01 mg, 19.0 μmol). **Gd.4a(R)** (2.5 mg, 17%) was obtained as a white powder. λ_{max} (H2O)/nm 275; ν_{max} cm^{-1} 3139, 3050, 1587 (C=O), 1438, 1402, 1320, 1085 (P–O); *m/z* (ESMS+) 759 $[M+H]^+$ (^{158}Gd).

6.7.7 Gadolinium(III) 1-[(S)-2-(diphenylphosphinylamino)propyl -4,7,10-tris(carboxymethyl)-1,4,7,10-tetraazacyclododecane, ***Gd.4a(S)***

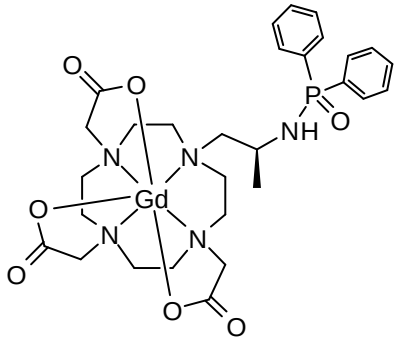

4a(S) (9.4 mg, 15.6 μmol) and $GdCl_3.6H_2O$ (5.7 mg, 15.6 μmol). **Gd.4a(S)** (4.7 mg, 39%) was obtained as a white powder. λ_{max} (H2O)/nm 274; ν_{max} cm^{-1} 3137, 3050, 1592 (C=O), 1402, 1319, 1084 (P–O); *m/z* (ESMS+) 759 $[M+H]^+$ (^{158}Gd).

*6.7.8 Samarium(III) 1-[2-(diphenylphosphinylamino)propyl]-4,7,10-tris(carboxymethyl)-1,4,7,10-tetraazacyclododecane, **Sm.4a***

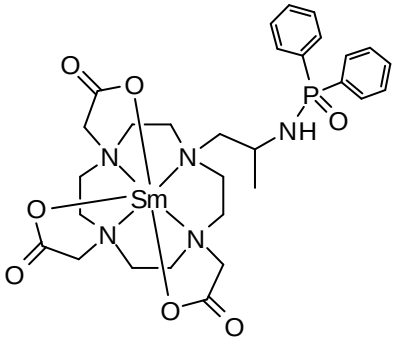

4a (8.3 mg, 13.7 μmol) and $SmCl_3.6H_2O$ (4.99 mg, 13.7 μmol). **Sm.4a** (8.7 mg, 84%) was obtained as a white powder; *m/z* (HR-ESMS+) $[M+H]^+$ calcd for $C_{29}H_{40}N_5O_7PSm$, 753.1857, found, 753.1852 (^{152}Sm).

*6.7.9 Terbium(III) 1-[2-(diphenylphosphinylamino)propyl]-4,7,10-tris(carboxymethyl)-1,4,7,10-tetraazacyclododecane, **Tb.4a***

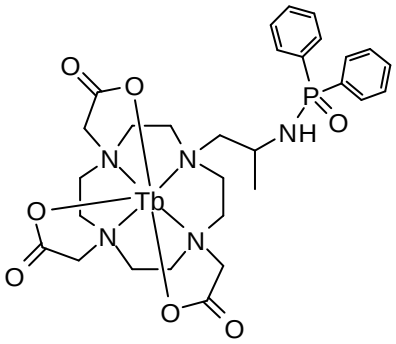

4a (20.5 mg, 34.0 μmol) and $TbCl_3.6H_2O$ (16.3 mg, 44.0 μmol). **Tb.4a** (15.0 mg, 58%.) was obtained as a white powder. λ_{max} (H_2O)/nm 275; ν_{max} cm^{-1} 3386. (NH), 2970, 1738 (C=O), 1630, 1414, 1100 (P–O); *m/z* (HR-ESMS+) $[M+H]^+$ calcd for $C_{29}H_{40}N_5O_7PTb$; 760.1913, found; 760.1914.

6.7.10 Europium(III) 1-[2'-(diphenylphosphinylamino)-2-(methyl)-propyl]-4,7,10-tris(carboxymethyl)-1,4,7,10-tetraazacyclododecane, ***Eu.4b***

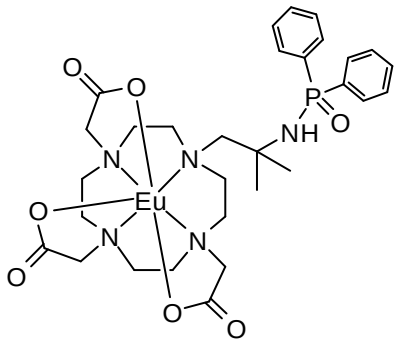

4b (14.4 mg, 23.0 μmol) and $EuCl_3.6H_2O$ (11.2 mg, 31.0 μmol). **Eu.4b** (8.1 mg, 46%) was obtained as a white powder; λ_{max} (H_2O)/nm 270; ν_{max} cm^{-1} 3369, 2868, 1590 (C=O), 1389, 1085 (P–O); δ_H (400 MHz; D_2O) 24.8 (1H, s, ring CH axial), 26.2 (1H, s, ring CH axial), 33.6 (1H, s, ring CH axial), 35.6 (1H, s, ring CH axial), typical of a square-anti prismatic geometry (SAP) about Eu, the remaining resonances span –20.4 to 9.1 ppm; *m/z* (HR-ESMS+) $[M+H]^+$ calcd for $C_{30}H_{42}N_5O_7PEu$; 768.2029, found; 768.2026 (^{153}Eu).

6.7.11 Gadolinium(III) 1-[2'-(diphenylphosphinylamino)-2-(methyl)-propyl]-4,7,10-tris(carboxymethyl)-1,4,7,10-tetraazacyclododecane, ***Gd.4b***

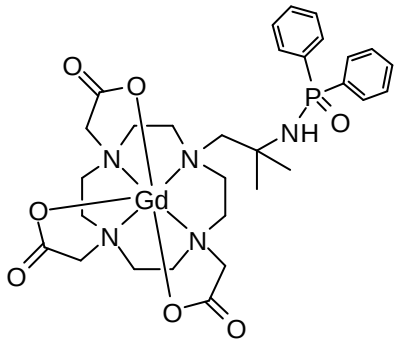

4b (21.7 mg, 35.0 μmol) and $GdCl_3.6H_2O$ (19.5 mg, 52.5 μmol). **Gd.4b** (17.3 mg, 64%) was obtained as a white powder. λ_{max} (H_2O)/nm 277; ν_{max} cm^{-1} 2628, 1575 (C=O), 1436, 1402, 1187, 1128, 1054 (P–O); *m/z* HR-ESMS+ $[M+H]^+$ calcd for $C_{30}H_{42}N_5O_7PGd$; 773.2057, found; 773.2060 (^{158}Gd).

6.7.12 Europium(III) 1-[2-(diphenylphosphinylamino)propyl]-4,7,10-tris[(4'-(carboxyl)-1'-carboxybutyl]-1,4,7,10-tetraazacyclododecane, ***[Eu.9]$^{3-}$***

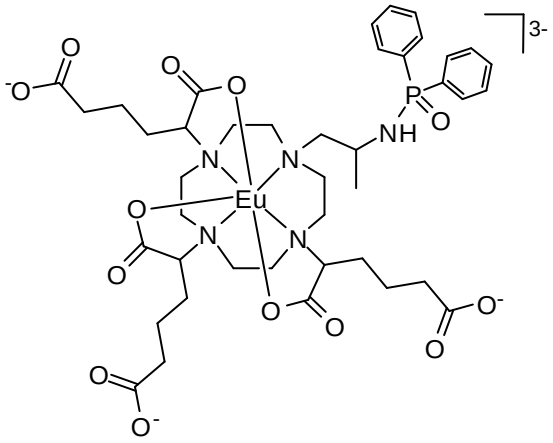

9 (16.1 mg,18.7 μmol) and $EuCl_3.6H_2O$ (7.0 mg, 19.0 μmol). **[Eu.9]$^{3-}$** (13.9 mg, 73%) was obtained as a white powder. λ_{max} (H_2O)/nm 273; ν_{max} cm^{-1} 3042, 1594 (C=O), 1400, 1085 (P–O); δ_H (400 MHz; D_2O; 4 ^oC) resonances span –19.4 to 7.4 ppm; *m/z* (MALDI) 1011 showing Eu splitting pattern $[M+H]^+$ (^{151}Eu).

6.7.13 Gadolinium(III) 1-[2-(diphenylphosphinylamino)propyl]-4,7,10-tris[(4'-(carboxyl)-1'-carboxybutyl]-1,4,7,10-tetraazacyclododecane, ***[Gd.9]$^{3-}$***

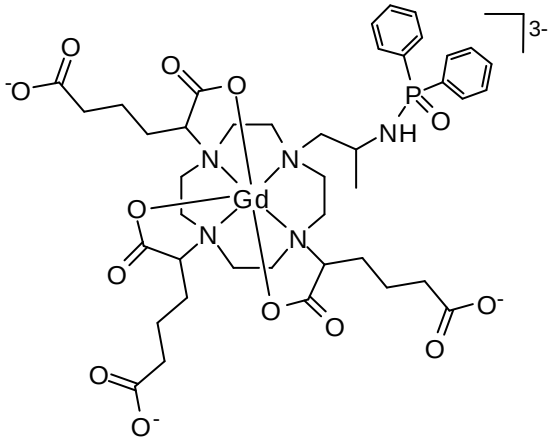

9 (16.1 mg, 18.7 μmol) and $GdC_3.6H_2O$ (7 mg, 19.0 μmol). **[Gd.9]$^{3-}$** (12.2 mg, 64%) was obtained as a white powder. λ_{max} (H_2O)/nm 266; ν_{max} cm^{-1} 3046, 1595, 1528 (C=O), 1402, 1350, 1084 (P–O); *m/z* (MALDI) 1018 showing Gd splitting pattern $[M+H]^+$ (^{158}Gd).

6.7.14 Gadolinium(III) 1-[(R)-2-(diphenylphosphinylamino)propyl]-4,7,10-tris[(4'-(carboxyl)-1'-carboxybutyl]-1,4,7,10-tetraazacyclododecane, ***Gd.9(R)]$^{3-}$***

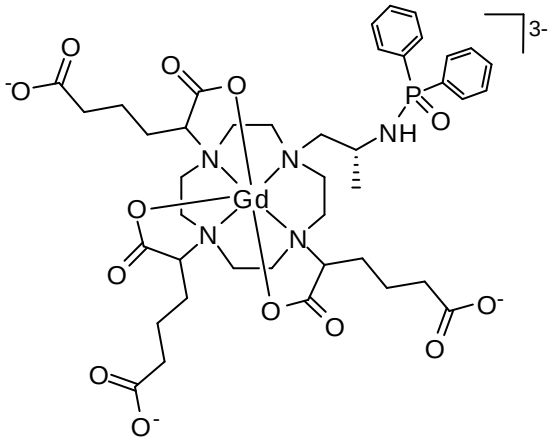

9(R) (18.6 mg, 21.5 μmol) and $GdCl_3.6H_2O$ (8.0 mg, 22.0 μmol). **[Gd.9(R)]$^{3-}$** (16.4 mg, 75%) was obtained as a white powder. λ_{max} (H_2O)/nm 265; ν_{max} cm^{-1} 3021, 1595 (C=O), 1399, 1126 (P–O); *m/z* (MALDI) 1040 showing Gd splitting pattern $[M+Na]^+$ (^{158}Gd).

6.7.15 Gadolinium(III) 1-[(S)-2-(diphenylphosphinylamino)propyl]-4,7,10-tris[(4'-(carboxyl)-1'-carboxybutyl]-1,4,7,10-tetraazacyclododecane, ***[Gd.9(S)]$^{3-}$***

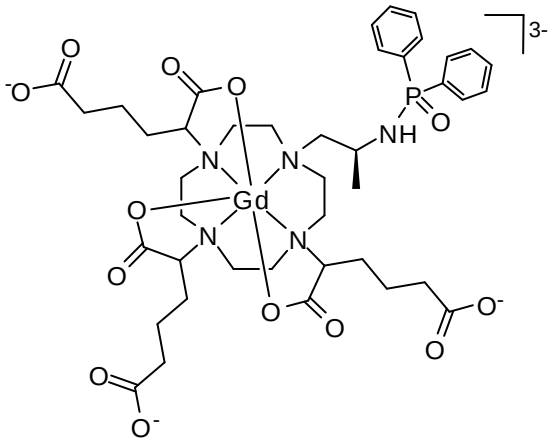

9(S) (27.0 mg, 31.4 μmol) and $GdCl_3.6H_2O$ (11.5 mg, 30.9 μmol). **Gd.9(S)]$^{3-}$** (24.9 mg, 78%) was obtained as a white powder. λ_{max} (H_2O)/nm 265; ν_{max} cm^{-1} 3039, 1591 (C=O), 1401, 1074 (P–O); *m/z* (MALDI) 1040 showing Gd splitting pattern $[M+Na]^+$ (^{158}Gd).

6.8 Esterase Activated Complex Synthesis

General synthesis: the appropriate pro-ligand was dissolved in water (10 ml) and $LnCl_3.6H_2O$ was added in slight excess to ensure all ligand used in complexation. The solution was adjusted to pH 5.5 using NaOH and was heated at 90^{o}C for 24 hours. After the solution was cooled the pH was raised to 10 and the solution was filtered through a celite plug to remove any $Ln(OH)_3$. The solution was then lowered to pH 5.5 and added to a suspension of Dowex MAC-3 weak acid-cation exchange resin and stirred for 10 minutes to remove any

unreacted Eu(III). This was monitored by addition of 200 μl aliquots of reaction solution to 800 μl of 0.1 mM xylenol orange solution (pH 5); if the solution remained orange in colour there was no free ion present; if turned pink free ion was still in solution. The solution was then decanted from the resin and lyophilised to give the Ln(III) complex.

For the preparation of **Ln.18** the reaction was carried out in MeOH and heated at 55°C. On removal of the solvent the residue was dissolved in water at pH 5.5. The solution was then loaded onto Dowex MAC-3 weak acid-cation exchange resin and the procedure continued as above.

6.8.1 Europium(III) 1,4,7-tris[(4'-(carboxyl)-1'-carboxybutyl]-1,4,7,10-tetraazacyclododecane, ***[Eu.10]$^{3-}$***

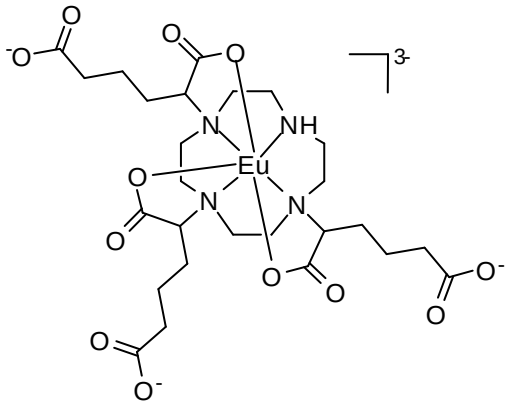

10 (52.3 mg, 86.0 μmol) and $EuCl_3.6H_2O$ (33.5 mg, 91.0 μmol). **[Eu.10]$^{3-}$** (32.6 mg, 50%) was obtained as a white powder. ν_{max} cm^{-1} 3040 (OH), 1560 (C=O), 1401; δ_H (300 MHz; D_2O) –30.0 to 30.0 ppm (broad peaks show complex ligand binding to Eu(III)); *m/z* (ESMS+) 755 showing Eu splitting pattern $[M+H]^+$, (ESMS–) 753 showing Eu splitting pattern $[M]^-$ (^{153}Eu).

6.8.2 Gadolinium(III) 1,4,7-tris[(4'-(carboxyl)-1'-carboxybutyl]-1,4,7,10-tetraazacyclododecane, ***[Gd.10]$^{3-}$***

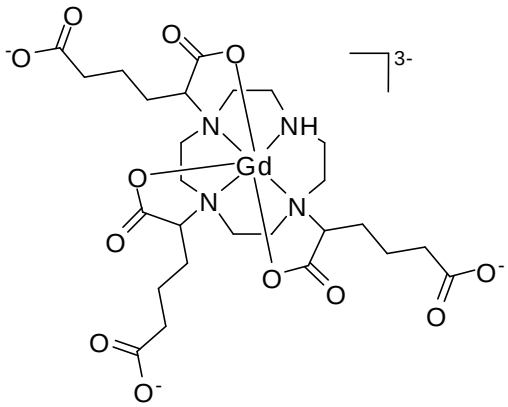

10 (52.25 mg, 86.0 μmol) and $GdCl_3.6H_2O$ (34.13 mg, 91.0 (^{153}Eu)). **[Gd.10]$^{3-}$** (29.1 mg, 44%) was obtained as a white powder. ν_{max} cm^{-1} 3042 (OH), 1559 (C=O), 1401; *m/z* (FAB+) 779 showing Gd splitting pattern $[M+Na]^+$ (^{158}Gd).

6.8.3 *Europium(III) 1,4,7-tris[(4'-(ethoxycarbonyl)-1'-carboxybutyl]-1,4,7,10-tetraazacyclododecane,* ***Eu.14***

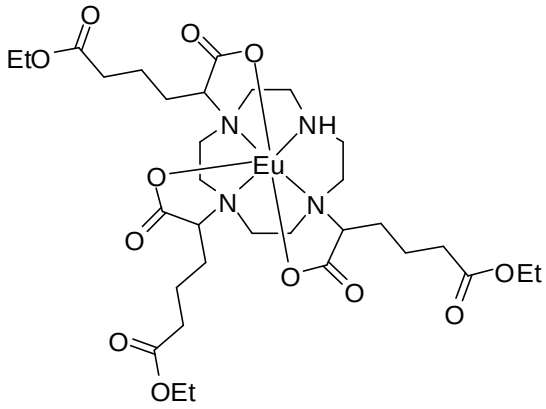

14 (49.9 mg, 72.4 μmol) and $EuCl_3.6H_2O$ (26.5 mg, 72.4 μmol). Around 5% MeOH was added to aid dissolving the ligand. **Eu.14 (**59.2 mg, 97%) was obtained as a white powder. ν_{max} cm^{-1} 3244, 1675, 1591, (C=O), 1423, 1198, 1137; δ_H (400 MHz; D_2O) –14.5 to 7.9 (broad peaks show complex ligand binding to Eu(III); *m/z* (HR-ESMS+) $[M+H]^+$ calcd for $C_{32}H_{54}N_4O_{12}Eu$; 837.2931, found; 837.2931 (^{151}Eu).

6.8.4 *Gadolinium(III) 1,4,7-tris[(4'-(ethoxycarbonyl)-1'-carboxybutyl]-1,4,7,10-tetraazacyclododecane,* ***Gd.14***

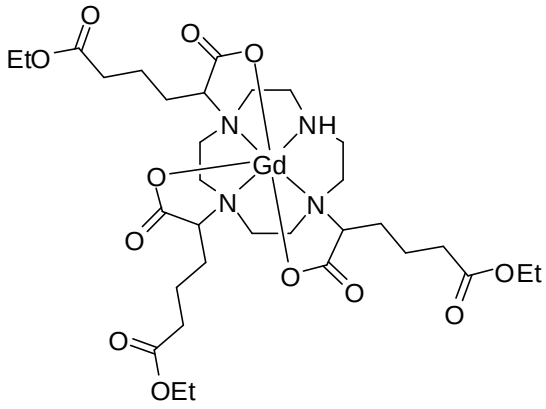

14 (68.5 mg, 99.4 μmol) and $GdCl_3.6H_2O$ (37.4 mg, 10.1 μmol). Around 5% MeOH was added to aid dissolving the ligand. **Gd.14** (65.4 mg, 78%) was obtained as a white powder. ν_{max} cm^{-1} 3328, 1674, 1579, (C=O), 1425, 1197, 1139; *m/z* (HR-ESMS+) $[M+H]^+$ calcd for $C_{32}H_{54}N_4O_{12}Gd$; 844.2974, found; 844.2968 (^{158}Gd).

6.8.5 Yttrium(III) 1,4,7-tris[(4'-(ethoxycarbonyl)-1'-carboxybutyl]-1,4,7,10-tetraazacyclododecane, ***Y.14***

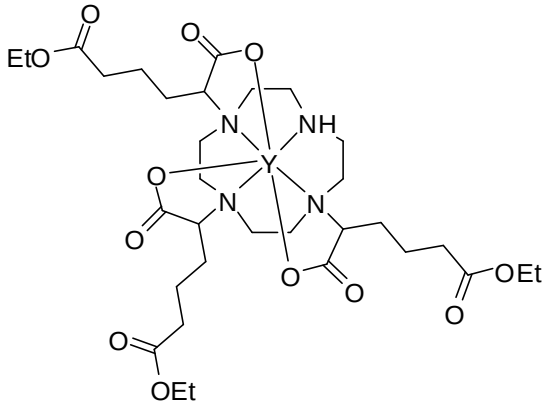

14 (43.6, 63.0 μmol) and $YCl_3.6H_2O$ (19.2 mg, 63.0 μmol). Around 5% MeOH was added to aid dissolving the ligand. **Y.14** (45.2 mg, 93%) was obtained as a white powder. ν_{max} cm^{-1} 1681, (C=O), 1624, 1378, 1204, 1175, 1127; δ_H (300 MHz; D_2O) 1.1 (9 H, t, $^3J_{HH}$ 7.2 Hz, ~$CO_2CH_2CH_3$), 1.3 – 1.8 (12 H, br, ~$CHNCH_2CH_2$~ and ~$CH_2CH_2CH_2$~), 2.3 (6H, br, ~$CH_2CH_2CO_2$~), 2.4 – 3.5 (19H, br, ring CH_2 (16 H) and ~CNH (3 H)), 4.0 (6 H, br q, $^3J_{HH}$ 7.1 Hz, ~$CO_2CH_2CH_3$); *m/z* (HR-ESMS+) $[M+H]^+$ calcd for $C_{32}H_{54}N_4O_{12}Y$; 775.2791, found; 775.2792.

6.8.6 Europium(III) 1,4,7-tris[(4'-(acetoxymethoxycarbonyl)-1'-carboxybutyl]-1,4,7,10-tetraazacyclododecane, ***Eu.18***

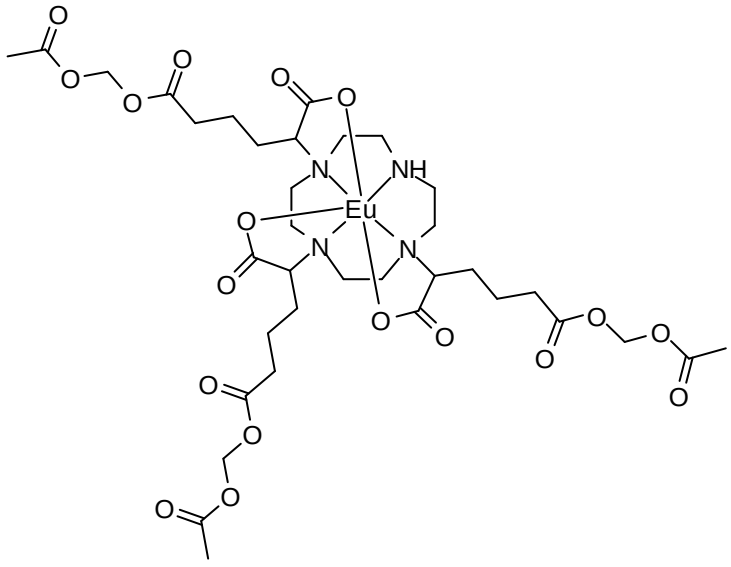

18 (39.1 mg, 47.6 μmol) and $EuCl_3.6H_2O$ (17.5 mg, 47.6 μmol). **Eu.18** (41.8 mg, 90%) was obtained as a white powder. ν_{max} cm^{-1} 2969, 1726, (C=O), 1619, 1419, 1368, 1202, 1142, 981; δ_H (400 MHz; D_2O) 1.2 to 5.7 (broad peaks show complex ligand binding to Eu(III); *m/z* (HR-ESMS+) $[M+H]^+$ calcd for $C_{35}H_{54}N_4O_{18}Eu$; 971.2640, found; 971.2630 (^{153}Eu).

6.8.7 Gadolinium(III) 1,4,7-tris[(4'-(acetoxymethoxycarbonyl)-1'-carboxybutyl]-1,4,7,10-tetraazacyclododecane, ***Gd.18***

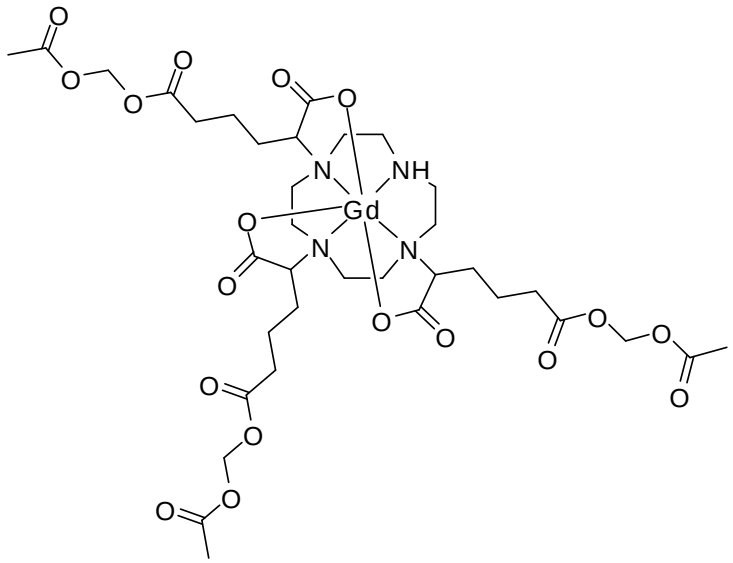

18 (28.2 mg, 34.4 μmol) and $GdCl_3.6H_2O$ (12.8 mg, 34.4 μmol). **Gd.18** (21.6 mg, 65%) was obtained as a white powder. ν_{max} cm^{-1} 2953, 1734 (C=O), 1619, 1416, 1368, 1202, 1144, 982; *m/z* (HR-ESMS+) 976 $[M+H]^+$ with Gd splitting pattern (^{157}Gd).

6.8.8 Yttrium(III) 1,4,7-tris[(4'-(acetoxymethoxycarbonyl)-1'-carboxybutyl]-1,4,7,10-tetraazacyclododecane, ***Y.18***

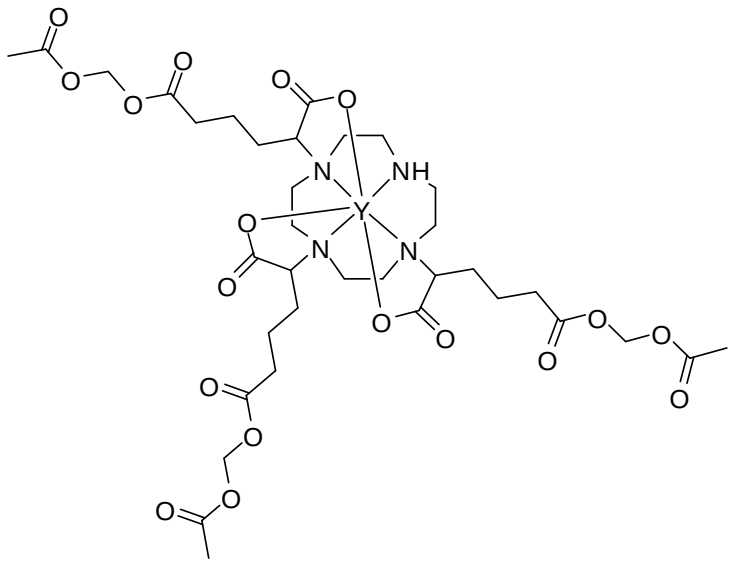

18 (28.2 mg, 34.4 μmol) and $YCl_3.6H_2O$ (10.4 mg, 34.4 μmol). **Y.18** (28.2 mg, 90%) was obtained as a white powder. ν_{max} cm^{-1} 2978, 1738 (C=O), 1415, 1370, 1198, 1139; δ_H (300 MHz; D_2O) 1.4 – 1.8 (12H, br, ~CHNCH_2CH_2~ and ~CH_2CH_2CH_2~), 1.9 (9H, s, ~CO_2CCH_3), 2.2 (6H, br, ~CH_2CH_2CO_2~), 2.4 – 3.4 (16 H, br, ring H) 3.6 (3H, s, ~CN*H*), 5.7 (6H, s, ~OCH_2O~); *m/z* (HR-ESMS+) $[M+H]^+$ calcd for $C_{35}H_{54}N_4O_{18}Y$; 907.2486, found; 907.2476.

*6.8.9 Europium(III) 1,4,7,10-tetra[(4'-(carboxyl)-1'-carboxybutyl]-1,4,7,10-tetraazacyclododecane, **[Eu.19]**$^{5-}$*

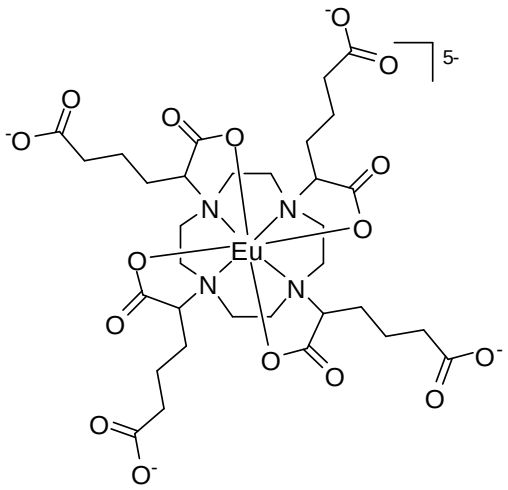

19 (11.4 mg, 15.2 μmol) and $EuCl_3.6H_2O$ (5.6 mg, 15.2 μmol). **[Eu.19]**$^{5-}$ **(**11.8 mg, 86%) was obtained as a white powder. ν_{max} cm^{-1} 3385, 1684, 1633, 1581 (C=O), 1419, 1206, 1145; δ_H (400 MHz; D_2O) selected resonances: δ = 19.1 (1H, s, ring CH axial), 20.5 (1H, s, ring CH axial), 22.8 (1H, s, ring CH axial)and 25.9 (1H, s, ring CH axial), typical of a twisted square-anti prismatic (TSAP) geometry about Eu and 37.1 (1H, s, ring CH axial), 38.5 (1H, s, ring CH axial), 42.5 (1H, s, ring CH axial), 42.9 (1H, s, ring CH axial), 44.4 (1H, s, ring CH axial), 49.3 (1H, s, ring CH axial), 47.7 (1H, s, ring CH axial) and 48.7 (1H, s, ring CH axial), typical of a square-anti prismatic (SAP) geometry about Eu. Integrations show 4:1 in favour of the SAP geometry. The remaining resonances span –27.9 to 8.6 ppm and 37.1 to 48.7 ppm; *m/z* (ESMS+) 897 showing Eu splitting pattern $[M+H]^+$ (^{153}Eu).

*6.8.10 Europium(III) 1,4,7,10-tetra[(4'-(ethoxycarbonyl)-1'-carboxybutyl]-1,4,7,10-tetraazacyclododecane, **[Eu.20]**$^{-}$*

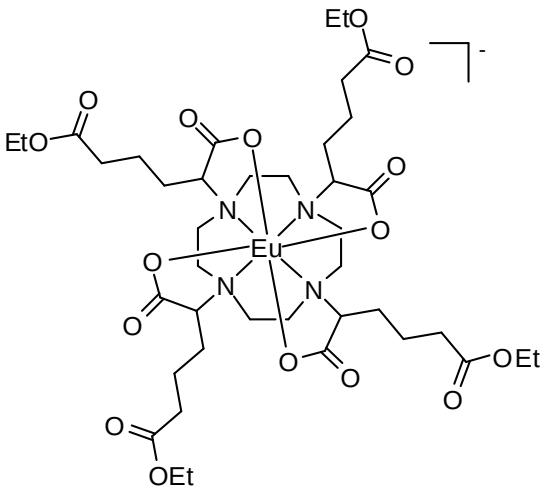

20 (39.5 mg, 45.8 μmol) and $EuCl_3.6H_2O$ (16.8 mg, 46.0 μmol). Around 5% MeOH was added to aid dissolving the ligand. **[Eu.20]**$^{-}$ **(**7.1 mg, 15%) was obtained as a white

powder. ν_{max} cm^{-1} 3407, 1682, 1617 (C=O), 1417, 1206, 1180, 1131; δ_H (400 MHz; D_2O) 19.4 (2H, s, ring CH axial), 26.2 (2H, s, ring CH axial), typical of a twisted square-anti prismatic (TSAP) geometry about Eu, and 38.4 (2H, s, ring CH axial) 48.8 (2H, s, ring CH axial), typical of a square-anti prismatic (SAP) geometry about Eu. Integrations show 5:1 in favour of SAP geometry. The remaining resonances span –27.9 to 9.4 and 38.4 and 48.8; *m/z* (FAB+) 1010 showing Eu splitting pattern $[M+H]^+$ (^{153}Eu).

Chapter 7

Appendix

7.1 Luminescent Decay Curves and Spectra

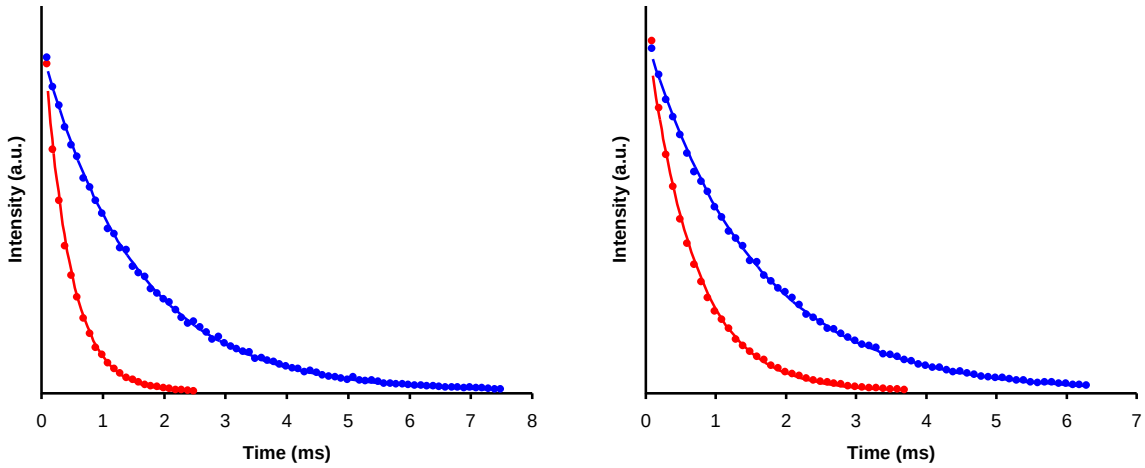

A1. **Eu.4a** excited state lifetime determination in H_2O (red) and D_2O (blue). Exp data (dots); calcd data (line). Left pH 5.45, right pH 10.45. 1.0 mM **Eu.4a**, 0.1 M NaCl, 25°C.

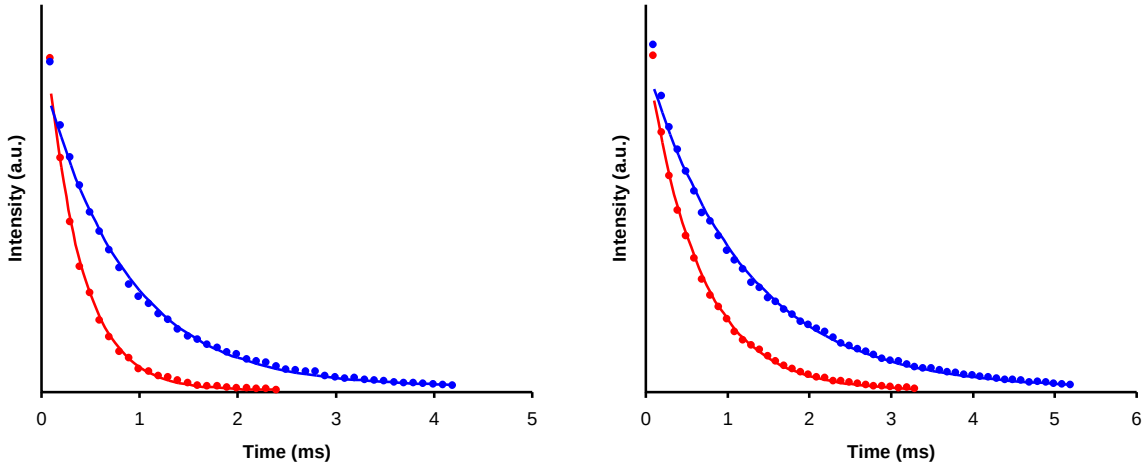

A2. **Eu.4b** excited state lifetime determination in H_2O (red) and D_2O (blue). Exp data (dots); calcd data (line). Left pH 5.45, right pH 10.45. 1.0 mM **Eu.4b**, 0.1 M NaCl, 25°C.

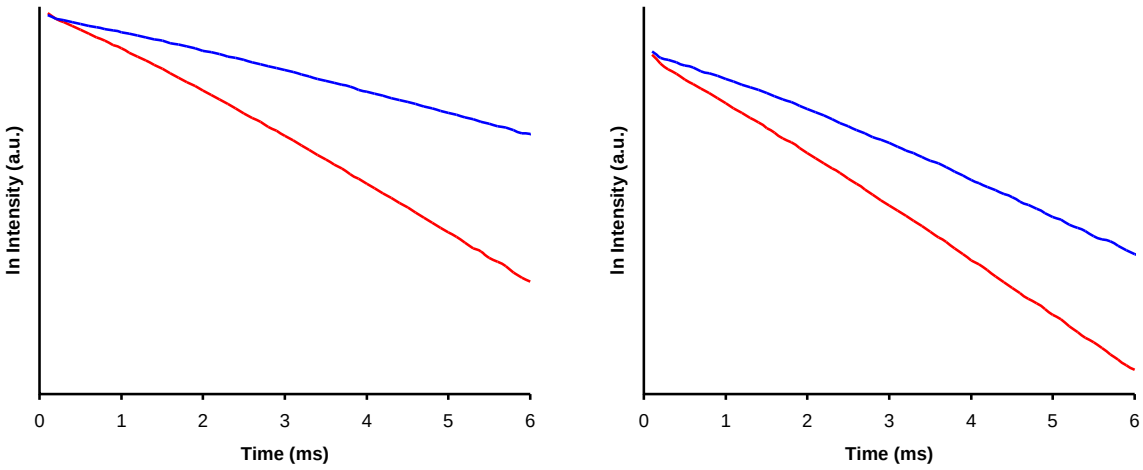

A3. **Tb.4a** excited state lifetime determination in H_2O (red) and D_2O (blue). Exp data (dots); calcd data (line). Left pH 5.0, right pH 10.0. 1.0 mM **Tb.4a**, 0.1 M NaCl, 25°C.

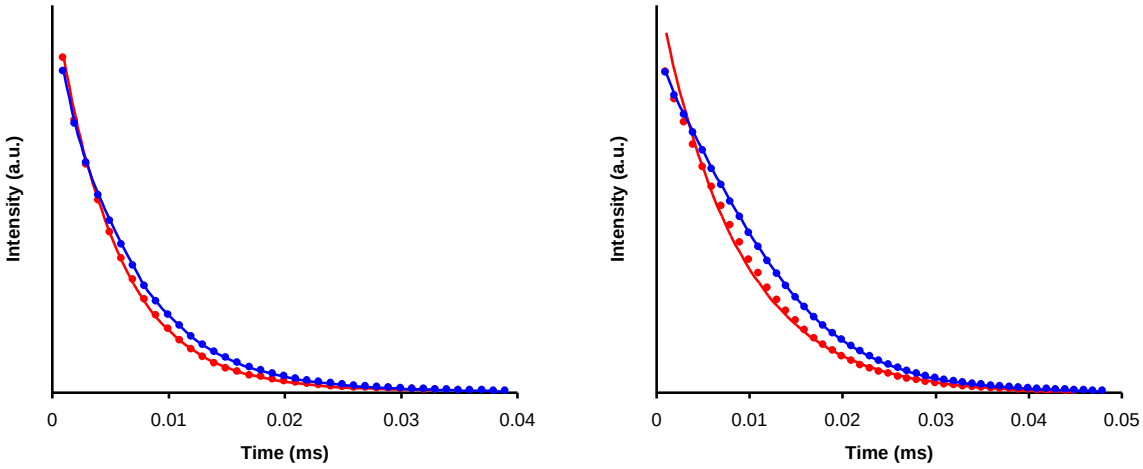

A4. **Dy.4a** (left) and **Sm.4a** (right) excited state lifetime determination in H_2O. Exp data (dots); calcd data (line) at pH 5.0 (red) and pH 10.0 (blue). 1.0 mM **Ln.4a**, 0.1 M NaCl, 25°C.

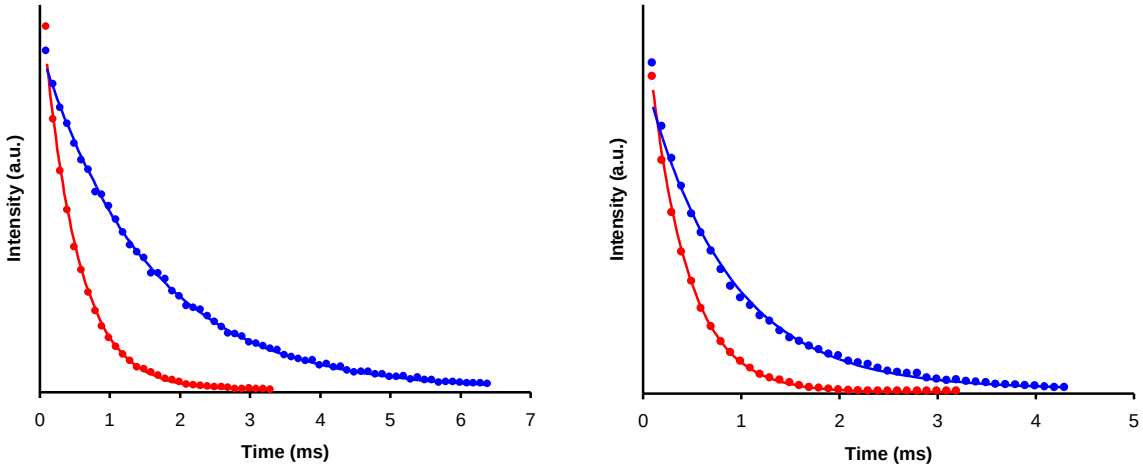

A5. **Eu.4a** (left) and **Eu.4b** (right) excited state lifetime determination in H_2O (red) and D_2O (blue) at pH 7.4. Exp data (dots); calcd data (line). 1.0 mM **Eu.4a**, 0.1 M NaCl, 25°C.

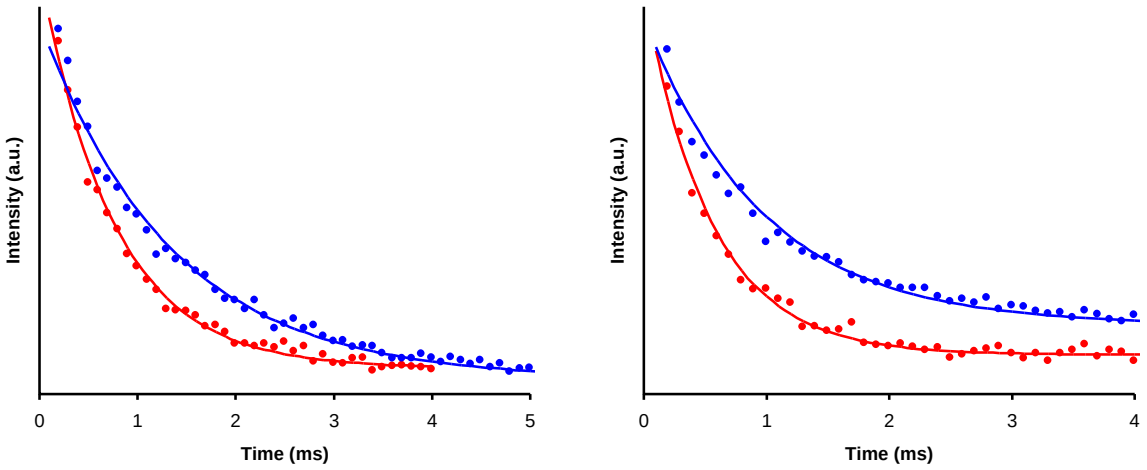

A6. **Eu.4a** (left) and **Eu.4b** (right) excited state lifetime determination in H_2O (red) and D_2O (blue). Exp data (dots); calcd data (line) in the presence of HSA (0.7 mM). 0.1 mM Eu, 0.1 M NaCl, λ_{ex} = 270 nm, pH 7.4 (0.2 M PBS), 25°C.

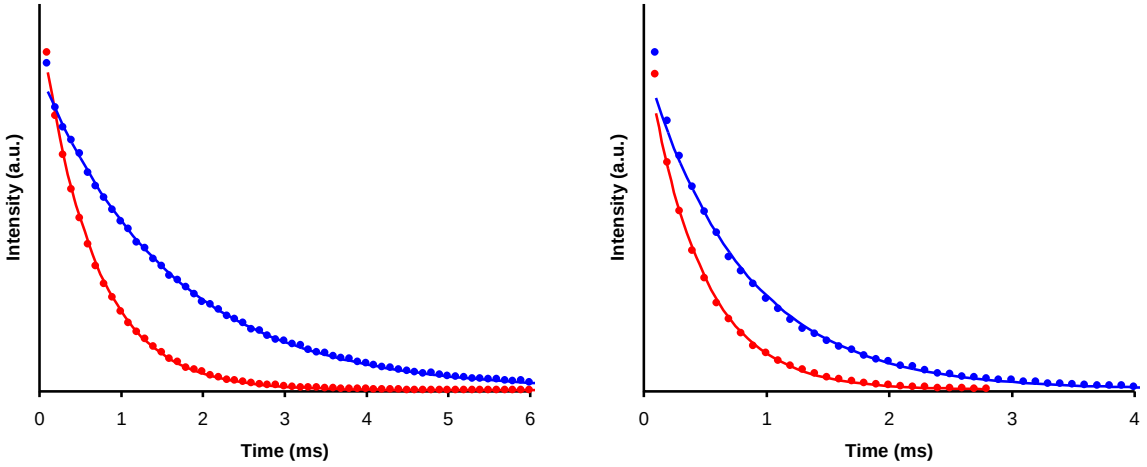

A7. **Eu.4a** (left) and **Eu.4b** (right) excited state lifetime determination in H_2O (red) and D_2O (blue). Exp data (dots); calcd data (line) in the presence of carbonate. 0.1 mM Eu, 0.1 M NaCl, 30 mM $NaHCO_3$, pH 7.4, 25°C.

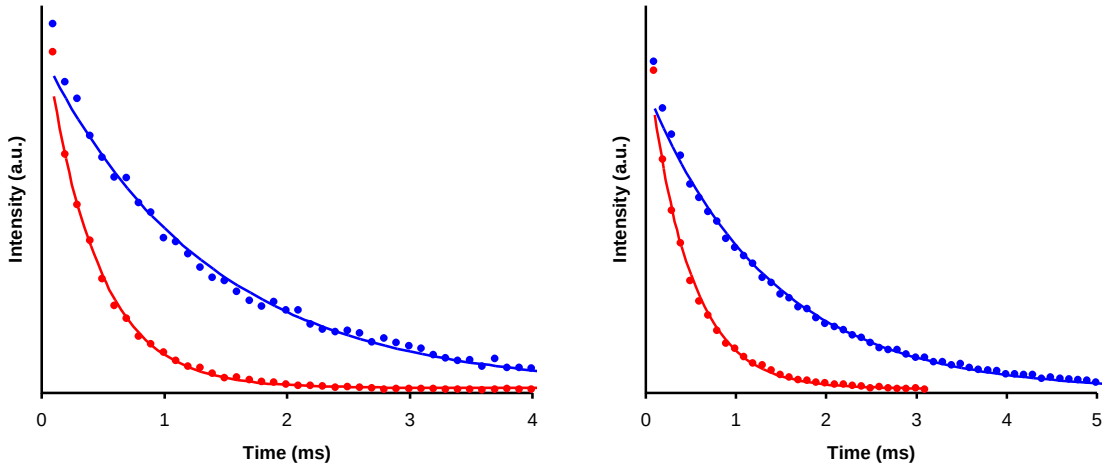

A8. **[Eu.9]$^{3-}$** excited state lifetime determination in H_2O (red) and D_2O (blue) in the absence (left) and presence (right) of carbonate. Exp data (dots); calcd data (line). 1.0 mM **[Eu.9]$^{3-}$**, 0.1 M NaCl, 30 mM $NaHCO_3$, pH 7.4, 25°C.

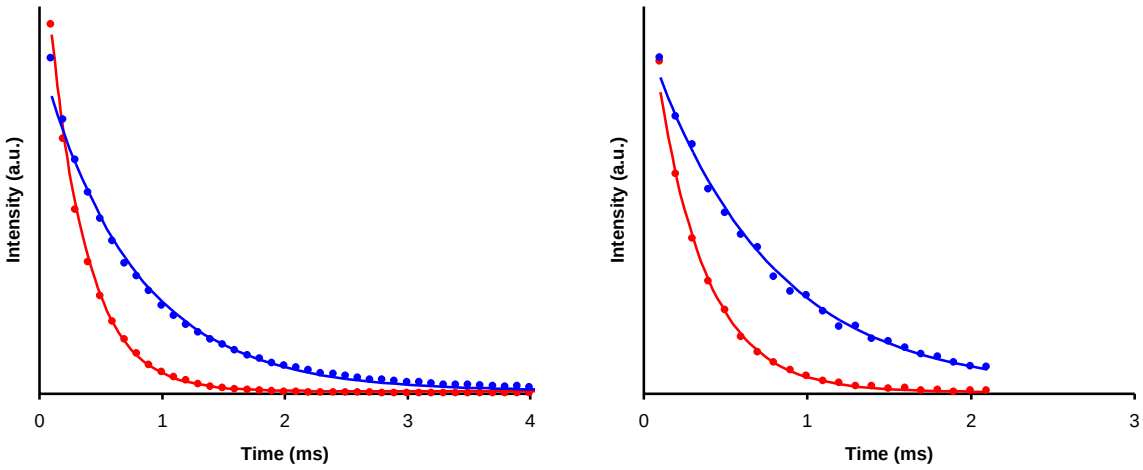

A9. **[Eu.10]**$^{3-}$ excited state lifetime determination in H_2O (red) and D_2O (blue) in the absence (left) and presence (right) of carbonate. Exp data (dots); calcd data (line). 1.0 mM **[Eu.10]**$^{3-}$, 0.1 M NaCl, 30 mM $NaHCO_3$, pH 7.4, 25°C.

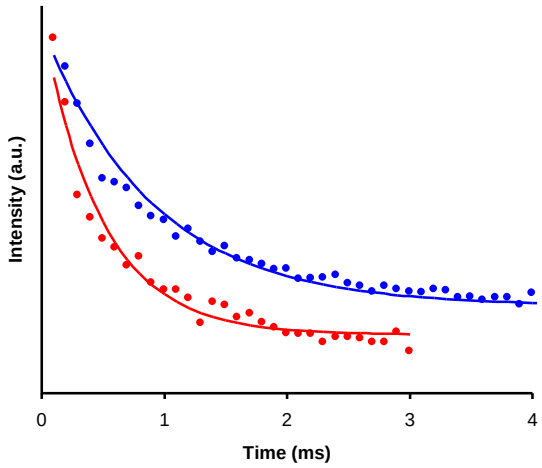

A10. **[Eu.9]**$^{3-}$ Excited state lifetime determination in H_2O (red) and D_2O (blue). Exp data (dots); calcd data (line) in the presence of HSA (0.7 mM). 0.1 mM **[Eu.9]**$^{3-}$, 0.1 M NaCl, λ_{ex} = 270 nm, pH 7.4 (0.2 M PBS), 25°C.

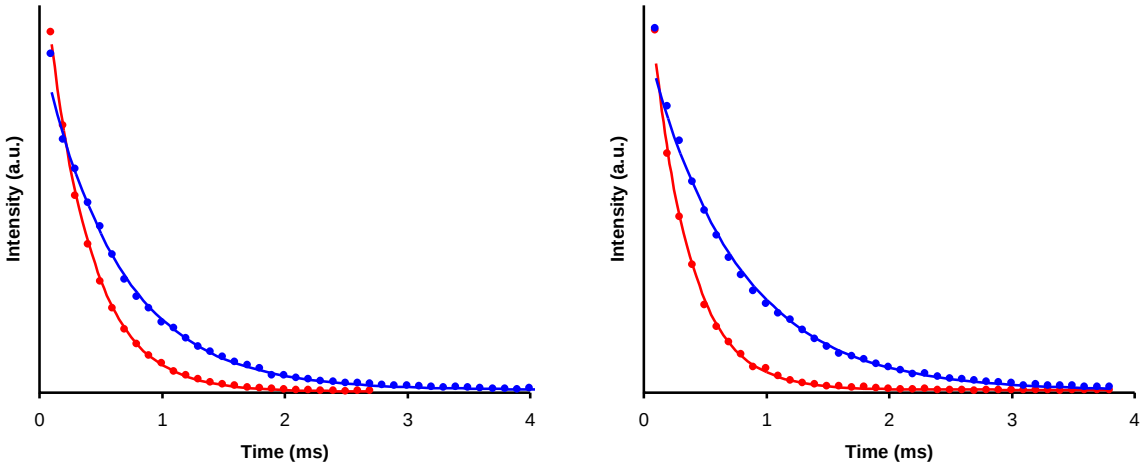

A11. **Eu.14** excited state lifetime determination in H_2O (red) and D_2O (blue) in the absence (left) and presence (right) of carbonate. Exp data (dots); calcd data (line). 1.0 mM **Eu.14**, 0.1 M NaCl, 30 mM $NaHCO_3$, pH 7.4, 25°C.

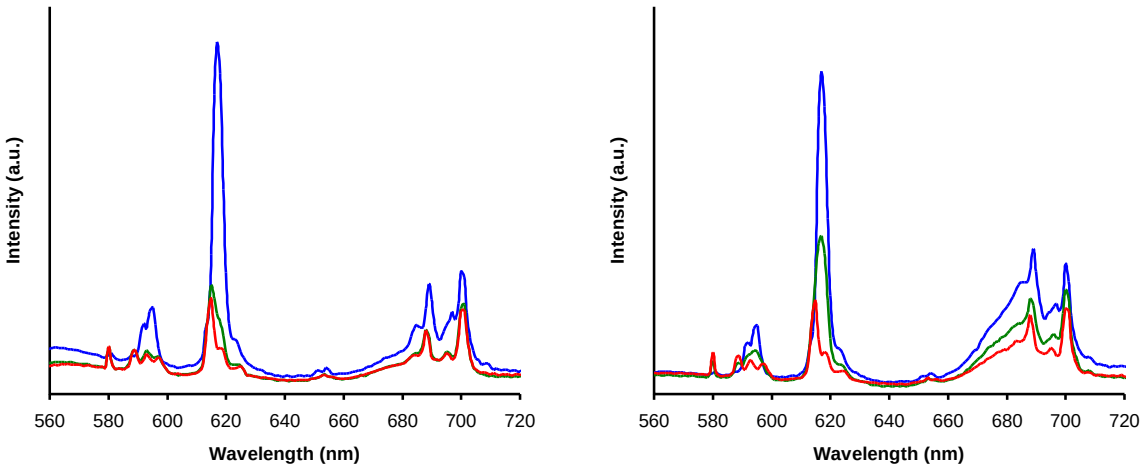

A12. **[Eu.10]**$^{3-}$ (left) and **Eu.14** (right) Eu(III) emission spectra at pH 10.0 (blue), 7.4 (green) and pH 5.0 (red) in the presence of carbonate. 1.0 mM Eu, 0.1 M NaCl, λ_{ex} = 395 nm, 30 mM $NaHCO_3$, pH 7.4, 25°C.

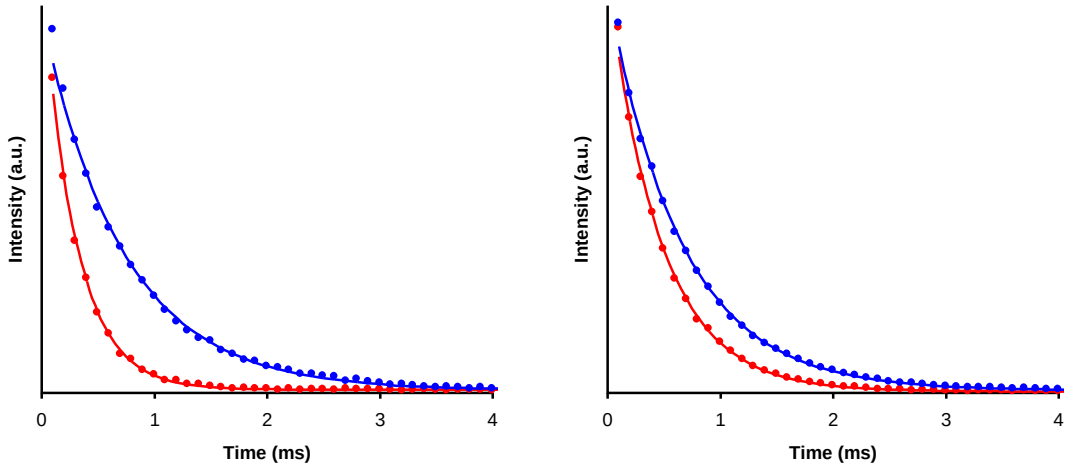

A13. **[Eu.10]**$^{3-}$ excited state lifetime determination in H_2O (red) and D_2O (blue) in the presence of carbonate. Exp data (dots); calcd data (line). Left pH 5.09, right pH 10.43. 1.0 mM **[Eu.10]**$^{3-}$, 0.1 M NaCl, 30 mM $NaHCO_3$, 25°C.

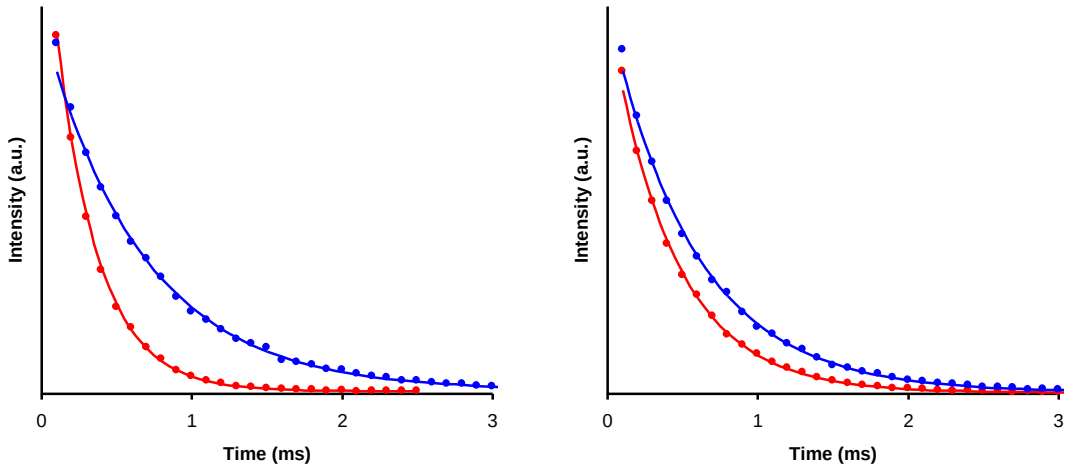

A14. **Eu.14** excited state lifetime determination in H_2O (red) and D_2O (blue) in the presence of carbonate. Exp data (dots); calcd data (line). Left pH 5.07, right pH 10.32. 1.0 mM **Eu.14**, 0.1 M NaCl, 30 mM $NaHCO_3$, 25°C.

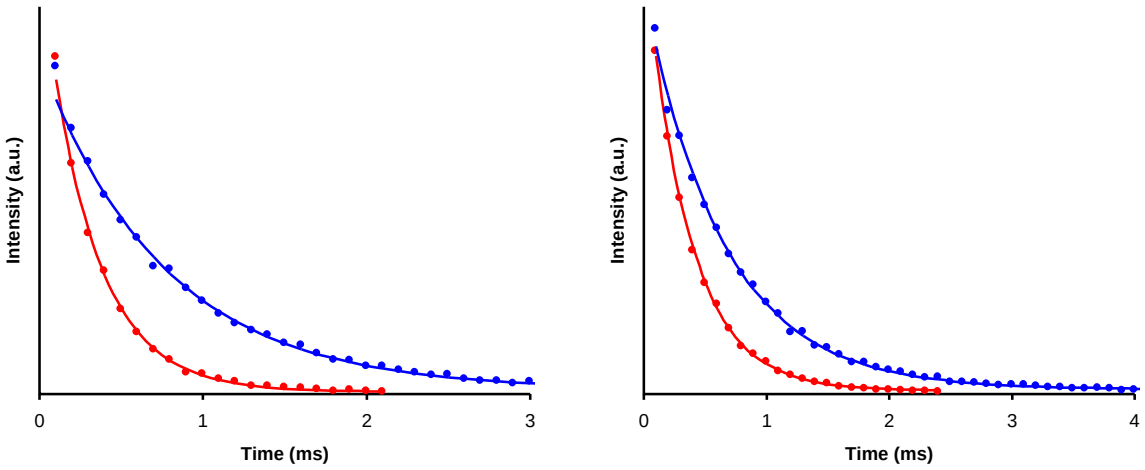

A15. **Eu.14** excited state lifetime determination in H_2O (red) and D_2O (blue) for esterase experiment solution 1 (left) and 2 (right) following incubation (37°C). Exp data (dots); calcd data (line). 0.1 M NaCl, pH 7.4, 25°C**.**

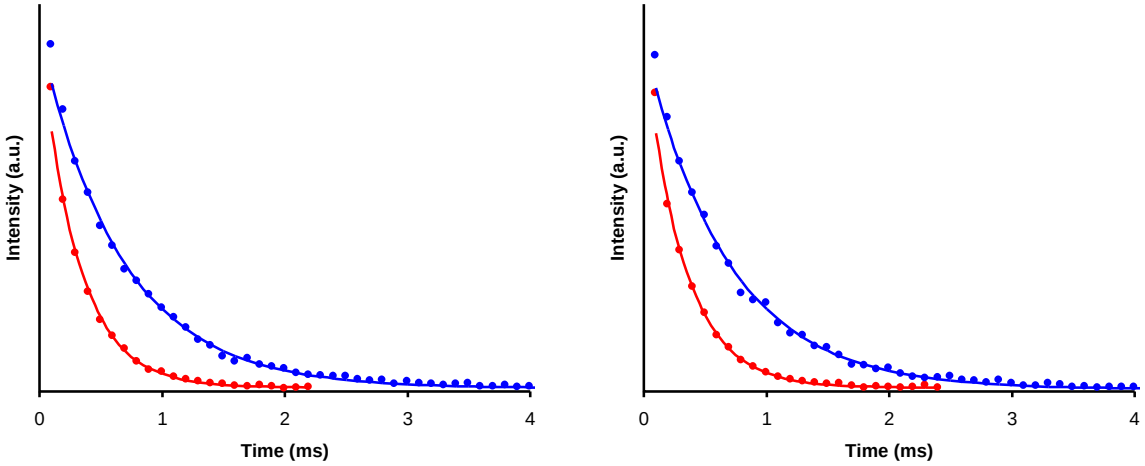

A16. **Eu.14** excited state lifetime determination in H_2O (red) and D_2O (blue) for esterase experiment solution 3 (left) and 4 (right) following incubation (37°C). Exp data (dots); calcd data (line). 0.1 M NaCl, pH 7.4, 25°C.

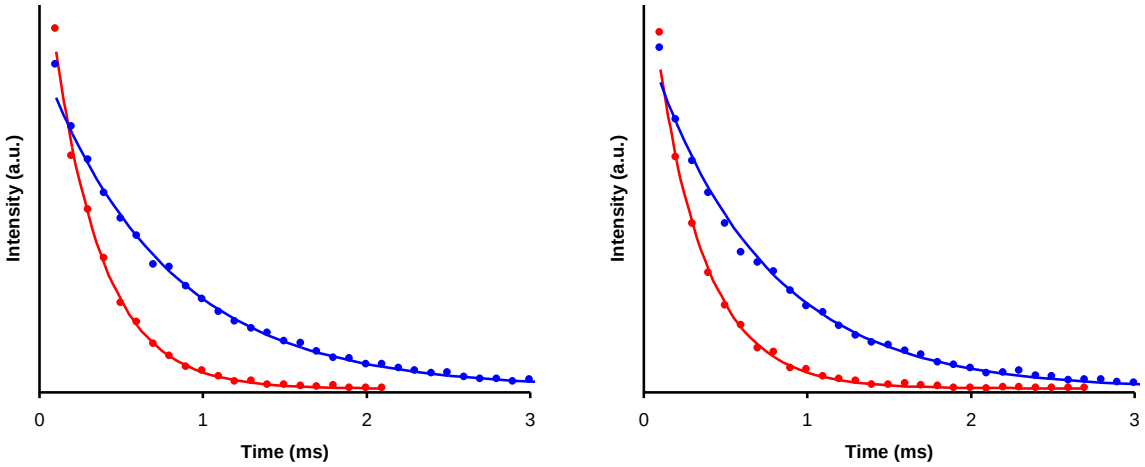

A17. [**Eu.10**]$^{3-}$ excited state lifetime determination in H_2O (red) and D_2O (blue) for esterase experiment solution 1 (left) and 2 (right) following incubation (37°C). Exp data (dots); calcd data (line). 0.1 M NaCl, pH 7.4, 25°C.

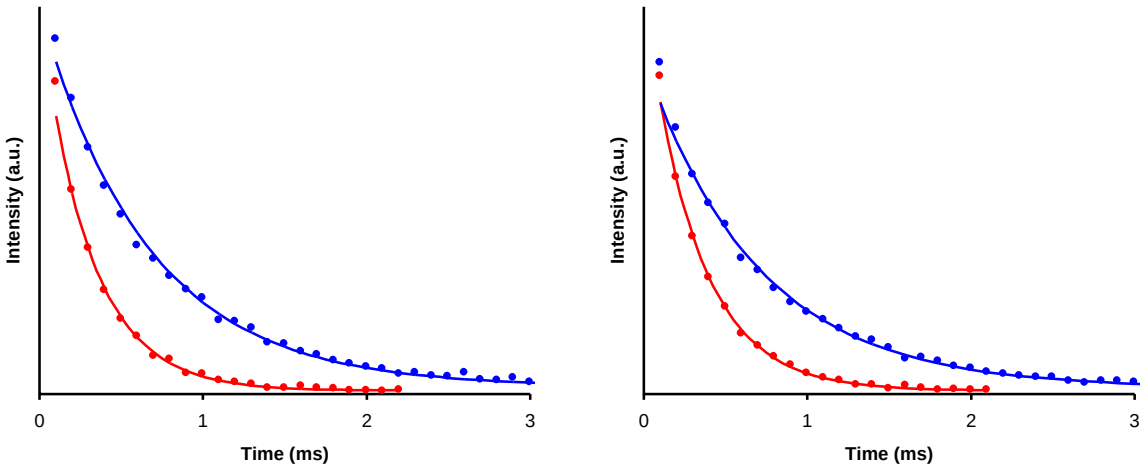

A18. **[Eu.10]**$^{3-}$ excited state lifetime determination in H_2O (red) and D_2O (blue) for esterase experiment solution 3 (left) and 4 (right) following incubation (37°C). Exp data (dots); calcd data (line). 0.1 M NaCl, pH 7.4, 25°C.

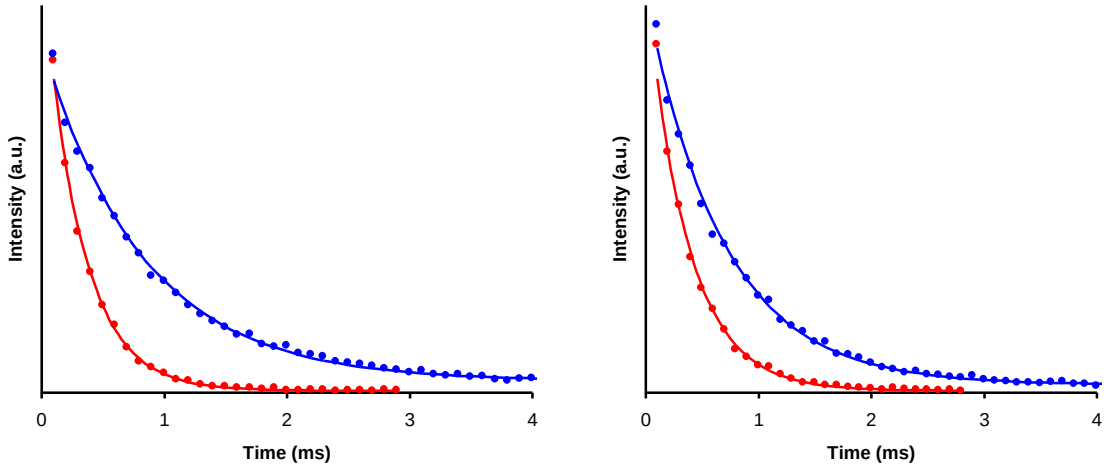

A19. **Eu.18** Excited state lifetime determination in H_2O (red) and D_2O (blue) in the absence (left) and presence (right) of carbonate. Exp data (dots); calcd data (line). 1.0 mM **Eu.18**, 0.1 M NaCl, 30 mM $NaHCO_3$ pH 7.4, 25°C.

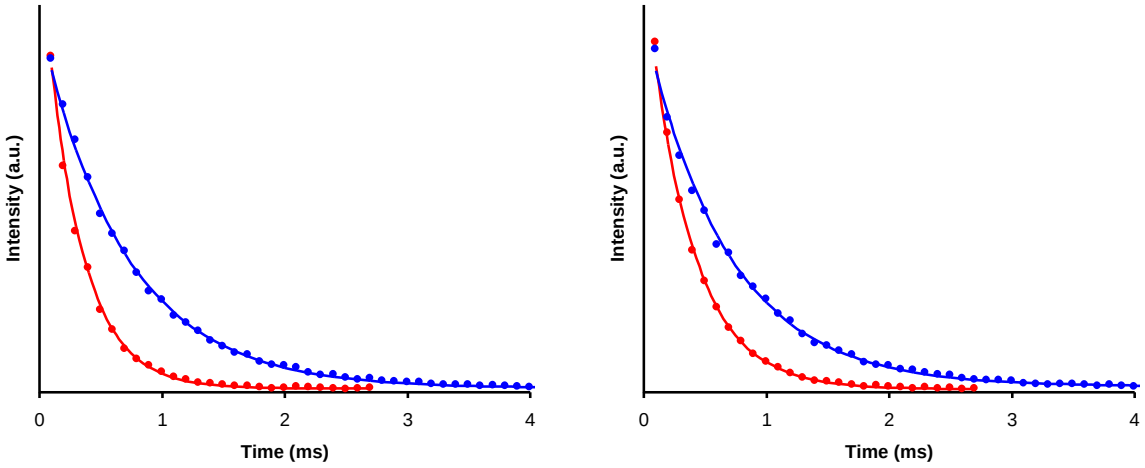

A20. **Eu.18** excited state lifetime determination in H_2O (red) and D_2O (blue) for esterase experiment solution 1 (left) and 2 (right) following incubation (37°C). Exp data (dots); calcd data (line). 0.1 M NaCl, pH 7.4, 25°C.

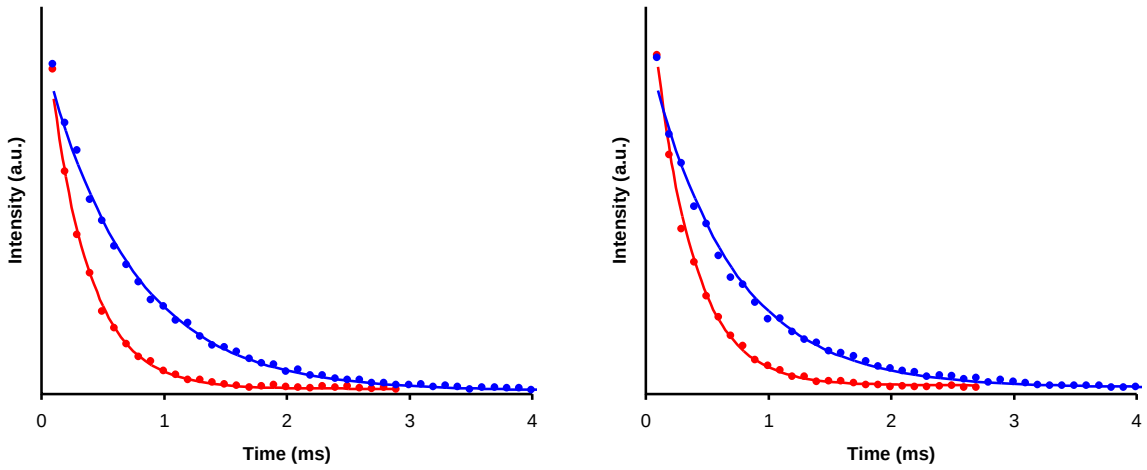

A21. **Eu.18** excited state lifetime determination in H_2O (red) and D_2O (blue) for esterase experiment solution 3 (left) and 4 (right) following incubation (37°C). Exp data (dots); calcd data (line). 0.1 M NaCl, pH 7.4, 25°C.

7.2 Derivation of Equations 56 and 57; pK_a Determination

At any point of the luminescence (Eu) or relaxivity (Gd) *vs*. pH titration the observed intensity is made up of contributions of Hdpp and dpp$^-$.

$$[\mathrm{Hdpp}] \quad {}^{K_a} \quad [\mathrm{H}^+][dpp^-]$$

$$I_{obs} = \left(\frac{[\mathrm{Hdpp}]}{[\mathrm{Hdpp}]+[\mathrm{dpp}^-]}\right) I_{Hdpp} + \left(\frac{[\mathrm{dpp}^-]}{[\mathrm{Hdpp}]+[\mathrm{dpp}^-]}\right) I_{dpp^-}$$

Note: shown here for Eu(III) emission intensity, where I_{obs} is the observed ratio I/I_o (ΔJ = 2) of Eu(III) emission and I_{Hdpp} and I_{dpp}- are the I/I_o (ΔJ = 2) Eu(III) emission ratios of the fully protonated and fully deprotonated dpp. The relaxivity (Gd) *vs*. pH titration pK_a equation derivation is identical with r_1 replacing I.

$$I_{obs}^{-1} = \left(\frac{[\mathrm{Hdpp}]+[\mathrm{dpp}^-]}{[\mathrm{Hdpp}]}\right) I_{Hdpp}^{-1} + \left(\frac{[\mathrm{Hdpp}]+[\mathrm{dpp}^-]}{[\mathrm{dpp}^-]}\right) I_{dpp^-}^{-1}$$

$$I_{obs}^{-1} = \left(1+\frac{[\mathrm{dpp}^-]}{[\mathrm{Hdpp}]}\right) I_{Hdpp}^{-1} + \left(1+\frac{[\mathrm{Hdpp}]}{[\mathrm{dpp}^-]}\right) I_{dpp^-}^{-1}$$

Since;

$$K_a = \frac{[\mathrm{H}^+][\mathrm{dpp}^-]}{[\mathrm{Hdpp}]}$$

Therefore;

$$\frac{[\mathrm{dpp}^-]}{[\mathrm{Hdpp}]} = \frac{K_a}{[\mathrm{H}^+]} \quad \text{and} \quad \frac{[\mathrm{Hdpp}]}{[\mathrm{dpp}^-]} = \frac{[\mathrm{H}^+]}{K_a}$$

Substitute into equation;

$$I_{obs}^{-1} = \left(1 + \frac{K_a}{[\mathrm{H}^+]}\right) I_{Hdpp}^{-1} + \left(1 + \frac{[\mathrm{H}^+]}{K_a}\right) I_{dpp^-}^{-1}$$

Expand;

$$I_{obs}^{-1} = \left(\frac{[\mathrm{H}^+] + K_a}{[\mathrm{H}^+]}\right) I_{Hdpp}^{-1} + \left(\frac{K_a + [\mathrm{H}^+]}{K_a}\right) I_{dpp^-}^{-1}$$

Invert;

$$I_{obs} = \left(\frac{[\mathrm{H}^+]}{[\mathrm{H}^+] + K_a}\right) I_{Hdpp} + \left(\frac{K_a}{K_a + [\mathrm{H}^+]}\right) I_{dpp^-}$$

Cancel identical denominators;

$$I_{obs} = \frac{[\mathrm{H}^+] I_{Hdpp} + K_a I_{dpp^-}}{[\mathrm{H}^+] + K_a} \tag{56}$$

where I_{obs} is the observed ratio I/I_o (ΔJ = 2) of Eu(III) emission intensity and I_{Hdpp} and I_{dpp}- are the I/I_o (ΔJ = 2) Eu(III) emission intensity ratios of the fully protonated and fully deprotonated dpp, known from the start and end points of the Eu(III) emission intensity *vs.* pH curve. $[\mathrm{H}^+]$ is determined from;

$$\mathrm{pH} = -\log_{10}[\mathrm{H}^+]$$

For relaxivity (Gd), where r_{1obs} is the observed relaxivity (Gd) and r_{1Hdpp} and r_{1dpp}- are the relaxivities of the fully protonated and fully deprotonated dpp;

$$r_{1obs} = \frac{[\mathrm{H}^+] r_{1Hdpp} + K_a r_{1dpp^-}}{[\mathrm{H}^+] + K_a} \tag{57}$$

Therefore, K_a is the only variable, determined using an iterative least-squares fitting procedure, operating in Microsoft Excel.

7.3 Derivations of Equations 60 and 61; HSA Binding Constant Determination

7.3.1 Concentration of HSA bound Ln(III) Complex, Equation 46

At any point of the luminescence (Eu) or observed longitudinal relaxation rate, R_{1obs}, (Gd) *vs*. [HSA] titration, the observed intensity is made up of contributions of the HSA bound (LnHSA) and unbound (Ln) complex (where Ln = Eu(III) or Gd(III)).

$$[\mathrm{HSA}]+[\mathrm{Ln}] \underset{}{\overset{K}{\rightleftharpoons}} [\mathrm{LnHSA}] \tag{45}$$

$$K = \frac{[\mathrm{LnHSA}]}{[\mathrm{HSA}][\mathrm{Ln}]}$$

Define;

$$[\mathrm{LnHSA}] = x$$

$$[\mathrm{HSA}] = [\mathrm{HSA}]_T - x$$

$$[\mathrm{Ln}] = [\mathrm{Ln}]_T - x$$

where $[\mathrm{HSA}]_T$ and $[\mathrm{Ln}]_T$ are the total concentrations of HSA and the Ln(III) complex.

Therefore;

$$K = \frac{x}{\left([\mathrm{HSA}]_T - x\right)\left([\mathrm{Ln}]_T - x\right)}$$

Expand;

$$K = \frac{x}{[\mathrm{HSA}]_T - [\mathrm{Ln}]_T - [\mathrm{HSA}]_T x - [\mathrm{Ln}]_T x + x^2}$$

Make x the subject;

$$x = K\left([\mathrm{HSA}]_T - [\mathrm{Ln}]_T - [\mathrm{HSA}]_T x - [\mathrm{Ln}]_T x + x^2\right)$$

Expand;

$$x = K[\mathrm{HSA}]_T[\mathrm{Ln}]_T - K[\mathrm{HSA}]_T x - K[\mathrm{Ln}]_T x + Kx^2$$

Therefore;

$$0 = Kx^2 - x - K[\mathrm{HSA}]_T\, x - K[\mathrm{Ln}]_T\, x + K[\mathrm{HSA}]_T[\mathrm{Ln}]_T$$

Collect x;

$$0 = Kx^2 - \left(K[\mathrm{HSA}]_T + K[\mathrm{Ln}]_T + 1\right)x + K[\mathrm{HSA}]_T[\mathrm{Ln}]_T$$

Solve as a quadratic equation;

$$ax^2 + bx + c = 0$$

$$x = \frac{-b \pm \sqrt{b^2 - 4ac}}{2a}$$

Where;

$$a = K$$
$$b = -\left(K[\mathrm{HSA}]_T + K[\mathrm{Ln}]_T + 1\right)$$
$$c = K[\mathrm{HSA}]_T[\mathrm{Ln}]_T$$

Therefore;

$$x = \frac{\left(K[\mathrm{HSA}]_T + K[\mathrm{Ln}]_T + 1\right) \pm \sqrt{\left(K[\mathrm{HSA}]_T + K[\mathrm{Ln}]_T + 1\right)^2 - 4K\left(K[\mathrm{HSA}]_T[\mathrm{Ln}]_T\right)}}{2K}$$

Cancel K;

$$x = \frac{\left([\mathrm{HSA}]_T + [\mathrm{Ln}]_T + 1/K\right) \pm \sqrt{\left([\mathrm{HSA}]_T + [\mathrm{Ln}]_T + 1/K\right)^2 - 4[\mathrm{HSA}]_T[\mathrm{Ln}]_T}}{2}$$

Recall;

$$[\mathrm{LnHSA}] = x$$

Therefore,

$$[\mathrm{LnHSA}] = \frac{\left([\mathrm{HSA}]_T + [\mathrm{Ln}]_T + 1/K\right) - \sqrt{\left([\mathrm{HSA}]_T + [\mathrm{Ln}]_T + 1/K\right)^2 - 4[\mathrm{HSA}]_T[\mathrm{Ln}]_T}}{2} \qquad (46)$$

7.3.2 [LnHSA] in terms of Emission Intensity (Eu) or Longitudinal Relaxation Rate (Gd), Equations 47 and 50

The theoretically determined emission intensity, I_{calc} (Eu), or longitudinal relaxation rate, R_{1calc} (Gd), is made up of contributions of both the HSA bound (LnHSA) and unbound (Ln) complexes (Ln = Eu(III) or Gd(III)).

$$I_{calc} = \frac{[\mathrm{Ln}]}{[\mathrm{Ln}]_T} I_{Ln} + \frac{[\mathrm{LnHSA}]}{[\mathrm{Ln}]_T} I_{LnHSA}$$

where I_{LnHSA} and I_{Ln} are the $\Delta J = 2$ emission intensity (Eu(III)) or the longitudinal relaxation rate R_1 (Gd(III)).

Remove common factor;

$$I_{calc} = \frac{1}{[\mathrm{Ln}]_T} \left([\mathrm{Ln}] I_{Ln} + [\mathrm{LnHSA}] I_{LnHSA} \right)$$

Recall;

$$[\mathrm{LnHSA}] = x$$

$$[\mathrm{Ln}] = [\mathrm{Ln}]_T - x$$

where $[\mathrm{HSA}]_T$ and $[\mathrm{Ln}]_T$ are the total concentrations of HSA and the Ln(III) complex.

Therefore;

$$I_{calc} = \frac{1}{[\mathrm{Ln}]_T} \left(\left([\mathrm{Ln}]_T - x \right) I_{Ln} + x I_{LnHSA} \right)$$

Expand;

$$I_{calc} = \frac{1}{[\mathrm{Ln}]_T} \left([\mathrm{Ln}]_T I_{Ln} - x I_{Ln} + x I_{LnHSA} \right)$$

Re-arrange;

$$I_{calc} = \frac{1}{[\mathrm{Ln}]_T} \left([\mathrm{Ln}]_T I_{Ln} + x I_{LnHSA} - x I_{Ln} \right)$$

Collect x;

$$I_{calc} = \frac{1}{[\mathrm{Ln}]_T} \left([\mathrm{Ln}]_T I_{Ln} + \left(I_{LnHSA} - I_{Ln} \right) x \right)$$

Recall;

$$[\mathrm{LnHSA}] = x$$

Therefore, in terms of theoretical Eu(III) emission intensity, I_{calc};

$$I_{calc} = \frac{1}{[\mathrm{Eu}]_T} \left([\mathrm{Eu}]_T I_{Eu} + \left(I_{EuHSA} - I_{Eu} \right) [\mathrm{EuHSA}] \right) \tag{47}$$

where I_{Eu} is the intensity of the Eu(III) complex when not bound to HSA (i.e. at the start of the titration) and I_{EuHSA} is the intensity of the Eu(III) complex when entirely bound to HSA (i.e. at the end of the titration).

In terms of Gd(III) theoretical longitudinal relaxation rate, R_{1calc};

$$R_{1calc} = \frac{1}{[\mathrm{Gd}]_T}\left([\mathrm{Gd}]_T R_{1Gd} + \left(R_{1GdHSA} - R_{1Gd}\right)[\mathrm{GdHSA}]\right) \tag{50}$$

where R_{1Gd} is the observed longitudinal relaxation rate of the Gd(III) complex when not bound to HSA (i.e. at the start of the titration) and R_{1GdHSA} is the observed longitudinal relaxation rate of the Gd(III) when entirely bound to HSA (i.e. at the end of the titration).

7.3.3 HSA Binding Constant Determination, Equations 60 and 61

Equation 46, which defines [LnHSA] and equations 47 and 50, which define [Ln(III)] in terms of emission intensity (Eu(III)) or longitudinal relaxation (Gd(III)) were combined in order to determine the HSA binding constant, K (M^{-1}).

$$I_{calc} = \frac{1}{[\mathrm{Eu}]_T}\left(\left(\begin{array}{c}\left(I_{Eu}\times[\mathrm{Eu}]_T\right)+\\ \left(I_{EuHSA}-I_{Eu}\right)\end{array}\right)\left(\begin{array}{c}\left([\mathrm{HSA}]_T+[\mathrm{Eu}]_T+1/K\right)-\\ \sqrt{\left([\mathrm{HSA}]_T+[\mathrm{Eu}]_T+1/K\right)^2-4[\mathrm{HSA}]_T[\mathrm{Eu}]_T}\end{array}\right)/2\right) \tag{60}$$

$$R_{1calc} = \frac{1}{[\mathrm{Gd}]_T}\left(\left(\begin{array}{c}\left(I_{Gd}\times[\mathrm{Gd}]_T\right)+\\ \left(R_{1GdHSA}-R_{1Gd}\right)\end{array}\right)\left(\begin{array}{c}\left([\mathrm{HSA}]_T+[\mathrm{Gd}]_T+1/K\right)-\\ \sqrt{\left([\mathrm{HSA}]_T+[\mathrm{Gd}]_T+1/K\right)^2-4[\mathrm{HSA}]_T[\mathrm{Gd}]_T}\end{array}\right)/2\right) \tag{61}$$

$[\mathrm{Ln}]_T$ and $[\mathrm{HSA}]_T$ are known, while I_{Ln} is obtained as the initial value of the emission intensity Eu(III) or the observed longitudinal relaxation rate, R_1 (Gd(III) *vs*. [HSA] titrations (i.e. when [HSA] = 0). The variables are I_{LnHSA} and K. The equation was iterated on I_{LnHSA} and minimized in terms of I_{LnHSA} and K assuming a 1:1 binding stoichiometry, operating in Microsoft Excel (Eu(III) or Microcal Origin (Gd(III)).

7.4 Courses and Conferences

7.4.1 Lecture Courses

Metals in Medicine, 5 credits, 2.1 grade

Bioorganic Chemistry, 10 credits, 2.1 grade

7.4.2 Training Courses

Departmental Induction, Prof. Hope, Dr. Malpass, Mr. Hisbent

Graduate School Induction

Cross-Faculty Induction

Introduction to Techniques, Mr. Lee, Dr. Fawcett, Dr. Griffith, Mr. Hisbent, Dr. Eaton

Advanced Departmental Safety Procedures and Fire Safety, Mr. Hisbent, Mr, Edwards

Demonstrating/Small Group Teaching, Mr. Clark (EDSC)

An Introduction to PowerPoint, Prof. Cullis

NMR Techniques, Dr. Griffith

Personal Skills Portfolio, Dr. Malpass

Writing Skills, Dr. Malpass, Dr. Grant (EDSC)

Molecular Modelling, Dr. Handa

Study Skills, Ms, Graal (EDSC)

Advanced Scientific Writing for Chemists, Dr. Malpass

Building a Career Skills Portfolio, Mr. Pennington (EDSC)

UK Grad Programme, Windermere. March 14th 2005

7.4.3 Conferences Attended

UK Macrocycles and Supramolecular Chemistry Meeting, University of Sheffield. January 8th 2004

Presented poster at CCDG, Leicester. July 12th 2004

Presented poster at UK Macrocycles, Newcastle. January 5th 2005

One of only 20 students selected for the RSC Manufacturing and Process Chemistry Industry Tour, Newcastle. 17th April 2005. Runner up poster prize

CCDG, Cardiff. July 11th 2005. Won poster prize

Presented poster at ICCC, Cape Town, South Africa. August 13th 2006

Oral Presentation at the RSC Dalton Division Midlands Meeting. September 14th 2006. Won oral presentation prize

Oral presentation at the COST D-38 Meeting, Eindhoven, Holland, May 4th 2007

7.4.4 Demonstrating

1st Year Inorganic Chemistry Demonstrating November 2003 – December 2003

1st Year Inorganic Chemistry Demonstrating November 2004 – December 2004

7.4.5 Seminars Attended

2003

Monday 6th October; Dr. Chris Richards (Queen Mary, University of London) *Very Active Planar Chiral Catalysts for Asymmetric Synthesis*

Wednesday 8th October; Prof. Iain Campbell, FRS (University of Oxford) - 2nd Tim Norwood Memorial Lecture *NMR and Proteins*

Monday 20th October; Dr. Sandie Dann (University of Loughborough) *Unusual Complex Oxides and Sulfides*

Monday 27th October; Dr. Chris Hayes (University of Nottingham) *Natural and Non-natural Products: Total Synthesis and Biological Applications*

Monday 3rd November; Prof. Helen Fielding (U.C.L.) *Controlling Electrons and Molecules using Light*

Monday 24th November; Prof. Thomas Wirth (Cardiff University) *Scope and Potential of Chiral Electrophiles in Stereoselective Synthesis*

Monday 8th December; Professor Peter Hore (University of Oxford) *Real-time NMR Techniques for Studying Protein Structure and Folding*

2004

Monday 19th January; Prof. Bill Levason (University of Southampton) *Recent Developments in the Chemistry of Antimony Ligands*

Monday 26th January; Prof. Roy Harrison (University of Birmingham) *Sources and Physico-Chemical Properties of Aerosols in Polluted Atmospheres*

Monday 2nd February; Dr. Adam Nelson (University of Leeds) *Beyond Breaking the Mirror Plane: Exploiting Stereochemistry in Chemistry and Biology*

Monday 16th February; Dr. John Owen (University of Southampton) *Accelerated Discovery of Electrochemical Materials*

Monday 23rd February; 3rd LEICESTER HALF-DAY CATALYSIS SYMPOSIUM

Prof. P. Braunstein (University of Strasbourg) – RSC Nyholm Lecture

Prof. Sue Gibson (Imperial College, London)

Dr. P. Kamer (University of Amsterdam)

Dr. Gregory Solan (University of Leicester

Monday 1st March; Dr. Iain Coldham (University of Sheffield) *Stereoselective Synthesis of Cyclic Amines using Chiral Organolithium Species and Cycloaddition Reactions*

Monday 8th March; Dr. Chris Kay (Free University Berlin) *Applications of Electron Spin Resonance Spectroscopy to Biological Problems*

Monday 15th March; Professor David Schiffrin (University of Liverpool) *Connectivity of Functionalised Nanoparticles and their Arrays*

Monday 29th March; Dr. Polly Arnold (University of Nottingham) *Tethered Carbenes*

Monday 26th April; Dr. Graham Sandford (University of Durham) *Fluorine in Organic Synthesis*

Monday 10th May; Dr. Dominic Wright (University of Cambridge) *Cation and Anion Coordination. Torocyclic Ligands*

Monday 17th May; Dr. Andy Bell (Defence Science & Technology Laboratory) *Ion Mobility Spectrometry – a Little-known Technique*

Monday 7th June; Prof. Peter Scott (University of Warwick) *Chiral Catalysis*

Monday 27th September; Dr. Randolph Kohn (University of Bath) *Triazacyclohexane Complexes of Chromium as Catalysts for the Polymerisation and Trimerisation of Olefins*

Monday 4th October; Dr. Stuart Warriner (University of Leeds)

Friday 15th October; Prof. Eric Herbst (Ohio State University) RSC Endowed Centenary Lecture *The Chemistry of Interstellar Space*

Monday 18th October; Prof. David Cole-Hamilton (University of St. Andrews)

Monday 25th October; Dr. Alan Armstrong (Imperial College) *New Methods and Synthetic Applications of Asymmetric Heteroatom Transfer*

Monday 1st November; Dr. Stuart MacKenzie (University of Warwick)

Monday, 8th November; Dr. Helen Aspinall (University of Liverpool)

Monday, 15th November; Dr. Gareth Pritchard (Loughborough University)

Monday 22nd November; Dr. Chris Mayhew (University of Birmingham)

Monday 29th November; Prof. Paul Walton (University of York) *Polymer Imprinting: Metal Clusters that make a Lasting Impression*

Monday 6th December; Dr. Robert Stockman (University of East Anglia) *Two-Directional Synthesis, Tandem Reactions and Rearrangements:Developing Efficient Strategies for Alkaloid Synthesis*

2005

Monday 24th January; Prof. Chris Abell (University of Cambridge)

Monday 14th February; Dr. Simon Jones (University of Sheffield)

Monday 7th March; Dr. Paul Clark (University of Nottingham)

2007

Monday 30th April; LEICESTER HALF-DAY METALS IN MEDICINE SYMPOSIUM

Dr Sofia Pascu (University of Oxford) *Designing Small Molecule-based Probes for In Vitro Fluorescence Imaging*

Prof. Nils Metzler-Nolte (Ruhr-Universitaet Bochum, Germany) *Labelling of Bioactive Peptides with Organometallic Compounds: From Basic Chemistry to Biomedical Applications*

Dr Gareth Williams (Durham University) *Sensing and Imaging with Cell-permeable Luminescent Platinum and Iridium Complexes*

Prof. Chris Orvig (University of British Columbia, Canada) *Carbohydrate Conjugates in Medicinal Inorganic Chemistry*

Chapter 8

References

1 Z. Guo and P. J. Sadler, *Angew. Chem. Int. Ed.*, 1999, **38**, 1512.

2 T. Storr, K. H. Thompson and C. Orvig, *Chem. Soc. Rev.*, 2006, **35**, 534.

3 O. Anderson, *Chem. Rev.*, 1999, **99**, 2683.

4 D. F. Shriver, P. W. Atkins and C. H. Langford, 'Inorganic Chemistry, Second Edition', Oxford University Press, 1994.

5 G. J. Kontoghiorghes, J. G. Goddard, A. N. Bartlett and L. Sheppard, *J. Clin. Pharm. Ther.*, 1990A, **48**, 255.

6 G. J. Kontoghiorghes, A. N. Bartlett, A. V. Hoffbrand and L. Sheppard, *Brit. J. Haematol.*, 1990B, **76**, 295.

7 A. Catsch and A. E. Harmuth-Hoehne, *Pharmacol. Therapeut.*, 1976, **A1**, 1.

8 D. Parker, *Chem. Brit.*, 1994, 818.

9 J. Leveille, G. Demonceau, M. de Roo, P. Rigo, R. Taillefer, R. A. Morgan, D. Kupranick and R. C. Walovitch, *J. Nucl. Med.*, 1989, **30**, 1902.

10 A. G. Jones, M. J. Abrams, A. Davidson, J. W. Brodack, A. K. Toothaker, S. J. Adelstein and A. I. Kassis, *Int. J. Nucl. Med. Biol.*, 1984, **11**, 225.

11 A. M. Forster, A. E. Storey, C. M. Archer, K. R. Nagle, F. S. Booker, B. Edwards, H. K. Gill, J. D. Kelly and M. McPartlin, *J. Nucl. Med.*, 1992, **33**, 850.

12 P. C. Lauterbur, *Biosci. Rep.*, 2004, **24**, 165.

13 P. Mansfield, *Angew. Chem. Int. Ed.*, 2004, **43**, 5456.

14 P. W. Atkins, 'Physical Chemistry, 6th Edition', Oxford University Press, 1998.

15 S. Mansson and A. Bjornerud, 'The Chemistry of Contrast Agents in Magnetic Resonance Imaging; Physical Principles of Medicinal Imaging by Nuclear Magnetic Resonance', ed. A. E. Merbach and E. Toth, Wiley, 2001.

16 V. Jaques and J. F. Desreux, 'Topics in Current Chemistry; New Classes of MRI Contrast Agents', ed. W. Krause, Springer, 2002.

17 G. Elizondo, C. J. Fretz, D. D. Stark, S. M. Rocklage, S. C. Quay, D. Worah, Y. M. Tsang, M. C. Chen and J. T. Ferrucci, *Radiology*, 1991, **178**, 73.

18 C. Hershko, R. W. Grady and G. Link, *Haematologia (Budap)*, 1984, **17**, 25.

19 B. Hoener, B. L. Engelstad, E. C. Ramos, H. A. Macapiniac, D. C. Price, T. R. Johnson and D. L. White, *J. Magn. Reson. Imaging*, 1991, **1**, 357.

20 N. Kaltsoyannis and P. Scott, 'The f Elements', ed. J. Evans, Oxford University Press, 1999.

21 R. B. Lauffer, *Chem. Rev.*, 1987, **87**, 901.

22 R. M. Weisskoff and P. Caravan, 'MR Contrast Agent Basics in Cardiovascular Magnetic Resonance', ed. A. Lardo, Z. A. Fayed, N. A. F. Chronos and V. Fuster, M. Dunitz, 2003.

23 D. K. Kim, M. Mikhaylova, F. H. Wang, J. Kehr, B. Bjelke, Y. Zhang, T. Tsakalakos and M. Muhammed, *Chem. Mater.*, 2003, **15**, 4343.

24 T. Murakami, R. L. Baron, M. S. Peterson, J. H. O. III, P. L. Davis, S. R. Confer and M. P. Federle, *Radiology*, 1996, **200**, 69.

25 R. D. Shannon and C. T. Prewitt, *Acta Cryst.*, 1969, **B25**, 925.

26 R. D. Shannon, *Acta Cryst.*, 1976, **A32**, 751.

27 S. P. Fricker, *Chem. Soc. Rev.*, 2006, **35**, 524.

28 H.-J. Weinmann, R. C. Brasch, W.-R. Press and G. E. Wesbey, *Am. J. Roentgenol.*, 1984, **142**, 619.

29 R. C. Brasch, *Western J. Med.*, 1985, **142**, 847.

30 J.-C. Bousquet, S. Saini, D. D. Stark, P. F. Hahn, M. Nigam, J. Wittenberg and J. T. Ferucci, *Radiology*, 1988, **166**, 693.

31 M. Bottrill, L. Kwok and N. J. Long, *Chem. Soc. Rev.*, 2006, **35**, 557.

32 K. Kumar, T. Jin, X. Wang, J. F. Desreux and M. F. Tweedle, *Inorg. Chem.*, 1994, **33**, 3823.

33 K. Kumar, C. A. Chang, L. C. Francesconi, D. D. Dischino, M. F. Malley, J. Z. Gougoutas and M. F. Tweedle, *Inorg. Chem.*, 1994, **33**, 3567.

34 K. Kumar and M. F. Tweedle, *Inorg. Chem.*, 1993, **32**, 4193.

35 D. H. White, L. A. Delearie, D. A. Moore, R. A. Wallace, T. J. Dunn, W. P. Cacheris, H. Imura and G. R. Choppin, *Invest. Radiol.*, 1991, **26**, S226.

36 A. E. Martell and R. M. Smith, 'Critical Stability Constants', Plenum, 1974.

37 R. M. Smith, R. J. Motekaitis and A. E. Martell, National Instituste of Standards and Technology, 1997.

38 P. Caravan, J. J. Ellison, T. J. McMurry and R. B. Lauffer, *Chem. Rev.*, 1999, **99**, 2293.

39 W. P. Cacheris, S. C. Quay and S. M. Rocklage, *Magn. Reson. Imaging*, 1990, **8**, 467.

40 V. M. Runge, D. Y. Gelblum and S. Jacobson, *Magn. Reson. Imaging*, 1991, **9**, 79.

41 K. Kumar, M. F. Tweedle, M. F. Malley and J. Z. Gougoutas, *Inorg. Chem.*, 1995, **34**, 6472.

42 D. Meyer, M. Schaefer and D. Doucet, *Invest. Radiol.*, 1990, **25**, S53.

43 M. P. Lowe, *Aust. J. Chem.*, 2002, **55**, 551.

44 E. Toth, L. Helm and A. E. Merbach, 'The Chemistry of Contrast Agents in Magnetic Resonance Imaging; Relaxivity of Gadolinium(III) Complexes: Theory and Machanism', ed. A. E. Merbach and E. Toth, Wiley, 2001.

45 P. Caravan, *Chem. Soc. Rev.*, 2006, **35**, 512.

46 J. Xu, D. G. Churchill, M. Botta and K. N. Raymond, *Inorg. Chem.*, 2004, **43**, 5492.

47 D. M. J. Doble, M. Botta, J. Wang, S. Aime, A. Barge and K. N. Raymond, *J. Am. Chem. Soc.*, 2001, **123**, 10758.

48 B. O'Sullivan, D. M. J. Doble, M. K. Thompson, C. Siering, J. Xu, M. Botta, S. Aime and K. N. Raymond, *Inorg. Chem.*, 2003, **42**, 2577.

49 V. C. Pierre, M. Botta, S. Aime and K. N. Raymond, *Inorg. Chem.*, 2006, **45**, 8355.

50 Z. Zhang, S. A. Nair and T. J. McMurry, *Curr. Med. Chem.*, 2005, **12**, 751.

51 S. Aime, M. Botta, S. G. Crich, G. Giovenzana, R. Pagliarin, M. Sisti and E. Terreno, *Magn. Reson. Chem.*, 1998, **36**, S200.

52 P. Caravan, A. V. Astashkin and A. M. Raitsimring, *Inorg. Chem.*, 2003, **42**, 3972.

53 A. M. Raitsimring, A. V. Astashkin, D. Baunte, D. Goldfarb and P. Caravan, *J. Phys. Chem. A.*, 2004, **108**, 7318.

54 N. Bloembergen and L. O. Morgan, *J. Chem. Phys.*, 1961, **34**, 842.

55 E. Toth, O. M. N. Dhubhghaill, G. Besson, L. Helm and A. E. Merbach, *Magn. Reson. Chem.*, 1999, **37**, 701.

56 E. Toth, D. Pubanz, S. Vauthey, L. Helm and A. E. Merbach, *Chem. Eur. J.*, 1996, **2**, 1607.

57 M. Botta, *Eur. J. Inorg. Chem.*, 2000, 399.

58 J. H. Freed, *J. Chem. Phys.*, 1978, **68**, 4034.

59 S. Aime, M. Botta, M. Fasano and E. Terreno, *Acc. Chem. Res.*, 1999, **32**, 941.

60 T. J. Swift and R. E. J. Connick, *J. Chem. Phys.*, 1962, **37**, 307.

61 S. Aime, M. Botta, M. Fasano, S. G. Crich and E. Terreno, *Coord. Chem. Rev.*, 1999, **185-186**, 321.

62 E. Toth, I. van Uffelen, L. Helm, A. E. Merbach, D. Ladd, K. Briley-Saebo and K. E. Kellar, *Magn. Reson. Chem.*, 1998, **36**, S125.

63 S. Aime, M. Botta, M. Fasano and E. Terreno, *Chem. Soc. Rev.*, 1998, **27**, 19.

64 D. H. Powell, O. M. N. Dhubhghaill, D. Pubanz, L. Helm, Y. S. Lebedev, W. Schlaepfer and A. E. Merbach, *J. Am. Chem. Soc.*, 1996, **118**, 9333.

65 R. Ruloff, E. Toth, R. Seopelliti, R. Tripier, H. Handel and A. E. Merbach, *Chem. Commun.*, 2002, 2630.

66 S. Laus, R. Ruloff, E. Toth and A. E. Merbach, *Chem. Eur. J.*, 2003, **9**, 3555.

67 M. Woods, M. Botta, S. Avedano, J. Wang and A. D. Sherry, *Dalton Trans.*, 2005, 3829.

68 F. Yerly, A. Borel, L. Helm and A. E. Merbach, *Chem. Eur. J.*, 2003, **9**, 5468.

69 M. Woods, S. Aime, M. Botta, J. A. K. Howard, J. M. Moloney, M. Navet, D. Parker, M. Port and O. Rousseaux, *J. Am. Chem. Soc.*, 2000, **122**, 9781.

70 S. Aime, M. Botta and G. Ermondi, *Inorg. Chem.*, 1992, **31**, 4291.

71 V. Jaques and J. F. Desreux, *Inorg. Chem.*, 1994, **33**, 4048.

72 S. Aime, A. Barge, M. Botta, A. S. de Sousa and D. Parker, *Angew. Chem. Int. Ed.*, 1998, **37**, 2673.

73 S. Aime, A. Barge, J. I. Bruce, M. Botta, J. A. K. Howard, J. M. Moloney, D. Parker, A. S. de Sousa and M. Woods, *J. Am. Chem. Soc.*, 1999, **121**, 5762.

74 J. A. K. Howard, A. M. Kenwright, J. M. Moloney, D. Parker, M. Port, M. Navet, O. Rousseau and M. Woods, *Chem. Commun.*, 1998, 1381.

75 D. M. Corsi, L. Vander Elst, R. N. Muller, H. van Bekkum and J. A. Peters, *Chem. Eur. J.*, 2001, **7**, 1383.

76 M. Woods, Z. Kovacs, S. Zhang and A. D. Sherry, *Angew. Chem. Int. Ed.*, 2003, **42**, 5889.

77 D. Messeri, M. P. Lowe, D. Parker and M. Botta, *Chem. Commun.*, 2001, 2742.

78 F. Botteman, G. M. Nicolle, L. Vander Elst, S. Laurent, A. E. Merbach and R. N. Muller, *Eur. J. Inorg. Chem.*, 2002, 2686.

79 C. Li, Y.-X. Li, G.-L. Law, K. Man, W.-T. Wong and H. Lei, *Bioconjugate Chem.*, 2006, **17**, 571.

80 C. Sudan, P. Ceroni, V. Vicinelli, M. Maestri, V. Balzani, M. Gorka, S.-K. Lee, J. van Heyst and F. Vogtle, *Dalton Trans.*, 2004, 1597.

81 V. C. Pierre, M. Botta and K. N. Raymond, *J. Am. Chem. Soc.*, 2005, **127**, 504.

82 H. Kobayashi and M. W. Brechbiel, *Curr. Pharm. Biotechnol.*, 2004, **5**, 539.

83 H. Kobayashi and M. Brechbiel, *Mol. Imaging*, 2003, **2**, 1.

84 R. Esfand and D. A. Tomalia, *Drug Discov. Today*, 2001, **6**, 427.

85 L. Henry Bryant Jr., M. W. Brechbiel, C. Wu, J. W. M. Butle, V. Herynek and J. A. Frank, *J. Magn. Reson. Imaging*, 1999, **9**, 348.

86 J. P. Cross, M. Lauz, P. D. Badger and S. Petoud, *J. Am. Chem. Soc.*, 2004, **126**, 16278.

87 J. Rudovsky, P. Hermann, M. Botta, S. Aime and I. Lukes, *Chem. Commun.*, 2005, 2390.

88 J. Rudovsky, M. Botta, P. Hermann, K. I. Hardcastle, I. Lukeš and S. Aime, *Bioconjugate Chem.*, 2006, **17**, 975.

89 D. A. Fulton, E. M. Elemento, S. Aime, L. Chaabane, M. Botta and D. Parker, *Chem. Commun.*, 2006, 1064.

90 D. A. Fulton, M. O'Halloran, D. Parker, K. Senanayake, M. Botta and S. Aime, *Chem. Commun.*, 2005, 474.

91 R. B. Lauffer, *Magn. Reson. Med.*, 1991, **22**, 339.

92 T. N. Parac-Vogt, K. Kimpe, S. Laurent, C. Pierart, L. Vander Elst, R. N. Muller and K. Binnemans, *Eur. Biophys. J.*, 2006, **35**, 136.

93 S. Torres, J. A. Martins, J. P. Andre, C. F. G. C. Geraldes, A. E. Merbach and E. Toth, *Chem. Eur. J.*, 2006, **12**, 940.

94 M. P. Lowe, *Curr. Pharm. Biotechnol.*, 2004, **5**, 519.

95 D. Artemov, Z. M. Bhujwalla and J. W. M. Butle, *Curr. Pharm. Biotechnol.*, 2004, **5**, 485.

96 G. M. Lanza, P. Winter, S. Caruthers, A. Schmeider, K. Crowder, A. Morawski, H. Zhang, M. J. Scott and S. A. Wickline, *Curr. Pharm. Biotechnol.*, 2004, **5**, 495.

97 S. Aime, A. Barge, C. Cabella, S. G. Crich and E. Gianolio, *Curr. Pharm. Biotechnol.*, 2004, **5**, 509.

98 J. F. Podulso, G. L. Curran, J. A. Peterson, D. J. McCornick, A. H. Fauq, M. A. Khan and T. M. Wengenack, *Biochemistry*, 2004, **43**, 6064.

99 L. M. de Leon-Rodriguez, A. Ortiz, A. L. Weiner, S. Zhang, Z. Kovacs, T. Kodadek and A. D. Sherry, *J. Am. Chem. Soc.*, 2002, **124**, 3514.

100 L. Frullano, J. Rohovec, S. Aime, T. Maschmeyer, M. I. Prata, J. J. Pedroso de Lima, C. F. G. C. Geraldes and J. A. Peters, *Chem. Eur. J.*, 2004, **10**, 5205.

101 S. Aime, C. Cabella, S. Colombatto, S. G. Crich, E. Gianolio and F. Maggioni, *J. Magn. Res. Imaging*, 2002, **16**, 394.

102 M. Woods, D. E. Woessner and A. D. Sherry, *Chem. Soc. Rev.*, 2006, **35**, 500.

103 S. Zhang, C. R. Malloy and A. D. Sherry, *J. Am. Chem. Soc.*, 2005, **127**, 17572.

104 S. Aime, A. Barge, D. Delli Castelli, F. Fedeli, A. Mortillaro, F. U. Nielsen and E. Terreno, *Magn. Reson. Med.*, 2002, **47**, 639.

105 G. R. Choppin, 'Lanthanide Probes in Life, Chemical and Earth Sciences, Theory and Practice; Chemical Properties of the Rare Earth Elements', ed. J.-C. G. Bunzli and G. R. Choppin, Elsevier, 1989.

106 H. C. Aspinall, 'Chemistry of the F-Block Elements', CRC Press, 2001.

107 H. B. Sibler and S. J. Paquette, *Met. Ions Biol. Syst.*, 2003, **40**, 69.

108 A. D. Sherry and C. F. G. C. Geraldes, 'Lanthanide Probes in Life, Chemical and Earth Sciences, Theory and Practice; Shift Reagents in NMR Spectroscopy', ed. J.-C. G. Bunzli and G. R. Choppin, Elsevier, 1989.

109 C. F. G. C. Geraldes and C. Luchinat, *Met. Ions Biol. Syst.*, 2003, **40**, 513.

110 J.-C. G. Bunzli, *Acc. Chem. Res.*, 2006, **39**, 53.

111 J. I. Bruce, M. P. Lowe and D. Parker, 'The Chemistry of Contrast Agents in Magnetic Resonance Imaging; Phototypical Aspects of Lanthanide(III) Complexes', ed. A. E. Merbach and E. Toth, Wiley, 2001.

112 J.-C. G. Bunzli and C. Piguet, *Chem. Soc. Rev.*, 2005, **34**, 1048.

113 J.-C. G. Bunzli, 'Lanthanide Probes in Life, Chemical and Earth Sciences, Theory and Practice; Luminescent Probes', ed. J.-C. G. Bunzli and G. R. Choppin, Elsevier, 1989.

114 W. D. Horrocks Jr. and D. R. Sudnick, *Acc. Chem. Res.*, 1981, **14**, 384.

115 W. D. Horrocks Jr. and D. R. Sudnick, *J. Am. Chem. Soc.*, 1979, **101**, 334.

116 A. Beeby, I. M. Clarkson, R. S. Dickins, S. Faulkner, D. Parker, L. Royle, A. S. de Sousa, J. A. G. Williams and M. Woods, *J. Chem. Soc.; Perkin Trans. 2*, 1999, 493.

117 D. Parker, R. S. Dickins, H. Puschmann, C. Crossland and J. A. K. Howard, *Chem. Rev.*, 2002, **102**, 1977.

118 M. N. Berberan-Santos, *PhysChemComm*, 2000, **5**, 18.

119 D. Parker and J. A. G. Williams, *J. Chem. Soc., Dalton Trans.*, 1996, 3613.

120 D. Parker, *Coord. Chem. Rev.*, 2000, **205**, 109.

121 A. Dossing, *Eur. J. Inorg. Chem.*, 2005, 1425.

122 K. Matsumoto and Z. Yuan, *Met. Ions Biol. Syst.*, 2003, **40**.

123 J. R. Lakowicz, 'Principles of Fluoresence Spectroscopy, 2nd Edition', Springer, 1999.

124 J. M. Haider and Z. Pikramenou, *Chem. Soc. Rev.*, 2005, **34**, 120.

125 B. P. Burton-Pye, S. L. Heath and S. Faulkner, *Dalton Trans.*, 2005, 146.

126 M. M. Castand-Briones, A. P. Bassett, L. L. Meason, P. R. Ashton and Z. Pikramenou, *Chem. Commun.*, 2004, 2832.

127 A. P. Bassett, S. W. Magennis, P. B. Glover, D. J. Lewis, N. Spencer, S. Parsons, R. M. Williams, L. de Cola and Z. Pikramenou, *J. Am. Chem. Soc.*, 2004, **126**, 9413.

128 P. Atkinson, Y. Bretonniere and D. Parker, *Chem. Commun.*, 2004, 438.

129 Y. Bretonniere, M. J. Cann, D. Parker and R. Slater, *Chem. Commun.*, 2002, 1930.

130 D. Parker and J. Yu, *Chem. Commun.*, 2005, 3141.

131 M. Stubbs, P. M. J. McSheehy, J. R. Griffiths and C. L. Bashford, *Mol. Med. Today*, 2000, **6**, 15.

132 J. Hall, R. Hanner, S. Aime, M. Botta, S. Faulkner, D. Parker and A. S. de Sousa, *New. J. Chem.*, 1998, 627.

133 S. Aime, A. Barge, M. Botta, J. A. K. Howard, R. Kataky, M. P. Lowe, J. M. Moloney, D. Parker and A. S. de Sousa, *Chem. Commun.*, 1999, 1047.

134 M. P. Lowe, D. Parker, O. Reany, S. Aime, M. Botta, G. Castellano, E. Gianolio and R. Pagliarin, *J. Am. Chem. Soc.*, 2001, **123**, 7601.

135 K. M. Brindle, M. P. Lowe and D. Parker, *Unpublished results*, 2001.

136 M. Woods, G. E. Kiefer, S. Bott, A. Castillo-Muzquiz, C. Eshelbrenner, L. Michaudet, K. McMillan, S. D. K. Mudigunda, D. Ogrin, G. Tircso, S. Zhang, P. Zhao and A. D. Sherry, *J. Am. Chem. Soc.*, 2004, **126**, 9248.

137 S. Aime, M. Botta, S. G. Crich, G. Giovenzana, P. Palmisano and M. Sisti, *Chem. Commun.*, 1999, 1577.

138 S. Aime, F. Fedeli, A. Sanino and E. Terreno, *J. Am. Chem. Soc.*, 2006, **128**, 11326.

139 S. Laus, A. Sour, R. Ruloff, E. Toth and A. E. Merbach, *Chem. Eur. J.*, 2005, **11**, 3064.

140 E. Toth, R. D. Bolskar, A. Borel, G. Gonzalez, L. Helm, A. E. Merbach, B. Sitharaman and L. J. Wilson, *J. Am. Chem. Soc.*, 2005, **127**, 799.

141 T. D. Ros and M. Prato, *Chem. Commun.*, 1999, 663.

142 R. Hovland, C. Glogard, A. J. Aasen and J. Klaveness, *J. Chem. Soc.; Perkin Trans. 2*, 2001, 929.

143 S. Zhang, K. Wu and A. D. Sherry, *Angew. Chem. Int. Ed.*, 1999, **38**, 3192.

144 N. Raghunand, C. Howison, A. D. Sherry, S. Zhang and R. J. Gillies, *Magn. Reson. Med.*, 2003, **49**, 249.

145 M. Woods, S. Zhang, V. H. Ebron and A. D. Sherry, *Chem. Eur. J.*, 2003, **9**, 4634.

146 K.-E. Lokling, S. L. Fossheim, R. Skurtveit, A. Bjornerud and J. Klaveness, *Magn. Reson. Imaging*, 2001, **19**, 731.

147 K.-E. Lokling, R. Skurtveit, S. L. Fossheim, G. Smistad, I. Henriksen and J. Klaveness, *Magn. Reson. Imaging*, 2003, **21**, 531.

148 K.-E. Lokling, S. L. Fossheim, J. Klaveness and R. Skurtveit, *J. Control. Release*, 2004, **98**, 87.

149 K.-E. Lokling, R. Skurtveit, A. Bjornerud and S. L. Fossheim, *Magn. Reson. Med.*, 2004, **51**, 688.

150 S. Faulkner and B. P. Burton-Pye, *Chem. Commun.*, 2005, 259.

151 M. P. Lowe and D. Parker, *Chem. Commun.*, 2000, 707.

152 M. P. Lowe and D. Parker, *Inorg. Chim. Acta*, 2001, **317**, 163.

153 S. Blair, M. P. Lowe, C. E. Mathieu, D. Parker, P. K. Senanayake and R. Kataky, *Inorg. Chem.*, 2001, **40**, 5860.

154 M. Woods and A. D. Sherry, *Inorg. Chem.*, 2003, **42**, 4401.

155 T. Gunnlaugsson, J. P. Leonard, K. Senechal and A. J. Harte, *J. Am. Chem. Soc.*, 2003, **125**, 12062.

156 R. Ramage, D. Hopton, M. J. Parrott, G. W. Kenner and G. A. Moore, *J. Chem. Soc.; Perkin Trans. 1*, 1984, **6**, 1357.

157 H. M. I. Osborn, A. A. Cantrill and J. B. Sweeney, *Tetrahedron Lett.*, 1994, **35**, 3159.

158 A. A. Cantrill, H. M. I. Osborn and J. B. Sweeny, *Tetrahedron*, 1998, **54**, 2181.

159 A. Beeby, L. Bushby, D. Maffeo and J. A. G. Williams, *J. Chem. Soc.; Dalton*, 2002, 48.

160 G. Brunisholz and M. Randin, *Helv. Chim. Acta*, 1959, **42**, 1927.

161 S. L. Murov, I. Carmichael and G. L. Hug, 'Handbook of Photochemistry, Second Edition', Marcel Dekker, 1993.

162 D. Parker, *Chem. Soc. Rev.*, 2004, **33**, 156.

163 S. W. Magennis, S. Parsons and Z. Pikramenou, *Chem. Eur. J.*, 2002, **8**, 5761.

164 M. D. Joesten and R. A. Jacob, 'Lanthanide Actinide Chemistry; Donor Properties of Pyrophosphate Derivitives', ed. R. F. Gould, *Am. Chem. Soc.*, 1967.

165 L. J. M. Kroft and A. de Roos, *J. Magn. Reson. Imaging*, 1999, **10**, 395.

166 R. B. Clarkson, 'Topics in Current Chemistry Vol 221; Blood Pool MRI Contrast Agents: Properties and Characterisation', ed. W. Krause, Springer, 2002.

167 A. L. Baert and K. Sartor, 'Magnetic Resonance Angiography, Second Edition', ed. I. P. Arlart, G. M. Bongartz and G. Marchal, Springer, 2002.

168 S. Gaillard, C. Kubiak, C. Stolz, B. Bonnemain and D. Chassard, *Invest. Radiol*, 2002, **37**, 161.

169 R. R. Edelman, *Radiology*, 2004, **232**, 653.

170 H. Kobayashi and M. W. Brechbiel, *Adv. Drug Deliver. Rev.*, 2005, **57**, 2271.

171 Z.-R. Lu, D. L. Parker, K. C. Goodrich, X. Wang, J. G. Dalle and H. R. Buswell, *Magn. Reson. Med.*, 2004, **51**, 27.

172 T. Ke, Y. Feng, J. Guo, D. L. Parker and Z.-R. Lu, *Magn. Reson. Imaging*, 2006, **24**, 931.

173 Y. Feng, Y. Zong, T. Ke, E.-K. Jeong, D. L. Parker and Z.-R. Lu, *Pharm. Res.*, 2006, **23**, 1736.

174 Y. Zong, J. Guo, T. Ke, A. M. Mohs, D. L. Parker and Z.-R. Lu, *J. Control. Release*, 2006, **112**, 350.

175 S. Curry, H. Mandelkow, P. Brick and N. Franks, *Nat. Struct. Mol. Biol.*, 1998, **5**, 827.

176 S. Curry, P. Brick and N. P. Franks, *BBA-Mol. Cell Biol. L.*, 1999, **1441**, 131.

177 G. Sudlow, D. J. Birkett and D. N. Wade, *Mol. Pharmacol.*, 1976, **12**, 1052.

178 G. Sudlow, D. J. Birkett and D. N. Wade, *Mol. Pharmacol.*, 1975, **11**, 824.

179 T. J. Peters, 'All About Albumin: Biochemistry, Genetics and Mediacal Applications', Academic Press, 1996.

180 V. S. Jisha, K. T. Arun, M. Hariharan, and D. Ramaiah, *J. Am. Chem. Soc.*, 2006, **128**, 6024.

181 M. T. Montero, R. Pouplana, O. Valls and S. Garcia, *J. Pharm. Pharmacol.*, 1986, **38**, 925.

182 U. Kragh-Hansen, *Pharmacol. Rev.*, 1981, **33**, 17.

183 R. B. Lauffer, D. J. Parmelee, H. S. Ouellet, R. P. Dolan, H. Sajiki, D. M. Scott, P. J. Bernard, E. M. Buchanan, K. Y. Ong, Z. Tyeklar, K. S. Midelfort, T. J. McMurry and R. C. Walovitch, *Acad. Radiol.*, 1996, **3**, S356.

184 R. B. Lauffer, USA, 1989.

185 R. B. Lauffer, D. J. Parmelee, S. U. Dunham, H. S. Ouellet, R. P. Dolan, S. Witte, T. J. McMurry and R. C. Walovitch, *Radiology*, 1998, **207**, 529.

186 D. J. Parmelee, R. C. Walovitch, H. S. Ouellet and R. B. Lauffer, *Invest. Radiol.*, 1997, **32**, 741.

187 P. Caravan, N. J. Cloutier, M. T. Greenfield, S. A. McDermid, S. U. Dunham, J. W. M. Butle, J. C. Amedio Jr., R. J. Looby, R. M. Supkowski, W. D. Horrocks Jr., T. J. McMurry and R. B. Lauffer, *J. Am. Chem. Soc.*, 2002, **124**, 3152.

188 P. Caravan, C. Comuzzi, W. Crooks, T. J. McMurry, G. R. Choppin and S. R. Woulfe, *Inorg. Chem.*, 2001, **40**, 2170.

189 J. H. Rapp, S. D. Wolff, S. F. Quinn, J. A. Soto, S. G. Meranze, S. Muluk, J. Blebea, S. P. Johnson, N. M. Rofsky, A. Duerinckx, G. S. Foster, K. C. Kent, G. Moneta, M. R. Middlebrook, V. R. Narra, B. D. Toombs, J. Pollak, E. K. Yucel, K. Shamsi and R. M. Weisskoff, *Radiology*, 2005, **236**, 71.

190 M. Goyen, M. Edelman, P. Perreault, E. O'Riordan, H. Bertoni, J. Taylor, D. Siragusa, M. Sharafuddin, E. R. Mohlerr III, R. Breger, E. K. Yucel, K. Shamsi and R. M. Weisskoff, *Radiology*, 2005, **236**, 825.

191 D. D. Suh, C. C. Yang, Y. Cao, J. R. Heiman, P. A. Garland and K. R. Maravilla, *J. Psychosom. Obstet. Gynecol.*, 2004, **25**, 153.

192 H. B. Eldredge, M. Spiller, J. M. Chasse, M. T. Greenwood and P. Caravan, *Invest. Radiol.*, 2006, **41**, 229.

193 T. N. Parac-Vogt, K. Kimpe, S. Laurent, L. Vander Elst, C. Burtea, F. Chen, R. N. Muller, Y. Ni, A. Verbruggen and K. Binnemans, *Chem. Eur. J.*, 2005, **11**, 3077.

194 R. N. Muller, B. Raduchel, S. Laurent, J. Platzek, C. Pierart, P. Mareski and L. Vander Elst, *Eur. J. Inorg. Chem.*, 1999, 1949.

195 J. Hamblin, N. Abboyi and M. P. Lowe, *Chem. Commun.*, 2005, 657.

196 S. Aime, E. Gianolio, D. Longo, R. Pagliarin, C. Lovazzano and M. Sisti, *ChemBioChem*, 2005, **6**, 818.

197 S. Aime, M. Botta, M. Fasano and E. Terreno, 'The Chemistry of Contrast Agents in Magnetic Resonance Imaging; Protein Bound Metal Chelates', ed. A. E. Merbach and E. Toth, Wiley, 2001.

198 S. Aime, E. Gianolio, E. Terreno, G. B. Giovenzana, R. Pagliarin, M. Sisti, P. Palmisano, M. Botta, M. P. Lowe and D. Parker, *J. Biol. Inorg. Chem.*, 2000, **5**, 488.

199 M. Botta, S. Quici, G. Pozzi, G. Marzanni, R. Pagliarin, S. Barra and S. G. Crich, *Org. Biomol. Chem.*, 2004, **2**, 570.

200 M. K. Thompson, D. M. J. Doble, L. S. Tso, S. Barra, M. Botta, S. Aime and K. N. Raymond, *Inorg. Chem.*, 2004, **43**, 8577.

201 D. Parker, 'Crown Compounds: Towards Future Applications; Tailoring Macrocycles for Medical Applications', ed. S. E. Cooper, VHC Publisher Inc., 1992.

202 J. I. Bruce, R. S. Dickins, L. J. Govenlock, T. Gunnlaugsson, S. Lopinski, M. P. Lowe, D. Parker, R. D. Peacock, J. J. B. Perry, S. Aime and M. Botta, *J. Am. Chem. Soc.*, 2000, **122**, 9674.

203 E. Schwenk and D. Papa, *J. Am. Chem. Soc.*, 1948, **70**, 3626.

204 L. Vander Elst, F. Chapelle, S. Laurent and R. N. Muller, *J. Biol. Inorg. Chem.*, 2001, **6**, 196.

205 K. Yamasaki, T. Maruyama, U. Kragh-Hansen and M. Otagiri, *Biochim. Biophy. Acta*, 1996, **1295**, 147.

206 A. L. Nivorozhkin, A. F. Kolodziej, P. Caravan, M. T. Greenfield, R. B. Lauffer and T. J. McMurry, *Angew. Chem. Int. Ed.*, 2001, **40**, 2903.

207 T. J. Meade, A. K. Taylor and S. R. Bull, *Curr. Opin. Neurobiol.*, 2003, **13**, 597.

208 A. Y. Louie, M. M. Huber, E. T. Ahrens, U. Rothbacher, R. Moats, R. E. Jacobs, S. E. Fraser and T. J. Meade, *Nat. Biotechnol.*, 2000, **18**, 321.

209 R. A. Moats, S. E. Fraser and T. J. Meade, *Angew. Chem. Int. Ed.*, 1997, **36**, 726.

210 J. A. Duimstra, F. J. Femia and T. J. Meade, *J. Am. Chem. Soc.*, 2005, **127**, 12847.

211 R. Weissleder and U. Mahmood, *Radiology*, 2001, **219**, 316.

212 S. Geninatti Crich, C. Cabella, A. Barge, S. Belfiore, C. Ghirelli, L. Lattuada, S. Lanzardo, A. Mortillaro, L. Tei, M. Visigalli, G. Forni and S. Aime, *J. Med. Chem.*, 2006, **49**, 4926.

213 S. Geninatti Crich, B. Bussolati, L. Tei, C. Grange, G. Esposito, S. Lanzardo, G. Camussi and S. Aime, *Cancer Res.*, 2006, **66**, 9196.

214 U. Himmelreich, S. Aime, T. Hieronymus, C. Justicia, F. Uggeri, M. Zenke and M. Hoehn, *Neuroimage*, 2006, **32**, 1142.

215 R. Y. Tsien, *Nature*, 1981, **290**, 527.

216 F. Katz, S. Malcom, B. Gibbons, R. Tilly, G. Lam, M. E. Robertson, B. Czepulkowski and J. Chessells, *Blood*, 1988, **71**, 1438.

217 M. Botta, S. Aime, A. Barge, G. Bobba, R. S. Dickins, D. Parker and E. Terreno, *Chem. Eur. J.*, 2003, **9**, 2102.

218 C. J. Bachmeier, W. J. Trickler and D. W. Miller, *J. Pharm. Sci.*, 2003, **93**, 932.

219 J. P. Whitehead, J. C. Molero, S. Clark, S. Martin, G. Meneilly and D. E. James, *J. Biol. Chem.*, 2001, **276**, 27816.

220 M. Tenopoulou, P.-T. Doulias, A. Barbouti, U. Brunk and D. Galaris, *J. Biochem.*, 2005, **387**, 703.

221 Y. N. Korystova, N. V. Ermakova, L. N. Kublika, M. K. Levitmana, V. V. Shaposhnikovaa, V. A. Mosinb, V. A. Drinyaevb, E. B. Kruglyakb, T. S. Novikb and T. S. Sterlina, *Eur. J. Pharmacol.*, 2004, **493**, 57.

222 T. van der Wijk, S. F. B. Tomassen, A. B. Houtsmuller, H. R. de Jonge and B. C. Tilly, *J. Biol. Chem.*, 2003, **278**, 40020.

223 S. I. Kang, R. S. Ranganathan, J. E. Emswiler, K. Kumar, J. Z. Gougoutas, M. F. Malley and M. F. Tweedle, *Inorg. Chem.*, 1993, **32**, 2912.

224 R. Rai and J. A. Katzenellenbogen, *J. Med. Chem.*, 1992, **35**, 4150.

225 M. M. Meijler, R. Arad-Yellin, Z. L. Cabantchik and A. Shanzer, *J. Am. Chem. Soc.*, 2002, **124**, 12666.

226 G. M. Cooper and E. E. Hausman, 'The Cell; A Molecular Approach 4th Edition', ASM Press, 2004.

227 A. K. Covington, *Chem. Soc. Rev.*, 1985, **14**, 265.

228 M. Mato-Iglesias, C. Platas-Iglesias, K. Djanashvili, J. A. Peters, E. Toth, E. Balogh, R. N. Muller, L. Vander Elst, A. de Blas and T. Rodriguez-Blas, *Chem. Commun.*, 2005, 4729.

229 E. J. Toone, M. J. Werth and J. B. Jones, *J. Am. Chem. Soc.*, 1990, **112**, 4946.

230 C. H. Tran and D. H. G. Crout, *J. Chem. Soc.; Perkin Trans. 1*, 1998, 1065.

231 A. K. Mishra, *J. Drug Target.*, 2004, **12**, 559.

232 S. Aime, M. Botta, M. Fasano and E. Terreno, *Spectrchim. Acta*, 1993, **49A**, 1315.

233 J. A. Peters, J. Huskens and D. J. Raber, *Prog. Nucl. Mag. Res. Spectrosc*, 1996, **28**, 283.

234 D. Corsi, C. Platas-Iglesias, H. van Bekkum and J. A. Peters, *Magn. Reson. Chem.*, 2001, **39**, 723.

235 G. Swarzenbach and H. Flaschka, 'Complexometric Titrations, 2nd English Edition', ed. M. C. Ltd, 1969.

236 A. Barge, G. Cravotto, E. Gianolio and F. Fedeli, *Contrast Med. Mol. Imaging*, 2006, 184.